

**TRANSPORT OF SOLAR WIND FLUCTUATIONS:
A TURBULENCE APPROACH**

by
Sean Oughton

A dissertation submitted to the Faculty of the University of Delaware in partial fulfillment
of the requirements for the degree of Doctor of Philosophy in Physics

May 1993

© 1993 Sean Oughton
All Rights Reserved

**TRANSPORT OF SOLAR WIND FLUCTUATIONS:
A TURBULENCE APPROACH**

by
Sean Oughton

Approved: _____
James B. Mehl, Ph.D.
Chairman of Department of Physics and Astronomy

Approved: _____
Carol E. Hoffecker, Ph.D.
Associate Provost for Graduate Studies

I certify that I have read this dissertation and that in my opinion it meets the academic and professional standard required by the University as a dissertation for the degree of Doctor of Philosophy.

Signed: _____

William H. Matthaeus, Ph.D.
Professor in charge of dissertation

I certify that I have read this dissertation and that in my opinion it meets the academic and professional standard required by the University as a dissertation for the degree of Doctor of Philosophy.

Signed: _____

Edward H. Kerner, Ph.D.
Member of dissertation committee

I certify that I have read this dissertation and that in my opinion it meets the academic and professional standard required by the University as a dissertation for the degree of Doctor of Philosophy.

Signed: _____

Stanley P. Owocki, Ph.D.
Member of dissertation committee

I certify that I have read this dissertation and that in my opinion it meets the academic and professional standard required by the University as a dissertation for the degree of Doctor of Philosophy.

Signed: _____

D. Aaron Roberts, Ph.D.
Member of dissertation committee

I certify that I have read this dissertation and that in my opinion it meets the academic and professional standard required by the University as a dissertation for the degree of Doctor of Philosophy.

Signed: _____

Gary P. Zank, Ph.D.
Member of dissertation committee

EPIGRAPH

A process cannot be understood by stopping it.
Understanding must move with the flow of the
process, must join it and flow with it.

— Frank Herbert: *Dune*

ACKNOWLEDGMENTS

I would like to thank and acknowledge my advisor, and friend, Bill Matthaeus for suggesting the problem addressed in this thesis; his contributions, advice, and physical insight have been of recurring value. I would also like to thank him for giving me the freedom to work as, when, and where I saw fit, while also providing valuable guidance in these and other matters.

The following people are also deserving of my thanks, for providing helpful conversations and/or instruction regarding this work and/or physics in general: Nick Arge, John Bieber, Dave Clements, Denis Donohue, Phil Isenberg, Ron Ghosh, Mel Goldstein, Perry Gray, Carl Greeff, Dave Huber, Murshed Hossain, Prof. Kerner, Larry Klein, Marty Lee, Daniel Martínez, Dave Montgomery, Dermott Mullan, Stan Owocki, Duane Pontius, Karl-Heinz Rädler, Aaron Roberts, Ed Serigar, Chuck Smith, Todd Story, Troy Stribling, Chan Yoo, and Gary Zank. The open and relaxed approach of many of the faculty members with whom I interacted at Bartol and the DPA was much appreciated, helping to make my stay here an enjoyable one. I thank all my teachers in proportion to their time and efforts.

Nick Arge and Dave Clements have also made valuable contributions in connection with this work, and I thank them for reading all or part of this manuscript. John Jebb's proof reading of some of the Chapters is gratefully acknowledged, as are Alex Fullerton's expert advice concerning IDL, and John van Stekelenborg's assistance with PostScript.

This work would not have been completed without the computational resources provided by the Bartol Research Institute and the San Diego Supercomputing Center. Financial support for the duration of this research was provided by the Bartol Research Institute, NASA, under the SPTP grant NAGW-2076, and the National Science Foundation, under grant ATM 8913627; for this, I am distinctly grateful.

On a less scientific note, I wish to extend my thanks to the office staff at Bartol and the DPA, for cheerful (and often last minute) assistance in matters administrative, and also to the staff at that fine establishment The Deer Park, for providing a refreshingly relaxing atmosphere at all times. Finally, to friends (both local and global) and family who have visited and/or fraternized with me here in Newark, and Mark Moir in particular, thanks.

TABLE OF CONTENTS

LIST OF FIGURES	x
LIST OF TABLES	xiv
 Chapter	
1 INTRODUCTION	1
1.1 Background	1
1.2 Overview	9
2 THE SOLAR WIND	11
2.1 Introduction	11
2.2 General Characteristics	11
2.3 Theory of the Large-Scale Structure	17
2.4 The MHD Description	20
2.4.1 The MHD Equations	20
2.4.2 MHD Waves	23
2.4.3 Applicability	25
2.5 Solar Wind Fluctuations	27
2.5.1 Introduction	27
2.5.2 Waves and WKB Theory	30
2.5.3 Turbulence	32
2.5.4 Review of Observationally Based Conclusions	33
2.5.4.1 Cross Helicity Evolution	34
2.5.4.2 Spectra	35
2.5.4.3 Compressional Effects	38
3 CORRELATION TENSORS FOR GENERAL HOMOGENEOUS TURBULENCE	40
3.1 Introduction	40
3.2 Definitions and Notation	40
3.3 Basic Results	45

3.4	Explicit Forms for the Tensors	47
3.4.1	Introduction	47
3.4.2	Theory for Construction of the Tensors	48
3.4.3	Tensor Forms and the Vector Potentials	49
3.4.4	Tensor Forms and the Scalar Potentials	51
3.5	Physical Interpretations of the Generating Scalar Functions	58
3.6	Special Cases	61
3.6.1	Isotropic Symmetry	62
3.6.2	Mirror Symmetry	63
3.6.3	Axisymmetry and the Presence of a Mean Field	63
3.6.4	Two-Dimensional Symmetry	63
3.6.5	Slab Symmetry	64
3.7	Theorem AA	64
3.8	Measurement Issues	66
3.9	Elsässer Variable Representations	67
4	THE SPECTRAL TRANSPORT MODEL	69
4.1	Introduction	69
4.2	Derivation and Approximations	70
4.3	Simplifications of the Transport Equations	80
4.4	The Mixing Tensors	84
4.5	Relationship to WKB	87
5	INERTIAL RANGE TRANSPORT	91
5.1	Introduction	91
5.2	The Linear Equations	91
5.2.1	Numerics	94
5.2.2	Isotropic Fluctuations	99
5.2.2.1	Reduced Spectra	99
5.2.2.2	Omni-Directional Spectra	103
5.2.3	Two-Dimensional Fluctuations	107
5.2.4	Slab Fluctuations	111
5.2.5	Approach to WKB Solutions	114
5.2.6	Comparison with Observations	116
5.3	Modeling of the Non-linear Terms	117
5.3.1	Introduction	117
5.3.2	Kolmogorov-style Approximations	118
5.3.3	Diffusion Approximations	120

5.3.4	Cross Helicity Effects	121
5.3.5	Energy Difference	123
5.3.6	Numerics	124
6	TRANSPORT OF ENERGY-CONTAINING FLUCTUATIONS	130
6.1	Introduction	130
6.1.1	Historical Background	130
6.2	The Linear Transport Terms	133
6.3	Modeling of the Non-Linear Terms	137
6.3.1	Equilibrium and Quasi-equilibrium Kolmogorov Turbulence	137
6.3.2	Homogeneous MHD Turbulence	139
6.4	Application to the Solar Wind	145
6.4.1	The Model	145
6.4.2	Numerics	148
6.4.3	Solutions	149
6.4.3.1	Isotropic Turbulence	150
6.4.3.2	Two-Dimensional Turbulence	152
6.4.4	Heating of the Solar Wind	154
6.5	Results from the Full Inertial Range Model	158
6.6	Discussion and Closing Remarks	161
Appendix		
A	MHD TURBULENCE	170
A.1	Introduction	170
A.2	Rugged Invariants	174
A.3	Spectral Transfer	176
A.4	The Alfvén Effect	178
A.5	Relaxation Processes	178
A.6	Compressional Turbulence	180
B	SCALAR POTENTIALS FOR SOLENOIDAL VECTOR FIELDS	181
C	SPECTRAL FORMS AND EVALUATION OF THE MIXING TENSORS	183
C.1	Matrix Forms for M_{ki}^{\pm}	183
C.2	Contraction with the small-scale tensors	184
C.2.1	Isotropic Turbulence	185
C.2.2	Two-Dimensional Turbulence	188

C.2.3 Slab Turbulence	189
D ANALYTIC SOLUTIONS FOR THE INERTIAL RANGE EQUATIONS . .	191
E PHYSICAL SCALES IN THE SOLAR WIND	194
BIBLIOGRAPHY	196

LIST OF FIGURES

1.1	Schematic diagram showing an average configuration for the radially directed solar wind velocity and the Archimedean spiral magnetic field. The indicated speed of 300 km/sec is an older average value; these days a more widely accepted value is approximately 400 km/sec. The fluctuations, which are the central focus of this thesis, are not shown. After <i>Hundhausen</i> [1972].	2
2.1	Schematic sketch showing some major features of the heliosphere and the surrounding region. Not all of the features shown have been observationally verified. The filled arrows indicate the flow of the supersonic solar wind, while the open straight arrows represent the interstellar wind. The approximate distances indicated are given in astronomical units (AU). After <i>Parks</i> [1991].	12
2.2	Schematic diagram showing the interaction of high- and low-speed solar wind streams in the ecliptic plane. After <i>Hundhausen</i> [1972].	14
2.3	Schematic diagram of the Parker spiral magnetic field and the radial solar wind in the ecliptic. (a) The geometry as it appears in an inertial frame, (b) the same situation viewed from a frame rotating with the sun. In order to understand why this geometry exists, it may help to visualize the water jets from a rotating garden sprinkler, or the sparks from a Catherine wheel at a fireworks display. After <i>Hundhausen</i> [1972].	16
2.4	Sketch of the four solution classes for the original Parker theory of a steady-state expanding corona. The abscissa is heliocentric distance measured in units of critical radii, while the ordinate is the flow velocity measured relative to the sound speed at the critical radius. After <i>Hundhausen</i> [1972].	19
2.5	Averaged Elsässer spectra for Helios data obtained near 0.3 AU. The upper curves are for “outward” fluctuations and the lower ones for the “inward” modes. The figure is taken from <i>Tu et al.</i> [1989].	37
4.1	Schematic diagram showing the structure of the linear portions of the transport equations for the traced spectra.	79
4.2	Plots of the effective mixing operators as a function of heliocentric distance in AU. (a) The case $V_{Ar0} = 0$ (for which $M^+ = M^-$), (b) the case $V_{Ar0} = U$. The isotropic versions are plotted using solid lines, and the 2D forms using broken lines. In (b) the M^- forms are indicated by the thinner solid line and the dotted line. The inner boundary is located at $R_0 = 10 R_{sun}$	86

- 4.3** Plots of the coefficients in the transport equations for the traced fields, as a function of heliocentric distance. The coefficient $(U + V_{Ar})/R$ is shown as the thin solid line, $(U - V_{Ar})/R$ as the thick solid line, U/R as the dashed, and M_{2D}^+ as the dotted line. The inner boundary is located at 10 solar radii, and $V_{Ar0} = U$. (a) The range $R = 10 R_{sun}$ to 1 AU, (b) the range 1–2 AU. 88
- 5.1** Diagram showing the distribution of the Gauss-Lobatto collocation points in the natural domain of the Chebyshev polynomials when $N = 32$. The “necklace” of diamonds shows the same information as the horizontal set, the only difference being that neighboring collocation points have been vertically offset. This vertical displacement is provided solely for clarity and has no intrinsic meaning. 96
- 5.2** Example plots showing the distributions of the Gauss-Lobatto points in R -space for each of the two types of mapping considered in the text. (a) Semi-infinite mapping with $L \equiv 1$ AU; (b) Finite mapping with $L \equiv 2$ AU. For pictorial clarity, $N = 32$ is used, a value which is much lower than the resolutions used in the production runs. The horizontal coordinate is R in units of AU. Note that in (a), only the points inside 5 AU are shown. See also Figure 5.1. 97
- 5.3** The effect of V_A on the radial evolution of the reduced spectra for isotropic turbulence. The quantities plotted are spectral amplitudes at a fixed but arbitrary inertial range wavenumber. The horizontal coordinates are all heliocentric distance in AU. The solar wind speed is 400 km/sec, $R_0 = 10 R_{sun}$, $\alpha = \frac{5}{3}$, and “standard” boundary conditions are imposed. The solid curves are for $V_{Ar0} = U$, and the dashed for $V_{Ar0} = 0$. See also the next two figures. 101
- 5.4** Expanded view of the region in which the M^+ operator for isotropic turbulence changes sign. Solid curve: P^+ , dashed curve: F , dotted curve: M^+ . The horizontal coordinate is heliocentric distance (AU), and for clarity the vertical scalings have been adjusted. The growth (decay) of P^+ when F and M^+ have opposite (same) signs is evident. 102
- 5.5** Radial evolution of the directly calculated reduced spectral amplitudes for isotropic turbulence. Shown are P^\pm , the normalized energy difference, and the normalized cross helicity when $U = V_{Ar0} = 400$ km/sec. The solid curves are for $\alpha = 1$, the dashed for $\alpha = \frac{5}{3}$, and the dotted for $\alpha = 2$. The inner boundary is at 10 solar radii. “Standard” boundary conditions apply. Horizontal coordinates are heliocentric distance in AU. 104
- 5.6** Radial evolution of the various omni-directional spectral densities for isotropic turbulence (at fixed inertial range wavenumber). “Standard” boundary conditions are imposed and $R_0 = 10 R_{sun}$. The horizontal coordinate is heliocentric distance (AU). Solid curves: $V_{Ar0}/U = 1$. Dashed curves: $V_{Ar0}/U = 0$ 106

- 5.7** Radial evolution of the normalized cross helicity and normalized energy difference of isotropic turbulence for some non-“standard” boundary conditions (spectral amplitude at fixed wavenumber). In each case $R_0 = 10 R_{sun}$, and $V_{Ar0} = U$. The evolution for two initial values of F is shown when $P^+ = 0.01$, $P^- = 1$: $F = 0.1$ (dashed curve), $F = 0.2$ (dotted curve). The solid curves are the solutions for “standard” boundary conditions. Solutions for $P_0^+ = 0.01$, $P_0^- = 1$, and $F_0 = 0$, are visually indistinguishable from the “standard” case when plotted at this scale. The horizontal coordinate is heliocentric distance (AU). 107
- 5.8** Radial evolution of various spectral densities for 2D turbulence (at an arbitrary inertial range wavenumber) . All plots are for “standard” bc’s and $R_0 = 10 R_{sun}$. The left-hand panels show the omni-directional (solid curves) and reduced (dotted curves) spectra for the case $V_{Ar0} = U$. The right-hand panels display the normalized cross helicity and normalized energy difference for the two cases $V_{Ar0}/U = 0$ (dashed curves) and 1 (solid curves). As usual, the horizontal coordinate is heliocentric distance in AU. 110
- 5.9** The radial evolution, or lack thereof, of various normalized quantities for slab fluctuations (spectral amplitudes at $k_1 = 50$). The solutions are for “standard” bc’s, $R_0 = 10 R_{sun}$, and $V_{Ar0} = U$. The lower plots should actually be plotted using vertical bounds of ± 1 , but such plots de-emphasize the oscillations. As usual, the horizontal coordinate is heliocentric distance in AU. 112
- 5.10** Comparison plots of the omni-directional and reduced spectral amplitudes for 2D and slab turbulence. All plots are for “standard” bc’s, $V_{Ar0} = U$, and $R_0 = 10 R_{sun}$. To avoid the oscillations seen in Figure 5.9, the slab curves are for $k_1 = 0$. Solid curves: omni-directional spectral amplitudes for both 2D and slab fluctuations; Dashed curves: reduced spectral amplitudes for 2D fluctuations; Dotted curves: reduced spectral amplitudes for slab fluctuations. The reduced curves are calculated for $\alpha = 5/3$. As usual, the horizontal coordinate is heliocentric distance in AU. 113
- 5.11** Plots showing the convergence of slab solutions towards WKB results as the wavenumber is increased (“standard” bc’s, $R_0 = 10 R_{sun}$, $V_{Ar0} = U$). Solid curves: $k = 0$; Dashed curves: $k = 2$; Dotted curves: $k = 5$. A unit wavenumber in code units is equivalent to $2\pi/R_0$ in physical units. This approach to WKB results has also been discussed by *Heinemann and Olbert [1980]* for linear toroidal waves. As usual, the horizontal coordinate is heliocentric distance in AU. 115
- 5.12** Plots of the numerical solutions to the linear transport equations for the normalized cross helicity and energy difference, with observational data points superimposed. 116

5.13	Numerical solutions for the spectrum of P^+ obtained using the diffusion model. There is no large-scale magnetic field imposed and $P^+ = P^-$. The initial conditions are shown as dotted lines, and the solutions after one characteristic time by the solid curves. The dashed lines, just visible underneath the solid curves, are the correct steady solutions ($\epsilon^{2/3}k^{-5/3}$). In the left-hand figure $\epsilon^\pm = 10$, and $\Delta t = 2.5 \times 10^{-6}$, while on the right $\epsilon^\pm = 0.01$, and $\Delta t = 2 \times 10^{-5}$. There are twenty wavenumbers per decade and $k_1 = 30$	127
5.14	Numerical solutions for the spectra of P^\pm obtained using the diffusion model with and without viscosity. The plots shown are for $P^+ = 0.01P^-$ at $t = 0$, and $V_A = 0$. The initial conditions are shown as dotted lines, and the dash-dot-dot-dot lines are $k^{-5/3}$ curves provided for comparison. The other curves are solutions after one characteristic time. Dashed lines: no viscosity; Solid lines: $\bar{\nu} = 10^{-4}$. In both cases $\epsilon^+ = 10^{-4}$, $\epsilon^- = 10^{-2}$, and $\Delta t = 2.5 \times 10^{-6}$. Twenty wavenumbers per decade are used and $k_1 = 30$	128
6.1	Radial evolution of various bulk quantities for isotropic turbulence when $U = 4$ (<i>i.e.</i> , solar wind speed of 400 km/sec).	151
6.2	Radial evolution of various bulk quantities for isotropic turbulence when $U = 7$ (<i>i.e.</i> , solar wind speed of 700 km/sec).	153
6.3	Radial evolution of various bulk quantities for 2D turbulence when $U = 4$ (<i>i.e.</i> , solar wind speed of 400 km/sec).	155
6.4	Radial evolution of various bulk quantities for 2D turbulence when $U = 7$ (<i>i.e.</i> , solar wind speed of 700 km/sec).	156
6.5	Radial profiles of the energy decay rate and fractional energy decay rate, for some of the solutions discussed in section 6.4.3.	157
6.6	Omni-directional spectra at several heliocentric distances, and radial evolution plots for several wavenumbers for the isotropic full inertial range model.	160
6.7	Omni-directional spectra at several heliocentric distances, and radial evolution plots for several wavenumbers for the 2D full inertial range model.	162
6.8	Spectra and radial evolution plots for the normalized cross helicity in the full 2D inertial range model run.	163

LIST OF TABLES

3.1	Some basic properties of the four “primary” spectral tensors. As far as the properties listed here are concerned, the v/b tensors behave in the same fashion as the “+” ones. See the text for details and the appropriate forms in x -space. . . .	47
3.2	Further properties of the symmetric and antisymmetric components of the “primary” spectral tensors. Note the anomalous behavior of the “minus” tensors. In x -space, columns 2, 4, and 5 still apply, but all quantities are of course purely real.	48
3.3	Summary of the properties of the generating scalar functions and their multiplying “parts with indices” for each of the “primary” tensors.	58
3.4	Some correlation functions and spectral tensors in terms of the primitive variables \mathbf{v} and \mathbf{b} . Primed ($'$) variables are evaluated at $\mathbf{x} + \mathbf{r}$ while unprimed variables are evaluated at \mathbf{x} . Note that in these tables, R and S no longer denote general tensors, but rather the specific ones associated with the total energy (kinetic plus magnetic) of the system. See the text for details.	68
3.5	Some correlation functions and spectral tensors in terms of Elsässer variables. Because of conflicts with the notation of later chapters, the I – J notation for the symmetric and antisymmetric components is not used in these tables; instead these pieces are denoted by the superscripts “ s ” and “ a ” respectively.	68
4.1	Some correlation functions and spectral tensors in terms of the primitive variables \mathbf{v} and \mathbf{b} . Primed ($'$) variables are evaluated at $\mathbf{x} + \mathbf{r}$, unprimed at \mathbf{x} . See Chapter 3 for further details, but be aware that some notational differences exist between the chapters; in particular, here \mathbf{b} is not measured in Alfvén speed units. All quantities are also functions of the large-scale spatial coordinate \mathbf{R}	75
4.2	Some correlation functions and spectral tensors in terms of Elsässer variables. The superscripts “ s ” and “ a ” denote the symmetric and antisymmetric parts of the tensor respectively. As in Table 4.1, the dependence of each form on the large-scale spatial coordinate \mathbf{R} has been suppressed.	76
4.3	Some useful relations involving the traces of various spectra. These definitions and identities hold for all three spectral types: modal, omni-directional, and reduced. All quantities are functions of the large-scale coordinate \mathbf{R} and appropriate components of the wave-vector \mathbf{k}	76

D.1	Coefficients in the general form of the mixing operators when $V_{Ar0}/U = 0$. See equation (D.1). Unless otherwise noted, these coefficients apply to the mixing operators appropriate for omni-directional spectra. See section 4.4 and Appendix C for further details regarding the mixing operators.	191
E.1	Characteristic Properties of the Solar Wind at 1 AU.	194
E.2	Characteristic Lengths associated with the Solar Wind.	194
E.3	Characteristic Speeds associated with the Solar Wind.	195
E.4	Characteristic Times associated with the Solar Wind.	195
E.5	Approximate Limits of the Inertial Range of Solar Wind Power Spectra at 1 AU. The frequencies and periods are those in the spacecraft frame, while the wavenumbers are calculated using the “frozen-in” flux approximation [<i>e.g.</i> , <i>Matthaeus and Goldstein, 1982a, b</i>].	195

ABSTRACT

Recently developed scale separated models for the transport of MHD scale turbulence in a weakly inhomogeneous background plasma, provide a basis for computing both radial and temporal dependence of solar wind fluctuations. Development of the new model was prompted by the inability of traditional approaches to explain the observed radial evolution properties of various quantities, and by the need for a formalism to provide information on the dynamical evolution of turbulence, for use in models of solar wind acceleration and heating.

In its most general form the model allows the evolution of wavenumber spectra to be followed; however, it may also be adapted to a simpler form, wherein the spectra are integrated over wavenumber to obtain spatial transport equations for bulk quantities characterizing the fluctuations, such as energy and cross helicity. When the solar wind fluctuations are considered to be MHD turbulence, the two forms of the model can respectively be used to obtain the evolution of the inertial range spectra and the energy-containing range quantities. The model includes the effects of advection, wave propagation, expansion, non-WKB “mixing,” as well as recently developed phenomenological models for non-linear decay of both the energy-containing and the inertial range fluctuations in MHD turbulence.

We derive the model and describe its numerical implementation, which is based upon a Chebyshev representation of the (large-scale) spatial dependence of the fluctuations. Solutions are obtained for the evolution of magnetic energy, kinetic energy, and cross helicity of the fluctuations, under the influence of linear transport effects and non-linear effects appropriate to 2D or 3D isotropic turbulence, with specified large scale flow and magnetic field. The model accurately reproduces WKB and other well known solutions (such as steady inertial range spectra) in special cases. Comparison of the solutions with observational data shows that, for some conditions, the models have the potential to partially explain the observed evolutions of the cross helicity and the kinetic-to-magnetic energy ratio.

Additionally, as an auxiliary problem, the general properties and forms of correlation functions and spectra for homogeneous MHD turbulence have been investigated in some detail. Several important and apparently new results have arisen from this work, which completes the theory of

homogeneous second order correlation functions for MHD turbulence of arbitrary rotational symmetry.

Chapter 1

INTRODUCTION

In a way, art is a theory about the way the world looks to human beings. It's abundantly obvious that one doesn't know the world around us in detail. What artists have accomplished is realizing that there's only a small amount of stuff that's important, and then seeing what it is.

— Mitchell Feigenbaum

1.1 Background

The solar wind is the extension of the sun's atmosphere out into interplanetary space, consisting largely of ionized hydrogen. The plasma is almost collisionless, magnetized, and, despite being highly ionized, approximately neutral. For the purposes of this introduction, we characterize the solar wind in terms of three major fields:

- (1) a supersonic velocity field, \mathbf{V} , essentially radially directed, with a speed approximately equal to the mean velocity of the thermal proton population;
- (2) a magnetic field, \mathbf{B} , of solar origin, twisted into a large Archimedean spiral (see Figure 1.1);
and
- (3) a density field, ρ , also dominated by the thermal proton population, and tenuous enough to make the interplanetary plasma essentially collisionless beyond a few solar radii.

Each of these fields exhibits a more or less reproducible character, so that it is meaningful to decompose them into mean pieces (\mathbf{U} , \mathbf{B}_0 , ρ_0)—which may still vary in space—and attendant fluctuations (\mathbf{v} , \mathbf{b} , $\delta\rho$). For various reasons, fluctuations at magnetohydrodynamic (MHD) scales in the solar wind, which have long been observed [*e.g.*, Coleman, 1966, 1967; Belcher and Davis, 1971], are of particular interest and importance. It is the transport and (radial) evolution of such fluctuations in the velocity and magnetic fields which is the central focus of this thesis. Using a transport model based on a multiple scales analysis of the dynamical equations for the solar wind, the evolution of the fluctuations will be computed as they move radially outwards away from the

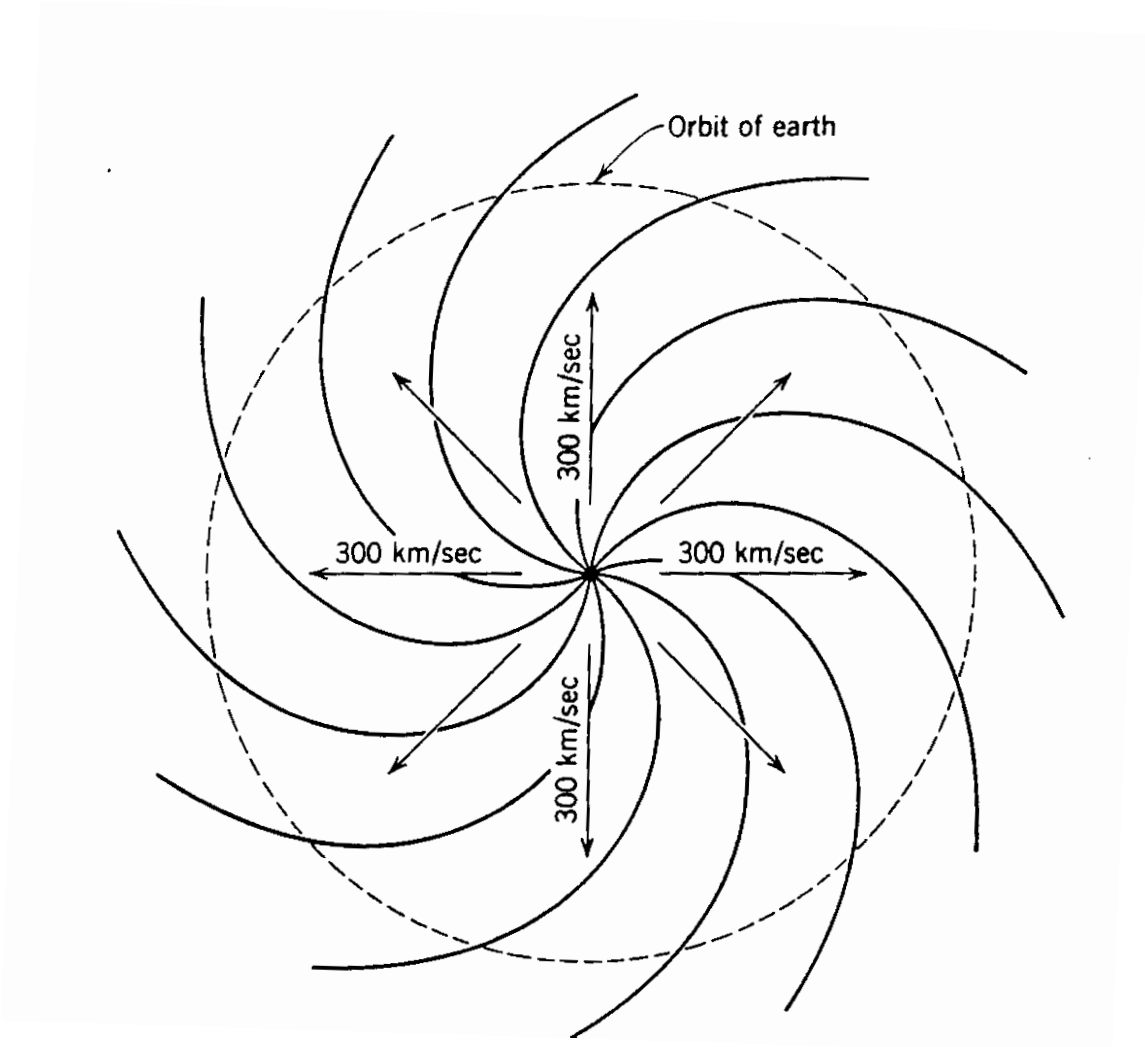


Figure 1.1: Schematic diagram showing an average configuration for the radially directed solar wind velocity and the Archimedean spiral magnetic field. The indicated speed of 300 km/sec is an older average value; these days a more widely accepted value is approximately 400 km/sec. The fluctuations, which are the central focus of this thesis, are not shown. After *Hundhausen* [1972].

sun. A major aim will be to reveal the extent to which couplings between the fluctuations and the mean fields influence this evolution, an effect we refer to as “mixing.” Additionally, models for the local turbulent dynamics of the fluctuations will be presented. Prefiguring the results, it has been found that in certain cases, notably two-dimensional turbulence, the “mixing” couplings are leading order linear effects that lead to solutions *qualitatively* different from those arising in more traditional approaches (*e.g.*, WKB theory, see below). These new solutions show potential for explaining the observed radial evolution of physical quantities like the kinetic and magnetic energy of solar wind fluctuations.

In fact, we will not usually work with the velocity and magnetic field fluctuations directly, but instead their sum and difference, $\mathbf{z}^{\pm} = \mathbf{v} \pm \mathbf{b}/\sqrt{4\pi\rho_0}$, the *Elsässer* [1950] variables. This in no way affects the underlying physics, merely affording an alternative interpretation in terms of “inward” and “outward” type fluctuations. For an outwardly directed \mathbf{B}_0 , fluctuations that have $\mathbf{v} = -\mathbf{b}/\sqrt{4\pi\rho_0}$, equivalent to $\mathbf{z}^+ = 0$, represent purely outwardly propagating Alfvén waves. Similarly, $\mathbf{v} = \mathbf{b}/\sqrt{4\pi\rho_0}$ fluctuations, are purely inwardly propagating waves. Variations of either kind, *i.e.*, $\mathbf{z}^{\pm} = 0$, are known as *Alfvénic fluctuations*. For convenience we will refer to the \mathbf{z}^+ fluctuations as “inward” propagating in character, whether or not $\mathbf{z}^- = 0$, and the \mathbf{z}^- disturbances as “outward” propagating fluctuations, independent of the vanishing of \mathbf{z}^+ .

One reason for investigating MHD fluctuations in the solar wind, is to obtain experimental data on the dynamics of MHD processes, including instabilities, relaxation processes, and turbulence. In general, such information cannot be obtained in terrestrial laboratories, because these facilities are often only capable of investigating regimes of more limited importance to MHD dynamics, especially with regard to systems with high mechanical and magnetic Reynolds numbers,¹ *i.e.*, turbulence. As a “natural laboratory” for the investigation of MHD processes, the solar wind has the dual advantages of being (a) relatively easy to probe, and (b) a dynamically active MHD environment, with many decades of interacting length and time scales, which is still somewhat reproducible (even if not under the experimentalist’s control). Increased understanding of the various instabilities and relaxation processes of MHD may be useful in applications ranging from the origin of galactic cosmic rays to more practical issues, such as commercial fusion technology.

Since the MHD description is an inherently fluid approach,² it is initially somewhat surprising that solar wind fluctuations can be treated on such a footing. Given that the interplanetary

¹ These dimensionless numbers provide a measure of the degree to which a fluid is turbulent. Values in excess of a few thousand generally indicate fully developed turbulence.

² Or more accurately a magnetofluid approach.

medium is an almost collisionless plasma, kinetic theory would seem to be more appropriate. The applicability of the fluid approach is discussed in Chapter 2; for now we take it for granted.

Observations indicate that the correlation lengths for MHD scale fluctuations are usually only a small fraction of the length scales characterizing variations in the mean fields. Thus, there is a natural *scale separation* in the problem and the possibility of exploiting it to obtain solutions. In the solar wind, it is also usually the case that the length scale characteristic of the magnetic helicity containing structures is greater than the analogous quantity for the energy-containing eddies [Matthaeus and Goldstein, 1982a]. This suggests that, at some point in its history, the magnetofluid has undergone turbulent evolution, and in particular may have experienced an *inverse cascade* of magnetic helicity. An inverse cascade of some quantity involves its transfer from smaller length scales to larger ones, and mandates the action of non-linear processes. Typically such cascades are seen in externally driven turbulence, such as is believed to occur in both the solar convection zone and the solar corona.

Consider now the spectral decomposition of the fluctuations. Power spectra are typically found to extend over many decades in frequency (or wavenumber) space. Furthermore, the spectra often exhibit powerlaw behavior for three or four of these decades; that is, these portions of the spectra are of the form $k^{-\alpha}$, where k is the wavenumber and α the spectral index. Typically these powerlaw portions have spectral slopes of somewhere between 1 and 2 [Sari and Valley, 1976], with values near $\alpha = \frac{5}{3}$ being rather common. This latter value is the same as that appropriate for incompressible, isotropic hydrodynamic turbulence [Kolmogorov, 1941]. The solar wind is certainly not incompressible, or even isotropic in general, and since the fluctuations have comparable kinetic and magnetic energies, the hydrodynamic description must be abandoned in favor of an MHD one. Thus, the appearance of Kolmogorov-like spectra in the solar wind would seem to be somewhat puzzling. However, it does suggest that ideas from incompressible turbulence are relevant to the solar wind, at least for the local dynamics. Recent work on *nearly incompressible* hydrodynamics and MHD [Montgomery et al., 1987; Matthaeus and Brown, 1988; Zank et al., 1990; Zank and Matthaeus, 1990, 1991, 1992a, b, 1993] has clarified the relevance somewhat, and will be discussed further in later chapters.

The powerlaw behavior of the spectra is another indication that at least one *non-linear* dynamical process has actively influenced the evolution of the solar wind plasma. The question which arises is: “Are the fluctuations still evolving non-linearly, or are they instead dynamically

passive, wave-like remnants of processes occurring in the lower solar atmosphere³ which are being advected outwards with the supersonic wind?” In the last decade or so, observational analyses [e.g., *Bavassano et al.*, 1982*a, b*; *Matthaeus and Goldstein*, 1982*a, b*; *Roberts et al.*, 1987*a, b*; *Tu et al.*, 1989; *Grappin et al.*, 1990; *Matthaeus et al.*, 1990] and theoretical advances [e.g., *Tu et al.*, 1984; *Tu*, 1988; *Zhou and Matthaeus*, 1990*a, b, c*; *Marsch and Tu*, 1989, 1990*b*; *Tu and Marsch*, 1990*b*; *Mangenev et al.*, 1991] have collaborated to establish that *in situ* dynamical turbulence is indeed active in the solar wind. However, fluctuations which are passive coronal remnants are also present, so that the current viewpoint is a blend of the wave and turbulence vistas.

Before continuing, it will be useful to review some familiar concepts appearing in descriptions of turbulence. Suppose that a turbulent fluid, with no mean velocity, is in a (statistically) steady state and confined to a volume of characteristic size L . We would like to know how much energy is typically associated with spatial structures (or “eddies”) of characteristic size l . Thus, we Fourier analyze the energy⁴ and investigate its wavenumber spectrum, $E(k)$, where $k \sim 1/l$. When the fluid is turbulent enough, that is, when its viscosity is *relatively* small, or equivalently its Reynolds number is large, it is found that the energy spectrum has several more or less distinct regions, each associated with the dominance of a different physical term in the governing equations(s) of motion.

Suppose we are in a position to make a log-log plot of $E(k)$ vs. k ; then at relatively low wavenumbers (but usually not the lowest ones) we will see a peak in the energy spectrum. Structures of about this size contain a substantial fraction of the total energy, and constitute the *energy-containing range* of the turbulence. They are associated with the “stirring length” of the system, or, more prosaically, the scales at which energy is being fed into the system as a whole.

At somewhat larger wavenumbers (smaller spatial scales), the *inertial range* begins. This subrange is characterized by powerlaw behavior (*i.e.*, a straight line on the log-log plot) which extends over many decades of wavenumbers. The actual extent of the inertial range depends on how turbulent the fluid is, the bigger the Reynolds number, the further it extends. For hydrodynamic turbulence the slope is well approximated by the value $-\frac{5}{3}$ [*Kolmogorov*, 1941; *Batchelor*, 1970], while for MHD turbulence with a mean magnetic field, the value $-\frac{3}{2}$ is believed to apply [*Kraichnan*, 1965]. For these wavenumbers, the dynamics are dominated by the non-linear terms of the equations of motion (*e.g.*, the $\mathbf{v} \cdot \nabla \mathbf{v}$ term in the Navier-Stokes equation). Further discussion of the inertial range for generic turbulence is contained in Appendix A.

³ Specifically, the processes occur in the corona, a region of dauntingly complicated magnetic structure and a temperature of around two million Kelvin.

⁴ Or more precisely the two-point velocity correlation.

As we move outwards in wavenumber space, the eddies eventually become so small that the dominant influence is viscous (and/or resistive) decay. Around this point the energy spectrum steepens in order to accommodate dissipation of the energy. This is the so called *dissipation range*, and is associated with kinetic (*i.e.*, discrete particle) effects. For smaller viscosities the range lies further out in k -space.

A useful way of looking at MHD fluctuations in the solar wind, is to first ask how they behave *locally* in space and time, say, on the scale of a few correlation lengths and times. This in itself is a formidable problem, particularly if, as is now generally believed [*e.g.*, *Roberts and Goldstein*, 1991; *Marsch*, 1991], the fluctuations are turbulent in nature. In this case models are needed to approximate the local non-linearities, since an exact treatment would represent the unlikely achievement of a full solution to the MHD turbulence problem. In Chapter 5 we will discuss the efficacy of two distinct but related models for the spectral forms of the non-linear terms associated with inertial range fluctuations of the “inward” and “outward” types [*Zhou and Matthaeus*, 1990c].

Assuming that the local behavior can indeed be satisfactorily understood and modeled, the next step is to ask how this characterization changes as the fluctuations evolve under the influence of the slowly varying mean fields. For example, because the mean wind is both supersonic and super-Alfvénic, the radial evolution of the fluctuations corresponds to a temporal evolution of each parcel of outward moving magnetofluid.

The first of these questions (local dynamics) has often been addressed by treating the fluctuations as propagating MHD waves, mostly Alfvén waves. In the inner heliosphere⁵ this view is supported by

- (i) Minimum variance direction arguments. Observations generally show that the fluctuations have substantially less power in the radial components, relative to that in two Cartesian directions transverse to the radial. Furthermore, the power in these two transverse components is approximately equally distributed. Since Alfvén waves are transverse disturbances which propagate along a mean magnetic field, this has been interpreted as supporting evidence for the wave description of the interplanetary fluctuations.
- (ii) The observed high correlations of plasma velocity and magnetic field fluctuations [*Belcher and Davis*, 1971]. Such correlations suggest that the fluctuations are predominantly outward

⁵ The boundary between the inner heliosphere and the outer is rather loosely defined. However, heliocentric distances of up to 1 astronomical unit are almost always considered to describe regions within the inner heliosphere. An astronomical unit (AU) is the mean distance from the sun to the earth ($\approx 1.5 \times 10^{13}$ cm). For a definition of the entire heliosphere see the opening pages of Chapter 2.

propagating Alfvén waves.

Alternatively, a viewpoint that the fluctuations are a form of actively evolving MHD turbulence affords an appealing mechanism for the observed heating of the solar wind [Coleman, 1968; Hollweg, 1986; Holweg and Johnson, 1988; Isenberg, 1990], while also providing a framework for a reasonably consistent interpretation of a variety of detailed statistical properties of the observations [Matthaeus and Goldstein, 1982a, b].

The second question, regarding the large scale transport and evolution of the fluctuations, has traditionally been addressed in the context of WKB theory [Weinberg, 1962; Parker, 1965; Hollweg, 1973b, 1974; Whang, 1973, 1980; Jacques, 1977; Barnes, 1979],⁶ which considers the transport of *non-interacting* waves as they advect through, and interact with, the *inhomogeneous* large scale features of the solar wind. The underlying physical picture for WKB theory, as it has been applied to the solar wind, is that the fluctuations are purely, or nearly purely, outward-traveling waves, *i.e.*, Alfvénic fluctuations, so that their basic, leading order physical properties can be studied by regarding them as passive remnants of coronal processes propagating away from the sun. Although WKB theory predicts behavior, reasonably in agreement with observations, for features such as the radial dependence of the magnetic fluctuation level in the outer heliosphere, it falls short of explaining a number of other important solar wind properties. The oldest and best known feature of this type, which one would like a transport theory to address, is the observed heating of the solar wind [Coleman, 1968], which appears to be consistent with heating by a turbulent cascade. In effect, WKB theory precludes such heating from the onset, by assuming that the fluctuations are non-interacting (waves). In addition, data from the Helios spacecraft [Bavassano *et al.*, 1982a, b], which visited the inner heliosphere (0.3–1 AU) in the late 70’s, indicates that the low⁷ frequency range spectral index depends on the heliocentric distance, *i.e.*, $\alpha = \alpha(\mathbf{R})$. However no such dependence is found in the high frequency range. WKB theory admits frequency (wavenumber) dependent effects only in higher order, and is evidently unable to explain these observational results. Another failing of WKB theory involves observations of the minimum variance direction (MVD) in the outer heliosphere [*e.g.*, Solodyna and Belcher, 1976; Klein *et al.*, 1991]. These suggest that the MVD is aligned with \mathbf{B}_0 , rather than the radial direction predicted

⁶ The review article by Barnes is a particularly worthwhile read.

⁷ Since physically important length and time scales in the solar wind span many orders of magnitude, inherently relative epithets like “low” and “high” can mean very different things to different groups. What is a high frequency for MHD purposes, for example, is probably a low frequency from the plasma theory perspective. We will only consider MHD scales in this thesis, but even here “high” and “low” frequencies (wavenumbers, *etc.*) vary, in part because the underlying physical scales are functions of heliocentric distance (R). For example, because $\mathbf{B} = \mathbf{B}(\mathbf{R})$, the ion gyrofrequency, which is an approximate upper bound for fluid frequencies, also varies with R .

by (leading order) WKB theory [*e.g.*, *Barnes, 1969; Volk and Alpers, 1975*]. Finally, several other physical quantities, which may be used to characterize the fluctuations, are known to undergo varying degrees of radial evolution (*e.g.*, the normalized cross helicity, σ_c , and the Alfvén ratio, r_A).⁸ Again, WKB theory cannot explain this evolution, either in leading order or with the inclusion of higher order corrections [*e.g.*, *Hollweg, 1990*].

To broaden the predictive power of transport theory for solar wind fluctuations, several extensions to the WKB formalism have been proposed [*e.g.*, *Hollweg, 1986; Tu et al., 1984; Tu, 1988*], including phenomenological heating terms due to an assumed turbulent cascade. Tu and coworkers [*Tu et al., 1984*] proposed a model for the frequency spectrum of incompressible outward traveling Alfvénic fluctuations, in which they assumed the existence of a small admixture of inward-propagating Alfvénic fluctuations. The model is WKB-like in the sense that linear transport of the outward waves is identical to that of WKB theory—but a model for the turbulence is also included. The non-linear interaction between the inward waves and the dominant outward waves results in a cascade, producing heating of the type suggested by *Coleman [1968]*, and allowing for radial evolution of the fluctuation spectral index, as seen in Helios observations [*Bavassano et al., 1982a*]. The Alfvénic condition is used in the same way as in WKB theory, to cancel the interactions between small scale fluctuations and large scale background field gradients [*Zhou and Matthaeus, 1990b*]. The Tu models, and their extension [*Tu et al., 1989b*], can be fitted to observational data in the inner heliosphere, but because they only consider a transport equation for outward traveling fluctuations, they share with WKB theory the inability to address the dynamics associated with arbitrary mixtures of “inward” and “outward” type fluctuations, such as are observed in the solar wind [*Roberts et al., 1987a, b*].

A recently developed more general transport model for the interplanetary MHD turbulence [*Matthaeus and Zhou, 1989b; Zhou and Matthaeus, 1989, 1990a*] addresses this remaining deficiency of both the WKB and Tu models, by separately considering transport of the spectra of *both* small-scale Elsässer fields. A similar transport model has been described by an independent group [*Marsch and Tu, 1989, 1990b; Tu and Marsch, 1990b, 1992, 1993*]. This is equivalent to consideration of arbitrary admixtures of “inward” and “outward” type fluctuations, or, in the language of turbulence theory, arbitrary cross helicity of the fluctuations.

A notable property of this theory is that it contains terms—at leading order—that mix “inward” and “outward” type fluctuations. These terms are *linear* and explicitly absent in the

⁸ These quantities are defined in later chapters, but for the impatient and/or curious, r_A is the ratio of kinetic to magnetic energy, and σ_c may be interpreted as a measure of the relative abundances of “inward” and “outward” type fluctuations.

analogous leading order transport equations of WKB theory. Based on simple solutions to the new transport model, *Zhou and Matthaeus* [1989, 1990a] have shown that such “mixing” effects can provide a partial explanation for the observed decrease of cross helicity with heliocentric distance [*Roberts et al.*, 1987a, b]. In this thesis we further investigate properties and solutions of this “ZM” model, as applied to the solar wind, and discuss conditions for which “mixing” effects are important. More specifically, we consider the radial evolution of several types of small-scale turbulence (isotropic, two-dimensional, and slab) in the presence of specified, slowly varying, large-scale fields. Transport and evolution of both energy-containing range and inertial range fluctuations is considered. It will be shown that the model can provide at least partial explanations for a number of observed solar wind phenomena that cannot be explained using the (non-interacting) wave-based WKB transport theory.

1.2 Overview

In outline, the approach taken in computing the transport of solar wind fluctuations is as follows:

- The time dependent transport equations for the energy-containing range are followed until steady solutions are achieved. As far as this range of scales is concerned, no further dynamical calculations are required.
- Next, the energy fluxes from the steady energy-containing solutions are used as inputs into the wavenumber transport of the inertial range model. The spatial and wavenumber transport of these fluctuations is followed until steady solutions are reached.

The output from this approach includes radial evolution profiles for the bulk quantities (*e.g.*, energy, cross helicity) associated with the energy-containing range, and a set of steady inertial range spectra of these bulk quantities—at each point in space. While there are many details to be filled in, this is the “big picture.”

The remainder of the thesis is structured as follows. Chapter 2 reviews in some detail the general properties of the solar wind, both at the large-scales and for the fluctuations. Both theory and observations are considered. The chapter also contains an abbreviated derivation of the MHD equations and a discussion of their applicability to the solar wind.

Chapter 3 deals with a particular sub-problem associated with the transport of correlation functions and spectra, namely the most general representation of these quantities when the turbulence is incompressible and homogeneous. Since we will be assuming that, locally, the solar wind

fluctuations are of this type, the results of this chapter will be of importance when we get to the transport theory. Much of the work in Chapter 3 has not been previously published.

In Chapter 4 the model for the spatial transport of solar wind fluctuations is derived, essentially from scratch; the derivation closely follows that given in *Zhou and Matthaeus [1990a]*. The transported quantities are the local correlation functions and spectra, formed from the fluctuating velocity and magnetic fields, and discussed independently in Chapter 3. Introductory discussions on the “mixing” effect and the models relationship to WKB theory are also given at this point.

Using the framework developed in Chapter 4, Chapter 5 presents analytic and numerical solutions for transport of the spectra of *inertial range* fluctuations in the solar wind. Solutions to the linear equations (at a single wavenumber) are considered first, for three particular types of fluctuations: (i) isotropic turbulence, (ii) two-dimensional turbulence in the planes perpendicular to \mathbf{B}_0 , and (iii) slab fluctuations, which correspond to Alfvén waves propagating along \mathbf{B}_0 . This is almost all new material. In the second half of the chapter, the model for the non-linear terms in the inertial range is developed. Short discussions on the numerical methods used to solve the equations are also included.

Chapter 6 considers the spatial transport of *energy-containing* range fluctuations in the solar wind. For fluctuations at these scales, two types of turbulence are considered: isotropic and two-dimensional (2D). Again this is largely new material. Models for the non-linear decay of homogeneous MHD turbulence are discussed, and the possibility that such decay assists in the observed heating of the solar wind is considered. The final set of solutions presented uses the steady-state energy fluxes from the energy-containing model, to drive the full inertial range model, complete with non-linear terms. Two production runs of this kind are discussed, one for isotropic turbulence and one for 2D. Various supporting appendices and a bibliography complete the document.

One further point regarding the small-scale turbulence should be stressed. Despite the fact that spacecraft observations reveal a (randomly) helical character to the fluctuations [*e.g.*, *Matthaeus and Goldstein, 1982a*], that is, velocity and magnetic helicities are in general non-zero, we will make the approximation that helicity effects can be ignored, and set such quantities to zero when applying the transport model to the solar wind.

Finally in this introduction, we note that the usual abbreviations for the various classes of differential equations (de’s), ordinary (ode’s) and partial (pde’s), will be used upon occasion. Similarly, bc’s will be used as a shorthand for boundary conditions, and R_{sun} denotes the radius of the sun.

Chapter 2

THE SOLAR WIND

The awful majesty of outer space.

— Adlai Stevenson

2.1 Introduction

The existence of the solar wind was predicted by *Parker* in 1958, and subsequent spacecraft observations have confirmed the general correctness of his model [*e.g.*, *Brandt*, 1970; *Hundhausen*, 1972]. This first model was based on a hydrodynamic description of the sun's atmosphere, and proposed that the solar wind was a smooth, spherically symmetric, time-steady outflow of plasma. Variations, either temporal or spatial, were not considered. Observational data however, indicates that fluctuations are part and parcel of the interplanetary medium. Indeed, the length and time scales associated with such fluctuations each span many orders of magnitude. Theories on the origin and evolution of solar wind fluctuations are as yet incomplete. We will consider only two of these theories, namely the wave and turbulence descriptions, where turbulent fluctuations do not satisfy a dispersion relation in general. It is important to note that these two pictures are *not* mutually exclusive, and in fact the actual state of the system probably involves some admixture of the two dynamical processes.

In order to set the context for the rest of this work, we now give a brief overview of the solar wind's physical properties and describe its large-scale structure. The chapter also includes a discussion of the MHD description of the interplanetary medium, and an introduction to the wave and turbulence theories of solar wind fluctuations.

2.2 General Characteristics

The medium which permeates the heliosphere¹ is known as the solar wind. Observations made over the last thirty years indicate that it consists of a gas of charged particles (*i.e.*, a plasma) flowing more or less radially outward from the sun (Figure 2.1). It is a hot, electrically neutral,

¹ This term is used to describe the region of space dominated by phenomena associated with the sun. Its boundaries are roughly defined by the distances where the total solar wind pressure drops to a value comparable to the pressure in the local interstellar medium.

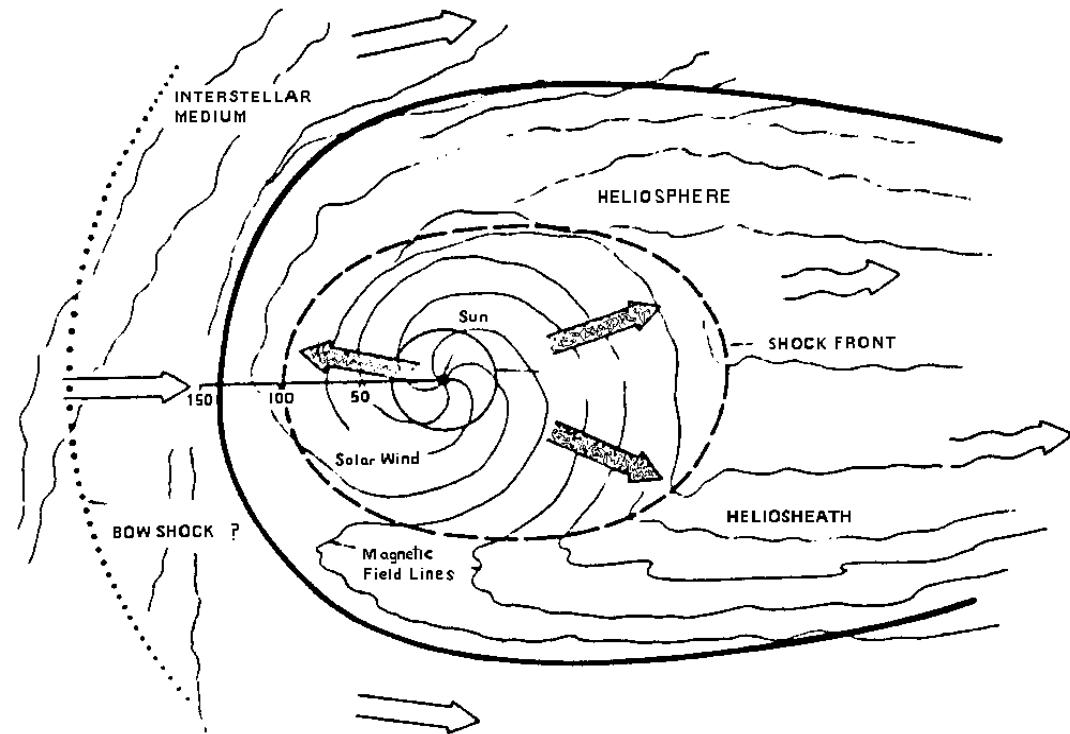


Figure 2.1: Schematic sketch showing some major features of the heliosphere and the surrounding region. Not all of the features shown have been observationally verified. The filled arrows indicate the flow of the supersonic solar wind, while the open straight arrows represent the interstellar wind. The approximate distances indicated are given in astronomical units (AU). After *Parks* [1991].

fully ionized plasma of extraordinarily low density by terrestrial standards. Appendix E tabulates values for some of the physical quantities and scales characterizing the solar wind.

The source of the solar wind is the sun itself. Gravitational (and magnetic) forces are unable to contain the million degree plus atmosphere of the sun (the corona), which thus “boils off” and streams out into the solar system in all directions. In other words the pressure difference between the corona and the inner heliosphere drives the initial flow.

Two quite distinct types of outflow are observed [*e.g.*, *Neugebauer*, 1991]. The first of these is more or less continuous in time and consists of *streams* of plasma whose mean speed is usually classifiable as either high or low. High-speed streams are believed to emanate from coronal holes—these being portions of the sun’s atmosphere in which the magnetic field lines are *not* closed loops, but instead open out into interplanetary space (Figure 2.2). Typically the magnetic field in a coronal hole is relatively weak and of a single polarity. Particle density is usually low in such regions. This suggests that the plasma within coronal holes enjoys reduced magnetic confinement in comparison to regions where the magnetic field lines are closed. The spatial origin of the slow streams is not known with certainty, however it appears that they arise in several distinct types of region. These include the edges of coronal holes, the area above closed field regions, and regions adjacent to magnetic sector boundaries (surfaces where the magnetic field reverses polarity).

The continuous (in time) outflow gives rise to a (statistically) *quasi-stationary* solar wind, characterized by slow variations in its large-scale features. In this case *slow* refers to temporal periods ranging from a week or so to several months. Such outflow is often referred to as the *quiet solar wind*, and is particularly characteristic of conditions at solar minimum.

The second type of outflow is transient in nature and originates within closed magnetic structures. Some areas of the photosphere (the sun’s visible surface) contain magnetic field lines which emerge from the surface and arc up into the corona, to a height of no more than a few solar radii, before falling back into the photosphere. Such closed field regions of the corona magnetically confine the associated plasma. However, for poorly understood reasons, the stability of this confinement varies and explosive ejections of coronal material occur, with a frequency that depends on the solar cycle phase and other parameters. Such energetic releases of plasma are known as coronal mass ejections (CMEs). The so called *transient solar wind* results from such CME’s and other disturbances of the background quasi-stationary medium. However, it is somewhat misleading to consider the solar wind as consisting of these two distinct components, since they can, and do, interact strongly (and non-linearly) with each other.

Having made it this far above the photosphere, the plasma is now accelerated to supersonic

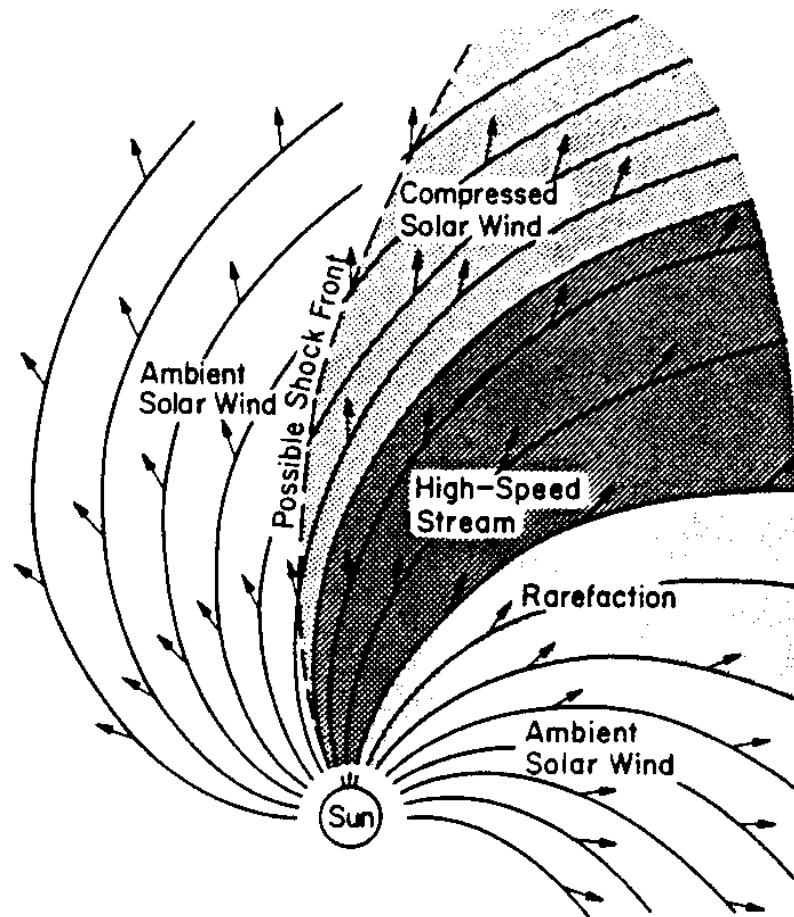


Figure 2.2: Schematic diagram showing the interaction of high- and low-speed solar wind streams in the ecliptic plane. After *Hundhausen* [1972].

speeds within a few tens of solar radii. The precise mechanism of the acceleration is yet to be fully, or even well understood. *In situ* measurements suggest that the average velocity of the solar wind is roughly constant throughout the heliosphere, being predominantly in the radial direction and having a typical magnitude of 300 – 700 km/sec. Flow speeds of 300 km/sec or less are usually referred to as slow, while speeds of greater than about 500 km/sec are termed fast. It should be noted that almost all of the *in situ* measurements have been made in the ecliptic, and that no such measurements have been made inside 0.3 AU. The approximately constant mean speed is both highly supersonic and highly super-Alfvénic (see below), and hence the solar wind is capable of supporting (collisionless) shock waves and related structures. Indeed planetary and cometary bowshocks are observed in the interplanetary medium (upstream of the appropriate objects), as are traveling shocks—which may occur, for example, as a result of CMEs or speed differences between adjacent regions of the solar wind. Such shocks are, in many cases, responsible for the generation of propagating waves and fluctuations, and may also result in the *in situ* generation of turbulence.

Significant fluctuations in velocity, about the mean value(s), are common. If we denote the mean speed by U , and the rms value of the fluctuating velocity by δU , then typically at 1 AU, $\delta U/U \approx 1/20$. Near the sun this ratio can take on values of order unity, suggesting that the flow is highly disordered in such regions. Spectral decomposition of the velocity fluctuations indicates that they are characterized by a wide range of length and time scales. Furthermore, there usually exists a range, spanning several decades of wavenumber or frequency, over which the fluctuations are self-similar. This *inertial range* of fluctuations will be considered in more detail in later chapters (see also Appendix A). The observed velocity fluctuations are assumed to result from wave and/or turbulence processes. For example, shear stress between a fast and slow stream is a possible mechanism for the generation of turbulent fluctuations [*e.g.*, Roberts *et al.*, 1992].

Despite its almost fully ionized state, any “small” volume of solar wind plasma will almost always be electrically neutral to an excellent approximation. This is a consequence of the high conductivity of the plasma. Recall that a conductor is in equilibrium when there are no electric fields present for the free charge carriers to respond to. Any departure from neutrality has an associated internal electric field. The low resistance of the solar wind plasma allows the electrons to respond to even small electric fields with alacrity; the net result being a return to overall neutrality and the elimination of the internal electric fields.² In other words, large restoring currents can result from very small charge separations (see also the discussion preceding equation (2.9)).

² Of course the ions also respond to such electric fields but their much greater mass (inertia) means that the electrons do most of the moving.

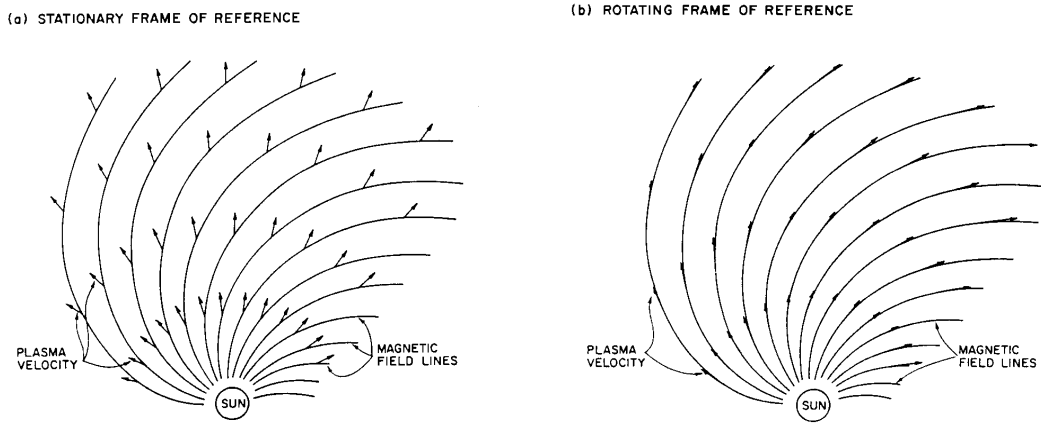


Figure 2.3: Schematic diagram of the Parker spiral magnetic field and the radial solar wind in the ecliptic. (a) The geometry as it appears in an inertial frame, (b) the same situation viewed from a frame rotating with the sun. In order to understand why this geometry exists, it may help to visualize the water jets from a rotating garden sprinkler, or the sparks from a Catherine wheel at a fireworks display. After *Hundhausen* [1972].

Naturally the charged particles will still be influenced by any electric and/or magnetic fields which they are unable to negate via their own redistribution. In particular, the presence of the solar magnetic field, which is carried out into the heliosphere with the solar wind plasma, means that the charged particles gyrate about the field lines.

Note that while the mean velocity field is approximately radial, the average magnetic field displays an almost Archimedean³ spiral geometry as a consequence of the rotation of the sun about its own axis. The sun's rotation rate and the average solar wind speed are such that at 1 AU the mean magnetic field in the ecliptic makes an angle of around 45° with the radial direction, and has a magnitude of approximately 5 nT. For comparison, the magnitude of the earth's magnetic field at sea level is about ten thousand times greater than this. The geometry of the magnetic field is shown in Figure 2.3, and discussed further in section 2.3

Magnetic fluctuations, with respect to the mean field, are also observed. As in the case for the velocity field, these fluctuations occur at many different wavelengths and frequencies. In fact, it is more usual to consider the fluctuations as a function of wave-vector (or perhaps frequency), that is, to spectrally decompose them using Fourier transform techniques. Again the fluctuations may represent either pure turbulence, pure (MHD) waves, or various mixtures of the two. Typically values of $\delta B/B_0$ are of order unity at 1 AU, where δB is the rms fluctuation about the mean field

³ The Archimedean spiral is also known as the Parker spiral after E. Parker who predicted its existence in 1958.

magnitude B_0 . Such a high value of $\delta B/B_0$ indicates that the magnetic fluctuations are strong and probably can not be neglected.

Density and pressure fluctuations are also observed in the solar wind, indicating that the interplanetary medium is a compressible one. However some *incompressible* models of *local* solar wind properties are in good agreement with data obtained from spacecraft flights. The possibility that the solar wind is a *nearly incompressible* medium will be discussed briefly below. The average ion (and electron) density at the earth's orbit is roughly 5 cm^{-3} , but (almost) order of magnitude fluctuations about this value are not uncommon. If we denote the heliocentric distance by R , then, on average the density is observationally $\sim 1/R^2$. This result is consistent with an approximately constant, radially directed solar wind speed, as can be seen by considering the conservation of mass: Denote the (mean) radial speed by U , and the mean mass density by ρ , then in spherical polar coordinates the time-steady equation of mass continuity reduces to

$$\frac{1}{R^2} \frac{d}{dR} (R^2 \rho U) = 0,$$

from which the result readily follows. Typically $\delta\rho/\rho \sim 1/10$ [Roberts *et al.*, 1987*a, b*].

To summarize, the solar wind may be described as a low density, approximately neutral collisionless plasma with the rough large-scale structure given by a radially directed, constant magnitude velocity field, and an Archimedean spiral magnetic field. The radial component of the magnetic field falls off as $1/R^2$, while the azimuthal component decays asymptotically as $1/R$. These aspects of the solar wind are now believed to be reasonably well understood (see section 2.3), and the challenge is to ascertain the physics relevant to solar wind fluctuations and other departures from the large-scale leading order behavior.

2.3 Theory of the Large-Scale Structure

As the average large-scale structure of the solar wind is predicted quite well by the Parker theory and its extensions, a brief synopsis of this theory is in order. More complete derivations are available in Parker's original paper [1958*a*], and in several monographs [*e.g.*, Brandt, 1970; Hundhausen, 1972]. These monographs also contain more extensive discussions of the large-scale structure of the solar wind, along with the early history of the subject. It should also be noted that while today we take Parker's theory almost for granted, at the time it was quite controversial, only gaining wide acceptance after satellite observations in the early 1960's lent their support [*e.g.*, Snyder and Neugebauer, 1964; Ness *et al.*, 1964; Neugebauer and Snyder, 1966, 1967].

The sun's atmosphere is treated as a dissipationless fluid, *i.e.*, perfectly conducting and non-viscous. The equations used represent the separate conservation of mass, energy, and momentum

for the system. In the earliest models, solution of the energy conservation equation was avoided through the use of a polytropic law, $p \propto \rho^{-\gamma}$, $\gamma \geq 1$, where p and ρ are respectively the pressure and density of the plasma. Note that this contains the isothermal approximation as a special case ($\gamma = 1$). As electric and magnetic forces were assumed to be negligible, the relevant forces are just two: gravitational attraction and fluid pressure gradients.

Let us first assume that a state of hydrostatic equilibrium exists [Chapman, 1957]. Solution of the equations reveals that the fluid pressure at infinite heliocentric distance is finite, essentially because the gravitational force approaches zero faster than the pressure gradient force as $R \rightarrow \infty$. Unfortunately this finite value of the pressure is many orders of magnitude greater than the inferred interstellar pressure [Chapman, 1957; Parker, 1958]. The physical implausibility of such a pressure jump implies that the sun’s atmosphere cannot be in hydrostatic equilibrium out to large heliocentric distances, and possibly not even at close ones.

The next simplest case to consider is one where the atmosphere undergoes spherically symmetric, time-steady outflow [Parker, 1958a]. Under such assumptions the equations of motion support four distinct classes of solution (Figure 2.4). Classes 3 and 4 are incompatible with observations, since they have supersonic velocities near the solar surface. Class 1 solutions yield pressures which are too big at infinity, as in the static case, and are therefore also rejected. Fortunately, the class 2 solutions, which pass through a sonic critical point,⁴ have the following observationally desirable features: (a) low (subsonic) velocity at the coronal base, (b) transition to a supersonic velocity within a few solar radii, (c) approximately constant outflow speed beyond ~ 10 solar radii (R_{sun}), and (d) zero pressure at infinite heliocentric distances, thus allowing merger of the outflow with the low pressure interstellar medium. Parker christened such an outflow the *solar wind*. While various modifications of and extensions to the original theory have been developed, the overall physical picture remains essentially unchanged.

As a final point in this section, note that the Archimedean spiral magnetic field is an immediate consequence of the physically relevant solutions in conjunction with (i) the existence of a magnetic field at the solar surface, (ii) the sun’s rotation, and (iii) the approximations involved. Since the plasma is taken to be perfectly conducting, the magnetic field lines are *attached* to the fluid particles—that is, the magnetic field lines correspond to the fluid particle streaklines. This is known as “frozen-in” flow, meaning that the field lines are constrained to move *with* the fluid—no drifting of the field lines perpendicular to the velocity streamlines being possible. Of course the

⁴ The sonic critical point is defined by the distance at which the fluid velocity equals the local sound speed [*e.g.*, Parker, 1958].

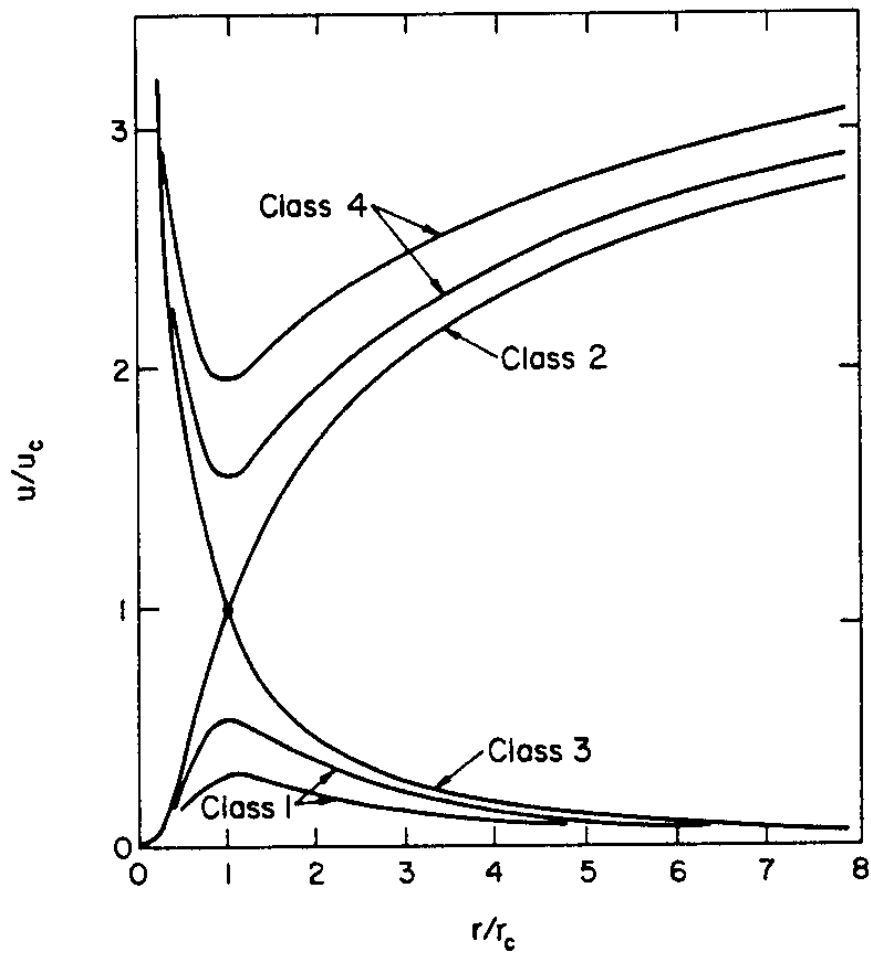


Figure 2.4: Sketch of the four solution classes for the original Parker theory of a steady-state expanding corona. The abscissa is heliocentric distance measured in units of critical radii, while the ordinate is the flow velocity measured relative to the sound speed at the critical radius. After *Hundhausen* [1972].

plasma is not really perfectly conducting and its finite resistivity causes the magnetic field lines to diffuse over long periods of time (see also the final paragraph of section 2.4 on page 27).

2.4 The MHD Description

In order to describe the solar wind mathematically we use the MHD approximation. Classical works on MHD are the texts of *Cowling* [1957] and *Shercliff* [1965], while a more modern presentation in the context of solar physics is *Priest's* [1982] graduate level text. In this section we state the MHD equations, and then discuss their applicability to the solar wind. A brief discussion of wave solutions to the linearized equations is also presented.

2.4.1 The MHD Equations

The equations used are applicable to single component magnetofluids, that is (continuous) fluids which can conduct electric current rather well. Examples include liquid metals and numerous types of plasmas in the low frequency, long wavelength limit. An important characteristic of such fluids is their ability to generate and maintain an *internal* magnetic field. This field is *non-linearly* coupled to the velocity field, and may also interact with externally imposed electromagnetic fields.

The fluid equations representing conservation of mass and momentum are

$$\frac{\partial \rho}{\partial t} + \nabla \cdot (\rho \mathbf{V}) = 0, \quad (2.1)$$

$$\left(\frac{\partial}{\partial t} + \mathbf{V} \cdot \nabla \right) \mathbf{V} = -\frac{1}{\rho} \nabla p + \frac{1}{\rho c} \mathbf{j} \times \mathbf{B} + \nu \nabla^2 \mathbf{V} + \frac{1}{3} \nu \nabla (\nabla \cdot \mathbf{V}), \quad (2.2)$$

where ρ is the mass density of the fluid, \mathbf{V} the fluid velocity, p the fluid pressure, \mathbf{j} the electric current density and \mathbf{B} the magnetic field. The kinematic viscosity is denoted by ν , and the speed of light in a vacuum by c . Gaussian cgs units are used, and all fields are functions of three-dimensional space (\mathbf{x}) and time (t). When considering a turbulent fluid it is often convenient to work in the (local) zero momentum frame, where the mean velocity is zero; \mathbf{V} then represents fluctuations about the mean. Such a zero momentum frame can always be achieved by making a Galilean boost. Here, however, we do not so specialize, since the mean velocity plays an important role in the transport of the interplanetary fluctuations.

The assumption of overall charge neutrality is present in these equations, as no terms involving an electric field appear. This may be justified on the basis of the high conductivity of the magnetofluid (see the discussion on page 15 and that preceding equation (2.9)).

Maxwell's equations describing the dynamics of electromagnetic fields in a vacuum are assumed to hold,

$$\nabla \cdot \mathbf{E} = 4\pi\rho_e, \quad (2.3)$$

$$\nabla \cdot \mathbf{B} = 0, \quad (2.4)$$

$$\nabla \times \mathbf{E} = -\frac{1}{c} \frac{\partial \mathbf{B}}{\partial t}, \quad (2.5)$$

$$\nabla \times \mathbf{B} = \frac{4\pi}{c} \mathbf{j} + \frac{1}{c} \frac{\partial \mathbf{E}}{\partial t}. \quad (2.6)$$

Here \mathbf{E} is the electric field strength and ρ_e the electric charge density.

Next we assume that Ohm's Law holds, in the form appropriate for a medium moving with (non-relativistic) velocity \mathbf{V} relative to the laboratory frame

$$\mathbf{j} = \sigma \left(\mathbf{E} + \frac{\mathbf{V}}{c} \times \mathbf{B} \right), \quad (2.7)$$

where σ is the scalar conductivity [*e.g.*, Nicholson, 1983]. This relation may be solved for \mathbf{E} , allowing the electric field to be removed from the dynamical equations. Substituting into Faraday's law (2.5) for \mathbf{E} and making use of the solenoidal nature of \mathbf{B} , and the vector identity⁵ for the curl of the curl, we find

$$\frac{\partial \mathbf{B}}{\partial t} = \nabla \times (\mathbf{V} \times \mathbf{B}) + \frac{c^2}{4\pi\sigma} \nabla^2 \mathbf{B}, \quad (2.8)$$

which is linear in \mathbf{B} . Upon expanding the vector triple product, equation (2.8) may be conveniently rewritten in terms of the convective derivative acting on \mathbf{B} . This form is shown below as equation (2.12). Note that if $\mathbf{V} = 0$, equation (2.8) reduces to a diffusion equation for \mathbf{B} . Thus the field lines decay on a time scale $\tau \sim 4\pi\sigma L^2/c^2$, where L is the characteristic length over which \mathbf{B} varies. For typical solar fields $\tau \sim 10^{10}$ years, and thus this term is usually ignored in solar wind work (see also the final paragraph in section 2.4.3).

The condition that the magnetofluid is a good conductor ensures that the displacement current term in Maxwell IV (equation 2.6) is negligible, since it implies that the electrons respond to changes in the electric field on timescales much shorter than those during which the field itself undergoes significant variation. In other words, small changes in the electric field are accompanied by rapid redistributions of the free charge carriers (*i.e.*, currents) occurring in such a way that the system is once again macroscopically neutral. Hence, the current is proportional to the curl of the magnetic field, and the term $\mathbf{j} \times \mathbf{B}/c$ in (2.2) becomes

$$\frac{1}{4\pi} (\nabla \times \mathbf{B}) \times \mathbf{B} = -\frac{1}{8\pi} \nabla B^2 + \frac{1}{4\pi} (\mathbf{B} \cdot \nabla) \mathbf{B}. \quad (2.9)$$

⁵ Hereafter various vector identities will be used without explicit reference.

The quantity $B^2/8\pi$ can be interpreted as an isotropic pressure gradient force, dependent only on the spatial variation of the magnitude of \mathbf{B} , while the second term on the right is associated with tension (stretching) *along* the field lines, and thus depends on both the direction and the strength of the magnetic field.

An equation is also needed for the energy evolution of the fluid. Since in this work we will not be concerned with such matters, we note only that assuming a polytropic law of the form $p\rho^{-\gamma} = \text{const}$, $\gamma \geq 1$, is one way of closing the equations.

Collecting everything together we arrive at our final set of equations:

$$\frac{\partial \rho}{\partial t} + \nabla \cdot (\rho \mathbf{V}) = 0, \quad (2.10)$$

$$\left(\frac{\partial}{\partial t} + \mathbf{V} \cdot \nabla \right) \mathbf{V} = -\frac{1}{\rho} \nabla P + \frac{1}{4\pi\rho} (\mathbf{B} \cdot \nabla) \mathbf{B} + \nu \nabla^2 \mathbf{V} + \frac{1}{3} \nu \nabla (\nabla \cdot \mathbf{V}), \quad (2.11)$$

$$\left(\frac{\partial}{\partial t} + \mathbf{V} \cdot \nabla \right) \mathbf{B} = (\mathbf{B} \cdot \nabla) \mathbf{V} - \mathbf{B} \nabla \cdot \mathbf{V} + \frac{c^2}{4\pi\sigma} \nabla^2 \mathbf{B}, \quad (2.12)$$

where P is the total (fluid plus magnetic) pressure. Taking the divergence of (2.12) (or more obviously its ancestor (2.8)) shows that if $\nabla \cdot \mathbf{B} = 0$ initially then it remains so, and thus the solenoidal character of the magnetic field need only be imposed as an initial condition. Note that the Navier-Stokes (NS) equations for hydrodynamic fluids are a special case of the MHD equations, recovered when the magnetic field is identically zero.

The equations may of course be put in non-dimensional form using appropriate choices of characteristic length and velocity scales (with p/ρ being conveniently scaled to the adiabatic sound speed, $c_s = \sqrt{\partial p / \partial \rho}$). Proceeding thus, we find that the dissipative terms are weighted by inverse Reynolds numbers or their magnetic counterparts, while the pressure term is multiplied by the plasma beta, this quantity being equal to the ratio of the thermal to magnetic pressure [*e.g.*, *Montgomery*, 1989].

As noted by *Elsässer* [1950] the velocity and magnetic fields may be treated symmetrically if the magnetic field is measured in Alfvén speed units, *i.e.*, $\mathbf{B} \rightarrow \mathbf{B}/\sqrt{4\pi\rho}$. The equations of motion may then be rewritten in terms of the *Elsässer* [1950] variables: $\mathbf{z}^\pm = \mathbf{V} \pm \mathbf{B}$. Consider a perfectly homogeneous fluid in the presence of an external d.c. magnetic field, and suppose that the fluctuations in the velocity and magnetic fields are small. It follows that a linear approximation to the equations of motion is valid. Under these conditions the *Elsässer* variables for the fluctuations represent the normal modes of the system, and correspond to Alfvén waves propagating in opposite directions along the d.c. field. As the solar wind is only weakly inhomogeneous it is sometimes

convenient to describe the associated fluctuations in \mathbf{V} and \mathbf{B} using Elsässer variables [*e.g.*, Marsch and Mangeney, 1987; Marsch and Tu, 1989, 1990a, b; Tu *et al.*, 1989; Tu and Marsch, 1990b; Zhou and Matthaeus, 1990a].

Together with appropriate boundary conditions (*e.g.*, no-slip, stress-free, perfect conductor, *etc.*) this system of coupled partial differential equations can in principle be solved to yield the space and time dependent fields. However, the non-linear nature of the equations means that (a) there is no general method of solving them, and (b) in general linear superpositions of known solutions do not also satisfy the equations. In fact analytic solutions are known in only a very few special cases. Researchers have thus turned to numerical simulation in order to find “solutions.” Unfortunately, the vexing problems of implementing realistic boundary conditions, and obtaining sufficient resolution for physically relevant Reynolds, Lundquist, *etc.* numbers in a reasonable amount of computer time, have so far restricted the majority of simulations to somewhat artificial and frequently two-dimensional (2D) cases [*e.g.*, Frisch *et al.*, 1975; Pouquet and Patterson, 1978; Matthaeus and Montgomery, 1980; Shebalin *et al.*, 1983; Matthaeus and Montgomery, 1984; Ting *et al.*, 1986; Goldstein *et al.*, 1989; Roberts *et al.*, 1991, 1992].

2.4.2 MHD Waves

The MHD equations admit wave solutions, some of which are observed in the solar wind. There are two basic types of waves in a conducting fluid: (1) low frequency MHD waves, associated with bulk motion of the fluid and no charge separation, and (2) high frequency plasma waves resulting from the Coulomb restoring force associated with ion-electron separation. Plasma waves will not be considered further.

To illustrate the nature of the MHD waves we simplify the equations of motion by considering an homogeneous, inviscid, perfectly conducting magnetofluid in the presence of a uniform magnetic field. The equations may be solved for small amplitude plane waves by linearizing about equilibrium solutions [*e.g.*, Jackson, 1975; Nicholson, 1983]. Additionally, plane solutions of *arbitrary* amplitude may be obtained using an approach introduced, in the context of the solar wind, by Barnes and Hollweg [1974], where spatial variations are permitted in one direction only (z say), and all the fields have a space-time dependence governed by a common characteristic function $\phi(z, t)$. We adopt this approach here [*e.g.*, Isenberg, 1990].

Three solution classes are obtained:

1. Non-propagating Structures

All quantities are functions of $\phi = z - v_z t$, with v_z and the total pressure being constants. The structures merely convect with the fluid. For $B_z = 0$ we have what is termed a tangential pressure balance. If the structure has infinitesimal thickness then it is known as a tangential (contact) discontinuity. When $B_z \neq 0$, the structure is an entropy wave, and the zero thickness form a contact discontinuity.

2. Alfvén Waves

As a result of the tension in the magnetic field lines, a magnetofluid, unlike an ordinary one, can support a shearing stress. This leads to the possibility of transverse waves in the medium.

Alfvén waves are transverse propagating modes which, in the absence of dissipation, are non-compressive and non-dispersive. They propagate along the magnetic field lines at the Alfvén speed, $c_{Az} = B_z / \sqrt{4\pi\rho}$, with v_z , ρ , p and B_\perp all being constant. The wave may be considered as a constant magnitude \mathbf{B} vector moving in an arc about the z (field) direction. The plasma associated with the wave “tracks” the magnetic field in the sense that $v_\perp / c_{Az} = \pm B_\perp / B_z$, the sign depending on the direction of propagation. The zero thickness case is known as a rotational discontinuity.

3. Magnetosonic Waves

These are compressive (longitudinal) and propagating in nature, being the generalization of hydrodynamic sound waves. Two propagation speeds exist for the magnetosonic modes, namely the fast and slow magnetosonic speeds defined by

$$V_{f,s}^2 = \frac{1}{2} \left[c_{Az}^2 + c_s^2 \pm \sqrt{(c_{Az}^2 + c_s^2)^2 - 4c_{Az}^2 c_s^2} \right], \quad (2.13)$$

with $c_s = \sqrt{\gamma p / \rho}$ the sound speed. Both modes are linearly polarized and may steepen into shocks if the dissipation is sufficiently weak.

Inclusion of the viscous and resistive terms in the equations of motion results in waves which dissipate, *i.e.*, damping of the oscillations. A fuller treatment also shows that dispersion is associated with many of the waves.

As far as the solar wind is concerned, observations suggest that Alfvén waves are present throughout the interplanetary medium, whereas magnetosonic modes are rarely seen. For conditions which are typical of the solar wind, Alfvén waves are essentially stable against the various

damping mechanisms (*e.g.*, Landau damping). However, it is possible that scattering of these modes by density and magnetic field irregularities leads to their conversion into magnetosonic waves, which are then readily damped [Valley, 1971, 1974].

As discussed by Barnes [1979], when the plasma beta is of order unity (*e.g.*, beyond the Alfvénic critical radius), the fast and slow magnetosonic waves are strongly damped. Thus, far from regions which are strongly disturbed, theory predicts that interplanetary fluctuations should consist of Alfvén waves, the various discontinuities and pressure balances, and perhaps variations which result from non-linear interactions amongst these modes, all of which is in general agreement with the observations. Below the Alfvénic critical point, where β is very small, the magnetosonic modes are also strongly damped. Finally, it should be noted that the observed wave amplitudes are often large, calling into question the applicability of linear wave theory in the solar wind.

2.4.3 Applicability

There are two major quandaries associated with the use of an MHD description of the solar wind. The first has to do with the continuum approximation, and the second with the treatment of the medium as a single fluid. The MHD equations are based on the assumption that the medium is a continuous fluid and, as such, that the particles have collisional mean free path lengths (mfpl) which are very much less than all macroscopic length scales characterizing the system. Indeed, it is possible to derive the MHD equations from the Boltzmann equation by taking various moments of the latter. However, the derivation assumes a Maxwellian distribution function, which almost requires that the gas be strongly collisional. Unfortunately this is not the case in the solar wind. Here the mfpl is on the order of 1 AU and thus the medium is essentially collisionless. Furthermore, many of the identifiable structures in the solar wind have sizes which are only a small fraction of an AU (*e.g.*, high and low speed stream widths, shock thicknesses, correlation lengths, and magnetic sector boundary widths). Thus, on this basis, it would seem that use of the MHD approximation cannot be justified.

Fortunately, however, the presence of a large scale magnetic field introduces a “small” length scale into the system, namely the particle gyroradius. In general, the charged particles of which the solar wind consists have a velocity and thus, ignoring other effects for the moment, execute spiral motion about the field lines. As is well known the gyroradius is given by $r_{gyro} = mv_{\perp}c/qB$, where q , m , v_{\perp} are respectively the charge, mass and perpendicular velocity of the particle. For protons at 1 AU, $r_{gyro} \lesssim 100$ km, which is much shorter than the macroscopic length scales pertaining to the solar wind. So at least in directions perpendicular to the local magnetic field the fluid

approximation seems to have some basis. The parallel direction is more problematic however.

As *Hasegawa and Sato* [1989] note, there are two empirical ways to justify the applicability of the MHD equations to space plasmas in general and the solar wind in particular. The first is to assume that “anomalous collisions,” resulting from microinstabilities associated with the plasma, act in such a fashion as to keep the particle distribution functions close to Maxwellian. The second rationale relegates the effects associated with departure from Maxwellian distribution functions to higher order, and is equivalent to neglecting thermal transport in the fluid.

A few words are in order regarding the treatment of the solar wind as a *one*-component magnetofluid. Such a description is usually considered appropriate for high density, low temperature fluids. In such cases the ions and neutrals in the fluid undergo collisions amongst themselves with a frequency sufficient to establish a state characterized by a single local velocity and a single local temperature. Electron motion relative to this local velocity manifests as electric current. However, as noted above, the density of the solar wind is such that collisions are rare. Thus, it is difficult to see how the various plasma components could achieve common local velocities and temperatures in this way, and indeed observations show that the proton and electron temperatures are often significantly different [*e.g.*, *Hundhausen*, 1972]. Electron and ion temperatures show considerable dependence on the nature of the flow (*e.g.*, high *vs* low speed streams), and, surprisingly, for high speed streams the proton temperature usually *exceeds* the electron temperature by about a factor of two.

Solar wind ions have thermal speeds which are much smaller than the mean flow speed⁶ and are generally characterized as slow and heavy; the electrons, on the other hand, are fast and light. The differences are such that the ions carry most of the momentum, and the electrons most of the electric current. A single fluid model of the solar wind therefore assumes that the ions correspond to the fluid particles, while the mobile electrons provide overall charge neutrality and high conductivity.

If neighboring ions move at approximately the same velocity we will have some basis for approximating the plasma as a one-component fluid. Spacecraft observations indicate that the solar wind has a typical ion composition (by number density) of $\simeq 96\%$ protons and $\simeq 4\%$ α -particles, with heavier ions present in trace quantities. Note that the fourfold greater mass of the α -particles results in their contributing significantly to the total momentum despite their relatively low abundance. The data also indicate that in regions where the solar wind flow is slow,

⁶ This is the sense in which the solar wind is supersonic.

the velocities of the protons and α -particles are comparable. However in the fast solar wind α -particles have significantly higher speeds than the protons, suggesting that, at least in this case, the fluid has two (or more) important components. We should thus keep in mind that a one-component description of the solar wind will not be appropriate in all circumstances.

Much work on the solar wind has been based on the further assumption that the medium is, at least locally, incompressible [e.g., *Matthaeus and Goldstein, 1982a; Zhou and Matthaeus, 1990a*], and some success in describing the observations has been achieved with such models. Clearly such a rarefied plasma is unlikely to be strictly incompressible, and, as mentioned above, density fluctuations are prevalent in solar wind data. In an attempt to reconcile this apparent contradiction, it has been suggested that the solar wind may be in a *nearly* incompressible state [*Montgomery et al., 1987; Matthaeus et al., 1990*]. The theory of nearly incompressible MHD has recently been put on firmer footing by, among others, Matthaeus, Brown, and Zank [*Matthaeus and Brown, 1988; Zank et al., 1990; Zank and Matthaeus, 1990a, 1991, 1992a, b, 1993; Matthaeus et al., 1991*], and observations of density and pressure fluctuations show some support for this nearly incompressible (NI) picture [*Roberts et al., 1987a, b; Matthaeus et al., 1990; Zank et al., 1990*].

Finally in this section we consider the *infinite conductivity approximation*. Recall that when the velocity is zero, equation (2.12) reduces to a diffusion equation for \mathbf{B} , indicating that the magnetic field lines diffuse into their surroundings over a time of order $4\pi\sigma L^2/c^2$, where L is a typical length scale associated with the magnetic field. In the solar wind the conductivity is usually large enough to allow diffusion of the magnetic field to be neglected. This is the infinite conductivity approximation and leads to the magnetic field being “frozen-in” to the plasma. More precisely (but less succinctly) if we follow a parcel of solar wind fluid as it moves through the heliosphere, we find that the magnetic field in the parcel remains attached to the same fluid “particles.” Thus, despite the fact that as the fluid parcel moves about, its form may undergo substantial geometric modification.

2.5 Solar Wind Fluctuations

2.5.1 Introduction

As mentioned in the introduction, it is now believed that the interplanetary MHD-scale fluctuations in \mathbf{V} and \mathbf{B} do indeed indicate the presence of dynamic non-linear processes in the solar wind, and are not just the passive remnants of disturbances produced close to the sun. Of

course, with its complex magnetic structure, the corona is undeniably a source of such fluctuations.⁷ The high mechanical and magnetic Reynolds numbers characteristic of coronal plasma, strongly suggest that various instabilities act to (a) excite waves, and (b) initiate turbulent cascades which in turn generate associated fluctuations at daughter scales. In this document the emphasis is on the latter possibility, with particular attention being paid to how such fluctuations evolve as they are transported outwards with the solar wind.

In general, the fast and slow magnetosonic modes produced in the lower corona are damped⁸ as the nascent solar wind flows outward, leaving the harder (large amplitude) Alfvén waves—which are essentially stable against wave-particle damping and non-linear effects⁹—to dominate the wave spectrum in this near-solar region of space. Non-wave fluctuations are almost certainly present in this region as well [*Parker, 1979*]. Some of the surviving fluctuations are able to convect and/or propagate out into interplanetary space with the solar wind. Here various dynamical processes, including expansion, compression, and velocity shear, act to substantially modify the original fluctuations, as well as generating new disturbances in their own right. It is this latter possibility—the *local* generation of fluctuations—which defines an essential difference between the leading order wave description and the turbulence approach. As we shall see, in the wave theory such effects only enter at higher order.

As discussed by *Barnes [1979]*, the principal solar wind fluctuations are hydromagnetic in character, and exist over the entire frequency range below the local ion gyrofrequency (this frequency is approximately equal to the dissipation scale). Furthermore, at these frequencies the solar wind plasma is essentially collisionless, and, when viewed at length scales of $\sim 1/100$ AU or less, appears as large amplitude, broadband magnetic and plasma variations superimposed on (locally) relatively uniform background fields.

At this point it is useful to give a brief summary of some of the physical processes influencing the evolution of solar wind fluctuations. We use the following categorization:

(a) **Expansion**

The supersonic expansion of the solar wind results in a falloff in fluctuation energies as heliocentric distance increases. While this is not a dominating effect, it is usually the strongest

⁷ Coronal magnetic structure is due, at least in part, to motion of the magnetic field line “footpoints,” which itself occurs because convection is active in the photosphere.

⁸ The dissipated wave energy assists in the heating of the corona, resulting in acceleration of the solar wind. The significance of this contribution is an open question however. See, for example, *Neugebauer [1991]* for a brief discussion and further references.

⁹ Recall that for perfect large-amplitude Alfvén waves the non-linear terms cancel exactly. However there are some kinetic effects to be considered.

in the sense that the overall decay with distance is governed approximately by expansion. The approximately spherical nature of this expansion (at least beyond a few 10's of solar radii) leads to energies per unit *mass* decaying, very roughly, as $1/R$. Since the density is approximately $O(1/R^2)$, energies per unit *volume* falloff as $1/R^3$.

(b) **Advection**

“Structures” whose length scales are much less than the length characterizing local large-scale velocity inhomogeneities will typically be carried along by the mean flow—without being distorted by it. Such fluctuations are of course free to evolve under the action of other dynamical processes. Structures which are near regions of large gradients in the mean velocity (*e.g.*, boundaries between high and low speed streams) clearly will not undergo simple advection with the background field, but will also be sheared and otherwise distorted by its structure.

(c) **Waves**

The usual set of MHD waves—Alfvén, magnetosonic, and shock—are all capable of interacting with the solar wind fluctuations. In fact, some of the fluctuations are such waves.

(d) **“Mixing”**

This is the name we give to a newly appreciated *linear* term, which is absent in leading order WKB theory. The term provides coupling between the “inward” and “outward” fluctuations, and depends explicitly on the large-scale gradients of the large-scale background fields. Much of this thesis will be concerned with showing that its effects can not always be neglected when considering the transport of fluctuations in a weakly homogeneous background medium; that is, solutions which are *qualitatively* different from those of leading order WKB theory ensue in certain cases.

(e) **Local Non-linear Couplings**

Spatially local turbulence effects are responsible for the generation of smaller scales from larger ones. Such cascades of energy to smaller and smaller length scales are important for the eventual dissipation of the energy, which occurs preferentially at small scales. This transfer may also play an important role in the observed heating of the solar wind (the radial temperature profile is hotter than that expected for a purely adiabatic expansion of the solar wind). The possibility of inverse cascades of some quantities also exists (see Appendix A). Any other effects not listed above are also considered to reside in this category.

Thus, while the overall amplitude evolution of the MHD-scale fluctuations is governed principally by the (approximately spherical) expansion of the solar wind, in a particular region of space any self-consistent blend of the modifying processes may exert primary influence on the local dynamics [Roberts *et al.*, 1987*a, b*].

In the next two subsections we present an overview and brief history of the two interpretations of solar wind fluctuations with which we will be concerned, namely the “wave” and “turbulence” pictures. Following that, a review of some observationally based constraints and conclusions applicable to solar wind fluctuations appears. Models attempting to explain interplanetary fluctuations must obviously keep these points in mind. More specifically, they should be able to account for the observed radial evolution of both the normalized cross helicity and the Alfvén ratio (see below).

2.5.2 Waves and WKB Theory

After the initial identification of “wave-like” phenomena in the solar wind [Coleman, 1966, 1967], it was a few years before the wave interpretation of interplanetary fluctuations was formulated [Belcher and Davis, 1971]. Using spacecraft data obtained in the inner heliosphere, Belcher and Davis showed that the high degree of correlation existing between the fluctuations in the velocity and magnetic fields was consistent with their being Alfvén waves. Furthermore, when the direction of the mean magnetic field was taken into account, the correlation indicated that the bulk of the modes had an outward sense of propagation.

On the theoretical side, evolution of solar wind fluctuations was modeled using WKB theory for Alfvén waves [*e.g.*, Hollweg, 1973*a, b*, 1974]. The theory is appropriate when considering waves propagating in a *weakly* inhomogeneous medium. In this context “weak” means that the waves have spatial wavelengths which are much shorter than any length scales over which the background fields defining the medium vary. It is essentially a perturbation approach to the problem, and for MHD scales in the solar wind such an approximation is usually valid. The resulting waves are transverse modes which may propagate in either direction along the mean magnetic field. At leading order, these modes are Alfvén waves for which linear superposition is a valid approximation. There is no coupling between the inward and outward propagating modes at this order. Hence no waves may be generated locally, and the fluctuations must originate in the corona and then advect and propagate out with the solar wind. Higher order corrections do involve couplings between the modes, and some consequences of these interactions might be expected to be observable.

If the waves are indeed of a coronal origin, then leading order WKB theory predicts that

only outward propagating modes should exist beyond the *Alfvénic critical radius*. This radius is defined by the distance where, as we move away from the sun, the increasing flow velocity becomes equal to the decreasing Alfvén velocity. Now since Alfvén waves propagate at the Alfvén velocity, the net direction of movement (flow velocity + wave velocity) below the critical point can be either inward or outward. By the same line of reasoning, inward propagating waves present at the critical point are actually stationary since here the flow velocity exactly cancels the wave speed. Thus, no inward modes generated below the critical point can “escape” into the exterior region. If the Alfvénic critical point is used as an inner boundary, the appropriate boundary condition is that the waves all be outward modes. In leading order WKB theory this absence of inward modes can not be modified; the observed dominance of outward modes is thus quite plausible at this level of approximation [Belcher and Davis, 1971; Hollweg, 1973b, 1974]. Currently observations [e.g., Lotova et al., 1985; Lotova, 1988] and theory [e.g., Weber and Davis, 1967] place the Alfvénic critical point somewhere between 7 and 30 R_{sun} . Note however that the observations are not well constrained.

While some results from WKB theory are sometimes in accord with observations (e.g., the radial profile of the energy in the outward modes), several predictions seem to be irreconcilable with the data. For example, the minimum variance direction (MVD) of the fluctuations is observed to be aligned with the mean magnetic field—the alignment becoming more pronounced as distance from the sun increases [e.g., Solodyna and Belcher, 1976; Klein et al., 1991]. Physically this comes about because waves propagating along \mathbf{B}_0 are refracted as they move outwards into regions of lower wave speed. Unfortunately WKB theory predicts that the MVD should be radially oriented [Barnes, 1969; Völk and Alpers, 1975], but Solodyna and Belcher [1976] claim that the behavior of the MVD for a superposition of waves would be in agreement with results from WKB theory.

Also, neither the radial dependence of the normalized cross helicity (σ_c) nor that of the Alfvén ratio (r_A) are given correctly by leading order WKB theory.¹⁰ In conjunction with the boundary conditions appropriate to the Alfvénic critical point, the leading order theory predicts that the normalized cross helicity should remain equal to its boundary value of +1 at all distances. Observationally σ_c is observed to decrease with increasing heliocentric distance, and by 1 AU it typically has a value of around a half in the inertial range. A similar situation exists for the Alfvén ratio, WKB theory predicting a value of unity and observations indicating a value of approximately one half, that is a 2 : 1 excess of magnetic energy over kinetic for the fluctuations.

Hollweg [1990] performed a singular perturbation analysis for WKB theory, and showed

¹⁰ These quantities are defined in section 2.5.4 below. See also Appendix A.

that corrections due to higher order terms are insufficient to account for the discrepancies between observations and WKB theory discussed above. A related point was considered by *Heinemann and Olbert* [1980] who investigated finite wavelength corrections to the WKB approximation, for the particular case of toroidal Alfvén waves in a simplified solar wind geometry where both the velocity and the magnetic fields were radially directed. Again, these corrections are unable to bring the solutions into agreement with observations. Thus, while applicable under some solar wind conditions, WKB theory cannot be the whole story.

2.5.3 Turbulence

The possibility that dynamically active turbulence plays an important *in situ* role in the solar wind was first raised seriously by *Coleman* in 1968. In the following decade the wave interpretation was favored and turbulent processes were considered to be of secondary importance in the interplanetary medium. Since then, however, focus has increasingly shifted towards a description based on turbulent interactions in the plasma. More complete data sets, along with theoretical advances, indicate that the fluctuations are more appropriately interpreted within a turbulence framework [e.g., *Matthaeus and Goldstein*, 1982a, 1983; *Montgomery*, 1983; *Roberts et al.*, 1987a, b; *Mangeney et al.*, 1991; *Marsch*, 1991; *Roberts and Goldstein*, 1991]. One should note that rather than suffering outright abandonment, the wave perspective has undergone a change in emphasis and interpretation and is retained as an important component of the unified description.

In an attempt to improve upon WKB theory, *Tu* and co-workers [*Tu et al.*, 1984; *Tu*, 1988] extended the theory to take into account a turbulent cascade of energy. These models predict heating of the plasma which is in reasonable agreement with observations. The radial dependence of the magnetic energy spectrum shape is also quite well accounted for. However, several of the assumptions and approximations involved in this extended WKB theory are quite limiting, in the sense that they cannot be true everywhere where the model is postulated to apply. As noted by *Zhou and Matthaeus* [1990a], there is a question as to the physical consistency of modeling the “inward” fluctuations as being a small fraction of the “outward” ones, and yet still having an appreciable heating rate due to the turbulence. These early *Tu* models include transport of the “outward” fluctuations, but not of the “inward.” A further limitation of the models is that they restrict the ratio of “inward” and “outward” energies in the fluctuations to be a (small) constant. Observations indicate that this quantity undergoes significant radial evolution, so that it is desirable to allow such variations in attempting to model interplanetary fluctuations.

Zhou and Matthaeus [1989, 1990a, b, c] have recently developed a scale-separated MHD

model of the solar wind which addresses some of these limitations. In particular, “inward” and “outward” fluctuations are treated on an equal footing with transport equations for both these and other quantities being derived in a self-consistent manner. The early, largely analytic, work associated with the Zhou-Matthaeus (ZM) model is in qualitative agreement with solar wind observations. The model, described in detail in Chapter 4, involves dynamical equations describing the evolution of the small-scale fluctuation fields, in the presence of specified large-scale, slowly varying “mean” fields. The small-scale fields are treated as homogeneous and incompressible, and their governing transport equations are, in general, coupled to each other as well as containing dependencies on the large-scale fields. It is the, in general, order one coupling together of the small-scale fields which represents the “new” physics of this model. Since much of this thesis is concerned with results obtained from this model and its extensions, we defer further discussion to later chapters. A similar model has also been developed by Marsch and Tu [*Marsch and Tu*, 1989, 1990*a, b*; *Tu and Marsch*, 1990*a, b*, 1992], and a group working in France has also been active in the field [*Grappin et al.*, 1990, 1991, 1992; *Mangeney et al.*, 1991; *Velli et al.*, 1989*a, b*, 1990*a, b*, 1992].

2.5.4 Review of Observationally Based Conclusions

In discussing interplanetary fluctuations it has proved useful to refer to the *normalized cross helicity*, $\sigma_c = 2H_c/E$, both in its spectral form and as a bulk value. The cross helicity, $H_c = \frac{1}{2} \langle \mathbf{v} \cdot \mathbf{b} \rangle$, is an unnormalized measure of the correlation between the fluctuating velocity and magnetic fields. Note that \mathbf{b} is measured in Alfvén speed units, and $\langle \dots \rangle$ represents an appropriate averaging operator (see the following two chapters). The total energy in the fluctuations is denoted by $E = \frac{1}{2} \langle v^2 \rangle + \frac{1}{2} \langle b^2 \rangle$. More details regarding these definitions are available in Appendix A. Since the bounding values of σ_c , namely ± 1 , correspond to purely Alfvénic fluctuations, the normalized cross helicity is often used as a diagnostic of the degree of Alfvénicity present in the solar wind. Fluctuations are termed Alfvénic when either of the vector equalities $\mathbf{v} = \pm \mathbf{b}$ holds. However, as noted by *Roberts et al.* [1987*a, b*], intermediate values of σ_c do not offer such a clean interpretation of the nature of the fluctuations. In particular, such values do not necessarily indicate a non-interacting superposition of oppositely propagating Alfvén waves. Despite this, cases in which σ_c is small will be referred to as “mixed,” complete “mixing” corresponding to $\sigma_c = 0$.

Another parameter useful in both observational and theoretical contexts is the *Alfvén ratio*, r_A , defined as the ratio of kinetic to magnetic energy. Again both the bulk value ($r_A = E^v/E^b$),

and the values at particular wavenumbers ($r_A(\mathbf{k}) = E^v(\mathbf{k})/E^b(\mathbf{k})$) are of interest.

It should be noted that the radial evolution of the fluctuations shows considerable dependence on stream structure, flow speed, and density. In part this is because the fluid in slow streams is “older” than that in fast ones at comparable distances, having taken longer to get there. Thus, it has had more time to evolve, linearly, non-linearly, or whatever.

2.5.4.1 Cross Helicity Evolution

In an analysis of Voyager and Helios spacecraft data spanning radial distances of 0.3 – 20 AU, *Roberts et al.* [1987a, b] found that relative to an initial state dominated by solar produced, outward propagating fluctuations ($\sigma_c \simeq +1$) there is a systematic tendency for σ_c to become more mixed with increasing heliocentric distance. This indicates that fluctuations of the “inward” type are being produced locally in the solar wind, and in particular beyond the Alfvén radius (see also page 31). In general, the large-scales usually display small σ_c by about 0.5 AU and the transition (via turbulent cascade of this non-Alfvénic energy) to highly mixed states at many inertial scales is accomplished by ~ 5 AU. Note however that such states have been observed as near as 0.3 AU, the current distance of closest approach to the sun for which data are available.

Roberts et al. also remark that this radial evolution in Alfvénicity seems to be inconsistent with the generation of fluctuations occurring predominantly in compression regions, the evidence being that regions of rarefaction show the same type of evolution, albeit at a slightly reduced rate. The implication is thus that it is the entire plasma which is evolving rather than particular subsets of it.

Their conclusion is that the initial population of solar generated, outwardly propagating broadband fluctuations is augmented by fluctuations (having mixed sign of σ_c) produced in regions where velocity stream shear is sufficiently high, and the dominant energy contribution is kinetic. Since the magnitude of the “mean” magnetic field decreases with increasing heliocentric distance ($\sim 1/r^2$ close to the sun), the kinetic energy first becomes dominant relatively close in, and for relatively small wavenumbers. Hence the initial generation of non-solar fluctuations should also occur close in and at the large scales, leading to a reduced value of the normalized cross helicity at such scales. Non-linear interactions will then induce a cascade of fluctuations (with mixed sign of σ_c) towards smaller wavelengths, yielding states which are “mixed” at many scales, despite the lack of kinetic energy dominance across the full range of length scales.

Note however, that recent simulation results [*Roberts et al.*, 1991, 1992] suggest that stream shear cannot produce the reduced σ_c at the large scales, and the authors suggest that the reduction

is due to a “mixing” effect associated with gradients in the stream structure.

Evolution of σ_c is observed to occur most strongly in the inner heliosphere [Roberts *et al.*, 1987*b*], a fact which is consistent with the above line of reasoning since both kinetic energy dominance and velocity shear are pronounced features of this region. The argument also implies that parcels of fluid dominated by solar produced “outward” fluctuations will only exist far from the sun if they are embedded in streams exhibiting predominantly weak shear. This is also in agreement with observations [Roberts *et al.*, 1987*a*, *b*].

Theoretical investigation of the turbulent relaxation process known as *dynamic alignment* [Dobrowolny *et al.*, 1980*a*, *b*], in which an initial preponderance of one type of Alfvénic fluctuation results in its amplification by the turbulence (see also Appendix A), lead to the suggestion that outward waves in the solar wind are generated by local turbulence [Matthaeus *et al.*, 1984]. However, on average, observational data does not support this suggestion.

While not observationally based, numerical work on the evolution of velocity shear layers¹¹ [Goldstein *et al.*, 1989; Roberts *et al.*, 1992] displays evolution of the cross helicity which is evocative of that seen in the solar wind. These simulations also indicate that the fluid tends to evolve *towards* anisotropy. Such evolution occurs because under these conditions spectral transfer in the direction of the mean field is suppressed.

2.5.4.2 Spectra

The power spectrum has frequently been observed to have a powerlaw (in frequency or wavenumber) inertial subrange with a spectral index consistent with the Kolmogorov $-5/3$ value and inconsistent with values of -2 and the Kraichnan $-3/2$ value [Matthaeus and Goldstein, 1982*a*; Marsch and Tu, 1990*a*; Roberts *et al.*, 1990*a*]. Clearly the solar wind is neither isotropic (the magnetic field, for example, introduces a preferred direction) nor time-stationary, and even its homogeneity is questionable in general. Kolmogorov theory is based on the assumption that these three conditions are met (in a statistical sense) in an hydrodynamic fluid, and thus it is not immediately clear why a Kolmogorov spectral index is observed in the interplanetary plasma. For finite times and specific parcels of fluid however, it is quite possible for any or all of these simplifying characteristics of the turbulence to be relevant. Matthaeus and Goldstein [1982*a*, *b*] analyzed various intervals of Voyager data and found that significant numbers of these intervals

¹¹ The MHD form of the Kelvin-Helmholtz instability.

were approximately time-stationary and weakly homogeneous.¹² It should be noted that many of the data intervals analyzed do *not* suggest that the power spectrum inertial range is given by a $k^{-5/3}$ dependence, in fact, spectral indices ranging from -1 to -2 have been reported [Sari and Valley, 1976]. Such powerlaw dependence is, however, indicative of the influence of at least one *non-linear* dynamical process and consistent with turbulence of some form.

In the studies just mentioned, the analyses were all performed in terms of the “primitive” \mathbf{v} and \mathbf{b} variables. Recent work [*e.g.*, Tu *et al.*, 1989; Grappin *et al.*, 1991] has instead used Elsässer variables, so that, for example, spectra for “inward” and “outward” fluctuations are presented. Using Helios data from near 0.3 AU, Tu *et al.* [1989] found that typically the “ \pm ” power spectra exhibited different behavior relative to each other, as well as showing dependence on mean flow speed.¹³

More specifically, referring to figure 2.5, taken from Tu *et al.*’s paper, it can be seen that in high speed (“younger”) flows the “ \pm ” spectra both contain two, fairly distinct, powerlaw regions. For the “inward” fluctuations the spectrum is steeper (spectral index $\alpha \approx -1.5$) at lower frequencies (wavenumbers), and shallower ($\alpha \approx -0.4$) at higher ones. Note that the spectral slope of the steeper portion is approximately the same as the value for the MHD inertial range derived from theoretical considerations [Kraichnan, 1965]. For the “outward” fluctuations, the reverse is seen, with a relatively shallow slope ($\alpha \approx -0.6$) at lower frequencies and a steeper range ($\alpha \approx -1.2$) at the high end. The “breakpoints” between these regions of differing spectral slopes occur at similar frequencies, the “outward” mode one occurring at a somewhat larger frequency. At a given frequency, power in the “outward” fluctuations is usually at least one, if not two, orders of magnitude greater than that associated with the “inward” modes. This characteristic structure has been referred to as “rhombic” in shape [Grappin *et al.*, 1990].

In the “older” low speed samples near 0.3 AU, the “outward” mode power spectra typically have a single powerlaw ($\alpha \approx -1.6$) throughout most of the inertial range, the resemblance to Kolmogorov spectra being quite striking. “Inward” mode spectra display a similar powerlaw for the lower “half” of the inertial range, and then break to a shallower slope ($\alpha \approx -1.2$).

The authors also found that the correlation lengths for the “inward” and “outward” power spectra were quite different: the “inward” one usually being 5 or 6 times larger than the “outward.”

¹² A fluid is said to be weakly homogeneous if for all fields $\mathbf{B}(\mathbf{x})$ associated with the fluid, both $\langle \mathbf{B}(\mathbf{x}) \rangle$ and $\langle \mathbf{B}_i(\mathbf{x})\mathbf{B}_j(\mathbf{x} + \mathbf{r}) \rangle$ are independent of \mathbf{x} , where $\langle \dots \rangle$ denotes an appropriate averaging procedure. Full homogeneity requires that all higher moments also depend only on the *relative* configurations of the evaluation locations.

¹³ Recall that, at a given heliocentric distance, slow speed solar wind has had more time to evolve than material in fast streams.

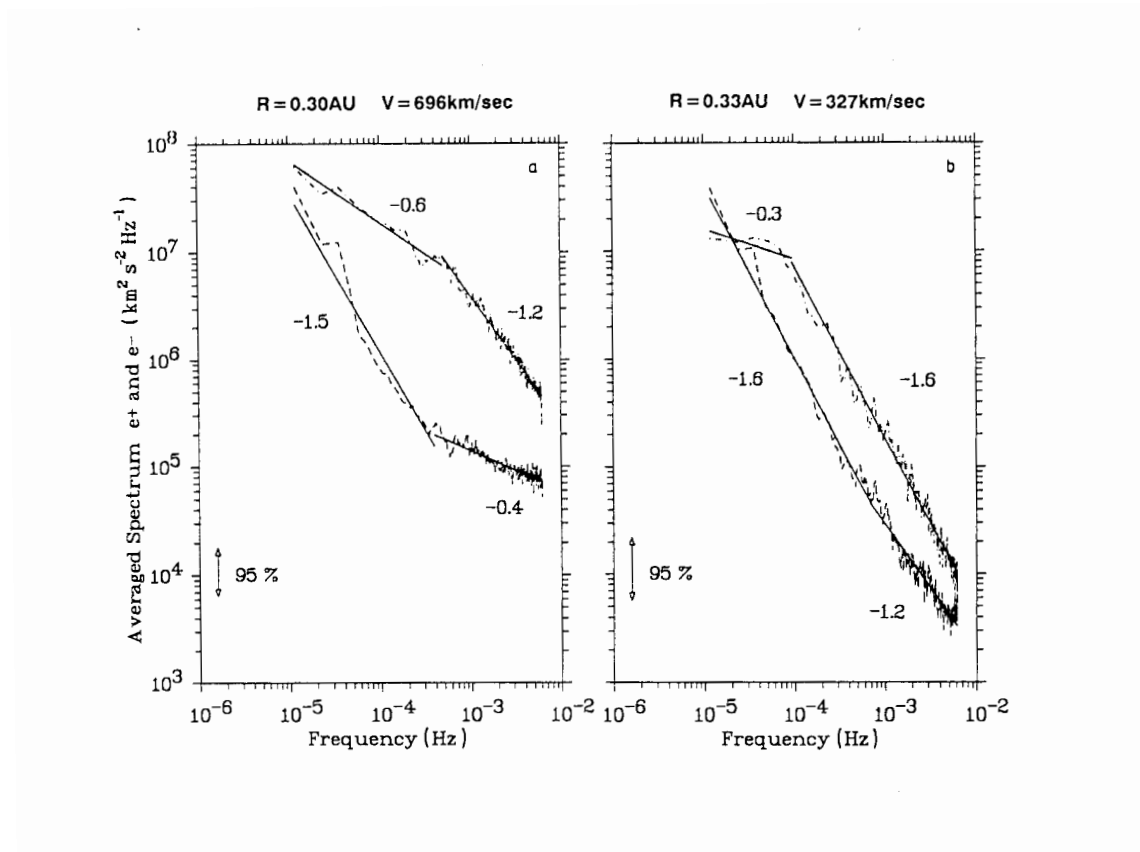


Figure 2.5: Averaged Elsässer spectra for Helios data obtained near 0.3 AU. The upper curves are for “outward” fluctuations and the lower ones for the “inward” modes. The figure is taken from *Tu et al.* [1989].

These correlation lengths do not seem to depend on stream structure, at least at this heliocentric distance, being approximately equal in the high and low speed samples. Typical values are approximately 0.01 AU for the “outward” fluctuations and 0.07 AU for the “inward” modes.

Finally the energy difference (kinetic minus magnetic) spectra in low speed streams typically displayed powerlaws with slope approximately equal to the Kolmogorov value of $-\frac{5}{3}$. In high speed (younger) flow, the energy difference data points are widely distributed and no clear power law is evident. This is evidence, admittedly circumstantial, that *in situ* turbulent evolution is occurring in the solar wind. In any case, no clear connection between these observations and WKB theory, even at higher order, has been established [*e.g.*, *Hollweg*, 1990].

2.5.4.3 Compressional Effects

Roberts et al. [1987*a*] also reported on number density fluctuations in the solar wind. They found that over distances of 1 – 11 AU small-scale density fluctuations (δn) were typically 10% or less of the (local) mean value. These results were seen to hold for both compression and rarefaction regions, regardless of the much larger mean field associated with the former. Qualitatively similar results hold for $\delta \mathbf{B}/\mathbf{B}$.

The correlation between density and magnetic field magnitude (or equivalently between density and B^2 , the latter being proportional to the magnetic pressure) can also provide information on the compressible nature of the solar wind. For small scales (frequencies $\gtrsim 1/\text{day}$) the correlation is significant and negative, and since the mechanical pressure fluctuations (δP_{mech}) are expected to be proportional to δn (*cf.* small amplitude sound waves) this implies that the total pressure is approximately constant. These nearly *pressure balanced structures* (PBSs) are observed in both compressive and rarefactive regions, and furthermore the correlation is independent of solar cycle [*Roberts et al.*, 1987*a*; *Roberts*, 1990*a*]. The theory of nearly incompressible MHD indicates that a second class of (nearly) PBSs may also be present in the solar wind [*Zank et al.*, 1990]. This class is characterized by a density-temperature anticorrelation and an almost constant magnetic field magnitude.

In regions where the omni-directional magnetic energy spectrum is proportional to $k^{-5/3}$, NI theory, applied to isotropic MHD turbulence, can explain density fluctuation spectra which are also proportional to $k^{-5/3}$ [*Montgomery et al.*, 1987; *Matthaeus and Brown*, 1988; *Matthaeus et al.*, 1990]. Such density spectra have been observed in the solar wind. Taken together, the theory and the observations have led to the suggestion that, rather than being dynamical modes, the density

fluctuations are quasi-static structures resulting from compressive effects [*Roberts and Goldstein, 1991*].

Roberts et al. [1987b] also make the observation that, at least in the outer heliosphere, there appears to be a clear distinction between the compressible nature of the small and large scales. The latter are dominated by compressive effects, while the former are frequently associated with PBSs which are consistent with NI MHD behavior. However, to the best of our knowledge, current models of solar wind fluctuations have yet to include either NI or compressible effects in a realistic fashion (but see *Roberts et al. [1991]*). Indeed, the present generation of models often invoke further simplifying assumptions, such as spherical symmetry and isotropic fluctuations, which are of questionable validity in the solar wind.

This concludes our discussion of the introductory and background material relevant to the solar wind. In the next chapter we take time out to consider some quantities of interest for general homogeneous turbulence, before moving on the transport theory itself.

Chapter 3

CORRELATION TENSORS FOR GENERAL HOMOGENEOUS TURBULENCE

You do not understand anything until you understand it
in more than one way.

— Marvin Minsky

3.1 Introduction

Before moving on to the transport model, it will be useful to present some information regarding structural aspects of the correlation functions, spectra, and related quantities of (statistically) homogeneous turbulent magnetofluids. These quantities and their properties are of importance within the transport theory, since the small-scale fluctuations are assumed to be, locally, of this type.

In part this chapter is a review of some well known material, since many results pertaining to two-point autocorrelation matrices for homogeneous solenoidal vector (true and pseudo) fields, for particular symmetries of the turbulence, have been known for some time now [*Taylor*, 1935; *Von Karman and Howarth*, 1938; *Robertson*, 1940; *Chandrasekhar*, 1950, 1951*a, b*; *Batchelor*, 1970; *Matthaeus and Smith*, 1981]. However, for general homogeneous turbulence, with no assumed rotational symmetries, a full exposition of the general form for such matrices, and also the cross correlation forms, does not appear to have been published. The new material in this chapter, which includes much of the work in section 3.4, is about to be submitted for publication [*Rädler et al.*, 1993].

It will be convenient to derive most of the results using the “primitive” \mathbf{v} and \mathbf{b} vectors. In anticipation of our desire to work with Elsässer variables ($\mathbf{z}^{\pm} = \mathbf{v} \pm \mathbf{b}$) in the transport theory, however, we will also summarize the results of this chapter in terms of these variables.

3.2 Definitions and Notation

The zero-mean proper and pseudo vector solenoidal fields are denoted by $\mathbf{v}(\mathbf{x}, t)$ and $\mathbf{b}(\mathbf{x}, t)$ respectively, where \mathbf{x} and t are the usual space and time coordinates. However, since this chapter is

primarily concerned with the kinematics and structural features of the tensors (*i.e.*, no dynamics), the time dependence of the fields will usually be suppressed. In terms of incompressible MHD, these quantities have obvious interpretations as the fluctuating parts of the velocity and magnetic fields.¹ We wish to consider the correlation between two spatially separated components of these fields—where both auto and cross correlations are of interest. Under the assumption of homogeneity such correlation matrices are invariant with respect to a change of coordinate origin, and thus depend only on the relative separation of the two points in space at which the fields are evaluated.

While we use the customary definitions for the autocorrelation functions, there are several ways to define the cross-correlation functions, each entailing different symmetry properties. For reasons which will become clear below, we adopt the following definitions:

$$R_{ij}^v(\mathbf{r}) = \langle v_i(\mathbf{x})v_j(\mathbf{x} + \mathbf{r}) \rangle = \langle v_iv'_j \rangle, \quad (3.1)$$

$$R_{ij}^b(\mathbf{r}) = \langle b_ib'_j \rangle, \quad (3.2)$$

$$R_{ij}^{vb}(\mathbf{r}) = \langle v_ib'_j \rangle, \quad (3.3)$$

$$R_{ij}^\pm(\mathbf{r}) = \frac{1}{2} \langle v_ib'_j \pm b_iv'_j \rangle, \quad (3.4)$$

where the prime denotes evaluation of the field at the spatially displaced position, and the angle brackets ($\langle \dots \rangle$) denote an appropriately defined ensemble average, usually taken to be equivalent to long-time averaging [*e.g.*, *Batchelor*, 1970]. R^{vb} is really only used as an intermediate correlation function, useful for obtaining its functionally symmetrized forms, R^\pm . Throughout this chapter, we will refer to R^v , R^b , and R^\pm as the four “primary” tensors. In order to avoid unnecessary repetition, previously established results pertaining to R^v and R^b will often only be quoted here; the relevant derivations may be found in *Batchelor* [1970] and *Matthaeus and Smith* [1981] for example.

Note that if \mathbf{v} and \mathbf{b} are interpreted as the usual MHD fields, then the “minus” tensor evaluated at the origin, $R_{ij}^-(0) = \langle v_ib_j - b_iv_j \rangle$, shows a clear relationship to the ensemble averaged induced electric field ($\mathcal{E} = -\langle \mathbf{v} \times \mathbf{b} \rangle$) of the MHD fluctuations. In fact it is straightforward to show that $J_{ij}^-(\mathbf{r} = \mathbf{0}) = -\epsilon_{ij\alpha} \mathcal{E}_\alpha$, where J^- is the index antisymmetric part of R^- (see below). We will have more to say regarding the induced electric field in later sections.

Before proceeding, we pause to make a few semantic and notational distinctions. First, the terms *symmetric* and *antisymmetric* will only be used in reference to the *index* symmetry of the tensors and correlation matrices (and their Fourier transforms). Likewise, the terms *even*

¹ Where \mathbf{b} is measured in Alfvén speed units, *i.e.*, $\mathbf{b} = \tilde{\mathbf{b}}/\sqrt{4\pi\rho}$, ρ the uniform mass density of the fluid.

and *odd* refer to the behavior of a form under coordinate inversion, whether the coordinate be \mathbf{r} or its Fourier conjugate \mathbf{k} . Second, unless otherwise stated, the absence of a “*v*”, “*b*”, “+”, or “-” superscript indicates that the equation, result, or definition applies equally well to all four correlation matrices, tensor forms, or scalar functions as appropriate. A sub/super-script “*v/b*” indicates the relation applies to both the “*v*” and “*b*” autocorrelation tensors, and is not to be confused with the superscript “*vb*” of equation (3.3) for example. Also, both the indexed and unindexed forms will be used to denote the same tensor/matrix, *e.g.*, $R_{ij} \equiv R$, except in cases where ambiguity or confusion is likely to result.

In order to illuminate the nature of the correlation matrices as clearly as possible it is convenient to decompose them in various ways. In the decompositions which follow, the proper or improper nature of the tensor elements under coordinate inversion will play an important role. Defining the coordinate inversion operator \mathcal{I} in the usual way, that is, as the improper rotation which maps the position vector \mathbf{r} to its negative, *i.e.*, $\mathcal{I}\mathbf{r} = -\mathbf{r}$, it is readily established that under coordinate inversion the coordinate basis vectors are mapped to their negatives, and a right-handed system maps to a left-handed one. Proper and improper tensors obey the following transformation rules: A proper (or true) tensor \mathbb{T} of rank n transforms as

$$\mathcal{I}\mathbb{T}(\mathbf{r}) = (-1)^n \mathbb{T}(\mathbf{r}),$$

while an improper (or pseudo) tensor of the n th rank, \mathbb{P} , satisfies

$$\mathcal{I}\mathbb{P}(\mathbf{r}) = (-1)^{n+1} \mathbb{P}(\mathbf{r})$$

In this context we will use “true” as a synonym for proper, and “pseudo” as a pseudonym for improper. We are now ready to proceed with the decompositions of the correlation functions.

First, suppose that a correlation function is of the following form,

$$R_{ij}(\mathbf{r}) = \left(\delta_{ij} - \frac{r_i r_j}{r^2} \right) A(\mathbf{r}) + \epsilon_{ij\alpha} \frac{\partial}{\partial r_\alpha} B(\mathbf{r}) + \dots, \quad (3.5)$$

so that each additive term is of the form a tensor “part with (free) indices” \times a (true or pseudo) scalar function of \mathbf{r} . In fact, this can be shown to be the case, and the true/pseudo nature of the “parts with indices” and the scalar functions will be of great importance in deducing certain results. At this point we merely wish to introduce the notation. The “parts with indices” are essentially geometrical aspects of the correlation functions; for example, $\delta_{ij} - r_i r_j / r^2$ is an isotropic form, invariant under rigid body rotations (of either the coordinate system or the turbulence), and also under coordinate reflection.

Next, a general second rank tensor may always be written as the sum of an index symmetric part and an index antisymmetric part. For the tensor R we denote these symmetric and antisymmetric parts by I and J respectively, where $I_{ij}(\mathbf{r}) = (R_{ij}(\mathbf{r}) + R_{ji}(\mathbf{r}))/2$, and $J_{ij} = (R_{ij} - R_{ji})/2$. For example,

$$R_{ij}^{\pm}(\mathbf{r}) = I_{ij}^{\pm}(\mathbf{r}) + J_{ij}^{\pm}(\mathbf{r}). \quad (3.6)$$

The Fourier representation of the correlation matrices is also of importance; the Fourier transform of $f(\mathbf{r})$ being denoted by $f(\mathbf{k})$ in general. However, in order to maintain agreement with the customary notation, we depart from this convention when $f(\mathbf{r})$ is one of the $R_{ij}(\mathbf{r})$ correlation matrices, and use instead the traditional $S(\mathbf{k})$ to denote the spectral tensor. Thus,

$$I_{ij}^{\pm}(\mathbf{k}) = \frac{1}{(2\pi)^3} \int d^3r I_{ij}^{\pm}(\mathbf{r}) e^{-i\mathbf{k}\cdot\mathbf{r}}, \quad (3.7)$$

but

$$S_{ij}^{\pm}(\mathbf{k}) = \frac{1}{(2\pi)^3} \int d^3r R_{ij}^{\pm}(\mathbf{r}) e^{-i\mathbf{k}\cdot\mathbf{r}}. \quad (3.8)$$

Certain other exceptions are also in effect for the Elsässer representation (see section 3.9). The definitions $k = |\mathbf{k}|$ and $\hat{\mathbf{k}} = \mathbf{k}/k$ are also of use, and, in general, a “hat” will be used to signify unit vectors.

As is well known, the reality of a function in x -space imposes a constraint on the form of its Fourier transform; namely if $f(\mathbf{x})$ is real then $f(-\mathbf{k}) = f^*(\mathbf{k})$, where a “*” denotes complex conjugation. Using this property and the assumed equivalence of ensemble and space averaging (via invocation of ergodicity), it can be shown that, for example,

$$S_{ij}^v(\mathbf{k}) \delta(\mathbf{k} + \mathbf{p}) = \langle v_i(\mathbf{k}) v_j(\mathbf{p}) \rangle. \quad (3.9)$$

The delta function on the left-hand side arises because we are dealing with perfectly homogeneous turbulence in an infinite domain. Thus, the integral of the absolute value of any non-zero function over the entire volume is unbounded. Consequently we must use Stieltjes integrals instead of the more familiar Riemann ones (see for example section 2.5 of *Batchelor* [1970]). This technicality may be sidestepped by working with velocity and magnetic fields whose integrals over all space are bounded, but which only differ from the perfectly homogeneous fields in physically unimportant ways. For example, taking \mathbf{v} and \mathbf{b} to be periodic with very large wavelengths allows Fourier series to be used, while supposing \mathbf{v} and \mathbf{b} to be zero outside a very large box means that Fourier

integrals may be used. In any case, for our purposes the distinction is unimportant and we will drop the δ functions in such equations, and use shorthand forms such as

$$\begin{aligned} S_{ij}^v(\mathbf{k}) &= \langle v_i(-\mathbf{k})v_j(\mathbf{k}) \rangle \\ &= \langle v_i^*(\mathbf{k})v_j(\mathbf{k}) \rangle, \end{aligned} \quad (3.10)$$

$$\begin{aligned} S_{ij}^\pm(\mathbf{k}) &= \langle v_i(-\mathbf{k})b_j(\mathbf{k}) \pm b_i(-\mathbf{k})v_j(\mathbf{k}) \rangle \\ &= \langle v_i^*(\mathbf{k})b_j(\mathbf{k}) \pm b_i^*(\mathbf{k})v_j(\mathbf{k}) \rangle. \end{aligned} \quad (3.11)$$

As the Fourier transform is a linear operator, results holding in one space have direct analogs in the inverse space. These dual forms of the relationships usually have closely related structural forms, although the associated interpretations may be quite different. Indeed, despite the equivalence, some properties are more clearly revealed in a particular space.

Quantities which will be of particular interest in later chapters include the so called *rugged invariants* of ideal non-dissipative incompressible MHD [Kraichnan and Montgomery, 1980; Frisch et al., 1975], which have been successfully used to characterize MHD turbulence phenomena in the solar wind [e.g., Matthaeus and Goldstein, 1982a]. Further discussion of these quantities is available in Appendix A and the references; here we merely define them. For 3D homogeneous MHD turbulence the three known rugged invariants are the *total energy* per unit mass $E^{tot} = E^k + E^m$, with kinetic and magnetic contributions E^k , E^m ; the *cross helicity* $H_c = \langle \mathbf{v} \cdot \mathbf{b} \rangle / 2$, and the *magnetic helicity* $H_m = \langle \mathbf{a} \cdot \nabla \times \mathbf{a} \rangle / 2$, where \mathbf{a} is the magnetic vector potential, with $\tilde{\mathbf{b}} = \nabla \times \mathbf{a}$ ($\tilde{\mathbf{b}} = \sqrt{4\pi\rho} \mathbf{b}$). Another quadratic quantity of interest is the helicity of the velocity field,² $H_k = \langle \mathbf{v} \cdot \nabla \times \mathbf{v} \rangle$. In 3D hydrodynamics this is an invariant, but is not thought to be rugged in the usual sense [Kraichnan, 1973]. The analogous magnetic quantity, $H_j = \langle \mathbf{j} \cdot \nabla \times \mathbf{j} \rangle$, is the helicity of the electric current density, and although not an ideal invariant, rugged or otherwise, it is of theoretical importance, for example, in dynamo theory [e.g., Krause and Rädler, 1980].

Along with the bulk values of the rugged invariants defined above, their wavenumber spectra are also of interest. Three distinct but related types of spectra are typically used, namely the *modal*, *omni-directional*, and *reduced* (a.k.a. one dimensional) forms [e.g., Batchelor, 1970]. Let Q^{tot} be the bulk value of a particular rugged invariant, with correlation function $R_{ij}(\mathbf{r})$. Then, denoting the three types of spectral tensors by $Q_{ij}^{mod}(\mathbf{k})$, $Q_{ij}^{omni}(k)$, and $Q_{ij}^{red}(k_1)$, it can be shown that

$$Q^{tot} = \int Q_{ii}^{mod}(\mathbf{k}) d^3\mathbf{k} \quad (3.12)$$

² We use the subscript k rather than the more usual v for this helicity to avoid notational conflicts later in the chapter.

$$= \int Q_{ii}^{omni}(k) dk \quad (3.13)$$

$$= \int Q_{ii}^{red}(k_1) dk_1, \quad (3.14)$$

where k_1 is a particular Cartesian component of the wave-vector \mathbf{k} . Often only the reduced spectrum will be available from experimental data, it being the one simply related to the readily observable correlation function:

$$Q_{ij}^{red}(k_1) = \frac{1}{2\pi} \int e^{-ik_1 r_1} R_{ij}(r_1, 0, 0) dr_1 \quad (3.15)$$

$$= \int Q_{ij}^{mod}(\mathbf{k}) dk_2 dk_3. \quad (3.16)$$

Examination of the four “primary” tensors indicates that various pieces of them are directly related to the rugged invariants. This is the subject of section 3.5.

While we will not have much to say about it in this chapter, there is one other tensor in which we are interested, namely the *energy difference* tensor

$$R_{ij}^D(\mathbf{r}) = R_{ij}^v - R_{ij}^b. \quad (3.17)$$

Its trace yields the energy difference spectrum, $D(\mathbf{k}) = E^k(\mathbf{k}) - E^m(\mathbf{k})$, also known as the residual energy spectrum [*e.g.*, Pouquet *et al.*, 1976; Grappin *et al.*, 1982, 1983]. We shall make extensive use of this quantity in the transport theory of later chapters. The antisymmetric portion of the difference spectrum tensor is related to the difference of the velocity helicity spectrum, $H_k(\mathbf{k})$, and the magnetic helicity spectrum, $H_m(\mathbf{k})$, by

$$\begin{aligned} J_{ij}^D(\mathbf{k}) &= S_{ij}^{D,anti}(\mathbf{k}) \\ &= \frac{i}{2} \epsilon_{ij\alpha} k_\alpha [H_k(\mathbf{k}) - H_m(\mathbf{k})]. \end{aligned} \quad (3.18)$$

Of course, omni-directional and reduced spectral forms may also be calculated. Since in the transport theory we will assume that neither velocity helicity nor magnetic helicity are present, J_{ij}^D will not be considered further here. Additional quantities will be defined as they arise.

3.3 Basic Results

Having established our fundamental definitions we now proceed to some basic results. First, the solenoidal nature of \mathbf{v} and \mathbf{b} means that

$$\frac{\partial}{\partial r_j} R_{ij}(\mathbf{r}) = \frac{\partial}{\partial r_i} R_{ij}(\mathbf{r}) = 0, \quad (3.19)$$

or equivalently in k -space

$$k_i S_{ij}(\mathbf{k}) = k_j S_{ij}(\mathbf{k}) = 0, \quad (3.20)$$

where, here and subsequently, we use the Einstein summation convention unless otherwise indicated (*i.e.*, repeated tensor indices imply summation over all coordinate directions—often Greek indices will be dummy and roman ones “real”). Similar results hold for the I and J tensors, so that the symmetric and antisymmetric parts are separately solenoidal, as may be seen by substitution into the definitions of I and J .

Next, homogeneity requires that

$$R_{ij}^{v/b}(-\mathbf{r}) = R_{ji}^{v/b}(\mathbf{r}), \quad (3.21)$$

$$R_{ij}^{\pm}(-\mathbf{r}) = \pm R_{ji}^{\pm}(\mathbf{r}), \quad (3.22)$$

as is easily seen by letting $\mathbf{x} \rightarrow \mathbf{x} - \mathbf{r}$ in the definitions. Note the reversed indices between the left and right-hand sides, and the overall negative sign associated with the “minus” tensor. Using the definitions of the I ’s and J ’s it is straightforward to show that each of these forms satisfies the same homogeneity condition as its “parent” R . In k -space the second relation takes the form $S_{ij}^{\pm}(-\mathbf{k}) = \pm S_{ji}^{\pm}(\mathbf{k})$, as a consequence of the linearity of the Fourier transform. Analogous results hold for $S^{v/b}$. As we shall see, this is not the only way in which the “minus” tensors are anomalous.

Matthaeus and Smith [1981] derived the result that “any homogeneous correlation matrix R of the form $R_{ij}(\mathbf{r}) = \langle b_i(\mathbf{x}) b_j(\mathbf{x} + \mathbf{r}) \rangle$, consists of the sum of a symmetric proper tensor and an antisymmetric pseudotensor,” which they refer to as Theorem A. The theorem holds independent of the vector or pseudovector nature of the field \mathbf{b} . Unfortunately it now seems that this theorem is incorrect, or more precisely, it only holds for the “parts with indices.” The correct, and slightly generalized, statement (Theorem AA) is now believed to be “ R^v and R^b are proper (true) tensors, while R^{\pm} are pseudotensors.” The point being that, in each case, the whole form has the same *overall* true or pseudo nature. The somewhat subtle nature of the arguments leading to these results is best appreciated when more is known about the form of the tensors, so that we defer discussion to section 3.7. A more complete discussion of the new theorem will also be found in *Rädler et al.* [1993]. These results have important consequences for correlation matrices. For the “ v/b ” tensors, for example, each additive component of R can only be a true tensor multiplied by a true scalar function, or a pseudotensor multiplied by a pseudoscalar function.

As discussed in the references [*e.g.*, *Batchelor*, 1970; *Orszag*, 1977; *Matthaeus and Smith*, 1981], by treating the correlation functions as inner products and applying the Schwartz inequality

Table 3.1: Some basic properties of the four “primary” spectral tensors. As far as the properties listed here are concerned, the v/b tensors behave in the same fashion as the “+” ones. See the text for details and the appropriate forms in x -space.

Property	Full Tensor	Symmetrized Components
Homogeneity	$S_{ij}^{\pm}(\mathbf{k}) = \pm S_{ji}^{\pm}(-\mathbf{k})$	$I_{ij}^{\pm}(\mathbf{k}) = \pm I_{ij}^{\pm}(-\mathbf{k})$ $J_{ij}^{\pm}(\mathbf{k}) = \mp J_{ij}^{\pm}(-\mathbf{k})$
Solenoidality	$k_i S_{ij}^{\pm} = k_j S_{ij}^{\pm} = 0$	$k_i I_{ij}^{\pm} = k_j I_{ij}^{\pm} = 0$ $k_i J_{ij}^{\pm} = k_j J_{ij}^{\pm} = 0$

to them, we can obtain upper and lower bounds on the magnitudes of the matrix elements. For example,

$$|R_{ij}(\mathbf{r})|^2 \leq R_{ii}(0) R_{jj}(0) \quad (\text{no sum implied}). \quad (3.23)$$

It follows that the diagonal components are bounded (in magnitude) by their values at $\mathbf{r} = 0$.

Using the properties outlined above it is straightforward to prove certain facts about the I 's and J 's. Consider the situation in k -space for the index symmetric portions of S^{\pm} :

$$\begin{aligned} I_{ij}^{\pm}(-\mathbf{k}) &= \pm I_{ji}^{\pm}(\mathbf{k}) && (\text{homogeneity}) \\ &= \pm I_{ij}^{\pm}(\mathbf{k}) && (\text{index symmetry}) \\ &= (I_{ij}^{\pm})^*(\mathbf{k}), && (\text{reality}) \end{aligned}$$

which implies that $I_{ij}^{\pm*}(\mathbf{k}) = \pm I_{ij}^{\pm}(\mathbf{k})$, and thus $I^+(\mathbf{k})$ is a real, index symmetric, even function of \mathbf{k} (\Rightarrow Hermitian), while $I^-(\mathbf{k})$ is a pure imaginary, index symmetric, odd function of \mathbf{k} (\Rightarrow anti-Hermitian). Similar results are obtained for $J_{ij}^{\pm}(\mathbf{k})$.

Some of the important properties of the S 's, I 's, and J 's are summarized in Tables 3.1 and 3.2. The anomalous behavior of the “minus” tensors is clearly displayed in these tables.

3.4 Explicit Forms for the Tensors

3.4.1 Introduction

We now wish to consider explicit tensorial forms for the correlation functions and spectra. More specifically, we wish to write each tensor as a sum of terms which are themselves products of “parts with indices” and scalar functions, *e.g.*, $\delta_{ij}A(\mathbf{r})$. In particular, we will show that for each

Table 3.2: Further properties of the symmetric and antisymmetric components of the “primary” spectral tensors. Note the anomalous behavior of the “minus” tensors. In x -space, columns 2, 4, and 5 still apply, but all quantities are of course purely real.

Tensor	Tensor Character	Real or Imaginary	Index Symmetry	\mathbf{k} parity	Hermitian Nature
$I^v(\mathbf{k}), I^b(\mathbf{k})$	True	Re	Sym	Even	Herm
$I^+(\mathbf{k})$	Pseudo	Re	Sym	Even	Herm
$I^-(\mathbf{k})$	Pseudo	Imag	Sym	Odd	Anti-Herm
$J^v(\mathbf{k}), J^b(\mathbf{k})$	True	Imag	Anti	Odd	Herm
$J^+(\mathbf{k})$	Pseudo	Imag	Anti	Odd	Herm
$J^-(\mathbf{k})$	Pseudo	Re	Anti	Even	Anti-Herm

R (or S) there are exactly four independent (and more or less arbitrary) such scalar functions.³ In association with the correct geometrical tensor forms (the “parts with indices”), these so-called *scalar generating functions* completely specify the correlation functions of homogeneous turbulence. In order to achieve this end it will be useful to decompose \mathbf{v} and \mathbf{b} into their poloidal and toroidal components (Appendix B).

3.4.2 Theory for Construction of the Tensors

The approach adopted here is to write the solenoidal fields in a general form, construct the correlation matrices, and then perform some algebraic sleight of hand in order to coax the representations into more convenient and revealing forms. Alternatively one could use the theory of isotropic tensors, developed by *Robertson* [1940] and *Chandrasekhar* [1950, 1951*a*, *b*]. Their procedure is to

- (i) List all possible dyadic “construction elements” which can be formed from combinations of the fundamental vectors in the problem and the two isotropic tensors δ_{ij} and ϵ_{ijm} (*e.g.*, $r_i r_j$, $\epsilon_{ijm} r_m$).
- (ii) Associate a (multiplying) scalar function with each construction element. These functions depend only on the invariant scalars formed from the inner products of the fundamental vectors of the problem. For example, $A(r^2, r_z)$, where $r^2 = \mathbf{r} \cdot \mathbf{r}$, and $r_z = \mathbf{r} \cdot \hat{\mathbf{B}}_0$. One of the sources of past confusion has been that such functions have sometimes been assumed to

³ Portions of this result have been known for some time, and in particular the antisymmetric parts of the auto-correlation tensors have been shown to require only a single generating scalar function [*e.g.*, *Matthaeus and Smith*, 1981; *Matthaeus et al.*, 1982].

be true scalars. This is implicit, for example, in discussions dating back to *Robertson* [1940]. However, as will be discussed in section 3.7, some of these functions are in fact pseudoscalars.

(iii) Forming the sum of all such terms, and

(iv) Imposing appropriate constraints (*e.g.*, solenoidal fields, homogeneity) on the resulting form.

This would lead to relationships among the various terms in the general expression, and thence to the minimum number of generating scalar functions.

3.4.3 Tensor Forms and the Vector Potentials

In this section we adopt an approach due to Rädler, based on a representation of the turbulent fields in terms of their vector potentials. The properties of the correlation tensors are deduced by direct construction in terms of these potentials.

As is well known, a solenoidal field may be expressed as the curl of a vector function of position, which itself is arbitrary to within the gradient of a scalar function of position, the so called gauge freedom. These results are also applicable in k -space. We use the following notation:

$$\mathbf{v}(\mathbf{x}) = \nabla \times \boldsymbol{\psi}(\mathbf{x}), \quad \mathbf{v}(\mathbf{k}) = i \mathbf{k} \times \boldsymbol{\psi}(\mathbf{k}), \quad (3.24)$$

$$\mathbf{b}(\mathbf{x}) = \nabla \times \mathbf{A}(\mathbf{x}), \quad \mathbf{b}(\mathbf{k}) = i \mathbf{k} \times \mathbf{A}(\mathbf{k}), \quad (3.25)$$

from which it follows that

$$\begin{aligned} \boldsymbol{\omega}(\mathbf{x}) &= \nabla \times \mathbf{v}(\mathbf{x}) & \boldsymbol{\omega}(\mathbf{k}) &= i \mathbf{k} \times \mathbf{v}(\mathbf{k}) \\ &= -\nabla^2 \boldsymbol{\psi} + \nabla \nabla \cdot \boldsymbol{\psi}, & &= k^2 \boldsymbol{\psi} - \mathbf{k}(\mathbf{k} \cdot \boldsymbol{\psi}), \end{aligned} \quad (3.26)$$

$$\begin{aligned} \mathbf{j}(\mathbf{x}) &= \nabla \times \mathbf{b}(\mathbf{x}) & \mathbf{j}(\mathbf{k}) &= i \mathbf{k} \times \mathbf{b}(\mathbf{k}) \\ &= -\nabla^2 \mathbf{A} + \nabla \nabla \cdot \mathbf{A}, & &= k^2 \mathbf{A} - \mathbf{k}(\mathbf{k} \cdot \mathbf{A}). \end{aligned} \quad (3.27)$$

When \mathbf{v} and \mathbf{b} are the usual MHD fields (in appropriate units), $\boldsymbol{\psi}$ is the velocity stream function, $\boldsymbol{\omega}$ the vorticity, and \mathbf{j} the electric current density.

Making the appropriate substitutions and using the odd identity or two, we obtain

$$\begin{aligned} S_{ij}^{vb}(\mathbf{k}) &= \langle v_i^* b_j \rangle \\ &= \langle \epsilon_{i\alpha\beta} k_\alpha \psi_\beta^* \epsilon_{j\mu\nu} k_\mu A_\nu \rangle \\ &= k^2 \left[\delta_{ij} - \frac{k_i k_j}{k^2} \right] \langle \boldsymbol{\psi}^* \cdot \mathbf{A} \rangle + \langle \mathbf{k} \cdot \boldsymbol{\psi}^* \{ A_i k_j - \delta_{ij} \mathbf{k} \cdot \mathbf{A} \} \rangle \\ &\quad + \langle \boldsymbol{\psi}_j^* \{ k_i \mathbf{k} \cdot \mathbf{A} - k^2 A_i \} \rangle. \end{aligned} \quad (3.28)$$

Note that in general terms like $\langle \psi_j^* A_i \rangle$ will be fully complex, with both the real and imaginary parts being non-zero. The trace of this equation has the equivalent forms

$$\begin{aligned} \langle \mathbf{v}^* \cdot \mathbf{b} \rangle &= \langle k^2 \boldsymbol{\psi}^* \cdot \mathbf{A} \rangle - \langle (\mathbf{k} \cdot \boldsymbol{\psi}^*) (\mathbf{k} \cdot \mathbf{A}) \rangle \\ &= \langle \boldsymbol{\omega}^* \cdot \mathbf{A} \rangle \\ &= \langle \boldsymbol{\psi}^* \cdot \mathbf{j} \rangle, \end{aligned} \quad (3.29)$$

the real parts of which are proportional to the cross helicity spectrum.

If we now specialize to the Coulomb gauge for both $\boldsymbol{\psi}$ and \mathbf{A} , *i.e.*, $\mathbf{k} \cdot \boldsymbol{\psi} = 0 = \mathbf{k} \cdot \mathbf{A}$, then

$$\begin{aligned} \langle k^2 \psi_i^* A_j \rangle &= \langle \omega_i^* A_j \rangle \\ &= \langle \psi_i^* j_j \rangle \end{aligned} \quad (3.30)$$

and so

$$S_{ij}^{vb}(\mathbf{k}) = \left[\delta_{ij} - \frac{k_i k_j}{k^2} \right] \langle k^2 \boldsymbol{\psi}^* \cdot \mathbf{A} \rangle - \langle k^2 \psi_j^* A_i \rangle. \quad (3.31)$$

The forms for the autocorrelations of \mathbf{v} and \mathbf{b} follow by letting $\mathbf{A} \mapsto \boldsymbol{\psi}$, and $\boldsymbol{\psi} \mapsto \mathbf{A}$ respectively.

Continuing to work in the Coulomb gauge, we may form the “ \pm ” tensors

$$\begin{aligned} S_{ij}^{\pm}(\mathbf{k}) &= S_{ij}^{vb} \pm (S_{ij}^{vb})^* \\ &= \left[\delta_{ij} - \frac{k_i k_j}{k^2} \right] \langle k^2 \boldsymbol{\psi}^* \cdot \mathbf{A} \pm h.c. \rangle \mp \langle k^2 \psi_i A_j^* \pm h.c. \rangle, \end{aligned} \quad (3.32)$$

where *h.c.* indicates the hermitian conjugate (transpose of the complex conjugate). Clearly, alternative representations of S^{\pm} can be formed using (3.30). Relations like

$$\langle \psi_i A_j^* \pm h.c. \rangle = 2\Re \langle \psi_i A_j^* \rangle^{\{sym, anti\}} + i 2\Im \langle \psi_i A_j^* \rangle^{\{anti, sym\}}, \quad (3.33)$$

may also be useful. The ugly symbols \Re and \Im denote the real and imaginary parts of a complex quantity. In this equation the first (second) term in a superscript enclosed by parenthesis applies to the “+” (–) sign on the left-hand side. Isolating the antisymmetric parts is a useful way to obtain the “helicities” (see the following section). We may now calculate the traces of the “ \pm ” tensors, where, conveniently, the forms obtained via contraction of equations (3.32) hold for all gauge conditions:

$$S_{ii}^+ = 2\Re \langle \mathbf{v}^* \cdot \mathbf{b} \rangle \quad (3.34)$$

$$S_{ii}^- = i 2\Im \langle \mathbf{v}^* \cdot \mathbf{b} \rangle. \quad (3.35)$$

Again equations (3.29) or (3.30) may be used to express these relations in alternative forms involving the vector potentials and related quantities.

3.4.4 Tensor Forms and the Scalar Potentials

We now show that for general homogeneous turbulence, each of the correlation functions (3.1)–(3.4) requires four independent scalar functions to “generate” it. As shown in Appendix B, a solenoidal vector field can always be written as the sum of two terms involving (i) two independent scalar potentials—the *poloidal* and *toroidal* scalar functions, (ii) an arbitrary unit vector \mathbf{e} , which is independent of the coordinates, and (iii) the gradient and curl operators. We use the following forms for \mathbf{v} and \mathbf{b} in x -space

$$\mathbf{v} = -\nabla \times (\mathbf{e} \times \nabla P_v) - \mathbf{e} \times \nabla T_v, \quad (3.36)$$

$$\mathbf{b} = -\nabla \times (\mathbf{e} \times \nabla P_b) - \mathbf{e} \times \nabla T_b, \quad (3.37)$$

where the P 's are the poloidal components, and the T 's the toroidal ones. Since \mathbf{v} is a true vector, P_v is a true scalar and T_v a pseudoscalar; similarly, P_b is a pseudoscalar and T_b a true scalar. This information will be of use for the proof of Theorem AA.

Even in cases where there are one or more preferred directions for the turbulence, the arbitrary vector \mathbf{e} does not have any intrinsic connection with these directions. While in some circumstances it may be useful to consider \mathbf{e} to coincide with such a preferred direction, by no means is this the necessary way to proceed. See also section 3.6.

Clearly the k -space forms of equations (3.36) and (3.37) may also be used, and, since they only involve algebraic operations, rather than the differential vector analysis present in x -space, it is in some ways a more transparent approach. However, for completeness we will perform at least one derivation in each space.

We begin with $R_{ij}^v(\mathbf{r})$. From equation (3.36) it follows that⁴

$$v_i(\mathbf{x}) = -e_i \frac{\partial^2 P(\mathbf{x})}{\partial x_\alpha \partial x_\alpha} + e_\alpha \frac{\partial^2 P(\mathbf{x})}{\partial x_i \partial x_\alpha} - \epsilon_{i\alpha\beta} e_\alpha \frac{\partial T(\mathbf{x})}{\partial x_\beta}, \quad (3.38)$$

$$v_j(\mathbf{x} + \mathbf{r}) = -e_j \frac{\partial^2 P(\mathbf{x} + \mathbf{r})}{\partial r_\mu \partial r_\mu} + e_\mu \frac{\partial^2 P(\mathbf{x} + \mathbf{r})}{\partial r_j \partial r_\mu} - \epsilon_{j\mu\nu} e_\mu \frac{\partial T(\mathbf{x} + \mathbf{r})}{\partial r_\nu}. \quad (3.39)$$

After multiplying these together, ensemble averaging, and expanding the Levi-Cevita product, we obtain

$$\begin{aligned} R_{ij}^v(\mathbf{r}) &= \langle v_i(\mathbf{x}) v_j(\mathbf{x} + \mathbf{r}) \rangle \\ &= e_i e_j \frac{\partial^4 A}{\partial r_\alpha \partial r_\alpha \partial r_\mu \partial r_\mu} - e_i e_\mu \frac{\partial^4 A}{\partial r_\alpha \partial r_\alpha \partial r_j \partial r_\mu} - e_j e_\alpha \frac{\partial^4 A}{\partial r_i \partial r_\alpha \partial r_\mu \partial r_\mu} \\ &\quad + e_\alpha e_\mu \frac{\partial^4 A}{\partial r_i \partial r_j \partial r_\alpha \partial r_\mu} \end{aligned}$$

⁴ Since no confusion should result, we drop the “ v ” subscripts on P_v and T_v for this derivation.

$$\begin{aligned}
& -\delta_{ij} \frac{\partial^2 B}{\partial r_\alpha \partial r_\alpha} - e_i e_\alpha \frac{\partial^2 B}{\partial r_j \partial r_\alpha} - e_j e_\alpha \frac{\partial^2 B}{\partial r_i \partial r_\alpha} \\
& + \frac{\partial^2 B}{\partial r_i \partial r_j} + \delta_{ij} e_\alpha e_\beta \frac{\partial^2 B}{\partial r_\alpha \partial r_\beta} + e_i e_j \frac{\partial^2 B}{\partial r_\alpha \partial r_\alpha} \\
& + e_i \epsilon_{j\mu\nu} e_\mu \frac{\partial^3 C_1}{\partial r_\alpha \partial r_\alpha \partial r_\nu} - \epsilon_{j\mu\nu} e_\mu e_\alpha \frac{\partial^3 C_1}{\partial r_i \partial r_\alpha \partial r_\nu} \\
& - e_j \epsilon_{i\mu\nu} e_\mu \frac{\partial^3 C_2}{\partial r_\alpha \partial r_\alpha \partial r_\nu} + \epsilon_{i\mu\nu} e_\mu e_\alpha \frac{\partial^3 C_2}{\partial r_j \partial r_\alpha \partial r_\nu}, \tag{3.40}
\end{aligned}$$

where $A(\mathbf{r}) = \langle PP' \rangle$, $B = \langle TT' \rangle$, $C_1 = \langle PT' \rangle$, and $C_2(\mathbf{r}) = \langle P'T \rangle = C_1(-\mathbf{r})$. For simplicity we suppress the “ v ” subscripts which should be attached to these functions and their descendants. In order to collect terms of like symmetry let $2D = C_1 + C_2$ and $2C = C_1 - C_2$. Using homogeneity it is straightforward to show that A , B , and D are even under the coordinate inversion ($\mathbf{r} \mapsto -\mathbf{r}$), while C is odd. Thus, after tidying up, we obtain

$$\begin{aligned}
R_{ij}^v(\mathbf{r}) &= \frac{\partial^2}{\partial r_i \partial r_j} (\mathbf{e} \cdot \nabla)^2 A - \left(e_i \frac{\partial}{\partial r_j} + e_j \frac{\partial}{\partial r_i} \right) (\mathbf{e} \cdot \nabla) \nabla^2 A + e_i e_j \nabla^2 \nabla^2 A \\
&- \delta_{ij} \left[\nabla^2 - (\mathbf{e} \cdot \nabla)^2 \right] B + \frac{\partial^2 B}{\partial r_i \partial r_j} - \left(e_i \frac{\partial}{\partial r_j} + e_j \frac{\partial}{\partial r_i} \right) (\mathbf{e} \cdot \nabla) B + e_i e_j \nabla^2 B \\
&+ (e_i \epsilon_{j\mu\nu} + e_j \epsilon_{i\mu\nu}) e_\mu \frac{\partial}{\partial r_\nu} \nabla^2 C - \left(\epsilon_{i\mu\nu} \frac{\partial}{\partial r_j} + \epsilon_{j\mu\nu} \frac{\partial}{\partial r_i} \right) e_\mu \frac{\partial}{\partial r_\nu} (\mathbf{e} \cdot \nabla) C \\
&- \epsilon_{ij\alpha} \frac{\partial}{\partial r_\alpha} \left[\nabla^2 - (\mathbf{e} \cdot \nabla)^2 \right] D. \tag{3.41}
\end{aligned}$$

Clearly only the term on the final line is index antisymmetric, while the others are strictly index symmetric. Since we are interested in obtaining terms of the form “parts with (free) indices” \times scalar functions, it is convenient to absorb factors like $\mathbf{e} \cdot \nabla$ into the scalar functions. Thus, let

$$\begin{aligned}
\nabla^2 E(\mathbf{r}) &= - \left[\nabla^2 - (\mathbf{e} \cdot \nabla)^2 \right] B(\mathbf{r}), \\
\nabla^2 F(\mathbf{r}) &= B(\mathbf{r}) + \nabla^2 A(\mathbf{r}), \\
H(\mathbf{r}) &= - \left[\nabla^2 - (\mathbf{e} \cdot \nabla)^2 \right] D(\mathbf{r}).
\end{aligned}$$

Using the evenness of A , B , and D under coordinate inversion, it follows that E , F , and H are also even functions of \mathbf{r} . From these definitions it can be shown that

$$(\mathbf{e} \cdot \nabla)^2 A + B = (\mathbf{e} \cdot \nabla)^2 F - E,$$

a relation which is useful in determining the final form

$$\begin{aligned}
R_{ij}^v(\mathbf{r}) &= \delta_{ij} \nabla^2 E_v - \frac{\partial^2 E_v}{\partial r_i \partial r_j} \\
&- \left(e_i \frac{\partial}{\partial r_j} + e_j \frac{\partial}{\partial r_i} \right) (\mathbf{e} \cdot \nabla) \nabla^2 F_v + e_i e_j \nabla^2 \nabla^2 F_v + \frac{\partial^2}{\partial r_i \partial r_j} (\mathbf{e} \cdot \nabla)^2 F_v
\end{aligned}$$

$$\begin{aligned}
& + (\delta_{i\alpha}\epsilon_{j\mu\nu} + \delta_{j\alpha}\epsilon_{i\mu\nu}) e_\mu \frac{\partial}{\partial r_\nu} \left[e_\alpha \nabla^2 - \frac{\partial}{\partial r_\alpha} (\mathbf{e} \cdot \nabla) \right] C_v \\
& + \epsilon_{ij\alpha} \frac{\partial H_v}{\partial r_\alpha},
\end{aligned} \tag{3.42}$$

where for completeness we have reinstated the “ v ” subscripts on the scalar functions.

Thus, we have the result that for incompressible homogeneous turbulence, the symmetric part (the first three lines of equation (3.42)) of the velocity correlation matrix can be generated from *three* independent scalar functions, while the antisymmetric part (the helicity) depends on a *single* such function. As mentioned above this “four-fold generation” of the correlation tensors will be shown to apply for both the auto- and the cross correlation tensors considered here. The parity of the scalar functions is also of interest, and we note that E_v , F_v , and H_v are even, whereas C_v is explicitly odd. Clearly an exactly analogous derivation, and thus final form, holds for R_{ij}^b , the true or pseudovector nature of the underlying field being immaterial for an autocorrelation. The spectral forms are easily obtained via application of the Fourier transform.

It is interesting to note that the result is *independent* of the true or pseudovector nature of \mathbf{e} . This follows since components of \mathbf{e} only appear in product pairs, *e.g.*, $e_i e_j$. This will be of importance when we consider homogeneous turbulence with an externally enforced preferred direction, such as that due to a (large-scale) d.c. magnetic field.

The result also shows a formal coincidence with that holding for *axisymmetric* homogeneous turbulence, and this correspondence will be discussed in a later section, along with other special cases; but note that in isotropic turbulence there can be no dependence on any particular direction, and thus no dependence on \mathbf{e} . Therefore we must have $F_v = C_v = 0$, and the well known result is recovered, if E_v and H_v are functions of $|\mathbf{k}|$.

Although we are not particularly concerned with doing so just here, it is straightforward to express the four final scalar functions (E_v , F_v , C_v , H_v) in terms of correlations between the original poloidal and toroidal scalar potentials. Indeed, doing so is useful for constructing a proof of Theorem AA (see below). However, in x -space the results are a little unwieldy, and we do not give them here. This is one of the cases where things are more aesthetic in k -space.

We turn now to the k -space derivation of the “ \pm ” cross correlation tensors. As discussed in Appendix B, it is convenient to choose the two scalar potentials to have the same dimensions. Using the k -space forms of equations (3.36) and (3.37), with the extra factors of $1/k$ inserted, we obtain

$$v_i^*(\mathbf{k}) = [k^2 e_i - \mathbf{e} \cdot \mathbf{k} k_i] \frac{P_v^*(\mathbf{k})}{k} + i (\mathbf{e} \times \mathbf{k}) T_v^*(\mathbf{k}), \tag{3.43}$$

$$b_j(\mathbf{k}) = [k^2 e_j - \mathbf{e} \cdot \mathbf{k} k_i] \frac{P_b(\mathbf{k})}{k} - i(\mathbf{e} \times \mathbf{k}) T_b(\mathbf{k}). \quad (3.44)$$

Reference to equation (3.11) shows that we need to calculate $S_{ij}^{vb} = \langle v_i(-\mathbf{k}) b_j(\mathbf{k}) \rangle$. With the definitions

$$\begin{aligned} A_1(\mathbf{k}) &= \langle P_v(-\mathbf{k}) P_b(\mathbf{k}) \rangle \\ &= \langle P_v^* P_b \rangle, \\ B_1(\mathbf{k}) &= \langle T_v^* T_b \rangle, \\ C_3(\mathbf{k}) &= \langle P_v^* T_b \rangle, \\ C_4(\mathbf{k}) &= \langle T_v^* P_b \rangle, \end{aligned}$$

and some algebra, we find

$$\begin{aligned} S_{ij}^{vb}(\mathbf{k}) &= \langle v_i^* b_j \rangle \\ &= \left[e_i e_j k^2 - \{e_i k_j + e_j k_i\} (\mathbf{e} \cdot \mathbf{k}) + k_i k_j (\mathbf{e} \cdot \hat{\mathbf{k}})^2 \right] A_1(\mathbf{k}) \\ &\quad + [\delta_{ij} \{k^2 - (\mathbf{e} \cdot \mathbf{k})^2\} + \{e_i k_j + e_j k_i\} \mathbf{e} \cdot \mathbf{k} - e_i e_j k^2 - k_i k_j] B_1(\mathbf{k}) \\ &\quad - i \left[e_i k - k_i \mathbf{e} \cdot \hat{\mathbf{k}} \right] \epsilon_{j\alpha\beta} e_\alpha k_\beta C_3(\mathbf{k}) \\ &\quad + i \left[e_j k - k_j \mathbf{e} \cdot \hat{\mathbf{k}} \right] \epsilon_{i\alpha\beta} e_\alpha k_\beta C_4(\mathbf{k}). \end{aligned} \quad (3.45)$$

Using the further definitions

$$\begin{aligned} C_3 &= D_{vb} + C_{vb}, \\ C_4 &= D_{vb} - C_{vb}, \\ E_{vb} &= [k^2 - (\mathbf{e} \cdot \mathbf{k})^2] B_1, \\ F_{vb} &= B_1 - A_1, \\ H_{vb} &= k[1 - (\mathbf{e} \cdot \hat{\mathbf{k}})^2] D_{vb}, \end{aligned}$$

and the *Chandrasekhar* [1950] identities

$$\begin{aligned} k_i \epsilon_{j\mu\nu} e_\mu k_\nu - k_j \epsilon_{i\mu\nu} e_\mu k_\nu &= k^2 \epsilon_{ij\alpha} e_\alpha - \mathbf{e} \cdot \mathbf{k} \epsilon_{ij\alpha} k_\alpha, \\ e_i \epsilon_{j\mu\nu} e_\mu k_\nu - e_j \epsilon_{i\mu\nu} e_\mu k_\nu &= \mathbf{e} \cdot \mathbf{k} \epsilon_{ij\alpha} e_\alpha - \epsilon_{ij\alpha} k_\alpha, \end{aligned}$$

this becomes

$$S_{ij}^{vb}(\mathbf{k}) = \left[\delta_{ij} - \frac{k_i k_j}{k^2} \right] E_{vb}$$

$$\begin{aligned}
& + \left[[e_i k_j + e_j k_i] (\mathbf{e} \cdot \mathbf{k}) - e_i e_j k^2 - \frac{k_i k_j}{k^2} (\mathbf{e} \cdot \mathbf{k})^2 \right] F_{vb} \\
& - i [\delta_{i\mu} \epsilon_{j\alpha\beta} + \delta_{j\mu} \epsilon_{i\alpha\beta}] e_\alpha k_\beta (e_\mu k^2 - k_\mu \mathbf{e} \cdot \mathbf{k}) C_{vb} \\
& + i \epsilon_{ij\alpha} k_\alpha H_{vb}.
\end{aligned} \tag{3.46}$$

As was the case for the velocity and magnetic field autocorrelation tensors, the first three lines are index symmetric while the fourth is index antisymmetric. Letting $P_b \rightarrow P_v$, $T_b \rightarrow T_v$ recovers the result for the velocity autocorrelation. However, the result is not equal to the Fourier transform of equation (3.41), because we are working with k -space potentials which are dimensionally equal. Also, various factors of -1 are floating around, *e.g.*, $-k^2 E_{vb}(\mathbf{k}) \leftrightarrow E_{vb}(\mathbf{r})$. The ‘‘part with indices’’ associated with C_{vb} may also be written $[\mathbf{k} \times (\mathbf{e} \times \mathbf{k})]_i (\mathbf{e} \times \mathbf{k})_j + [\mathbf{k} \times (\mathbf{e} \times \mathbf{k})]_j (\mathbf{e} \times \mathbf{k})_i$, a form which cleanly shows C_{vb} cannot contribute to the trace.

Note that when the turbulence is *isotropic* it must be the case that there are equal amounts of energy associated with the poloidal and toroidal components. This means that $A_1 = B_1$, and thus $F_{vb} = 0$, providing another proof that the F scalar functions vanish for isotropic turbulence.

We now have everything we need to form the spectral versions of the ‘‘ \pm ’’ tensors. Using equations (3.11) and (3.46) it follows that

$$\begin{aligned}
S_{ij}^\pm(\mathbf{k}) & = \left[\delta_{ij} - \frac{k_i k_j}{k^2} \right] E^\pm \\
& + \left[[e_i k_j + e_j k_i] (\mathbf{e} \cdot \mathbf{k}) - e_i e_j k^2 - \frac{k_i k_j}{k^2} (\mathbf{e} \cdot \mathbf{k})^2 \right] F^\pm \\
& - i [\delta_{i\mu} \epsilon_{j\alpha\beta} + \delta_{j\mu} \epsilon_{i\alpha\beta}] e_\alpha k_\beta (e_\mu k^2 - k_\mu \mathbf{e} \cdot \mathbf{k}) C^\mp \\
& + i \epsilon_{ij\alpha} k_\alpha H^\pm,
\end{aligned} \tag{3.47}$$

where $E^\pm(\mathbf{k}) = E_{vb}(\mathbf{k}) \pm E_{vb}(-\mathbf{k})$, *etc.*, with the ‘‘+’’ (‘‘-’’) form being explicitly even (odd) in \mathbf{k} . An inverse Fourier transform yields the correlation matrices. Note that the ‘‘+’’ tensor involves C^- , not C^+ , and *vice versa*.

So again the representation is one where three scalar functions⁵ are required for the symmetric terms, and one for the antisymmetric portion. For the ‘‘plus’’ matrix, these scalar functions have the same parity as their autocorrelation cousins, *i.e.*, E^+ , F^+ , and H^+ are even, and C^- odd under $\mathbf{k} \mapsto -\mathbf{k}$. The ‘‘minus’’ matrix, however, exhibits precisely complementary behavior with E^- , F^- , and H^- being odd, and C^+ even. Thus, aside from the true/pseudo nature of the tensors (see Table 3.2), S_{ij}^+ is formally equivalent to S_{ij}^v and S_{ij}^b , and similarly for their Fourier transforms. We will subsequently refer to these tensors and their component scalar functions as

⁵ ‘‘1 longitudinal and 2 transverse.’’ Note from Potsdam notes.

“normal,” denoting a generic member with the superscript “ n ,” e.g., R_{ij}^n , H^n . The equivalence means that mathematical results which hold for any one of the three also hold for the other two.⁶ The “minus” matrix and its associated scalar functions will be referred to as “anomalous.”

We have thus proved that for general homogeneous turbulence, four is the minimum number of independent scalar functions required for complete specification of the correlation matrices and their Fourier transforms. All appropriate constraints pertaining to incompressible homogeneous MHD turbulence have been taken into account.

Further Mathematical Consequences

Having derived the most general form of all four correlation matrices, we now establish some consequences of these forms. Where the results in x - and k -space are essentially equivalent, we will usually only state one form.

We begin with the trace. Clearly only the symmetric parts will contribute to this quantity. In fact, in all cases, only the E and F functions contribute

$$S_{\alpha\alpha}(\mathbf{k}) = 2E(\mathbf{k}) + [(\mathbf{e} \cdot \mathbf{k})^2 - k^2] F(\mathbf{k}). \quad (3.48)$$

For isotropic turbulence, this will reduce still further to just $2E(\mathbf{k})$. In x -space, equation (3.48) takes the form⁷

$$R_{\alpha\alpha}(\mathbf{r}) = 2\nabla^2 E(\mathbf{r}) + [\nabla^2 - (\mathbf{e} \cdot \nabla)^2] \nabla^2 F(\mathbf{r}). \quad (3.49)$$

Now, for each of the “primary” tensors, its trace is either a pseudoscalar or a scalar. For example, $R_{ii}^v(\mathbf{r}) = \langle \mathbf{v} \cdot \mathbf{v}' \rangle$, is clearly a true scalar, whereas $R_{ii}^\pm(\mathbf{r}) = \langle \mathbf{v} \cdot \mathbf{b}' \pm \mathbf{b} \cdot \mathbf{v}' \rangle$, are both pseudoscalars. It follows that $E_{v/b}$ and $F_{v/b}$ must be true scalars, and E^\pm and F^\pm pseudoscalars. This information will be very useful when we prove Theorem AA. Note that the true or pseudoscalar character of the generating functions, is unrelated to their even or oddness under $\mathbf{r} \mapsto -\mathbf{r}$ (see below).

Writing the scalar functions in terms of the poloidal and toroidal functions is also revealing. Referring back to the k -space derivation of the S^\pm tensors, we have

$$E^\pm = [\langle T_v^* T_b \rangle \pm c.c.] \{1 - (\mathbf{e} \cdot \hat{\mathbf{k}})^2\} k^2, \quad (3.50)$$

$$F^\pm = \langle T_v^* T_b - P_v^* P_b \rangle \pm c.c., \quad (3.51)$$

$$2C^\mp = \langle P_v^* T_b - T_v^* P_b \rangle \mp c.c., \quad (3.52)$$

$$2H^\pm = [\langle P_v^* T_b + T_v^* P_b \rangle \pm c.c.] \{1 - (\mathbf{e} \cdot \hat{\mathbf{k}})^2\} k, \quad (3.53)$$

⁶ Provided the results do not depend on the true or pseudotensor character of the forms.

⁷ See the remark in the paragraph below equation (3.46) for an explanation of the non-equivalence of equation (3.49) and the Fourier transform of equation (3.48).

where *c.c.* denotes the complex conjugate. Using the properties of complex numbers it follows immediately that the four “plus” functions are all purely real scalar functions, while the “minus” forms are pure imaginary. Referring to equation (3.47), it can now be seen that the symmetric parts of S^+ (S^-) are all purely real (imaginary), with the reverse applying for the antisymmetric pieces. Recall that this result was obtained independently in section 3.2. See Table 3.2.

By letting the “*b*” subscript on the poloidal and toroidal functions become a “*v*,” and ignoring the *c.c.* terms, we recover the scalar generating functions for S^v . In this case E_v , F_v , and H_v are pure real, whereas C_v is pure imaginary. Identical results hold for S^b . As expected, these results are also in agreement with those summarized in Table 3.2.

Recall that the even or odd nature of the scalar functions under the parity transformation⁸ $\mathbf{k} \mapsto -\mathbf{k}$ was obtained during the derivation of each “primary” tensor. In particular it was found that $C^{v/b}$ and the “-” scalar functions are odd, and all the others even.

We are also interesting in determining the true or pseudoscalar nature of the scalar functions. One might (speciously) think that since a scalar that changes sign under coordinate inversion is really a pseudoscalar, the even or odd nature of the scalar functions under \mathbf{k} reflection also determines their true or pseudoscalar character. Unfortunately this is not so. For example, as shown above during the consideration of the trace of the “primary” tensors, even though E^+ is even and E^- odd, both are pseudoscalars. We defer discussion on the reasons why this approach fails to section 3.7, instead using another method to determine this property of the scalar functions.

As noted at the start of this subsection, the true vector nature of \mathbf{v} requires that its poloidal and toroidal scalar functions are respectively true and pseudoscalars. For \mathbf{b} the situation is obviously reversed. Having established these results, it is now straightforward to determine such properties for the E , F , C , and H functions. We find that E^\pm , F^\pm are pseudoscalars, C^\mp , H^\pm true scalars, with the reverse holding for the “*v/b*” forms.

Table 3.3 summarizes many properties of the generating scalar functions, along with some related ones for the multiplying “parts with indices.” When consulting this table, it may be helpful to recall that (i) δ_{ij} is an isotropic true tensor of second rank, (ii) ϵ_{ijl} is an isotropic pseudotensor of third rank, (iii) multiplication, including contraction, of a true (pseudo) tensor with a true (pseudo) tensor produces a true (true) tensor, and (iv) multiplication of true by pseudo yields pseudo. As is to be hoped for, Table 3.3 is in complete agreement with Table 3.2.

⁸ This transformation is equivalent to reflection of the coordinate system through the origin, that is, coordinate inversion.

Table 3.3: Summary of the properties of the generating scalar functions and their multiplying “parts with indices,” for each of the “primary” tensors. “R” and “I” indicate the real or imaginary nature of the term, “E” and “O” its even or odd nature under $\mathbf{k} \mapsto -\mathbf{k}$, and “T” and “P” its true or pseudo tensor character. The final column is the net result for the entire term. See equation (3.47), for example, and the text.

Term	Scalar Function	“Part with indices”	Index Symmetry	Net Character
$E^{v/b}$	RET	RET	Sym	RET
$F^{v/b}$	RET	RET	Sym	RET
$C^{v/b}$	IOP	IOP	Sym	RET
$H^{v/b}$	REP	IOP	Anti	IOT
$E^+ (E^-)$	REP (IOP)	RET	Sym	REP (IOP)
$F^+ (F^-)$	REP (IOP)	RET	Sym	REP (IOP)
$C^- (C^+)$	IOT (RET)	IOP	Sym	REP (IOP)
$H^+ (H^-)$	RET (IOT)	IOP	Anti	IOP (REP)

Examination of the final column of Table 3.3, shows that we have serendipitously achieved a proof of Theorem AA, which may be stated succinctly as “The forms $R^{v/b}$ are true tensors, R^\pm pseudotensors.” Further discussion on the theorem is given in section 3.7.

At this point we again remind the reader that the results of this section are *independent* of the true or pseudovector nature of \mathbf{e} , since components of \mathbf{e} always appear in product pairs. On the other hand, the true or pseudovector nature of any preferred directions influencing the turbulence, in general also affects the scalar functions. In this connection we note that the earlier work of *Matthaeus and Smith* [1981] is wrong with regard to some statements concerning pseudotensors. Some of the cases discussed in section 3.6 involve preferred directions.

3.5 Physical Interpretations of the Generating Scalar Functions

In this section \mathbf{v} and \mathbf{b} are assumed to represent the fluctuating components of the velocity and magnetic fields characterizing a homogeneous turbulent magnetofluid. As physicists we will then be interested in the physical content of the various tensors, and we now attempt to extract such information. Much of this material has also been discussed by *Zhou and Matthaeus* [1990a], albeit with some notational differences.

Consider first the “ v ” and “ b ” tensors. The antisymmetric components are of the form

$$J_{ij}^{v/b}(\mathbf{k}) = i \epsilon_{ij\alpha} k_\alpha H_{v/b}(\mathbf{k}), \quad (3.54)$$

so that, as is well known [e.g., *Matthaeus and Smith*, 1981; *Matthaeus et al.*, 1982], H corresponds to twice the helicity spectrum of the defining field. That is, $H_v(\mathbf{k}) = \langle \mathbf{v}^* \cdot \boldsymbol{\psi} \rangle$, and $H_b(\mathbf{k}) = \langle \mathbf{b}^* \cdot \mathbf{A} \rangle$, where, as discussed in other sections, both quantities are pseudoscalars.

Integrating these quantities over all \mathbf{k} we obtain,

$$H_{v/b}(\mathbf{r} = 0) = \int H_{v/b}(\mathbf{k}) d^3\mathbf{k}, \quad (3.55)$$

which is twice the bulk helicity. As discussed by *Moffatt* [1969, 1978], for example, the magnetic helicity may be interpreted as a measure of the topological linkage of magnetic flux tubes. Note that because $H_{v/b}$ is an even function of \mathbf{k} , the integral of $J_{ij}^{v/b}(\mathbf{k})$ over all \mathbf{k} is identically zero. In x -space this result takes the form $J_{ij}^{v/b}(\mathbf{r} = 0) = 0$. Recalling the definitions, it is clear that this must be the case, since at $\mathbf{r} = 0$, $R_{ij}^{v/b}$ are manifestly symmetric.

What about the three scalar functions associated with the symmetric parts of $S^{v/b}(\mathbf{k})$? Suppose the turbulence is isotropic, so that

$$S_{ij}^{v/b}(|\mathbf{k}|) = \left(\delta_{ij} - \frac{k_i k_j}{k^2} \right) E_{v/b}(|\mathbf{k}|) + i \epsilon_{ij\alpha} k_\alpha H_{v/b}(|\mathbf{k}|). \quad (3.56)$$

Thus, $E_{v/b}(\mathbf{k})$ is equal to $4\pi k^2$ times the omni-directional energy spectrum [e.g., *Batchelor*, 1970], and the scalar functions $F_{v/b}$ and $C_{v/b}$ are associated with departures from isotropy. An examination of the trace (equation (3.48)), indicates that for non-isotropic turbulence $F_{v/b}$ contributes to the energy spectrum but $C_{v/b}$ does not. At the present time we do not know precisely what physical roles C_v and C_b play. However, since they are pseudoscalar functions, it is true that they vanish when the turbulence is completely mirror symmetric.

Consider next the ‘‘plus’’ tensor. From the definitions of R_{ij}^+ and the cross helicity H_c , it can be shown that⁹

$$2H_c = R_{\alpha\alpha}^+(\mathbf{r} = 0) \quad (3.57)$$

$$= \int I_{\alpha\alpha}^+(\mathbf{k}) d^3\mathbf{k}, \quad (3.58)$$

so that $I_{\alpha\alpha}^+(\mathbf{k}) = 2E^+(\mathbf{k}) + [(\mathbf{e} \cdot \mathbf{k})^2 - k^2]F^+(\mathbf{k})$, is twice the cross helicity spectrum. The cross helicity is also interpretable as a linkage [*Moffatt*, 1969]; specifically, it is a measure of that between vorticity tubes and magnetic flux tubes. Yet another interpretation of the cross helicity is that it is proportional to the (average) correlation between \mathbf{v} and \mathbf{b} . In this regard it is convenient to introduce the *normalized cross helicity*,

$$\sigma_c = \frac{2H_c}{E^{tot}}$$

⁹ Some care is necessary here, since the notation is replete with ‘‘ H ’’ functions. Unlike the other H ’s, H_c is *not* a scalar function associated with the antisymmetric part of a ‘‘ c ’’ tensor, but the cross helicity defined in section 3.2.

$$= \frac{2 \langle \mathbf{v} \cdot \mathbf{b} \rangle}{\langle v^2 \rangle + \langle b^2 \rangle}, \quad (3.59)$$

which is bounded by ± 1 . The extremal values correspond to $\mathbf{v} = \pm \mathbf{b}$, which is the Alfvénicity condition introduced in Chapter 2. A spectral form of this equation also holds.

By direct analogy with the “ v ” and “ b ” tensors, we refer to $H^+(\mathbf{k})$ as (twice) the spectrum of the “helicity of the cross helicity,” since it has the same mathematical relation to $H_c(\mathbf{k})$ as does $H_b(\mathbf{k})$ to $E^m(\mathbf{k})$. However, this “helicity of the cross helicity” is somewhat different in nature than the velocity and magnetic helicities. It is still an even function of \mathbf{k} , as is H_m for example, so that in general there is a bulk value as well as a spectrum, but it is a true scalar rather than a pseudo one. Furthermore, from the Schwartz inequality, it must vanish when the cross helicity vanishes.

Finally we turn to the physical content of the “minus” tensor. From the definition (equation (3.4)) we see that,

$$R_{ij}^-(\mathbf{r} = 0) = \langle v_i b_j - b_i v_j \rangle, \quad (3.60)$$

which clearly is related to the ensemble averaged induced electric field,¹⁰ $\mathcal{E} = -\langle \mathbf{v} \times \mathbf{b} \rangle = -\nabla \Phi$. The function $\Phi(\mathbf{r}) \equiv H^-(\mathbf{r})$ being the electric potential. In fact, it is not hard to show that the electric field is contained only in the antisymmetric components,

$$\begin{aligned} J_{ij}^-(\mathbf{r} = 0) &= -\epsilon_{ij\alpha} \mathcal{E}_\alpha \\ &= \epsilon_{ij\alpha} \left. \frac{\partial \Phi}{\partial r_\alpha} \right|_{\mathbf{r}=0}. \end{aligned} \quad (3.61)$$

This leads to the k -space interpretation of $\Phi(\mathbf{k}) \equiv H^-(\mathbf{k})$, as the spectrum of the electric potential. As will be shown in section 3.8, this result enables information on the spectral anisotropy of the electric field to be obtained from the reduced spectra of $J_{ij}^-(\mathbf{k})$.

When the turbulence is isotropic, but not necessarily mirror symmetric (see also section 3.6), the induced electric field vanishes. Mathematically this follows since $H^-(\mathbf{k})$ must then be a function of k^2 , but is also explicitly odd; the only function which satisfies both these conditions is $H^-(\mathbf{k}) = 0$. This behavior is opposite to that of the helicities of the “ v/b ” tensors, $H_{v/b}$, which must vanish for completely mirror symmetric turbulence, but not necessarily for isotropic geometries. They are even pseudoscalar functions, whereas H^- is an odd, true scalar function. It follows that the presence of an induced (ensemble averaged) electric field is associated with anisotropy of the turbulence. This result will probably be of interest in mean field dynamo theory [*e.g.*, Krause and Rädler, 1980], particularly in connection with the α -dynamo closure.

¹⁰ We will usually refer to this quantity as just the electric field, but its origin as the ensemble average of $\mathbf{v} \times \mathbf{b}$ should always be kept in mind. In the general case, a large-scale electric field may also be present.

Note that while $\langle \mathbf{v} \times \mathbf{b} \rangle$ vanishes for isotropic turbulence, the mean values of the square, $\mathcal{E}_{rms}^2 = \langle (\mathbf{v} \times \mathbf{b})^2 \rangle$ is non-zero in general. Under these conditions, and assuming that the v_i and b_i are Gaussian random variables, it can be shown that

$$\mathcal{E}_{rms}^2 = \frac{\langle v^2 \rangle \langle b^2 \rangle - \langle \mathbf{v} \cdot \mathbf{b} \rangle^2}{3}, \quad (3.62)$$

and is thus prescribed—not just bounded—once the energies and the cross helicity are given. Clearly \mathcal{E}_{rms} is maximal when the cross helicity is zero.

Taking into account the anomalous nature of the “minus” tensor, *Zhou and Matthaeus [1990a]* have suggested that its symmetric parts contain the “helicity of the electric field.” In particular they refer to the trace of the “minus” tensor,

$$\begin{aligned} S_{ii}^-(\mathbf{k}) &= i 2\Im \langle \mathbf{v}^* \cdot \mathbf{b} \rangle \\ &= 2E^-(\mathbf{k}) - [(\mathbf{e} \cdot \mathbf{k})^2 - k^2] F^-(\mathbf{k}). \end{aligned} \quad (3.63)$$

by this name. The integral of this quantity over all wave-vectors is identically zero. In x -space this is the obvious statement $R_{ii}^-(0) = \langle \mathbf{v} \cdot \mathbf{b} - \mathbf{b} \cdot \mathbf{v} \rangle = 0$, so that despite having a non-zero spectrum, the “helicity of the electric field” always has a bulk value of zero. As shown in the following section, for isotropic turbulence the traced spectrum (*i.e.*, equation (3.63)) is also zero, a property that may be tested for when analyzing observational/experimental data.

To summarize, for incompressible homogeneous turbulence—with *arbitrary* rotational symmetry—each of the following quantities, or its spectrum, is generated by a *single* scalar function: velocity helicity, magnetic helicity, helicity of the cross helicity, and the induced emf. In each case, the quantity is associated with the antisymmetric portion of its correlation function/spectral tensor. Recall also that the magnetic helicity is a rugged invariant of ideal MHD. The symmetric pieces of the “ v/b ” spectral tensors hold the associated energy spectra, their (traced) sum forming the spectra of another rugged invariant (total energy). The third rugged invariant, cross helicity, is contained in the trace of the “+” tensor. Unfortunately, the quantities associated with the symmetric parts of the “−” tensor, while undoubtedly physical in character, are less well understood at this point in time.

3.6 Special Cases

We now present some specializations of the above results for particular rotational symmetries of the turbulence. It will be most convenient to do so using the k -space forms of section 3.4.4,

which were derived using the poloidal and toroidal scalar potentials. Unless otherwise noted the results hold for all four of the “primary” spectral tensors, so that we use the generic form,

$$\begin{aligned}
S_{ij}(\mathbf{k}) &= \left[\delta_{ij} - \frac{k_i k_j}{k^2} \right] E(\mathbf{k}) \\
&+ \left[[e_i k_j + e_j k_i] (\mathbf{e} \cdot \mathbf{k}) - e_i e_j k^2 - \frac{k_i k_j}{k^2} (\mathbf{e} \cdot \mathbf{k})^2 \right] F(\mathbf{k}) \\
&- i [\delta_{i\mu} \epsilon_{j\alpha\beta} + \delta_{j\mu} \epsilon_{i\alpha\beta}] e_\alpha k_\beta (e_\mu k^2 - k_\mu \mathbf{e} \cdot \mathbf{k}) C(\mathbf{k}) \\
&+ i \epsilon_{ij\alpha} k_\alpha H(\mathbf{k}).
\end{aligned} \tag{3.64}$$

Insertion of the appropriate sub/super-scripts will generate a specific tensor. Beware, however, that C^- is associated with the “plus” tensor and *vice versa*, and also that the parity of the scalar functions may differ from tensor to tensor (see Table 3.3).

3.6.1 Isotropic Symmetry

In an isotropic system there can obviously be no dependence on any preferred direction. Thus, all terms in equation (3.64) involving \mathbf{e} must vanish, that is, $F = C = 0$, leading to the well known result [*e.g.*, Batchelor, 1970]. We do not write the result here, since it may be read off with ease from equation (3.64). However, this lack of dependence on \mathbf{e} is not the only constraint which isotropic turbulence must obey: The scalar functions must also depend only on the wave-vector magnitude, $k = |\mathbf{k}|$. But, the “minus” scalar functions and $C_{v/b}$ are explicitly odd in \mathbf{k} , so that they must all be identically zero for isotropic turbulence. It follows that the full “−” tensor is identically zero for isotropic turbulence, since each of its scalar functions vanishes. Hence, only six independent scalar functions are needed to specify isotropic turbulence: an E and an H for each of the “ v/b ” and “+” tensors. This is to be contrasted with the general case where sixteen such functions are required.

In all cases the trace reduces to dependence on a single scalar function: $S_{ii}(k) = 2E(k)$. It follows that the trace of the “minus” tensor is identically zero, and there is no “helicity of the electric field” in isotropic turbulence. This result has important consequences for the transport theory of subsequent chapters, particularly in association with the effect we call “mixing.”

Note that, excepting the “minus” tensor, isotropic turbulence does not preclude the presence of helicity, H . However, when considering the transport of isotropic fluctuations in the solar wind, we will assume that the helicities vanish. As has been remarked upon, the vanishing of H^- for isotropic turbulence means that no ensemble averaged induced electric field exists when there are no preferred directions in the turbulence.

3.6.2 Mirror Symmetry

When the turbulence is mirror or reflectionally symmetric (that is, isotropic in the sense used by *Batchelor* [1970], but not many current workers), only terms exhibiting overall even parity in \mathbf{k} may be non-zero. Thus, the three helicities, H_v , H_b , and H^+ which are a measure of mirror asymmetry, are all identically zero, as are E^- , F^- , and C^+ . The anomalous nature of the “minus” tensor is particularly clearly revealed when we consider turbulence which is mirror symmetric.

As far as the trace is concerned, the “normal” tensors are unaffected by the presence or absence of mirror symmetry. In stark contrast to this, S_{ii}^- collapses to zero when mirror symmetry is imposed. Indeed, for the “minus” tensor, the only term that remains is the antisymmetric piece, which has been shown to contain the spectrum of the electric potential.

3.6.3 Axisymmetry and the Presence of a Mean Field

When conditions of axisymmetry are imposed upon the turbulence, that is, when the statistical properties of the turbulence are invariant with respect to rotations about a fixed axis, our results require no modifications. Provided, that is, that we no longer allow \mathbf{e} to be arbitrary, instead constraining it to be parallel to the axis of symmetry. As remarked above, the results of section 3.4.4 are independent of the true or pseudovector nature of \mathbf{e} (components of \mathbf{e} always appear in pairs), so that, for example, it does not matter whether the preferred direction is associated with either a mean flow or a d.c. magnetic field.

3.6.4 Two-Dimensional Symmetry

This is a special case of axisymmetric turbulence. We interpret \mathbf{e} as being parallel to the symmetry axis, which might be due to a uniform magnetic field \mathbf{B}_0 , for example. The further specialization is that we insist that all wave-vectors are perpendicular to this axis of symmetry, *i.e.*, $\mathbf{e} \cdot \mathbf{k} = 0$. Equation (3.64) then reduces to

$$\begin{aligned} S_{ij}(\mathbf{k}) &= \left[\delta_{ij} - \frac{k_i k_j}{k^2} \right] E(\mathbf{k}) - e_i e_j k^2 F(\mathbf{k}) \\ &\quad - i \left[e_i (\mathbf{e} \times \mathbf{k})_j + e_j (\mathbf{e} \times \mathbf{k})_i \right] k^2 C(\mathbf{k}) \\ &\quad + i \epsilon_{ij\alpha} k_\alpha H(\mathbf{k}), \end{aligned} \tag{3.65}$$

where $\mathbf{k} \equiv \mathbf{k}_\perp$, the wave-vector in the plane perpendicular to \mathbf{e} . Note that we may have helicity.

If we now insist that, in addition to $\mathbf{k} \cdot \mathbf{e}$ being zero, the fluctuations themselves are perpendicular to \mathbf{e} , then

$$S_{ij}(\mathbf{k}) = \left[\delta_{ij} - \frac{k_i k_j}{k^2} - e_i e_j \right] E(\mathbf{k}). \tag{3.66}$$

This is simplest to see by considering a Cartesian coordinate system, with \mathbf{e} in the “1” direction say. Then, since $k_1 = 0$, it follows that $S_{11} = E - k^2 F$, and as this is energy in components parallel to the symmetry axis we require that it be zero. Consideration of S_{12} and S_{21} leads to the conclusion that $H = C = 0$. Physically this geometry is believed to be relevant in situations where a strong d.c. magnetic field threads a turbulent magnetofluid [*e.g.*, *Shebalin et al.*, 1983]. The relevance increasing as the energy density of the d.c. field, measured relative to the energy density of the fluctuations, increases.

We may also specialize to the isotropic 2D case, where $E(\mathbf{k})$ depends only on $|\mathbf{k}|$. In later chapters, this isotropic form of 2D turbulence will be used to represent some types of solar wind fluctuations. Note, however, that even for the non-isotropic case, such turbulence is completely specified by a *single* scalar function.

3.6.5 Slab Symmetry

Finally, we consider the slab geometry. Again this is a particular case of axisymmetric turbulence, this time with the wave-vectors parallel to \mathbf{e} , so that $\mathbf{e} \cdot \mathbf{k} = \pm k$, and $\mathbf{e} \times \mathbf{k} = 0$. For such symmetries, all dependence on C drops out, and we are left with

$$\begin{aligned} S_{ij}(\mathbf{k}) &= \left[\delta_{ij} - \frac{k_i k_j}{k^2} \right] E(\mathbf{k}) \\ &+ [(e_i k_j + e_j k_i) \mathbf{e} \cdot \mathbf{k} - e_i e_j k^2 - k_i k_j] F(\mathbf{k}) \\ &+ i \epsilon_{ij\alpha} k_\alpha H(\mathbf{k}), \end{aligned} \tag{3.67}$$

with trace $2E$. Again, helicity may be present. The transport of slab fluctuations in the solar wind will also be considered below.

3.7 Theorem AA

In this section we give a proof of Theorem AA, which may be stated as “The forms R^v and R^b are true tensors, R^\pm pseudotensors.” A distinct proof was encountered in section 3.4.4, and we will also discuss this proof and some related points here. In order to prove the theorem we may show that it holds for each additive term in a correlation function, and thus for the entire tensor. Since the tensor character of the “parts with indices” is easily established by inspection and the use of well known results, the major task involved is to establish the character of the scalar functions.

We begin by considering the antisymmetric piece of the “ v ” correlation function

$$R_{ij}^v(\mathbf{r}) = \langle v_i(\mathbf{x}) v_j(\mathbf{x} + \mathbf{r}) \rangle. \tag{3.68}$$

Taking its curl with respect to \mathbf{r} gives

$$\begin{aligned}\epsilon_{l\alpha\beta} \frac{\partial}{\partial r_\alpha} R_{i\beta}^v(\mathbf{r}) &= \langle v_i(\mathbf{x}) \epsilon_{l\alpha\beta} \frac{\partial}{\partial r_\alpha} v_\beta(\mathbf{x} + \mathbf{r}) \rangle \\ &= \langle v_i (\nabla \times \mathbf{v}')_l \rangle.\end{aligned}\quad (3.69)$$

Referring to equation (3.42), it follows that (after simplification)

$$\begin{aligned}\langle v_i (\nabla \times \mathbf{v}')_l \rangle &= [\mathbf{e} \nabla^2 - \nabla(\mathbf{e} \cdot \nabla)]_i [\mathbf{e} \nabla^2 - \nabla(\mathbf{e} \cdot \nabla)]_l C(\mathbf{r}) \\ &\quad - (\mathbf{e} \times \nabla)_i [\nabla^2(\mathbf{e} \times \nabla)]_l C(\mathbf{r}) - \left[\delta_{il} \nabla^2 + \frac{\partial^2}{\partial r_i \partial r_l} \right] H_v,\end{aligned}\quad (3.70)$$

Taking the trace yields

$$\begin{aligned}\langle \mathbf{v} \cdot \nabla \times \mathbf{v}' \rangle &= \langle \mathbf{v} \cdot \boldsymbol{\omega}' \rangle \\ &= -2\nabla^2 H_v,\end{aligned}\quad (3.71)$$

but $\langle \mathbf{v} \cdot \boldsymbol{\omega}' \rangle$ is manifestly a pseudoscalar, and therefore so is $\nabla^2 H_v$. Taking further curls of equation (3.71), shows that *every* term in the power series expansion for $H_v(\mathbf{r})$ is a pseudoscalar, proving that H_v is as well.¹¹ This is consistent with the theorem, since when H_v is multiplied by its associated “part with indices” ($\epsilon_{ij\alpha} \frac{\partial}{\partial r_\alpha}$), the result is a term which has a net true tensor character.

To complete the proof for R^v we must now show that its symmetric pieces are also net true tensors. Taking the trace of $R_{ij}^v(\mathbf{r})$, we obtain

$$\begin{aligned}R_{\alpha\alpha}(\mathbf{r}) &= \langle \mathbf{v} \cdot \mathbf{v}' \rangle \\ &= 2\nabla^2 E_v(\mathbf{r}) + [(\mathbf{e} \cdot \nabla)^2 - \nabla^2] F_v(\mathbf{r}),\end{aligned}\quad (3.72)$$

which is a true scalar, suggesting that E_v and F_v are as well. Indeed, taking Laplacians (with respect to \mathbf{r}) of this result, produces the terms in the power series expansions for E_v and F_v , all of which can be shown to be true scalars. It remains to show that the term involving C_v also behaves itself. This can be done by a consideration of terms like

$$\begin{aligned}e_i e_l \epsilon_{l\alpha j} \frac{\partial}{\partial r_\alpha} R_{ij}^v(\mathbf{r}) &= \langle (\mathbf{e} \cdot \mathbf{v}) (\nabla \times \mathbf{v}') \cdot \mathbf{e} \rangle \\ &= [\nabla^2 - (\mathbf{e} \cdot \nabla)^2] C_v(\mathbf{r}) - [\nabla^2 + (\mathbf{e} \cdot \nabla)^2] H_v(\mathbf{r}).\end{aligned}\quad (3.73)$$

This is clearly a pseudoscalar (independent of \mathbf{e} 's character), and since we have already proved that H is a pseudoscalar, it follows that the term involving C_v is as well. Inserting further curls (or

¹¹ The first term in the series may be obtained by “uncurling” equation (3.68).

uncurls) before taking the second dot product with \mathbf{e} produces the remaining terms in the power series expansion for C_v . This completes the proof for R^v . An identical sequence of steps proves the theorem for R^b , the pseudovector nature of \mathbf{b} being irrelevant for autocorrelation functions. For the “ \pm ” tensors, the arguments are closely analogous, and we obtain the desired result that E^\pm , F^\pm are pseudoscalars, and C^\mp , H^\pm true scalars. Hence, the R^\pm are pure second rank pseudotensors. Further discussion along these lines will be found in *Rädler et al.* [1993].

3.8 Measurement Issues

Some results of the previous sections are now considered within the context of data analysis. In particular, we have in mind the determination of appropriate properties of the solar wind, for which extensive plasma and magnetic field datasets are available.

As shown in section 3.5 the (mean) electric field induced by the fluctuating velocity and magnetic fields is related to the antisymmetric part of the “ $-$ ” tensor, *i.e.*, $J_{ij}^-(\mathbf{r} = \mathbf{0}) = -\epsilon_{ij\alpha}\mathcal{E}_\alpha$. Hence, knowledge of the off-diagonal components of R_{ij}^- evaluated at the origin, yields the (bulk) induced electric field. Given data intervals of sufficient length and quality, it is straightforward to calculate the appropriate correlation matrix and then extract the induced emf [*e.g.*, *Marsch and Tu*, 1992]. However, our results indicate that the underlying fundamental quantity is $\Phi(\mathbf{k})$.

Furthermore, this is not the only information available regarding the induced electric field. As we now show, the spectrum of J^- can be used to construct a measure of the spectral anisotropy of \mathcal{E} . From equation (3.47) we have

$$J_{ij}^-(\mathbf{k}) = i\epsilon_{ij\alpha}k_\alpha H^-(\mathbf{k}),$$

and thus $J_{23}^- = ik_1H^-$, *etc.* Integrating this last equation over all \mathbf{k} yields $J_{23}^-(\mathbf{r} = \mathbf{0}) = \mathcal{E}_1$. As discussed in section 3.5, we can interpret $H^-(\mathbf{k}) = \Phi(\mathbf{k})$ as the spectrum of the electric potential. Now suppose that the observation direction and the “1” direction coincide. Integrating (reducing) over the “2” and “3” directions then gives

$$\begin{aligned} \Phi^{red}(k_1) &= \int \Phi(k_1, k_2, k_3) d\mathbf{k}_\perp \\ &= -\frac{i}{k_1} \int J_{23}^-(\mathbf{k}) d\mathbf{k}_\perp \\ &= -i \frac{J_{23}^-, red}{k_1}, \end{aligned} \tag{3.74}$$

where $d\mathbf{k}_\perp = dk_2 dk_3$, is the Cartesian Jacobian for the integrals. Reducing the J_{12}^- and J_{31}^- components leads to mean wavenumbers associated with the directional components of the electric

field. For example,

$$\begin{aligned}
\bar{k}_3 &= \frac{\int k_3 \Phi(\mathbf{k}) d\mathbf{k}_\perp}{\int \Phi(\mathbf{k}) d\mathbf{k}_\perp} \\
&= -i \frac{\int J_{12}^-(\mathbf{k}) d\mathbf{k}_\perp}{\Phi^{red}(k_1)} \\
&= -i \frac{J_{12}^-,red(k_1)}{\Phi^{red}(k_1)}. \\
&= k_1 \frac{J_{12}^-,red(k_1)}{J_{23}^-,red(k_1)}. \tag{3.75}
\end{aligned}$$

Thus, we can obtain information about the spectrum of the electric field in directions *perpendicular* to that in which the measurements were made! We are currently attempting to extract such information from some available solar wind data sets.

As was shown in section 3.5, the induced electric field vanishes when the turbulence is isotropic, and \mathcal{E}_{rms} is not an independent parameter. Comparing these theoretical predictions for \mathcal{E} and \mathcal{E}_{rms} to their experimentally determined values may also provide a useful measure of the degree of departure from isotropy.

In an analysis of solar wind fluctuations in terms of Elsässer variables *Tu et al.* [1989], found that frequency spectra of the “helicity of the electric field,” which they denote by $e^S(f)$, equivalent to the reduced form of our $S_{ii}^-(\mathbf{k})$, have both positive and negative contributions, and that there is also a fairly wide scatter in the data points, no clean power laws being evident. The presence of both signs in such spectra is of course necessary to ensure that when the integration over all wavenumbers (frequencies) is performed, the net result will be zero, in accordance with the results of section 3.5. In their paper *Tu et al.* did not comment on this necessary property of the spectrum.

Issues associated with determining the magnetic helicity given R^b have been discussed by *Matthaeus and Smith* [1981] and *Matthaeus et al.* [1982].

3.9 Elsässer Variable Representations

Most of the above results may also be expressed in terms of Elsässer variables. Clearly this may be accomplished either by (i) substituting $\mathbf{z}^\pm = \mathbf{v} \pm \mathbf{b}$ into the final forms of this section, or (ii) starting with correlation functions defined in terms of the \mathbf{z}^\pm (e.g., $H_{ij}^\pm = \langle z_i^\pm z_j^{\pm'} \rangle$) and proceeding from there. In some applications these forms may be a more convenient notation. Tables 3.4 and 3.5 provide a summary of some of the Elsässer forms we will be using in subsequent chapters (see also Tables 4.1 through 4.3). This completes our somewhat lengthy excursion into tensor forms. The remaining chapters all deal directly with the transport of solar wind fluctuations.

Table 3.4: Some correlation functions and spectral tensors in terms of the primitive variables \mathbf{v} and \mathbf{b} . Primed (') variables are evaluated at $\mathbf{x} + \mathbf{r}$ while unprimed variables are evaluated at \mathbf{x} . Note that in these tables, R and S no longer denote general tensors, but rather the specific ones associated with the total energy (kinetic plus magnetic) of the system. See the text for details.

Symbol	Definition	Description	Fourier Transform	Homogeneity Condition
$R_{ij}^v(\mathbf{r})$	$\langle v_i v_j' \rangle$	Kinetic Energy	$S_{ij}^v(\mathbf{k})$	$R_{ij}^v(\mathbf{r}) = R_{ji}^v(-\mathbf{r})$
$R_{ij}^b(\mathbf{r})$	$\langle b_i b_j' \rangle$	Magnetic Energy	$S_{ij}^b(\mathbf{k})$	$R_{ij}^b(\mathbf{r}) = R_{ji}^b(-\mathbf{r})$
$R_{ij}(\mathbf{r})$	$R_{ij}^v + R_{ij}^b$	Total Energy	$S_{ij}(\mathbf{k})$	$R_{ij}(\mathbf{r}) = R_{ji}(-\mathbf{r})$
$R_{ij}^D(\mathbf{r})$	$R_{ij}^v - R_{ij}^b$	Energy Difference	$S_{ij}^D(\mathbf{k})$	$R_{ij}^D(\mathbf{r}) = R_{ji}^D(-\mathbf{r})$
$R_{ij}^\pm(\mathbf{r})$	$\frac{1}{2} \langle v_i b_j' \pm b_i v_j' \rangle$	“Cross Energies”	$S_{ij}^\pm(\mathbf{k})$	$R_{ij}^\pm(\mathbf{r}) = \pm R_{ji}^\pm(-\mathbf{r})$

Table 3.5: Some correlation functions and spectral tensors in terms of Elsässer variables. Because of conflicts with the notation of later chapters, the I – J notation for the symmetric and antisymmetric components is not used in these tables; instead these pieces are denoted by the superscripts “s” and “a” respectively.

Symbol	Definition	v – b Form	Fourier Transform	Homogeneity Condition
$H_{ij}^\pm(\mathbf{r})$	$\langle z_i^\pm z_j^{\pm'} \rangle$	$R_{ij} \pm 2R_{ij}^+$	$P_{ij}^\pm(\mathbf{k})$	$H_{ij}^\pm(\mathbf{r}) = H_{ji}^\pm(-\mathbf{r})$
$\Lambda_{ij}(\mathbf{r})$	$\langle z_i^+ z_j^{-'} \rangle$	$R_{ij}^D - 2R_{ij}^{vb,-}$	$\Theta_{ij}(\mathbf{k})$	$\Lambda_{ij}(\mathbf{r}) = \tilde{\Lambda}_{ij}(-\mathbf{r})$
$\tilde{\Lambda}_{ij}(\mathbf{r})$	$\langle z_i^{+'} z_j^- \rangle$	$R_{ji}^D + 2R_{ji}^{vb,-}$	$\tilde{\Theta}_{ij}(\mathbf{k})$	
$F_{ij}(\mathbf{r})$	$\langle \Lambda_{ij} + \tilde{\Lambda}_{ij} \rangle$	$2R_{ij}^{Ds} - 4R_{ij}^{-a}$	$F_{ij}^\pm(\mathbf{k})$	$F_{ij}(\mathbf{r}) = F_{ij}(-\mathbf{r})$
$J_{ij}(\mathbf{r})$	$\langle \Lambda_{ij} - \tilde{\Lambda}_{ij} \rangle$	$2R_{ij}^{Da} - 4R_{ij}^{-s}$	$J_{ij}(\mathbf{k})$	$J_{ij}(\mathbf{r}) = -J_{ij}(-\mathbf{r})$

Chapter 4

THE SPECTRAL TRANSPORT MODEL

It is the mark of an educated mind to rest satisfied with the degree of precision that the nature of the subject admits, and not to seek exactness where only an approximation is possible.

— Aristotle: *Nicomachian Ethics*

4.1 Introduction

The problem of how to adequately describe the physics of fluctuations of the interplanetary medium has been present since the earliest spacecraft observations revealed that such fluctuations are ubiquitous in the solar wind. In this chapter, we derive the model on which our transport theory is based, and discuss the approximations and assumptions associated with it. Introductory discussions of the recently illuminated “mixing” effect and the models relationship to WKB theory are also given.

Traditionally, the approach taken in modeling the evolution of solar wind fluctuations has centered around WKB theory [*e.g.*, Parker, 1965; Hollweg, 1973*a*, *b*, 1974]. However, Zhou and Matthaeus [1989, 1990*a*, *b*, *c*] have recently developed a distinct but related theory for the transport of MHD scale turbulence in a *weakly* inhomogeneous background plasma, and here we apply this theory in the context of the solar wind. This newer theory can be shown to be more general than that of WKB, since it remains applicable in cases where the WKB approach is no longer valid [Zhou and Matthaeus, 1990*b*; Matthaeus *et al.*, 1992; Matthaeus *et al.*, 1993*b*]. A similar theory has also been developed by an independent group [Marsch and Tu, 1989, 1990*b*; Tu and Marsch, 1990*b*, 1992, 1993]. In the derivations that follow, references to the corresponding work of these two authors will often be omitted, since we will follow closely the approach and notation introduced by Zhou and Matthaeus [1989, 1990*a*].

An important distinguishing feature of this new approach is that it supports completely arbitrary ratios of energies in the “inward” and “outward” fluctuations. Indeed, separate transport equations for both these (and other) quantities arise quite naturally in the model. This is to be contrasted with WKB theory [*e.g.*, Parker, 1965; Hollweg, 1973*b*, 1974] and the earlier models of Tu

and colleagues [Tu *et al.*, 1984; Tu, 1988], which only considered the case when this ratio is small, and often further restricted to be a constant independent of heliocentric distance. Observations [*e.g.*, Bavassano *et al.*, 1982*a, b*; Roberts *et al.*, 1987*a, b*] show that while such an approximation is sometimes valid in the solar wind, there are also many instances when it is not. In an attempt to overcome some of these limitations, we investigate solutions of the more general theory of Zhou and Matthaeus [1990*a*] (see also the Marsch and Tu references given above). We should also note Heinemann and Olbert's [1980] consideration of small amplitude toroidal Alfvén waves in a model solar wind allowed for an arbitrary ratio of inward to outward fluctuation energy.

4.2 Derivation and Approximations

A complete derivation of the model equations, along with an extensive discussion of its relative merits and limitations, has been given previously [Zhou and Matthaeus, 1990*a, b, c*]; here we present an outline of the procedure used, in order to provide appropriate contextual information. As discussed in Chapter 2, we assume that the interplanetary medium can be adequately represented, at least for our purposes, as a single component magnetofluid obeying the usual compressible MHD fluid equations. The appropriate equations, given in section 2.4.1 as equations (2.10)–(2.12), are now repeated for convenience

$$\frac{\partial \rho}{\partial t} + \nabla \cdot (\rho \mathbf{V}) = 0, \quad (4.1)$$

$$\left(\frac{\partial}{\partial t} + \mathbf{V} \cdot \nabla \right) \mathbf{V} = -\frac{1}{\rho} \nabla P + \frac{1}{4\pi\rho} (\mathbf{B} \cdot \nabla) \mathbf{B}, \quad (4.2)$$

$$\left(\frac{\partial}{\partial t} + \mathbf{V} \cdot \nabla \right) \mathbf{B} = (\mathbf{B} \cdot \nabla) \mathbf{V} - \mathbf{B} \nabla \cdot \mathbf{V}, \quad (4.3)$$

where ρ is the mass density, \mathbf{V} the velocity, \mathbf{B} the magnetic field, P the total pressure, and the dissipation terms have been dropped. While dissipative effects are probably essential to the formation of turbulence, their direct effects are believed to be important only at scales much smaller than those characterizing the inertial range. As we are only considering the transport of solar wind fluctuations in either the energy-containing or inertial ranges, this provides a motivation for dropping such terms [*cf.* Zhou and Matthaeus, 1990*a*]. Note that at this point we are *not* working with dimensionally equivalent \mathbf{v} and \mathbf{b} fields (*cf.* Elsässer variables).

This leaves a set of equations which could be used to describe the dynamics of the solar wind under appropriate conditions. However, the non-linear nature of the equations indicates considerable complexity, and, at least to date, has precluded the uncovering of general closed form solutions. Moreover, the ranges of length and time scales that are dynamically important in the solar wind (see Appendix E) are so large that direct simulation of the system is still computationally

out of the question, although simulations of just the local properties are possible. However, since we wish to consider the transport and the local evolution, we must simplify the equations.

The approach adopted—essentially a perturbation technique—involves a *two-scale* decomposition of the equations, where both length and time scales are so decomposed. As discussed by *Zhou and Matthaeus* [1990a], such an approach has solid observational support: the average *large-scale* properties of the solar wind varying over distances of the order of the local heliocentric distance \mathbf{R} , that is, relatively slowly [*e.g.*, *Hundhausen*, 1972]. The fluctuations, however, while broadband, usually have correlation lengths, λ , which are a small fraction of R ; in other words, $\epsilon = \lambda/R$ is typically very much less than unity, particularly beyond about half an AU. For example, at 1 AU, $\epsilon \sim 10^{-2}$.

Thus, while the approximation of separation of length scales in the solar wind is an incomplete description of the physics, it does allow insight into the evolution of the fluctuations to be obtained. Similarly, the time scales associated with the average large-scale features of the interplanetary medium and its fluctuations are well separated. Fortunately the large-scale features are also relatively reproducible [*e.g.*, *Hundhausen*, 1972], so that it should not be too drastic an approximation to neglect local variations in the mean fields. As noted in section 2.2, the mean velocity corresponds to approximately constant speed, radially directed flow, while the mean magnetic field is typically in an Archimedean spiral configuration; such reproducibility is particularly characteristic of the “quiet” solar wind.

The physical picture being considered, then, is one where the large-scale “mean” fields are slowly varying functions of both space and time. Superimposed on these background fields are attendant sets of broadband fluctuations at much smaller length and time scales. These “fast” fluctuations are generally viewed as being random, or more precisely stochastic, quantities.

In accordance with this approximation for the solar wind, we define an ensemble averaging operator $\langle \dots \rangle$, that allows the total fields to be decomposed into *mean* (spatially slowly varying) and *fluctuating* (rapidly varying) components. These two pieces will also be referred to as the *large-scale* and *small-scale* components respectively.

Note that such a scale-separated approach is not without shortcomings [*e.g.*, *Montgomery and Chen*, 1984; *Chen and Montgomery*, 1987; *Zhou and Matthaeus*, 1990a]. As shown below, and in *Zhou and Matthaeus* [1990a], the procedure used here leads to two sets of equations: one describing the evolution of the *large-scale* fields given certain information about the small-scale ones, and the other describing the evolution of the *small-scale* fields in the presence of large-scale fields. Thus, the small-scale equations involve both couplings amongst the small-scale fields, and

also couplings between the small- and large-scale components. Analogous results apply for the large-scale equations. Due to the nature of the approximation, however, couplings associated with the intermediate scales have been discarded, and hence some physics has also been lost. In the spirit of perturbation theory, one assumes that the accuracy of the method increases as the scale separation parameter (ϵ) becomes small relative to unity. The energy spectra are continuous at all observed MHD scales, so that in this sense scale-separation does not exist. However, we can still talk of scale-separation between the mean fields and fluctuations at scales less than or of order the correlation length.

Applying the ensemble averaging operator to the four fields we are using to describe the interplanetary medium, namely the velocity, magnetic, density, and total pressure fields, we obtain the following decompositions

$$\begin{aligned}\mathbf{V} &= \mathbf{U} + \mathbf{v}, \\ \mathbf{B} &= \mathbf{B}_0 + \mathbf{b}, \\ \rho &= \rho_0 + \delta\rho, \\ P &= P_0 + \delta P,\end{aligned}$$

where $\mathbf{U} = \langle \mathbf{V} \rangle$, $\mathbf{B}_0 = \langle \mathbf{B} \rangle$, *etc.*, and the lower case and “ δ ” components represent the (possibly turbulent) fluctuations about the mean fields. As a practical point, recall that for *ergodic* systems, long-time averages are equivalent to ensemble averages. In an observational study of the solar wind, *Matthaeus and Goldstein [1982b]* showed that time averaging in the spacecraft reference frame is an adequate way to achieve such a decomposition. They also found that fluctuations computed in this fashion are locally spatially (weakly) homogeneous¹ and approximately time stationary, in the usual statistical sense. In deriving transport equations for the fluctuations, we assume that the small-scale fields obey both of these (local) properties exactly.

Before continuing with the derivation we pause to consider the spatial dependence of the decomposed components. As discussed in *Zhou and Matthaeus [1990a]*, the total spatial coordinate, \mathbf{X} , is considered to consist of two independent pieces: a slowly varying portion \mathbf{R} , and a local rapidly varying piece \mathbf{x} . The function of the operator $\langle \dots \rangle$ is to average over \mathbf{x} at a fixed \mathbf{R} . Consider the velocity field

$$\mathbf{V}(\mathbf{X}) = \mathbf{U}(\mathbf{R}) + \mathbf{v}(\mathbf{R}, \mathbf{x}).$$

¹ See the footnote on page 36 for a definition of weak homogeneity.

The symbol \mathbf{R} denotes the large-scale heliocentric coordinate vector, and can be thought of as locating a parcel of solar wind fluid in a coarse-grained sense. Inside this little box of fluid, distances are measured relative to some origin within the box; such local, small-scale distances being denoted by \mathbf{x} . Furthermore, *within* each box the large-scale fields are invariant, although they do of course vary (slowly) from box to box. Thus, our approximation is such that within any “small” volume of interplanetary space, the background fields are uniform and time-steady. This “locally uniform” approximation considerably simplifies the situation. To reiterate, the fluctuating components are functions of *both* the slowly varying and the rapidly varying spatial coordinates, whereas the mean fields depend only on the slowly varying coordinate. For systems which are strongly scale separated, there is no practical distinction between \mathbf{X} and \mathbf{R} for the large-scale fields, *e.g.*, $\mathbf{U}(\mathbf{X}) \equiv \mathbf{U}(\mathbf{R})$.

We are now ready to proceed with the derivation of the transport equations for the fluctuating fields. Applying the averaging operator $\langle \dots \rangle$ to equations (4.1)–(4.3), and then subtracting the results from the original equations leads to

$$\nabla \cdot \rho_0 \mathbf{v} = 0, \quad (4.4)$$

and

$$\begin{aligned} \frac{\partial \mathbf{v}}{\partial t} + \mathbf{U} \cdot \nabla \mathbf{v} + \mathbf{v} \cdot \nabla \mathbf{U} - \frac{1}{4\pi\rho_0} [(\mathbf{B}_0 \cdot \nabla) \mathbf{b} + (\mathbf{b} \cdot \nabla) \mathbf{B}_0] \\ = -\frac{1}{\rho_0} \nabla \delta P + \mathbf{N}^v, \end{aligned} \quad (4.5)$$

$$\begin{aligned} \frac{\partial \mathbf{b}}{\partial t} + \mathbf{U} \cdot \nabla \mathbf{b} + \mathbf{v} \cdot \nabla \mathbf{B}_0 - (\mathbf{B}_0 \cdot \nabla) \mathbf{v} - (\mathbf{b} \cdot \nabla) \mathbf{U} \\ = -(\nabla \cdot \mathbf{U}) \mathbf{b} - (\nabla \cdot \mathbf{v}) \mathbf{B}_0 + \mathbf{N}^b, \end{aligned} \quad (4.6)$$

where the small-scale non-linear terms, \mathbf{N}^v and \mathbf{N}^b , are given explicitly by

$$\mathbf{N}^v = -[(\mathbf{v} \cdot \nabla) \mathbf{v} - \langle (\mathbf{v} \cdot \nabla) \mathbf{v} \rangle] + \frac{1}{4\pi\rho_0} [(\mathbf{b} \cdot \nabla) \mathbf{b} - \langle (\mathbf{b} \cdot \nabla) \mathbf{b} \rangle], \quad (4.7)$$

$$\mathbf{N}^b = -[(\mathbf{v} \cdot \nabla) \mathbf{b} - \langle (\mathbf{v} \cdot \nabla) \mathbf{b} \rangle] + [(\mathbf{b} \cdot \nabla) \mathbf{v} - \langle (\mathbf{b} \cdot \nabla) \mathbf{v} \rangle]. \quad (4.8)$$

The non-linear terms resemble those occurring in mean field MHD and dynamo theory [*e.g.*, Krause and Rädler, 1980]. We will later model these terms using one-point closures (Chapters 5 and 6). In deriving these equations we have assumed that the small-scale fluctuations are incompressible, *i.e.*, $\delta\rho = 0$ and $\nabla_{\mathbf{x}} \cdot \mathbf{v} = 0$. Thus, $\rho = \rho_0$ and for simplicity we drop the zero subscript hereafter. The assumption of small-scale incompressibility has several advantages. First, it simplifies the equations. Second, as mentioned in sections 2.2 and 2.5.4.3, typically $\delta\rho/\rho \sim 1/10$ in the solar

wind, so that one might expect the leading order physics to be approximately the same when $\delta\rho/\rho$ is identically zero. The recently developed theory of nearly incompressible MHD also suggests that, in certain situations, the incompressible limit is a valid approximation to use when considering such fluids [Matthaeus and Brown, 1988; Zank *et al.*, 1990; Zank and Matthaeus, 1990a, 1991, 1992a, b, 1993; Matthaeus *et al.*, 1991]. Finally, since the theory of incompressible turbulence is more developed than its compressible counterpart, and we have in mind to adopt a turbulent description of the fluctuations, this is a useful starting point. This said, however, it is important to realize that the *large-scale* fields are neither incompressible nor homogeneous in general. In fact, many of the evolutionary changes undergone by the fluctuations, as they move away from the sun, depend upon the compressible nature of the interplanetary medium.

Equations (4.4)–(4.6) describe the evolution of the fluctuating velocity and magnetic fields in the presence of given mean fields \mathbf{U} , \mathbf{B}_0 , and ρ . The equations governing the evolution of these large-scale fields (the averaged forms of (4.2) and (4.3)) are not considered here; instead we take the mean fields to be *specified*, time-steady functions of the large-scale spatial coordinate \mathbf{R} . Frequently we will choose \mathbf{U} to represent constant speed radial flow, \mathbf{B}_0 to be the standard Parker [1958] spiral, and $\rho \propto 1/R^2$. For the solar wind, all of these approximations are observationally well grounded, and often used to describe the quiet solar wind. [Hundhausen, 1972]. While the model supports large-scale fields of a much more general nature than those just mentioned, these approximations to the true mean fields will provide a useful starting point for comparisons with spacecraft observations.

Equations (4.5)–(4.6) may also be expressed in terms of the *Elsässer* [1950] variables, defined by $\mathbf{z}^\pm = \mathbf{v} \pm \mathbf{b}/\sqrt{4\pi\rho}$. Making this change of variables we obtain

$$\begin{aligned} \frac{\partial \mathbf{z}^\pm}{\partial t} + (\mathbf{U} \mp \mathbf{V}_A) \cdot \nabla \mathbf{z}^\pm + \frac{\mathbf{z}^\pm}{2} \nabla \cdot \left(\frac{\mathbf{U}}{2} \pm \mathbf{V}_A \right) \\ + \mathbf{z}^\mp \cdot \left[\nabla \mathbf{U} \pm \frac{1}{\sqrt{4\pi\rho}} \nabla \mathbf{B}_0 - \frac{1}{2} \nabla \cdot \left(\frac{\mathbf{U}}{2} \pm \mathbf{V}_A \right) \right] = -\frac{1}{\rho} \nabla \delta P + \mathbf{N}_0^\pm, \end{aligned} \quad (4.9)$$

where $\mathbf{V}_A = \mathbf{B}_0/\sqrt{4\pi\rho}$ is the large-scale Alfvén velocity, and \mathbf{l} is the unit tensor. As noted in section 2.4.1, the Elsässer variables represent the (linearized) normal modes of an incompressible magneto-fluid in the presence of a large-scale magnetic field, corresponding to linear Alfvén waves propagating in opposite directions along \mathbf{B}_0 . Marsch and Mangeney [1987] have suggested that the representation is also a convenient one to use when considering compressible flows. When Elsässer variables are adopted, the equations of motion have an appealing symmetry of form, for both the general [Marsch and Mangeney, 1987] and the scale-separated cases [Marsch and Tu, 1989; Tu and Marsch, 1990b; Zhou and Matthaeus, 1990a]. As discussed in the introduction, for convenience we

Table 4.1: Some correlation functions and spectral tensors in terms of the primitive variables \mathbf{v} and \mathbf{b} . Primed ($'$) variables are evaluated at $\mathbf{x} + \mathbf{r}$, unprimed at \mathbf{x} . See Chapter 3 for further details, but be aware that some notational differences exist between the chapters; in particular, here \mathbf{b} is not measured in Alfvén speed units. All quantities are also functions of the large-scale spatial coordinate \mathbf{R} .

Symbol	Definition	Description	Fourier Transform	Homogeneity Condition
$R_{ij}^v(\mathbf{r})$	$\langle v_i v_j' \rangle$	Kinetic Energy	$S_{ij}^v(\mathbf{k})$	$R_{ij}^v(\mathbf{r}) = R_{ji}^v(-\mathbf{r})$
$R_{ij}^b(\mathbf{r})$	$\frac{\langle b_i b_j' \rangle}{4\pi\rho}$	Magnetic Energy	$S_{ij}^b(\mathbf{k})$	$R_{ij}^b(\mathbf{r}) = R_{ji}^b(-\mathbf{r})$
$R_{ij}(\mathbf{r})$	$R_{ij}^v + R_{ij}^b$	Total Energy	$S_{ij}(\mathbf{k})$	$R_{ij}(\mathbf{r}) = R_{ji}(-\mathbf{r})$
$R_{ij}^D(\mathbf{r})$	$R_{ij}^v - R_{ij}^b$	Energy Difference	$S_{ij}^D(\mathbf{k})$	$R_{ij}^D(\mathbf{r}) = R_{ji}^D(-\mathbf{r})$
$R_{ij}^{vb,\pm}(\mathbf{r})$	$\frac{\langle v_i b_j' \pm b_i v_j' \rangle}{2\sqrt{4\pi\rho}}$	“Cross Energies”	$S_{ij}^{vb,\pm}(\mathbf{k})$	$R_{ij}^{vb,\pm}(\mathbf{r}) = \pm R_{ji}^{vb,\pm}(-\mathbf{r})$

will respectively refer to the \mathbf{z}^+ and \mathbf{z}^- fluctuations as “inward” and “outward” type disturbances, even though the interpretation in terms of non-interacting inwardly and outwardly propagating waves is only correct for small amplitude disturbances (see also section 2.5.4). Note that while making the change to Elsässer variables, large-scale gradients of the density have been eliminated in favor of large-scale gradients of \mathbf{U} and/or \mathbf{V}_A [Zhou and Matthaeus, 1990a].

The terms in square brackets in equation (4.9) will be referred to as the *mixing tensors*. Their role in coupling the two small-scale fields together is clearly evident, and we will have much more to say about them below.

Since we are principally concerned with the transport of *statistical* properties of the turbulent fluctuations, it is appropriate to construct transport equations for the *correlation functions* and *spectra* of the fluctuation variables. For inertial range fluctuations, the spectra are the more studied forms, while in the energy-containing range the emphasis is usually on the bulk x -space quantities. Properties of some correlation functions and spectra we will have need of in this chapter are summarized in Tables 4.1–4.3. Further details are available in Chapter 3 and the references [e.g., Batchelor, 1970; Zhou and Matthaeus, 1990a].

Consider first transport of the autocorrelation of the \mathbf{z}^+ and \mathbf{z}^- fields. By definition we have

$$\begin{aligned}
 \frac{d}{dt} H_{ij}^{\pm}(\mathbf{R}, \mathbf{r}) &= \frac{d}{dt} \langle z_i^{\pm}(\mathbf{R}, \mathbf{x}) z_j^{\pm}(\mathbf{R}, \mathbf{x} + \mathbf{r}) \rangle \\
 &= \langle z_i^{\pm} \frac{dz_j^{\pm'}}{dt} + \frac{dz_i^{\pm}}{dt} z_j^{\pm'} \rangle.
 \end{aligned} \tag{4.10}$$

Table 4.2: Some correlation functions and spectral tensors in terms of Elsässer variables. The superscripts “*s*” and “*a*” denote the symmetric and antisymmetric parts of the tensor respectively. As in Table 4.1, the dependence of each form on the large-scale spatial coordinate \mathbf{R} has been suppressed.

Symbol	Definition	<i>v</i> - <i>b</i> Form	Fourier Transform	Homogeneity Condition
$H_{ij}^{\pm}(\mathbf{r})$	$\langle z_i^{\pm} z_j^{\pm'} \rangle$	$R_{ij} \pm 2R_{ij}^{vb,+}$	$P_{ij}^{\pm}(\mathbf{k})$	$H_{ij}^{\pm}(\mathbf{r}) = H_{ji}^{\pm}(-\mathbf{r})$
$\Lambda_{ij}(\mathbf{r})$	$\langle z_i^{+} z_j^{-'} \rangle$	$R_{ij}^D - 2R_{ij}^{vb,-}$	$\Theta_{ij}(\mathbf{k})$	$\Lambda_{ij}(\mathbf{r}) = \tilde{\Lambda}_{ij}(-\mathbf{r})$
$\tilde{\Lambda}_{ij}(\mathbf{r})$	$\langle z_i^{+'} z_j^{-} \rangle$	$R_{ji}^D + 2R_{ji}^{vb,-}$	$\tilde{\Theta}_{ij}(\mathbf{k})$	
$F_{ij}(\mathbf{r})$	$\langle \Lambda_{ij} + \tilde{\Lambda}_{ij} \rangle$	$2R_{ij}^{Ds} - 4R_{ij}^{vb,-a}$	$F_{ij}(\mathbf{k})$	$F_{ij}(\mathbf{r}) = F_{ij}(-\mathbf{r})$
$J_{ij}(\mathbf{r})$	$\langle \Lambda_{ij} - \tilde{\Lambda}_{ij} \rangle$	$2R_{ij}^{Da} - 4R_{ij}^{vb,-s}$	$J_{ij}(\mathbf{k})$	$J_{ij}(\mathbf{r}) = -J_{ij}(-\mathbf{r})$

Table 4.3: Some useful relations involving the traces of various spectra. These definitions and identities hold for all three spectral types: modal, omni-directional, and reduced. All quantities are functions of the large-scale coordinate \mathbf{R} and appropriate components of the wave-vector \mathbf{k} .

$S_{\alpha\alpha}^v = 2E^v$	$P^{\pm} = \langle (\mathbf{z}^{\pm})^* \cdot \mathbf{z}^{\pm} \rangle = 2E \pm 4H_c$
$S_{\alpha\alpha}^b = 2E^b$	$F = 2 \operatorname{Re} \{ \langle (\mathbf{z}^+)^* \cdot \mathbf{z}^- \rangle \} = 4(E^v - E^b)$
$S_{\alpha\alpha} = 2E = 2(E^v + E^b)$	$\sigma_D = \frac{F}{P^+ + P^-} = \frac{E^v - E^b}{E^v + E^b}$
$H_c = \frac{\langle \mathbf{v}^* \cdot \mathbf{b} \rangle}{2\sqrt{4\pi\rho}} = \frac{1}{8}(P^- - P^+)$	$r_A = \frac{E^v}{E^b} = \frac{1 + \sigma_D}{1 - \sigma_D}$
$\sigma_c = \frac{2H_c}{E} = \frac{P^- - P^+}{P^- + P^+}$	$J = -4 \operatorname{Im} \left\{ \frac{\mathbf{v}^* \cdot \mathbf{b}}{\sqrt{4\pi\rho}} \right\}$

Straightforward algebraic manipulations of this equation and (4.9), in conjunction with the properties of $\langle \cdots \rangle$ and local homogeneity, lead to the following transport equation for H_{ij}^\pm

$$\frac{\partial H_{ij}^\pm}{\partial t} + (\mathbf{U} \mp \mathbf{V}_A) \cdot \nabla H_{ij}^\pm + \nabla \cdot \left(\frac{\mathbf{U}}{2} \pm \mathbf{V}_A \right) H_{ij}^\pm + \Pi_{ij}^\pm = N_{ij}^\pm, \quad (4.11)$$

where $\nabla = \partial/\partial \mathbf{R}$ is the purely large-scale spatial gradient operator. As with the equations for the vector fluctuations we do not write explicit forms for the non-linear terms, but merely symbolically lump them together on the right-hand side of the equation as N_{ij}^\pm [Zhou and Matthaeus, 1990a]. The terms Π_{ij}^\pm are intimately related to the mixing tensors, and have the form

$$\Pi_{ij}^+ = \Lambda_{ik} M_{kj}^+ + \tilde{\Lambda}_{jk} M_{ki}^+, \quad (4.12)$$

$$\Pi_{ij}^- = \tilde{\Lambda}_{ki} M_{kj}^- + \Lambda_{kj} M_{ki}^-, \quad (4.13)$$

where

$$M_{ki}^\pm(\mathbf{R}) = \frac{\partial \mathbf{U}_i}{\partial \mathbf{R}_k} \pm \frac{1}{\sqrt{4\pi\rho}} \frac{\partial \mathbf{B}_{0i}}{\partial \mathbf{R}_k} - \frac{1}{2} \delta_{ik} \nabla \cdot \left(\frac{\mathbf{U}}{2} \pm \mathbf{V}_A \right), \quad (4.14)$$

are the actual mixing tensors. Note that Π^\pm involve the Λ cross-correlation functions, and thus, in order to close the model, we will also need transport equations for these quantities. The point to note here is that the mixing tensors couple the small-scale tensor fields together at *leading* order. Such couplings are absent in leading order WKB theory (see below).

Taking the Fourier transform of (4.11) with respect to the small-scale separation parameter \mathbf{r} (conjugate variable \mathbf{k} , *cf.* Chapter 3) we obtain the evolution equations for the “inward” and “outward” energy spectra

$$\frac{\partial}{\partial t} P_{ij}^\pm(\mathbf{R}, \mathbf{k}) + (\mathbf{U} \mp \mathbf{V}_A) \cdot \nabla P_{ij}^\pm + \nabla \cdot \left(\frac{\mathbf{U}}{2} \pm \mathbf{V}_A \right) P_{ij}^\pm + \Phi_{ij}^\pm = N_{ij}^\pm(\mathbf{k}), \quad (4.15)$$

with

$$\Phi_{ij}^+ = \Theta_{ik} M_{kj}^+ + \tilde{\Theta}_{jk} M_{ki}^+, \quad (4.16)$$

$$\Phi_{ij}^- = \tilde{\Theta}_{ki} M_{kj}^- + \Theta_{kj} M_{ki}^-. \quad (4.17)$$

Note that the left-hand sides of both (4.11) and (4.15) are linear; thus, in cases where the right-hand sides, that is the non-linear terms, may be dropped, superposition of solutions is supported. The same equations also appear in Zhou and Matthaeus [1990a]; however, this treatment differs from theirs, in that the transport equations are derived for spectral tensors dependent upon the *full* wave-vector \mathbf{k} , not the reduced component k_1 .

Proceeding in an analogous fashion for the $\Lambda_{ij} = \langle z_i^+ z_j^- \rangle$ correlation function, we obtain its transport equation

$$\frac{\partial}{\partial t} \Lambda_{ij}(\mathbf{R}, \mathbf{r}) + \mathbf{U} \cdot \nabla \Lambda_{ij} + \left(\nabla \cdot \frac{\mathbf{U}}{2} \right) \Lambda_{ij} + 2\mathbf{V}_A \cdot \nabla_{\mathbf{r}} \Lambda_{ij} + H_{ik}^+ M_{kj}^- + H_{kj}^- M_{ki}^+ = N_{ij}^\Lambda, \quad (4.18)$$

where all the non-linear terms are again written symbolically on the right-hand side, this time as N_{ij}^Λ . In contrast to equation (4.11), (4.18) has a term involving the gradient with respect to the small-scale separation parameter \mathbf{r} . This new feature, associated with small-scale waves, will turn out to be crucially important in recovering WKB-like behavior in the solutions.

The Fourier transform of (4.18) is

$$\frac{\partial \Theta_{ij}}{\partial t} + \mathbf{U} \cdot \nabla \Theta_{ij} + \left(\nabla \cdot \frac{\mathbf{U}}{2} \right) \Theta_{ij} + 2i\mathbf{k} \cdot \mathbf{V}_A \Theta_{ij} + P_{ik}^+ M_{kj}^- + P_{kj}^- M_{ki}^+ = N_{ij}^\Lambda(\mathbf{k}). \quad (4.19)$$

Equations for $\tilde{\Lambda}$ and $\tilde{\Theta}$ may either be obtained directly in a similar fashion to that just described, or via use of the respective symmetry conditions: $\Lambda_{ij}(\mathbf{r}) = \tilde{\Lambda}_{ij}(-\mathbf{r})$ and $\Theta(\mathbf{k}) = \Theta^*(\mathbf{k}) = \Theta(-\mathbf{k})$, which may be derived from the definitions and the homogeneity condition.

Using the definitions of $F_{ij}(\mathbf{k})$ and $J_{ij}(\mathbf{k})$ listed in Table 4.2, it is now straightforward to obtain the transport equations for these tensors

$$\frac{\partial F_{ij}}{\partial t} + \mathbf{U} \cdot \nabla F_{ij} + \left(\nabla \cdot \frac{\mathbf{U}}{2} \right) F_{ij} + 2i\mathbf{k} \cdot \mathbf{V}_A J_{ij} + 2 \left[P_{ik}^{+s} M_{kj}^- + P_{kj}^{-s} M_{ki}^+ \right] = N_{ij}^F(\mathbf{k}), \quad (4.20)$$

$$\frac{\partial J_{ij}}{\partial t} + \mathbf{U} \cdot \nabla J_{ij} + \left(\nabla \cdot \frac{\mathbf{U}}{2} \right) J_{ij} + 2i\mathbf{k} \cdot \mathbf{V}_A F_{ij} + 2 \left[P_{ik}^{+a} M_{kj}^- + P_{kj}^{-a} M_{ki}^+ \right] = N_{ij}^J(\mathbf{k}), \quad (4.21)$$

where the superscripts “ s ” and “ a ” respectively denote the symmetric and antisymmetric portions of the tensors. The coupling nature of the “mixing” terms is again evident in these equations. Essentially the same equations are given in *Zhou and Matthaeus [1990a]*, as equations 61–64, although the reader should be aware that several index and sign errors appear there, and that a slightly different notation is in effect. For example, our $F_{ij}(\mathbf{r})$ is equal to their $F_{ij}^+(\mathbf{r})$, which in turn is equal to $F_{ji}^-(\mathbf{r})$, *i.e.*, $F_{ij} = F_{ij}^+ = F_{ij}^{-T}$, where the superscript T indicates the transpose operation. We will briefly make use of this F^\pm notation in some forms of the P_{ij}^\pm transport equations presented below.

Terms involving the pressure no longer appear explicitly in our equations. There are several justifications for their absence [*Zhou and Matthaeus, 1990a*]. First, for strictly (and also nearly) incompressible fluids, the sole role of the pressure is to enforce this incompressibility (see Appendix A). Thus, provided we ensure that the fluctuations, correlation functions, and spectra are indeed solenoidal (*e.g.*, $k_i S_{ij}(\mathbf{k}) = k_j S_{ij}(\mathbf{k}) = 0$), it should not be necessary to retain the pressure terms. Second, the non-linear nature of the pressure (see Appendix A) suggests that we may

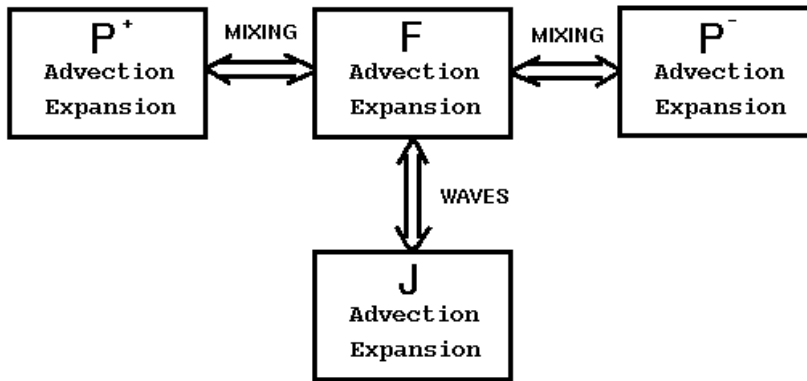


Figure 4.1: Schematic diagram showing the structure of the linear portions of the transport equations for the traced spectra.

incorporate such terms into our symbolic representation of the other non-linear terms, which will later be modeled. Further discussion of this issue may be found in the references [Tu *et al.*, 1984; Zhou and Matthaeus, 1990a].

Equations (4.15), (4.20), and (4.21) form a system of four coupled transport equations in the independent variables $P^\pm(\mathbf{R}, \mathbf{k})$, $F(\mathbf{R}, \mathbf{k})$, and $J(\mathbf{R}, \mathbf{k})$. These four quantities represent the small-scale spectra for the “inward” and “outward” energies, the energy difference, and the helicity of the electric field at each point in space. Given specified large-scale fields and modeled forms for the non-linear terms this model is closed. The physical effects represented in the equations include *advection* ($\mathbf{U} \cdot \nabla$ terms) and *expansion* ($\nabla \cdot \mathbf{U}$ and $\nabla \cdot \mathbf{V}_A$ terms) operating separately on the four tensor fields; *wave propagation* ($\mathbf{k} \cdot \mathbf{V}_A$ terms), a consequence of coupling between F and J ; *non-linearities*, and, finally, “*mixing*” effects, which linearly couple the tensor fields together and depend on the existence of spatial gradients in the large-scale fields (Figure 4.1). In contrast to the case of WKB transport, *all* of these effects, including “mixing,” are in general present in the *leading* order equations. As will be shown below, the distinct couplings associated with “mixing” and waves tend to be adversarial in nature, in the sense that the presence of waves tends to turn off “mixing” effects and drive the solutions towards those appropriate to WKB theory.

At this point we again emphasize that *no* approximations regarding the relative abundances of the “inward” and “outward” modes have been made. The model supports completely arbitrary admixtures of these modes.

A complete closed model will be obtained when (1) definite assumptions regarding the

rotational symmetry properties of the small-scale turbulence are made. This aspect is discussed in the next section; (2) appropriate modeling of the non-linear terms is achieved. This is a difficult problem, particularly for inertial range quantities which are not conserved, *e.g.*, F and J [Zhou and Matthaeus, 1990c]. Of course the modeling adopted should take into consideration the symmetry properties of the turbulence, so that different models for, say, isotropic and slab turbulence will be required. We defer discussion on the topic to the following chapters.

4.3 Simplifications of the Transport Equations

In their full tensor glory, the spectral transport equations (4.15), (4.20), and (4.21), are rather intimidating to view, let alone solve. Indeed, as shown in Chapter 3, for general homogeneous turbulence there are 16 independent scalar functions involved in these equations, along with the directional aspects indicated by the tensor indices. To further simplify the system of equations we contract the indices to obtain transport equations for the tensor traces. Thus,

$$\frac{\partial P^\pm}{\partial t} + (\mathbf{U} \mp \mathbf{V}_A) \cdot \nabla P^\pm + \nabla \cdot \left(\frac{\mathbf{U}}{2} \pm \mathbf{V}_A \right) P^\pm + F_{ik}^\pm M_{ki}^\pm = NL^\pm, \quad (4.22)$$

$$\frac{\partial F}{\partial t} + U \cdot \nabla F + \nabla \cdot \left(\frac{U}{2} \right) F - (2\mathbf{k} \cdot \mathbf{V}_A) J + 2 [P_{ik}^{-s} M_{ki}^+ + P_{ik}^{+s} M_{ki}^-] = NL^F, \quad (4.23)$$

$$\frac{\partial J}{\partial t} + U \cdot \nabla J + \nabla \cdot \left(\frac{U}{2} \right) J + (2\mathbf{k} \cdot \mathbf{V}_A) F = NL^J, \quad (4.24)$$

where $P^\pm = P_{\alpha\alpha}^\pm = \text{Trace}(P_{ij}^\pm)$, $F = F_{\alpha\alpha}$, and $iJ = J_{\alpha\alpha}$. The functional dependence upon \mathbf{R} and \mathbf{k} has been suppressed. Except where they are contracted with the mixing tensors, the tensor fields have been reduced to scalar functions which admit useful physical interpretations: $P^\pm(\mathbf{R}, \mathbf{k})$ are the energy spectra for the “inward” and “outward” Elsässer fluctuations, F is proportional to the spectrum of the energy difference, that is the kinetic energy spectrum minus the magnetic one, while J is related to the spectrum of the helicity of the induced electric field (see Chapter 3). As will be shown below, it is also possible to write the “mixing” terms as the products of effective mixing operators and the traced fields, when particular conditions on the large-scale fields and the symmetry properties of the small-scale turbulence are assumed (see Appendix C).

Note that no “mixing” terms appear in the evolution equation for J . This is a consequence of our assumption² that the anti-symmetric parts of P^\pm are zero, or more physically, that the velocity helicity, magnetic helicity, and helicity of the cross helicity (see Chapter 3) are all identically zero. While such an approximation is certainly not warranted in general in the solar wind, we nonetheless make it since it is a simpler case to consider. Additionally, observations [Matthaeus and Goldstein,

² See the final page of Chapter 1.

1982a] suggest that, at a given inertial range wave number, the magnetic helicity is typically something like an order of magnitude smaller than the magnetic energy. When the mixing tensors are symmetric, such an approximation is unnecessary, as the trace of a symmetric tensor multiplied by an antisymmetric one is identically zero. However, except in the $V_{Ar0}/U \rightarrow 0$ limit (see below) the mixing tensors we use are not symmetric. Of course the divergence terms in M^\pm , which are multiplied by the unit tensor, always vanish when contracted with an antisymmetric tensor, so that only the “grad” terms contribute anyway.

Having derived the general form of the transport equations for the spectra, we now specialize to particular forms for the large-scale fields. We choose the density to be proportional to $1/R^2$, the solar wind velocity to be constant and radially outward, and the magnetic field to be the standard *Parker* [1958] spiral. Specifically, using heliocentric spherical polar coordinates (R, θ, ϕ) , where R is the radial distance from the center of the sun, θ the co-latitude with respect to the solar rotation axis, and ϕ the azimuthal angle,

$$\rho = \rho_0 \left(\frac{R_0}{R} \right)^2, \quad (4.25)$$

$$\mathbf{U} = U \hat{\mathbf{R}}, \quad (4.26)$$

$$B_{0r} = B_{0r}^0 \left(\frac{R_0}{R} \right)^2, \quad (4.27)$$

$$B_{0\theta} = 0, \quad (4.28)$$

$$B_{0\phi} = -B_{0r}^0 \frac{\Omega R_0}{U} \frac{R_0}{R} \left(1 - \frac{R_0}{R} \right) \sin \theta, \quad (4.29)$$

U being the constant, radially directed mean wind speed and Ω the solar rotation rate. The two constants ρ_0 and B_{0r}^0 represent the values of the density and magnetic field at some reference radius R_0 . Usually we will take R_0 to correspond to the Alfvénic critical radius R_c , which is believed to lie in the range 7–30 R_{sun} [Weber and Davis, 1967; Lotova *et al.*, 1985; Lotova, 1988]. The values of ρ_0 and B_{0r}^0 may then be chosen so that at 1 AU, ρ and \mathbf{B}_0 are in approximate agreement with observations. Numerically, we have chosen to restrict the situation somewhat further, so that only the combination $V_{Ar0} = B_{0r}^0 / \sqrt{4\pi\rho_0}$ is available as a parameter in the codes. Note that while $B_{0r} \sim 1/R^2$ asymptotically, $B_{0\phi} \sim 1/R$, so that, as is well known, the azimuthal field dominates for large R . Recall also, from Chapter 2, that once the form of either \mathbf{U} or ρ is chosen, the other quantities form is determined by the equation of (mass) continuity.

In principle B_{0r}^0 may easily be generalized to support dependence on the co-latitude θ ; however, for our purposes the monopole-like behavior of \mathbf{B}_0 will usually suffice (see also Appendix C). The observed sector structure of \mathbf{B}_0 is therefore absent in this form of the model. Similarly there

is no current sheet in the solar magnetic equatorial plane.³ This restriction can be overcome by taking B_{0r}^0 as positive in one hemisphere (say, the northern one) and equal in magnitude but negative in the other hemisphere. The discontinuity in \mathbf{B}_0 at the equator is then associated with a (planar) current sheet. With this choice of constants, the mean magnetic field is directed outwards in the northern hemisphere and inwards in the southern, corresponding to away and toward “sectors,” respectively.

On a related note, the structureless forms chosen for ρ and \mathbf{U} preclude the existence of both shocks and solar wind streams. However, by choosing the value of U appropriately, we may approximate conditions associated with either high or low speed streams. Furthermore, since (i) we will often assume that the small-scale fluctuations correspond to strong turbulence, and (ii) shock fronts and stream structure boundaries are likely candidates for regions where *in situ* turbulence is generated, their presence is perhaps being tacitly assumed in order to keep the turbulence strong, even though strictly speaking such interaction cannot occur with this choice of mean fields. These points should be kept in mind when comparing results from the model with spacecraft data.

It follows immediately that the non-zero components of the large-scale Alfvén velocity may be written

$$\begin{aligned} V_{Ar} &= \frac{B_{0r}^0}{\sqrt{4\pi\rho_0}} \frac{R_0}{R} \\ &= V_{Ar0} \frac{R_0}{R}, \end{aligned} \tag{4.30}$$

$$V_{A\phi} = -V_{Ar0} \left(\frac{\Omega R_0}{U} \right) \left(1 - \frac{R_0}{R} \right) \sin \theta. \tag{4.31}$$

Thus, $V_{A\phi}$ approaches a constant as $R \rightarrow \infty$, while $V_{Ar} \rightarrow 0$. For typical solar wind parameters, $|\mathbf{V}_A| \approx V_{A\phi}$, beyond about 2 AU.

At this point it is also useful to define the field *winding angle*, $\psi(\mathbf{R})$ [Parker, 1958], which is the angle between \mathbf{B}_0 and the radial direction. Thus,

$$\begin{aligned} \tan \psi &= \frac{B_{0\phi}}{B_{0r}} \\ &= \frac{\Omega R_0}{U} \left(\frac{R}{R_0} - 1 \right) \sin \theta. \end{aligned} \tag{4.32}$$

Taking R_0 as 10–20 R_{sun} , $U \approx 400$ km/sec, and using the observed solar rotation rate of $2\pi/(27$ days), leads to values of ψ at 1 AU of about 45° , in satisfactory agreement with the average observational value. Increasing either R_0 or U produces looser winding. The winding angle will be particularly relevant when we consider 2D and slab turbulence, coming into play in both the

³ For simplicity we assume that the magnetic and rotational axes of the sun coincide.

mixing operators and in the forms of the spectra. Note that mathematically speaking, it has a well defined value in the limit $B_{0r}^0 \rightarrow 0$.

Substituting these expressions for the large-scale fields into equations (4.22)–(4.24), and assuming that the P^\pm are independent of ϕ , we obtain

$$\frac{\partial P^\pm}{\partial t} + (U \mp V_{Ar}) \frac{\partial P^\pm}{\partial R} + \left(\frac{U \pm V_{Ar}}{R} \right) P^\pm + F_{ik}^\pm M_{ki}^\pm = NL^\pm, \quad (4.33)$$

$$\frac{\partial F}{\partial t} + U \frac{\partial F}{\partial R} + \frac{U}{R} F - (2\mathbf{k} \cdot \mathbf{V}_A) J + 2 [P_{ik}^{-s} M_{ki}^+ + P_{ik}^{+s} M_{ki}^-] = NL^F, \quad (4.34)$$

$$\frac{\partial J}{\partial t} + U \frac{\partial J}{\partial R} + \frac{U}{R} J + (2\mathbf{k} \cdot \mathbf{V}_A) F = NL^J, \quad (4.35)$$

where we postpone evaluating the contractions with the mixing tensors until the following section (see also Appendix C). Recall that $F = F^+ = F^{-T}$. This constitutes our final set of equations for the transport of general homogeneous fluctuations in the inertial range of the interplanetary medium. In order to make further progress, we will restrict the fluctuations to be isotropic, 2D, or slab in nature.

The choice of what type of spectra/spectral tensors to work with still remains. We consider three options: modal, omni-directional, reduced (also know as one-dimensional) [*e.g.*, *Batchelor*, 1970]. Whereas the three-dimensional modal spectra are functions of vector \mathbf{k} , the reduced spectra depend only on $k_r = \mathbf{k} \cdot \hat{\mathbf{R}}$. For isotropic turbulence, a unique relationship between the reduced and modal spectra exists, so that the choice of which to use is one of convenience rather than necessity. For more general turbulence, however, the modal spectra contain information which cannot be recovered from the reduced forms. Since the vast bulk of observational data has been obtained via single spacecraft measurements, only reduced spectra may be calculated from such data. Hence, even if our model were to be completely correct, it would still be impossible to interpret the observational data unambiguously, unless perchance the small-scale turbulence was purely isotropic. Still, in order to facilitate comparisons with observations, it would seem sensible to take \mathbf{r} to be in the radial direction and therefore work with spectra which have been reduced over directions perpendicular to $\hat{\mathbf{R}}$ (*e.g.*, Appendix C of *Zhou and Matthaeus*, 1990a).

For isotropic turbulence this presents no problem, but for the 2D and slab cases, difficulties arise because the preferred directions of the turbulence change as a function of \mathbf{R} . In particular, at $R = R_0$, $\hat{\mathbf{R}}$ and \mathbf{B}_0 are aligned, so that the reduced spectra for 2D turbulence vanish (for $k \neq 0$), the reduction direction being perpendicular to all the wave-vectors (see section 5.2.3). Hence *all* the boundary conditions are zero. To avoid this difficulty we will usually work with omni-directional spectra. That said, for isotropic turbulence, some results obtained using reduced spectra will also be presented.

Omni-directional spectra are obtained from the modal forms by averaging over all wave-vectors \mathbf{k} with the same magnitude k . In three dimensions this is equivalent to averaging over spherical shells in k -space. For 2D turbulence the average is over rings in the plane of the turbulence, while for slab fluctuations no averaging is necessary when only the positive k vectors have non-zero spectral amplitudes. In each case the omni-directional spectrum, $E(k)$, has the following relationship to the total energy, E ,

$$E = \int_0^\infty E(k) dk \quad (4.36)$$

When contracting the small-scale spectra with the mixing tensors (see below), the relative simplicity of the omni-directional spectral tensors (\sim diagonal) is advantageous. Furthermore, as shown in Appendix C, once the omni-directional spectrum is known, an integral gives the reduced spectrum, which may then be compared with the forms obtained from observational data.

4.4 The Mixing Tensors

Before moving on to the results, a few preliminary/introductory words are in order regarding the nature of the mixing tensors. As shown in the previous section, these tensors take the form:

$$M_{ki}^\pm(\mathbf{R}) = \frac{\partial \mathbf{U}_i}{\partial \mathbf{R}_k} \pm \frac{1}{\sqrt{4\pi\rho}} \frac{\partial \mathbf{B}_{0i}}{\partial \mathbf{R}_k} - \frac{1}{2} \delta_{ik} \nabla \cdot \left(\frac{\mathbf{U}}{2} \pm \mathbf{V}_A \right),$$

which is completely determined by the *large-scale* gradients of the *mean* fields. However, because the tensors always appear coupled to *small-scale* spectral tensors (*e.g.*, $Q_{jk} M_{ki}^\pm$), “mixing” also depends on the nature and symmetry properties of the small-scale turbulence. In general these symmetry properties of the turbulence hold only in a *statistical* sense, since for a turbulent fluid, the velocity (and magnetic) fluctuations are considered to be stochastic variables. However, appropriate averaging procedures (*e.g.*, ensemble averaging) allow determination of the turbulent flow’s symmetry properties in the statistical sense [Batchelor, 1970].

Mathematically, the mixing tensors mediate couplings between the independent small-scale fields; physically, they may be interpreted as acting to scatter the \mathbf{z}^\pm modes off large-scale gradients of the mean fields. Another interpretation is associated with the MHD analog of the Reynolds stresses [*e.g.*, Tennekes and Lumley, 1972]. In this view the mixing tensors are a sort of mean rate of strain in the large-scale fields, from which energy may be fed to smaller scales. Note that the tensors vanish when the large-scale fields are uniform.

Tu and Marsch [1993] have recently discussed the nature of the “mixing” tensors when $\mathbf{V}_A = 0$. In this limit $M^+ = M^-$, but, as discussed by these authors, the Elsässer variable representation actually obscures the physics somewhat, since there is no \mathbf{B}_0 . Considering just the

linear terms in the transport equations for the (traced) spectra of the (small-scale) kinetic energy, magnetic energy, and cross helicity (*cf.* those for P^\pm and F), it becomes clear that these equations are independent, *i.e.*, no coupling amongst the small-scale fields occurs (see Appendix B of their paper, and Appendix D of this thesis). As stated in their paper, the basic physics then consists of advection and expansion of the vorticity and magnetic field fluctuations. While it is still true that the Elsässer fluctuations are “mixed,” Tu and Marsch’s point—that, in the absence of a large-scale magnetic field (and non-linearities), the velocity and magnetic field fluctuations decouple—is well taken, and serves as a reminder regarding the interpretation of the Elsässer variables for such situations (see also equations (4.5)–(4.6)).

Assuming that the small-scale turbulence is either isotropic, 2D, or slab enables the trace of $Q_{jk}M_{ki}^\pm$ to be evaluated and written as $M^\pm Q$, where $Q = Q_{\alpha\alpha}$, and the M^\pm are *effective* mixing operators. As shown in Appendix C, the type of spectra used (*e.g.*, omni-directional, reduced) plays a role in determining the forms of the M^\pm . For all three types of turbulence we work with omni-directional spectra, and, in addition, for isotropic turbulence direct solutions are obtained using reduced spectra. In order to make headway with the reduced spectra, we assume a powerlaw dependence of the inertial range fluctuations, α being the spectral slope (see Appendix C). Important values of α include those associated with the theories of Kolmogorov ($\alpha = 5/3$) and Kraichnan ($\alpha = 3/2$). Below we list the final forms of the effective mixing operators appropriate for use with omni-directional spectra:

$$M_{iso}^\pm = \frac{1}{2R} \left[\frac{U}{3} \mp V_{Ar} \right], \quad (4.37)$$

$$M_{2D}^\pm = \frac{1}{2R} \left[U \cos^2 \psi \pm V_{Ar} (3 \cos^2 \psi - 2) \right. \\ \left. \pm \frac{1}{2} V_{Ar0} \left(\frac{\Omega R_0}{U} \right) \left(2 - \frac{3R_0}{R} \right) \sin \theta \sin 2\psi \right], \quad (4.38)$$

$$M_{slab}^\pm = M_{2D}^\pm, \quad (4.39)$$

where ψ is the “winding angle” of the Parker spiral magnetic field, introduced in equation (4.32). The equality of the 2D and slab mixing operators is a consequence of the formal equivalence of the omni-directional spectra for the two cases. In both situations, the fluctuation energy is all in spectral tensor components perpendicular to \mathbf{B}_0 , but the interpretations are distinctly different (*e.g.*, Appendix C). For the transport of isotropic turbulence in terms of reduced spectra, the appropriate mixing operators are

$$M_{iso}^\pm = \frac{\alpha}{\alpha + 2} \frac{1}{2R} \left[U \mp \left(\frac{4}{\alpha} - 1 \right) V_{Ar} \right]. \quad (4.40)$$

As suggested by Figure 4.2, when $R \gtrsim 2$ AU the effective operators are all essentially the

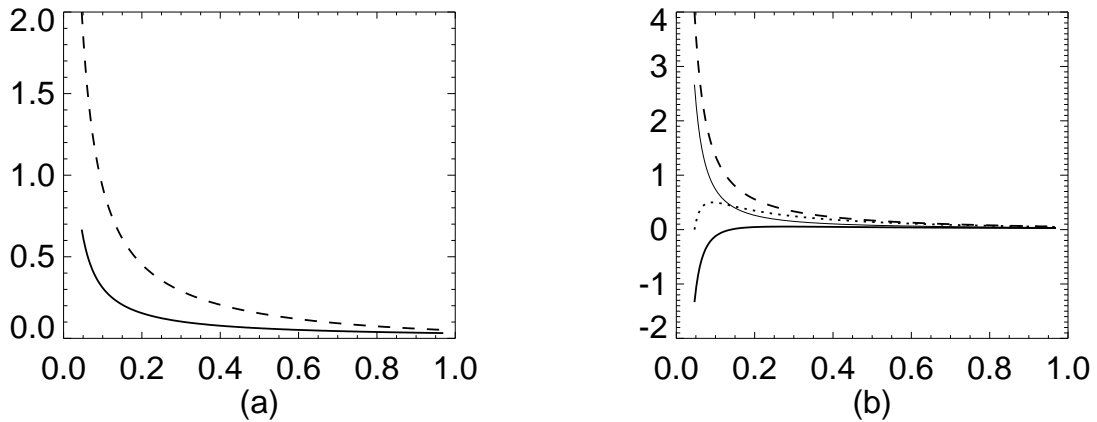


Figure 4.2: Plots of the effective mixing operators as a function of heliocentric distance in AU. (a) The case $V_{Ar0} = 0$ (for which $M^+ = M^-$), (b) the case $V_{Ar0} = U$. The isotropic versions are plotted using solid lines, and the 2D forms using broken lines. In (b) the M^- forms are indicated by the thinner solid line and the dotted line. The inner boundary is located at $R_0 = 10 R_{sun}$.

same. Inside 1 AU, however, important differences exist between both the plus and minus versions for the same type of turbulence, and also between M^\pm for different types of rotational symmetry.

While the mixing operators display important dependence on the Alfvén velocity, we can elucidate their general features by considering two particular cases, namely $V_{Ar0}/U = 0$ and 1. The first situation is associated with the absence of a large-scale magnetic field, and thus would be appropriate, for example, within a (planar) current sheet. The second case corresponds to choosing R_0 equal to the Alfvénic critical radius, R_c . In all cases, the mixing operators are $O(1/R)$ for large R , leading to their asymptotic approach towards zero (from above). This is a consequence of the assumed forms for the large-scale fields becoming more nearly uniform as $R \rightarrow \infty$.

When $V_{Ar0} = 0$, it is always true that $M^+ = M^-$, and while there are differences in the constants and trigonometric terms multiplying the U/R factor, qualitatively speaking, the type of turbulence is unimportant in determining the form of the mixing operators for this case. The operators all decrease towards zero monotonically, from initial (positive) peaks at $R = R_0$ (Figure 4.2(a)). Quantitatively, of course, the multiplying factors do lead to noticeable differences in the solutions, as will be discussed below.

When $V_{Ar0} = U$, however, the situation is considerably different, the most anomalous forms are associated with isotropic turbulence (Figure 4.2(b)). Here M_{iso}^+ actually starts negative and then crosses over to a positive peak at a few R_0 , before decaying towards zero. For 2D and slab turbulence, the M^+ operators are strictly monotonically decreasing from initial positive

values, behavior which is similar to the $V_A = 0$ cases. The anomalous behavior of M_{iso}^+ , is largely responsible for the strongly reduced “mixing” of isotropic turbulence relative to 2D turbulence.

For $V_{Ar0} \neq 0$, the M^- operators are no longer equal to their “plus” counterparts. Again the behavior of the isotropic form is qualitatively different from that of the others. In particular, for $V_{Ar0} = U$, and 2D and slab turbulence, the M^- rise from zero at $R = R_0$ to a peak, and thereafter decay monotonically towards zero. For isotropic turbulence, however, M^- decays monotonically from its positive maximum at R_0 , behavior that is essentially the same as that of the 2D and slab M^+ operators. Further details will be given in the discussion of the actual solutions to the transport equations

In the solar wind, the gradients in the mean fields are largest in the inner heliosphere, so that the components of the mixing tensors are also largest in magnitude in this region. Furthermore, since the mixing operators act as non-constant coupling coefficients between the small-scale fields,⁴ it seems likely that any significant influence exerted by the mixing tensors on the radial evolution of the fluctuating quantities, will also occur close to the sun. Once $R \gtrsim 2$ AU, the gradients in the mean fields are so weak that the mixing operators become too small, relative to the other coefficients in the transport equations, to produce any real modifications. In support of this statement, Figure 4.3 shows the radial dependence of some of the coefficients of equations (4.33)–(4.35), for 2D turbulence (the case for which the mixing operators are largest). Within the first few tenths of an AU, M_{2D}^+ differs from the other coefficients by no more than a factor of two. By 2 AU, however, it is an order of magnitude less than the other coefficients. Similar results apply when $V_{Ar0} = 0$.

4.5 Relationship to WKB

At this point it is useful to compare the model to other formalisms for the transport of solar wind fluctuations, and WKB theory in particular. To facilitate such comparisons we introduce the following abbreviated notation for the spectral transport equations,

$$\frac{\partial P^\pm}{\partial t} + L_{WKB}^\pm P^\pm + FM^\pm = NL^\pm, \quad (4.41)$$

$$\frac{\partial F}{\partial t} + L_{WKB}F - (2\mathbf{k} \cdot \mathbf{V}_A)J + 2[P^-M^+ + P^+M^-] = NL^F, \quad (4.42)$$

$$\frac{\partial J}{\partial t} + L_{WKB}J - (2\mathbf{k} \cdot \mathbf{V}_A)J = NL^J, \quad (4.43)$$

⁴ See equations (4.33) and (4.34) for example.

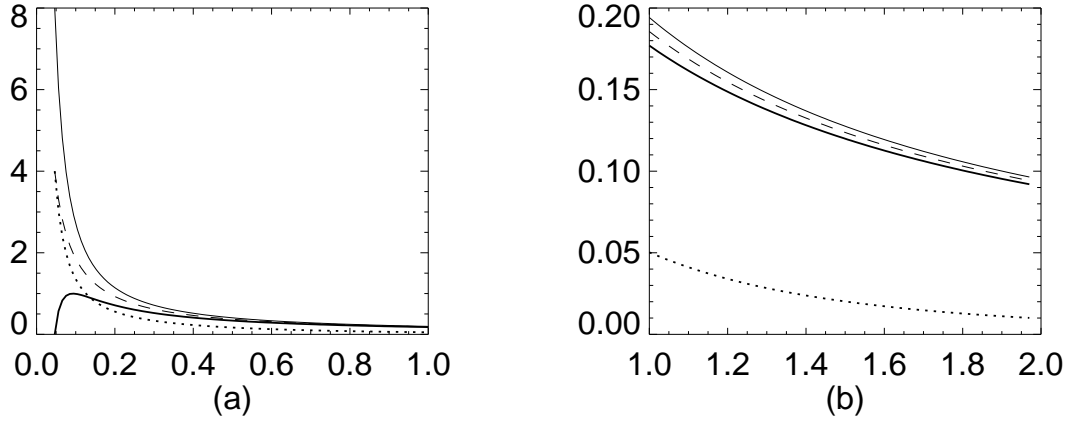


Figure 4.3: Plots of the coefficients in the transport equations for the traced fields, as a function of heliocentric distance. The coefficient $(U + V_{Ar})/R$ is shown as the thin solid line, $(U - V_{Ar})/R$ as the thick solid line, U/R as the dashed, and M_{2D}^+ as the dotted line. The inner boundary is located at 10 solar radii, and $V_{Ar0} = U$. (a) The range $R = 10 R_{sun}$ to 1 AU, (b) the range 1–2 AU.

where

$$L_{WKB}^{\pm} = (\mathbf{U} \mp \mathbf{V}_A) \cdot \nabla + \nabla \cdot \left(\frac{\mathbf{U}}{2} \pm \mathbf{V}_A \right), \quad (4.44)$$

$$L_{WKB} = U \cdot \nabla + \nabla \cdot \left(\frac{U}{2} \right), \quad (4.45)$$

and the M^{\pm} are the effective mixing operators introduced in the previous section.

As in the rest of this work, the spectra for “outward” fluctuations are denoted by P^- , and those for the “inward” modes by P^+ . Appropriate boundary conditions are required, and for most cases considered in this section we take the inner boundary to correspond to the Alfvénic critical radius, so that only “outward” fluctuations exist at this distance. Symbolically, $P_0^+ = F_0 = J_0 = 0$, where the zero subscript indicates evaluation at R_0 . While we have not done so here, it can be shown that these transport equations do support the existence of critical points, and in particular the distance at which $V_{Ar} = U$ is such a point.

Traditionally, WKB theory has been the formalism of choice when considering the transport of solar wind fluctuations [Parker, 1965; Hollweg, 1973b, 1974; Barnes, 1979]. As mentioned in section 2.5.2, this describes the transport of MHD waves whose wavelengths (λ) are much shorter than the scale lengths ($\sim R$) characterizing inhomogeneities in the background fields, so that λ/R is a small parameter in which perturbation expansions may be carried out. In the context of solar wind transport, WKB theory includes the effects of advection, expansion, and wave propagation.

In our notation the appropriate leading order transport equation is

$$\frac{\partial P^-(\mathbf{k})}{\partial t} + L_{WKB}^- P^-(\mathbf{k}) = 0, \quad (4.46)$$

where, as advertised, we are imposing the condition $P^+(\mathbf{k}) = 0$, with F and J vanishing at leading order. The absence of the *linear* “mixing” terms at this order is immediately apparent, and is associated with the assumption that the waves are transverse Alfvén modes with equipartition of kinetic and magnetic energy, *i.e.*, zero F . As a consequence of working with Elsässer variables—for which \mathbf{b} is measured in Alfvén speed units (*i.e.*, normalized by $1/\sqrt{4\pi\rho}$)—numerical factors in L_{WKB}^\pm differ superficially from those appearing when the more traditional \mathbf{v} and \mathbf{b} variables are used.

With this choice of boundary/initial conditions $L_{WKB}^+ P^+$ is identically zero, so that (at leading order) no “inward” fluctuations can be generated if there are none present to start with. If we now return to equation (4.41), it is apparent that because of the linear coupling associated with the mixing operators, an initial population of P^- immediately generates a non-zero value of F , which in turn generates P^+ fluctuations. In other words, despite being absent in the initial data, “inward” fluctuations may be generated from “outward” ones through the action of *leading order, linear* terms which do not appear in the usual WKB equation.

The natural question to ask is: What causes this leading order difference? In brief, the answer is that a second, independent, expansion parameter, related to the *frequencies* of the “waves,” must also be considered [Zhou and Matthaeus, 1990b; Matthaeus *et al.*, 1992; Matthaeus *et al.*, 1993b]. As shown in the latter two references, a multiple scales analysis of the transport equations for the \mathbf{z}^\pm variables reveals this quite cleanly; here we note only that there are at least three distinct situations when the “mixing” terms are important at leading order, and that in order to reduce “mixing” effects to higher order, two conditions must be satisfied. In connection with this, recall that the dispersion relation for linear Alfvén waves in a moving medium is,

$$\omega^\pm = \mathbf{k} \cdot (\mathbf{U} \pm \mathbf{V}_A) \quad (4.47)$$

[*e.g.*, Nicholson, 1983; Zhou and Matthaeus, 1990b]. Note that the same frequency is obtained when $\mathbf{k} \rightarrow \mathbf{k} + \mathbf{q}$, where $\mathbf{q} \cdot (\mathbf{U} \pm \mathbf{V}_A) = 0$, so that, at least in three dimensions, the dispersion relation is not uniquely dependent on \mathbf{k} .

The two conditions on the frequencies and wave-vectors of the \mathbf{z}^+ and \mathbf{z}^- fluctuations which must be enforced in order to relegate “mixing” to higher order are that (i) they satisfy an exact dispersion relation, that is, one frequency for each wavenumber, and (ii) the two frequencies

are different enough to cause $\Lambda_{ij} = \langle z_i^{+*}(\mathbf{k}^+, \omega^+) z_j^-(\mathbf{k}^-, \omega^-) \rangle$ to be non-resonant, *i.e.*, small. Referring to equation (4.47), we can see that these conditions are violated in each of the following situations:

- (a) $\mathbf{k} \cdot \mathbf{V}_A \approx 0$, that is, when the wave-vectors are nearly perpendicular to the large-scale magnetic field, leading to near equality of ω^+ and ω^- .
- (b) $V_A/U \approx 0$, so that again $\omega^+ \approx \omega^-$. This is the weak magnetic field limit.
- (c) When wave-wave couplings are strong enough to disrupt the applicability of the (linear) dispersion relation; such situations arise in broadband turbulence for example.

As noted by *Zhou and Matthaeus [1990b]*, the crucial feature of cases (a) and (b), is that even when the fluctuations have wavelengths which are arbitrarily small, so that $\lambda/R \rightarrow 0$ (the usual condition for the applicability of WKB theory), there are situations in which the wave frequencies in the plasma frame are also small. However, for low wave frequencies, the frequency expansion parameter (*cf.* ϵ'_1 in *Zhou and Matthaeus [1990b]*) is not small, and it is inappropriate to use the standard leading order WKB transport equation.

In the following chapter we present solutions to the linear equations showing that when case (a) and/or (b) holds, results which are qualitatively different from those of (leading order) WKB theory ensue. Indeed, as either $\mathbf{k} \cdot \mathbf{V}_A$ or V_A/U moves away from zero, the solutions quickly approach those belonging to WKB theory. To see why this occurs, we may consider the coupling between the F and J equations. The terms of interest are those involving the factor $\mathbf{k} \cdot \mathbf{V}_A$. Ignoring the other terms, the transport equations are of the form

$$\frac{\partial F}{\partial t} - 2\mathbf{k} \cdot \mathbf{V}_A J = A, \quad (4.48)$$

$$\frac{\partial J}{\partial t} + 2\mathbf{k} \cdot \mathbf{V}_A F = 0, \quad (4.49)$$

where A represents the effects of “mixing” with P^\pm . These equations indicate that F and J tend to execute bounded oscillations with a frequency dependent on the “WKB enforcing factor,” $\mathbf{k} \cdot \mathbf{V}_A$; F oscillates about zero, and J about a positive value related to A . The approach towards WKB when $\mathbf{k} \cdot \mathbf{V}_A \not\approx 0$ can now be understood: the coupling between F and J keeps F close to zero (implying approximate equipartition of kinetic and magnetic energy, such as occurs in Alfvén waves). However, since the only linear coupling which occurs in the P^+ transport equation involves F , this drastically curtails the systems ability to generate “inward” fluctuations from “outward” ones. In effect, “mixing” is turned off in the presence of (parallel propagating) Alfvén waves because F is approximately zero.

Chapter 5

INERTIAL RANGE TRANSPORT

To penetrate the opaque depths of its innermost folds,
to pick out and immobilize the innumerable flutterings
that agitate it.

— Michel Eyquem de Montaigne

5.1 Introduction

The subject of this chapter is the radial evolution of solar wind fluctuations belonging to the MHD inertial range. A later chapter will be concerned with the analogous problem for the energy-containing range. We begin by considering the linear equations and discussing appropriate boundary conditions and initial data. Next a short discussion of the numerical techniques used to solve the equations is given. Following that, numerical and analytic solutions for the linear equations are presented. Finally, models for the inertial range non-linear terms are discussed.

5.2 The Linear Equations

For the next few sections we focus upon the properties of the linear terms in the transport equations, dropping all non-linear contributions. This should provide some insight into the transport of inertial range fluctuations in cases where the non-linear terms are either weak, or for states where the turbulence is fully developed (a.k.a. strong turbulence), since in this latter case there is no *net* spectral transport of the P^\pm fields in the inertial range, *i.e.*, $NL^\pm = 0$.

As noted at the end of section 4.2, we usually solve the equations for the omni-directional spectra, and, where appropriate, calculate the reduced spectra from them. However, for isotropic turbulence, direct solutions for the reduced spectra are also obtained. In all cases the solutions obtained may be put in a form suitable for comparison with observational data, and the underlying equations have the form

$$\frac{\partial P^\pm}{\partial t} + (U \mp V_{Ar}) \frac{\partial P^\pm}{\partial R} + \left(\frac{U \pm V_{Ar}}{R} \right) P^\pm + M^\pm F = 0, \quad (5.1)$$

$$\frac{\partial F}{\partial t} + U \frac{\partial F}{\partial R} + \frac{U}{R} F - (2\mathbf{k} \cdot \mathbf{V}_A) J + 2 [P^- M^+ + P^+ M^-] = 0, \quad (5.2)$$

$$\frac{\partial J}{\partial t} + U \frac{\partial J}{\partial R} + \frac{U}{R} J + (2\mathbf{k} \cdot \mathbf{V}_A) F = 0, \quad (5.3)$$

where as discussed in section 4.3, we are assuming particular forms for the large-scale fields.

As shown in Chapter 3, when the turbulence is isotropic (in two or three dimensions), J is identically zero and the above equations reduce to a three equation model. Since we are also assuming that the velocity helicity and magnetic helicity are zero, the model is complete in the sense that we are following the evolution of three independent scalar functions, and this is precisely how many such functions there are for completely mirror symmetric, isotropic turbulence.

The inner boundary position, $R = R_0$, is usually chosen to correspond to 10 solar radii, and often further interpreted as the Alfvénic critical radius, R_c , where the decreasing (radial) Alfvén velocity becomes equal to the (radial) flow velocity. In order to compute solutions to equations (5.1)–(5.3), a single (inner) boundary condition must be supplied for each field. Consider the behavior of fluctuations near the Alfvénic critical radius. Fluctuations that are purely P^+ or P^- have traditionally been identified as Alfvénic disturbances propagating along the mean magnetic field in one direction only. For example, $P^+ = 0$ implies $\mathbf{b} = -\mathbf{v}$, which is appropriate for Alfvén waves traveling parallel to the mean magnetic field. Thus, for B_{0r} positive, only waves moving outward from the sun will exist. Similarly, $P^- = 0$ describes purely inward traveling waves. While these disturbances move sunward in the rest frame of the outflowing plasma, in the sun’s reference frame net propagation is radially outward for super-Alfvénic flow, though clearly slower than for outward moving waves. Thus, in both the sub- and super-Alfvénic flow regions, inward traveling waves propagate away from the Alfvénic point. Therefore in this traditional picture, unless inward traveling disturbances are produced *at* the critical point, only outward traveling fluctuations can exist there. Note, however, that *Hollweg* [1990] has recently challenged this view by showing that the standard WKB expansion is not uniformly convergent. He concludes that a finite admixture of inward propagating waves should be expected even at the critical radius. Boundary conditions corresponding to purely “outward” fluctuations in the traditional sense, *i.e.*, $P_0^+ = F_0 = J_0 = 0$, $P_0^- > 0$, are referred to as “standard.” As before, the zero subscript indicates evaluation at R_0 . Non-zero boundary conditions on P^+ , F , and J have also been investigated.

A major objective of the following subsections will be to show some of the circumstances for which “mixing” effects are important. In this context we will sometimes refer to the “mixing” effects as *strong*, meaning that the solutions obtained under the specified conditions are significantly different from the leading order WKB ones with “standard” boundary conditions. Similarly, *weak* will indicate that “mixing” effects are relatively unimportant, and thus that the solutions are close to the WKB forms.

Steady-state solutions to equations (5.1)–(5.3) depend on the large-scale speeds only through the three ratios V_{Ar0}/U , $|\hat{\mathbf{k}} \cdot \mathbf{V}_A|/U$, and $\Omega R_0/U$, the latter quantity determining the degree of winding of the magnetic field (section 4.3). For isotropic turbulence, only the first ratio comes into play, so that the solutions are essentially independent of the absolute values of U and \mathbf{V}_A . For the linear equations, we will only present solutions for one value of U , namely 400 km/sec. Values of V_{Ar0}/U used lie between 0 and 1 inclusive. When $V_{Ar0}/U = 0$ there is no large-scale magnetic field present, so that conditions are similar to those which would exist in a planar current sheet. At the other extreme, when $V_{Ar0}/U = 1$ the inner boundary corresponds to an Alfvénic critical radius. Intermediate values may be interpreted as the inner boundary lying beyond this critical radius.

Examination of the transport equations (5.1) for P^\pm shows that when $V_{Ar0} = U$, near the critical point the behavior of the coefficients for the advection and expansion terms is quite different for the “inward” and “outward” fields. More specifically, in this region the “outward” modes undergo strong advection but relatively weak expansion, while the situation is reversed for “inward” fluctuations. Speaking very loosely, the growing bubbles of “inward” modes are left behind by jets of “outward” fluctuations.

In the limit that V_A/U approaches zero, analytic solutions for the steady case may be obtained. Their derivation is outlined in Appendix D, for turbulence which is isotropic, 2D, or slab. For the isotropic case such solutions were first obtained by *Zhou and Matthaeus [1990a]*. We defer discussion of the analytic solutions to the sections dealing with the numerical results.

We will present solutions to the linear equations using plots of the spectral amplitudes of quantities such as P^\pm and σ_c . For isotropic and 2D turbulence, the spectral amplitude is evaluated at a fixed but arbitrary inertial range wavenumber. The figure captions in the following subsections will not necessarily make this explicit; however, it should always be understood that this is the case. It is possible to present the plots in this way because for turbulence of these types there is no explicit k dependence in the linear equations. In contrast, the slab geometry is k dependent at the linear level, and so the particular inertial range wavenumber used is important.

Two useful quantities to plot are the *normalized cross helicity* σ_c , and the *normalized energy difference* σ_D . These quantities have been discussed in the earlier chapters; however, we remind the reader that the former is interpretable as a measure of the relative abundances of “inward” and “outward” modes, the extremal values $\sigma_c = \pm 1$ corresponding to purely “outward” and purely “inward” waves respectively. It is also the normalized correlation coefficient for $\mathbf{v} \cdot \mathbf{b}$, so that it conveys information on the degree of alignment existing between the small-scale fields.

The normalized energy difference is, as its name suggests, the ratio of the difference in kinetic and magnetic energy to their sum. The same information is contained in the *Alfvén ratio*, $r_A = E^v/E^b$; however, the bounded character of σ_D makes it a more convenient quantity to plot. Many of the numerical results will be presented and discussed in terms of σ_c and σ_D .

5.2.1 Numerics

In order to solve the equations we have, in most cases, resorted to numerical techniques. Readers not interested in the numerical particulars may safely skip this section. The time dependent transport equations are solved using a spectral method [Gottlieb and Orszag, 1977; Canuto *et al.*, 1988], in which the radial dependence of the fields is expanded in terms of a finite number of Chebyshev polynomials. For various reasons, we wished to use a spectral method, and since Chebyshev techniques

- (a) support arbitrary boundary conditions, while still retaining the spectral method property of exponential convergence to the solutions as the number of retained modes is increased,
- (b) have practical fast (cosine) transforms available,
- (c) have a maximum pointwise error which is close to the smallest one achievable using any polynomial expansion of the same order, and
- (d) exhibit inherently high resolution near the boundaries—a consequence of the clustering of computational points near the ends of the domain,

they were the natural choice for our purposes.

The Chebyshev polynomial of degree $n = 0, 1, 2, \dots$, is defined by $T_n(y) = \cos n\theta$, where $y = \cos \theta$, and θ is an auxiliary variable which has no relationship to the heliocentric coordinate of the same designation. Clearly the domain of the Chebyshev polynomials is $y \in [-1, 1]$. Typically one keeps the first $N+1$ modes, numbered 0 through N , where for transform purposes N is usually chosen as a power of two. For example, $P^+(R, t)$ might be represented by

$$P^+(R, t) = \sum_{n=0}^N a_n(t) T_n, \quad (5.4)$$

where for the moment we are ignoring the necessity of mapping R onto the domain of the Chebyshev's.

By performing such expansions in the eigenfunctions of singular Sturm-Liouville operators (*e.g.*, Fourier series, Chebyshev polynomials), pde's may be converted into sets of ode's in the

remaining independent variable t . The time integration can then be performed using one of the standard finite differencing methods, *e.g.*, Runge-Kutta (RK) or Adams-Bashforth (AB). Implicit or semi-implicit time stepping methods may also be used [Gottlieb and Orszag, 1977; Canuto *et al.*, 1988]. For reasons to be discussed below, time integration was usually performed using an explicit first order method.

The defining property of the spectral method we use, known as *collocation* or pseudospectral [Gottlieb and Orszag, 1977; Canuto *et al.*, 1988], is that at *each* of the $N + 1$ collocation (grid) points, the approximation to the true solution satisfies its governing differential equation, and the boundary conditions, *exactly*. Thus, the computed solution is an N th order interpolant of the true solution. Most of our simulations were performed with relatively modest values of N —either 64 or 128. When compared to the available analytic solutions, such resolutions produced numerical solutions of ample accuracy. Furthermore, the smoothness of all the (linear) isotropic and 2D solutions suggested that higher resolutions were unnecessary. The Alfvén waves associated with slab turbulence often demanded higher spatial resolution, and where necessary such runs were performed. For the transport problems we consider in this chapter and the next, it is only necessary to impose boundary conditions at the inner boundary (R_0). Since the flow is everywhere supersonic, information only flows outwards.

We now return to the issue of mapping. As the Chebyshev's are defined on the domain $y \in [-1, 1]$, it is necessary to map $R \in [R_0, \infty)$ onto this domain. For later convenience, we normalize R by R_0 , so that its range becomes $[1, \infty)$. We have experimented with two distinct types of mapping, in both cases making the standard choice for the collocation points in y -space. These *Gauss-Lobatto* (G-L) points, which are equally spaced in θ , are defined by

$$y_j = \cos\left(\frac{\pi j}{N}\right), \quad (5.5)$$

where N is the degree of the highest Chebyshev polynomial retained, as defined above. The equal spacing in θ means that the collocation points cluster near the extremal values of y , their spacing being $O(1/N^2)$ in these regions. The distribution is sparsest around $y = 0$. An example for $N = 32$ is shown in Figure 5.1.

The first mapping is a semi-infinite algebraic transformation, involving a parameter L , which is such that approximately half the collocation points lie in the range $[1, L]$. In production runs, L was almost always chosen to correspond to 1 AU. The mapped and unmapped variables are related by

$$R = L \frac{1 + y + 2/L}{1 - y}, \quad (5.6)$$

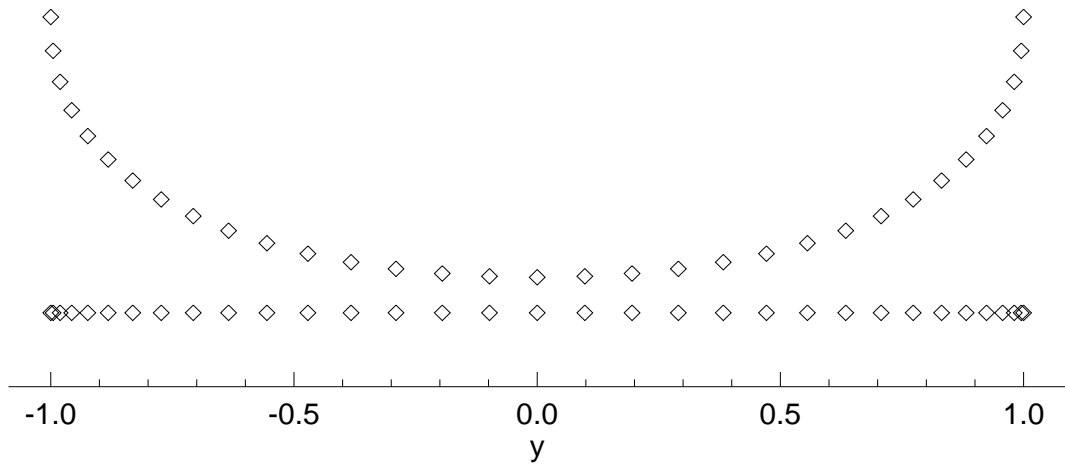


Figure 5.1: Diagram showing the distribution of the Gauss-Lobatto collocation points in the natural domain of the Chebyshev polynomials when $N = 32$. The “necklace” of diamonds shows the same information as the horizontal set, the only difference being that neighboring collocation points have been vertically offset. This vertical displacement is provided solely for clarity and has no intrinsic meaning.

$$y = \frac{R - L - 2}{R + L}. \quad (5.7)$$

This mapping has the advantage that it covers the entire domain of R , but, since we are mostly interested in the evolution occurring in the inner heliosphere, many of the grid points beyond a few AU are “wasted.” No special boundary conditions need be imposed at $R = \infty$ ($y = +1$) with this mapping. The nature of the G-L collocation points means that R -space is most highly resolved near R_0 ; as this is also the region where the solutions show the most structure, resolution of this nature is desirable. Figure 5.2(a) illustrates this mapping, in R -space, when $N = 32$.

The second choice is a finite algebraic mapping from $R \in [1, L]$ to the Chebyshev domain, where L is now the outer boundary. In this case the independent variables are related by

$$R = \frac{(L - 1)y + (L + 1)}{2}, \quad (5.8)$$

$$y = \frac{2R - L - 1}{L - 1}. \quad (5.9)$$

Thus all the grid points lie in a finite region of the heliosphere, with denser clustering at the extremes, as shown in Figure 5.2(b) for the case $N = 32$. The linear nature of this mapping is also evident in the similarity of Figures 5.1 and 5.2(b).

Solutions obtained using the different types of mappings are in excellent agreement in the regions of R -space in which they overlap. With the exception of section 5.2.2.1, most of the results

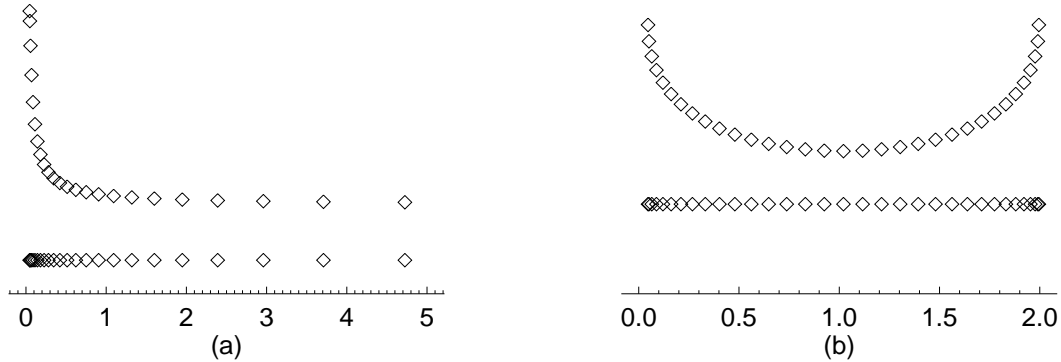


Figure 5.2: Example plots showing the distributions of the Gauss-Lobatto points in R -space for each of the two types of mapping considered in the text. (a) Semi-infinite mapping with $L \equiv 1$ AU; (b) Finite mapping with $L \equiv 2$ AU. For pictorial clarity, $N = 32$ is used, a value which is much lower than the resolutions used in the production runs. The horizontal coordinate is R in units of AU. Note that in (a), only the points inside 5 AU are shown. See also Figure 5.1.

presented below are from codes using finite mappings.

Note that since each mapping is a change of variable, it follows that, in general, the coefficients in the de's will also be modified. In fact, constant coefficients in front of derivatives are likely to become y dependent. This additional complexity is not difficult to deal with numerically: the coefficients may be evaluated and stored before the time integration is started, and then referenced as necessary.

One of the advantages of spectral methods is that it is possible to work either in coordinate space, transform space, or both. With collocation methods all of the calculations may be performed in coordinate space; however, when evaluating derivatives it is often more efficient to move to the transform space, form the derivative and then transform back, rather than using the coordinate space direct matrix multiply method. We employ such a transform technique, based on the routines listed in *Canuto et al.* [1988].

The flip-side of the coin is that in order to assure stability, Chebyshev spectral techniques often require extremely small timesteps (Δt) to be used with explicit methods. Usually where spectral methods are concerned, the stability of an explicit scheme implies accuracy [Gottlieb and Orszag, 1977]. Let the degree of the maximum spatial derivative appearing in the de(s) be m , then for explicit methods the stability criterion is usually something like $\Delta t \lesssim 1/N^{2m}$, which may be heuristically derived using the CFL condition [Gottlieb and Orszag, 1977]. Fortunately, in our

transport equations m is only equal to 1. Still, given this restriction it would seem unnecessary to introduce the additional computational expense of a high order time-stepping scheme (\gtrsim a factor of 2), and we therefore use first-order Euler integration.

For isotropic and 2D turbulence, the solutions are integrated in time until steady-state solutions of sufficient accuracy are obtained; typically this takes 1 to $1\frac{1}{2}$ “box crossings” for the finite mapping algorithms. For slab codes the integration is carried out for a similar number of timesteps; the waves associated with slab turbulence pre-empting the existence of a true steady-state. The codes may also be run using a second order RK integration algorithm and for testing purposes this has been done.

Further testing of the codes used to solve the linear equations included

- (a) Setting $\Delta t = 0$ and counting the number of timesteps for which the initial conditions are propagated through the code without change. Typically this number was in excess of 100,000 for single precision codes.
- (b) Comparison of the numerical solutions with available analytic ones. Each of the three types of turbulence we consider admits analytic solutions when both V_A and the non-linear terms are zero. The codes faithfully reproduce these solutions at the lowest production resolution used ($N = 64$, $\Delta t = 6/N^2$). For codes using the infinite mapping, relative errors near the inner boundary are typically $\sim 10^{-6}$, increasing to $\sim 10^{-2}$ at about $2/3$ of the propagation distance. For finite mappings, the maximum relative error in the entire domain after $1\frac{1}{2}$ box crossings is typically $\sim 10^{-4}$.
- (c) For isotropic turbulence, an independent numerical method, involving integration along the characteristics of the equations, was also used. Solutions obtained from the two methods are in excellent agreement, and visually indistinguishable when plotted as functions of the heliocentric distance R .

The methods associated with calculation of the modeled non-linear terms also warrant some comment. For non-linear terms which are not modeled as derivatives in k -space, for example all of those in the energy-containing models, and those for F in the inertial range models, evaluation is straightforward. The appropriate terms are just directly constructed in y -space, using the field values from the previous timestep. For conserved quantities, such as P^\pm [*e.g.*, Zhou and Matthaeus, 1990c], the non-linear terms contain k -space derivatives of energy fluxes. Such derivatives are calculated using finite difference methods. Specifically we use centered differences at the interior points, and 3-point forward or backward differences at the endpoints, so that second order accuracy

is obtained at all grid points. Because we are interested in the spectral evolution of the inertial range, which extends over multiple decades in k -space, for computational efficiency we use grid points whose logarithms are equally spaced. In other words, each spectral decade contains the same number of grid points, typically around 20 in the production runs (testing with up to 50 points per decade was performed in order to verify the adequacy of the lower resolution). Further discussion on the numerics associated with the non-linear terms may be found in section 5.3.

In an attempt to conform to modern software philosophies, the codes are well commented and rather modular. As such, third parties should find them relatively easy to modify. All the codes run without source change under the VMS, Ultrix, and Unicos (San Diego Supercomputing Center Cray Y/MP) operating systems. Single precision arithmetic is used in most cases.

When running the code, a suite of input parameters must be supplied. These include the positions of the inner (and outer) boundaries, (inner) boundary conditions for each field, and values for U , V_{Ar0} , k , and Δt (*cf.* section 4.3). Support for time dependent boundary conditions is also included in the codes, but for our purposes use of this feature was not essential.

5.2.2 Isotropic Fluctuations

We now consider actual solutions to the linear equations. In this subsection those appropriate for isotropic turbulence are presented and discussed. As mentioned above, for this case direct solutions will be presented for both reduced and omni-directional spectra. By isotropic turbulence we mean that the fluctuations feel no preferred directions, so that the correlation functions and spectra exhibit complete rotational symmetry (see Chapter 3). We are also assuming that neither velocity helicity nor magnetic helicity is present.

We have already noted that J is zero for isotropic turbulence so that there are only three coupled transport equations to solve. Furthermore, the vanishing of J permanently nullifies the influence of the WKB enforcing terms ($\sim \mathbf{k} \cdot \mathbf{V}_A$), so that “mixing” is expected to play an influential role (see sections 4.4 and 4.5). Note also, that in this incarnation of the equations, there is no explicit k dependence to either the equations or the solutions. Such dependence will reappear when the non-linear terms are reinstated.

5.2.2.1 Reduced Spectra

When the modal spectra are integrated over all directions perpendicular to the radial direction, we are left with reduced spectra (see section 4.3). These are of the same form as those obtainable from single spacecraft data, so that solving the transport equations for such spectra supports immediate comparison with the observational data. As discussed in section 4.3 and

Appendix C, we assume that the inertial range spectra follow a powerlaw in wavenumber, with spectral slope α , that is, that they are proportional to $k_1^{-\alpha}$. At this level of approximation, α is the only parameter which characterizes the turbulence.¹ Of course the structure of real spectra is more complicated than a simple powerlaw, but this approximation is a useful starting point. Solutions for four values of α have been investigated, namely $\alpha = 1$, $\frac{3}{2}$, $\frac{5}{3}$, and 2. These values approximately span the range of observed spectral slopes [*Sari and Valley*, 1976; *Bieber et al.*, 1993a]. As is well known $\alpha = \frac{3}{2}$ is the value appropriate for the Kraichnan spectrum obtained in the presence of a strong magnetic field [*Kraichnan*, 1965], and $\alpha = \frac{5}{3}$ is applicable for *Kolmogorov* [1941] hydrodynamic turbulence. *Matthaeus and Zhou* [1989a] have recently shown how to smoothly move between these two limits.

Figure 5.3 shows the influence of the ratio V_{Ar0}/U on the linear solutions. The plots depict the radial evolution of the reduced spectral amplitudes (at a fixed but arbitrary inertial range wavenumber) for the “standard” critical point boundary conditions when $V_{Ar0}/U = 0$ (dashed curves) and 1 (solid curves); α has the Kolmogorov value of $\frac{5}{3}$ and $R_0 = 10 R_{sun}$. As noted above, an analytic (time-steady) solution for the $\mathbf{V}_A = 0$ case has previously been derived [*Zhou and Matthaeus* 1990a], and this provided a useful test of our numerical accuracy.

While substantial differences exist between the two sets of solutions shown in the figure, beyond a tenth of an AU the general trends are the same for both cases. In particular, the normalized cross helicity decays with heliocentric distance, and the normalized energy difference appears to be leveling off at a more or less constant negative value, indicating an excess of magnetic energy over kinetic. Both of these features are in qualitative agreement with the behavior seen in observational data. The behavior of the analytic solutions (holding when $V_{Ar0}/U = 0$), has captured the essence of solutions for the more general cases where $V_{Ar0}/U \neq 0$.

Within the first few tens of solar radii, however, the solutions are qualitatively different. The different form for M^+ in each case is responsible for the distinctions. From section 4.4, the appropriate forms for the effective mixing operators are

$$M_{iso}^{\pm} = \frac{\alpha}{\alpha + 2} \frac{1}{2R} \left[U \mp \left(\frac{4}{\alpha} - 1 \right) \frac{V_{Ar0}}{R} \right],$$

where R is measured in units of R_0 . As discussed above, M^+ undergoes a sign change when

$$R = \left(\frac{4}{\alpha} - 1 \right) \frac{V_{Ar0}}{U},$$

¹ We do not consider the amplitude, which is set by the steady-state energy flux in k -space, as a parameter here, since the equations are linear, and thus solutions arbitrary to within an overall multiplying constant.

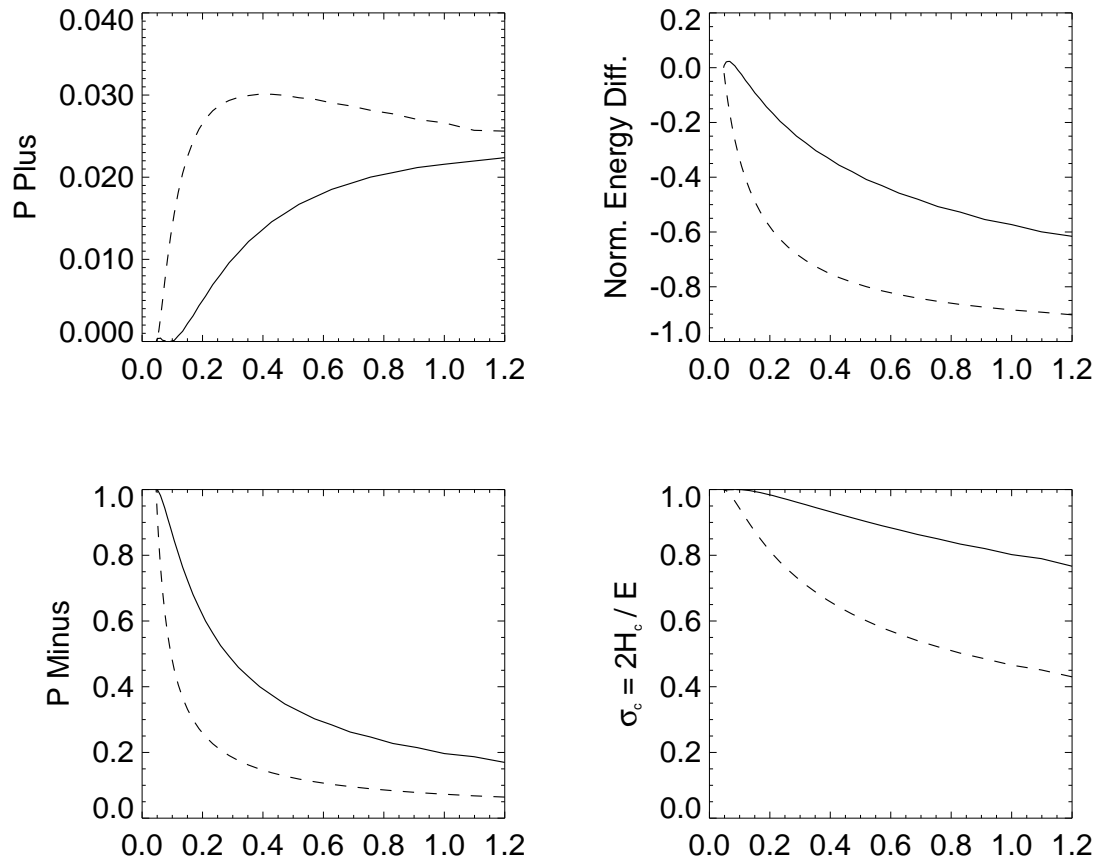


Figure 5.3: The effect of V_A on the radial evolution of the reduced spectra for isotropic turbulence. The quantities plotted are spectral amplitudes at a fixed but arbitrary inertial range wavenumber. The horizontal coordinates are all heliocentric distance in AU. The solar wind speed is 400 km/sec, $R_0 = 10 R_{sun}$, $\alpha = \frac{5}{3}$, and “standard” boundary conditions are imposed. The solid curves are for $V_{Ar0} = U$, and the dashed for $V_{Ar0} = 0$. See also the next two figures.

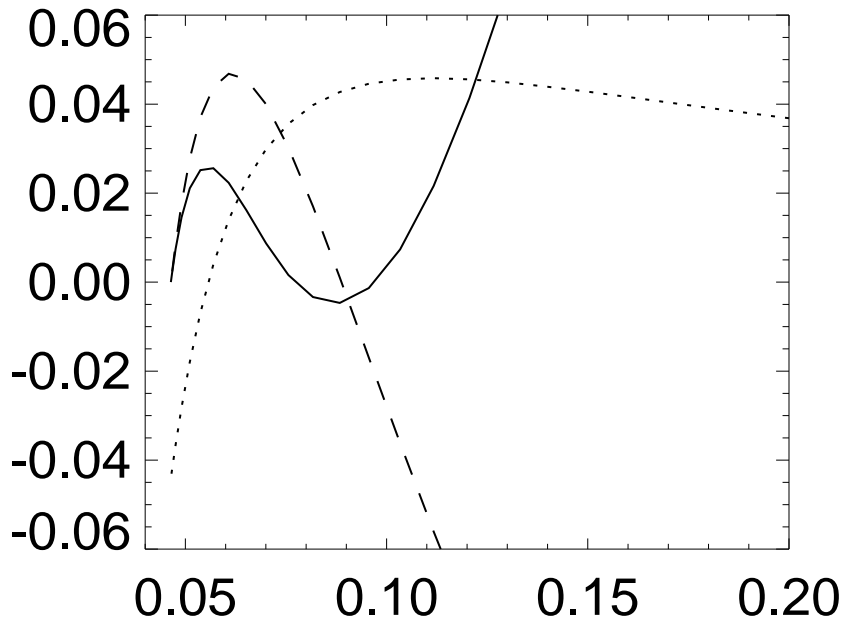


Figure 5.4: Expanded view of the region in which the M^+ operator for isotropic turbulence changes sign. Solid curve: P^+ , dashed curve: F , dotted curve: M^+ . The horizontal coordinate is heliocentric distance (AU), and for clarity the vertical scalings have been adjusted. The growth (decay) of P^+ when F and M^+ have opposite (same) signs is evident.

a distance which decreases with increasing α . Of course when $V_{Ar0} = 0$, M^+ is always non-negative. Consider first this latter case. Referring to equations (5.1) and (5.2), we can see that $M_0^+ > 0$ and $P_0^- > 0$ drives F negative just above R_0 (from its initial negative value). The coupling of P^+ to F , via M^+ , then drives P^+ towards larger positive values. As we move radially outwards, this interplay continues, but the strength of the effect diminishes because M^\pm generally decay with increasing R .

For the other case, when $V_{Ar0}/U = 1$, M^+ is negative for the first few R_0 , and consequently F is driven positive. As long as M^+ and F are of opposite sign, the coupling between P^+ and F still acts to drive P^+ positive (Figure 5.4). However, when M^+ changes sign, it takes a short distance for the energy difference to “catch up” and also change sign. During this period, F and M^+ act to drive P^+ towards smaller values, thus undoing at least some of its earlier growth. By the time F and M^+ are back in phase, the magnitude of M^+ has decreased enough to prevent P^+ from attaining levels as high as those occurring when $V_A = 0$.

This is all in accordance with the discussion given in section 4.5, where it was argued that “mixing” becomes more important as V_A/U decreases towards zero. Solutions for intermediate

values of this parameter have also been computed, and, as expected, they lie between those shown in Figure 5.3.

The influence of the spectral slope on the solutions is shown in Figure 5.5, again for cases with “standard” boundary conditions and $R_0 = 10 R_{sun}$. The large-scale speeds are equal at the boundary ($U = V_{Ar0} = 400$ km/sec). It is clear from the figure that steeper spectral slopes are associated with stronger “mixing,” in the sense that at a given heliocentric distance, increasing α moves the solutions further away from the WKB ones.² Mathematically the reasons for this behavior are easy to understand, again by considering the form of the effective mixing operators: increasing α (a) increases the magnitude of the multiplying constant attached to the M^\pm , and (b) pushes the distance at which M^+ crosses through zero closer to R_0 . This second effect means that the second growth spurt for P^+ is associated with bigger values of the R dependent mixing operators (see also the figures in section 4.4). Similar results are obtained for other values of V_{Ar0}/U .

For isotropic turbulence, choosing a different value for R_0 merely rescales the radial axis. Thus, for runs which differ only in the value of R_0 used, the solution curves are identical, but the value at a particular physical distance changes. When $R_0 = 20 R_{sun}$, for example, the distance scales in Figures 5.3–5.5 must all be doubled, leading to reduced “mixing” at a given heliocentric distance. Physically this reduction occurs because as the Alfvénic critical point is moved outwards, the distance between it and a fixed observation point decreases, so that the turbulence has less time to evolve en route between the two points—we are sampling “younger” turbulence.

5.2.2.2 Omni-Directional Spectra

We now consider solutions for isotropic turbulence obtained in terms of omni-directional spectra. The mixing operators for this case are qualitatively the same as those appropriate for use with reduced spectra, so that essentially the same evolutionary trends in the solutions are seen (see equations (4.40) and (4.37)). As discussed in Appendix C, assuming that the omni-directional spectrum is a powerlaw in wavenumber ($k^{-\alpha}$), leads to a reduced spectrum equivalent to $\frac{1}{2\alpha}$ times the omni-directional spectrum evaluated at $k = k_1$ (equation (C.16)). It follows that normalized quantities, such as σ_c and the Alfvén ratio, look the same in both cases since the $\frac{1}{2\alpha}$ factors cancel. On the other hand, for a given wavenumber, the raw spectral density levels are lowered for the reduced spectra relative to the omni-directional ones. Because, for isotropic turbulence,

² Recall that the leading order WKB solution for these boundary conditions is $P^- \propto 1/R$, and $P^+ = F = 0$. Thus, beyond the critical point, $\sigma_c = +1$, independent of distance.

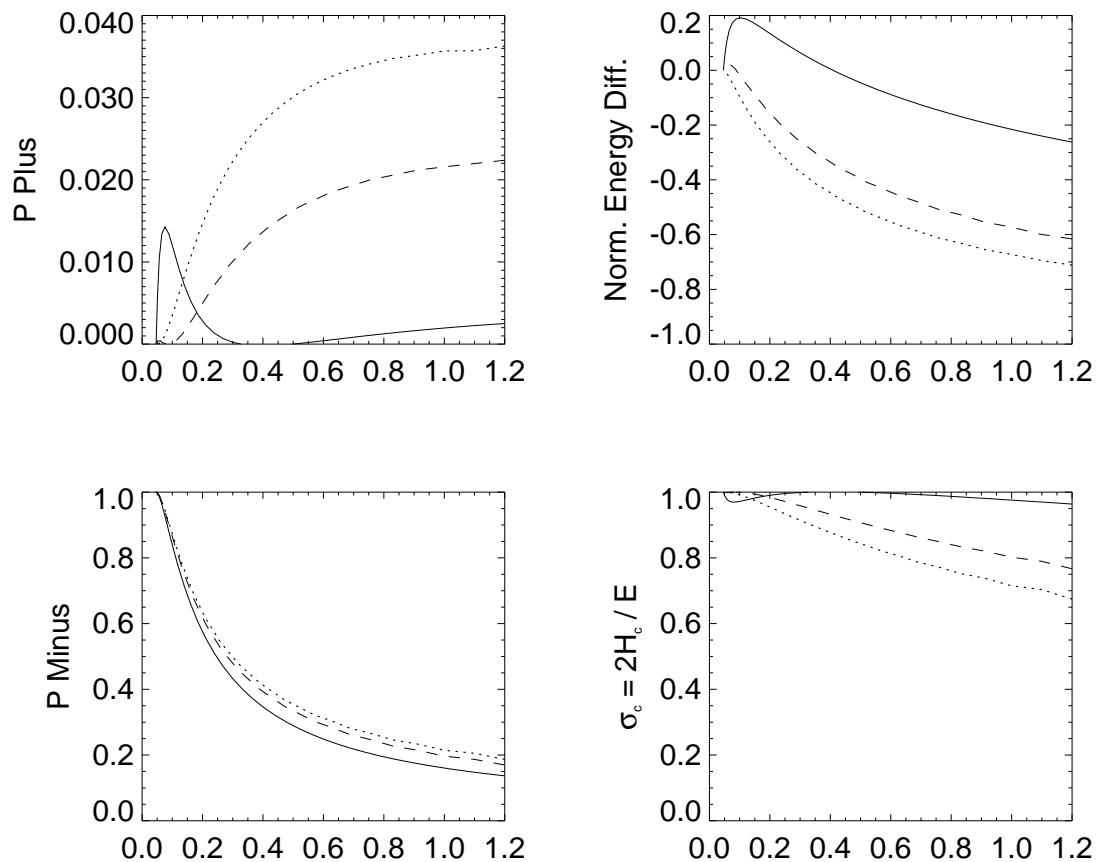


Figure 5.5: Radial evolution of the directly calculated reduced spectral amplitudes for isotropic turbulence. Shown are P^\pm , the normalized energy difference, and the normalized cross helicity when $U = V_{Ar0} = 400$ km/sec. The solid curves are for $\alpha = 1$, the dashed for $\alpha = \frac{5}{3}$, and the dotted for $\alpha = 2$. The inner boundary is at 10 solar radii. “Standard” boundary conditions apply. Horizontal coordinates are heliocentric distance in AU.

the relationship between the two spectral forms is so simple, we will not show plots of the reduced spectral amplitudes derived from the numerically computed omnidirectional forms.

Figure 5.6 shows omnidirectional spectral amplitudes for the two cases $V_{Ar0}/U = 0$ and 1. “Standard” boundary conditions are in place and $R_0 = 10 R_{sun}$. The similarity to the directly computed reduced spectral densities is evident. Clearly, when $V_{Ar0}/U = 1$ (or more generally when it is big enough to cause a sign change in M^+), there is a strong tendency for the turbulence to contain a sizable excess of small-scale kinetic energy just above the critical point ($r_A \approx 1.5$). However, within a few critical radii the situation reverses and magnetic energy is favored at inertial range scales ($r_A \approx 0.5$).

Since the turbulence is isotropic, the reader may have suspected that solutions obtained in this section and the previous one would be equivalent (for the same parameters), and indeed that there would be complete equality of the two—independently computed—reduced spectra. In fact this is not the case, largely because the full mixing tensors are non-isotropic, and thus the transport equations break the assumed symmetry of the small-scale turbulence. If we consider each field, then its diagonal components (*e.g.*, F_{11} , F_{22} , F_{33}) obey differential equations which are in general distinct, so that speaking colloquially, “different things happens to different components.” However, despite the large-scale anisotropies, we are still insisting on the small-scale turbulence being isotropic, and therefore following the trace is not equivalent to separately following its three components and then adding the results together. We will say no more about this large-scale breakage of the imposed small-scale symmetries.

As far as non-“standard” boundary conditions are concerned, the equations are relatively insensitive to the value chosen for the “inward” boundary condition, provided the energy difference at R_0 is still held at zero. For such conditions, choosing P_0^+ larger than about half a percent of P_0^- causes P^+ to immediately plummet to a value which is approximately the same one it has when P_0^+ is zero, *i.e.*, enforced equipartition of the small-scale energy at R_c is associated with at most a tiny fraction ($\sim 10^{-3}$) of “inward” type modes relative to “outward” ones just above the critical point. The subsequent evolution of P^+ is practically indistinguishable from that occurring when $P_0^+ = 0$.

When the equipartition restriction at R_c is relaxed, however, visible changes in the radial evolution of the fields ensue. The choice of F is not completely arbitrary for such cases, since the energy difference is constrained by several inequalities. First, using the definition of F (section 4.2) and the Schwartz inequality it can be shown that $|F| \leq 2\sqrt{P^+P^-}$. Second, since the energy difference cannot be greater than the total energy we must also have $|F| \leq P^+ + P^-$. Figure 5.7

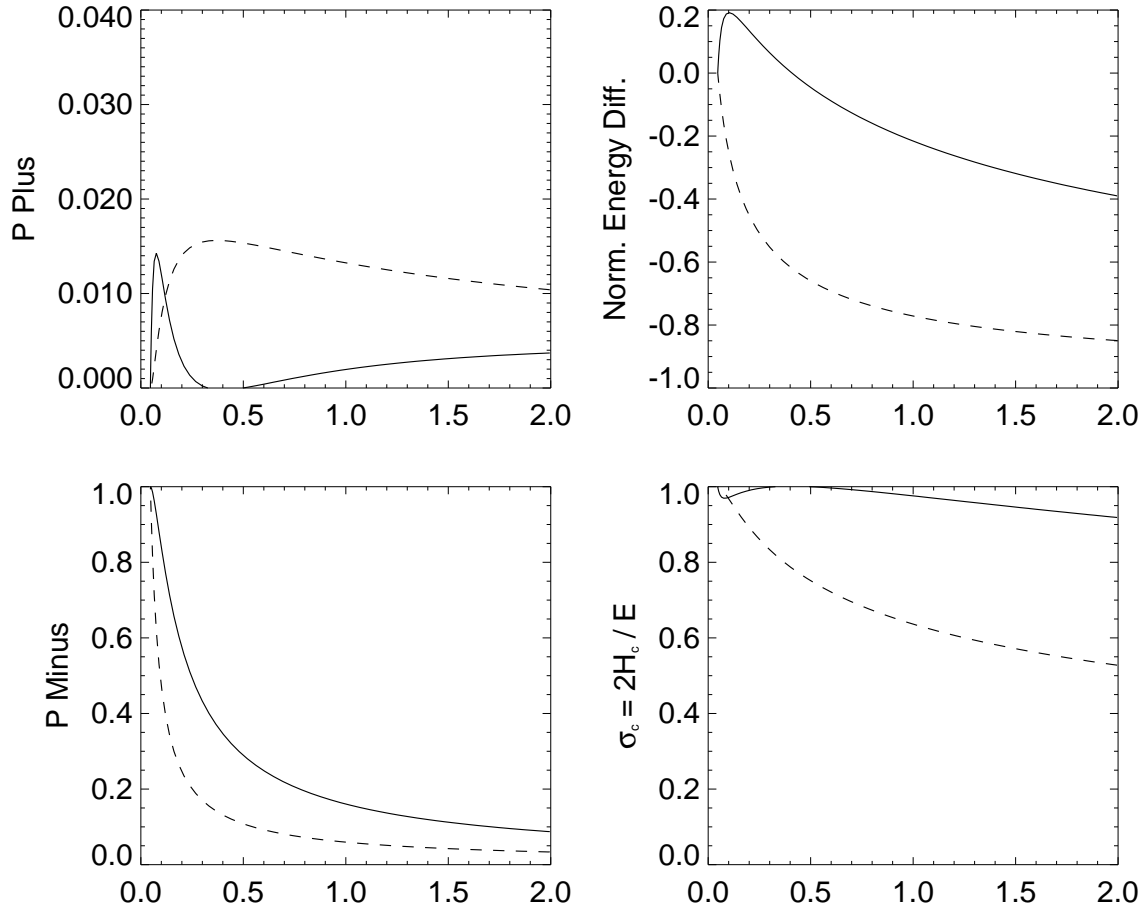


Figure 5.6: Radial evolution of the various omnidirectional spectral densities for isotropic turbulence (at fixed inertial range wavenumber). “Standard” boundary conditions are imposed and $R_0 = 10 R_{sun}$. The horizontal coordinate is heliocentric distance (AU). Solid curves: $V_{Ar0}/U = 1$. Dashed curves: $V_{Ar0}/U = 0$.

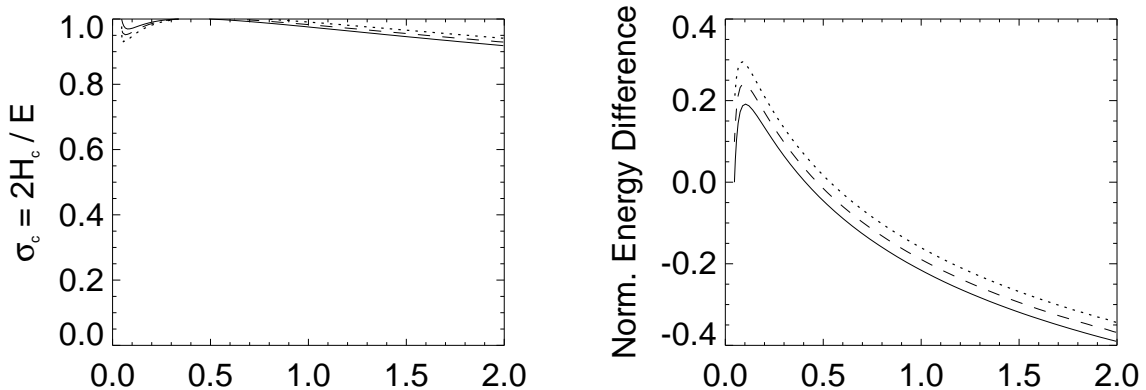


Figure 5.7: Radial evolution of the normalized cross helicity and normalized energy difference of isotropic turbulence for some non-“standard” boundary conditions (spectral amplitude at fixed wavenumber). In each case $R_0 = 10 R_{sun}$, and $V_{Ar0} = U$. The evolution for two initial values of F is shown when $P^+ = 0.01$, $P^- = 1$: $F = 0.1$ (dashed curve), $F = 0.2$ (dotted curve). The solid curves are the solutions for “standard” boundary conditions. Solutions for $P_0^+ = 0.01$, $P_0^- = 1$, and $F_0 = 0$, are visually indistinguishable from the “standard” case when plotted at this scale. The horizontal coordinate is heliocentric distance (AU).

shows the situation for $P_0^+ = 0.01$, $P_0^- = 1$, and two choices of F_0 , namely 0.1 and 0.2, the latter number being F_0 ’s maximum allowed value for these conditions. While negative values of F_0 are not ruled out mathematically, it is the case that the equations tend to drive F positive in this region, and we have therefore elected not to investigate these cases. It can be seen that for fixed P_0^\pm , increasing the kinetic energy excess at the boundary leads to mildly weaker “mixing” at a given heliocentric distance, with no significant change in the evolutionary trends.

5.2.3 Two-Dimensional Fluctuations

As noted in section 3.6, we define 2D turbulence by the following properties: (a) $\mathbf{k} \perp \mathbf{B}_0$, (b) the fluctuations are perpendicular to both \mathbf{k} and \mathbf{B}_0 , and (c) the fluctuations are distributed isotropically in the planes normal to \mathbf{B}_0 . In general we will also assume that the spectra follow a powerlaw in wavenumber, with spectral index α (see the preceding section). As a consequence of this geometry $\mathbf{k} \cdot \mathbf{V}_A \equiv 0$, ensuring that F and J are decoupled, and thence that “mixing” is always strong. It is also the case that J is identically zero, for reasons which are essentially the same as those applying in the fully isotropic case (see also section 3.5).

Results from simulation studies of incompressible 2D MHD turbulence with a mean magnetic field (\mathbf{B}_0) present, have shown that in such geometries, energy is transferred to the perpendicular

wave-vector components of the fluctuations much more rapidly than it is to the parallel ones [Shebalin *et al.*, 1983]. In other words the 2-D spectrum “switches on” first. This suggests that 2D fluctuations may be relevant to the solar wind system with its approximately Parker spiral \mathbf{B}_0 . Indeed, there is also some observational evidence that the solar wind can be modeled as an admixture of slab ($\mathbf{k} \parallel \mathbf{B}_0$) and 2-D fluctuations [Matthaeus *et al.*, 1990], a possibility we consider further below.

Furthermore, the theoretical analysis of nearly incompressible MHD turbulence [Zank and Matthaeus, 1992a, b, 1993], also suggests that when the plasma beta is of order unity (as it is in much of the solar wind), the turbulence may consist of two components: (1) Alfvén waves propagating along \mathbf{B}_0 , and (2) incompressible 2D MHD turbulence in the planes perpendicular to \mathbf{B}_0 . In the solar wind such 2D planes would be advected outwards by the supersonic flow.³ At higher orders, non-linear interactions between the two components can also occur [Zank and Matthaeus, 1992b, 1993].

Analytic solutions are again available for the strong “mixing” situation $V_{Ar0}/U = 0$, and these are derived in Appendix D. As can be seen in the figures presented below, the analytic solutions have again captured the essence of solutions applying in the more general case ($V_{Ar0}/U \neq 0$). Note that even when $V_{Ar0} = 0$, the field winding angle $\psi(\mathbf{R})$ is still well defined and non-zero (section 4.3). In fact, for our choice of \mathbf{V}_A , ψ is independent of V_{Ar0} . For the $V_{Ar0} = 0$ case, we may interpret ψ as the angle between the radial direction and a “ghost” Parker spiral field, which otherwise has no influence on the dynamics.

As shown in Appendix C, for 2D turbulence the relation between the reduced and omnidirectional spectra is

$$\begin{aligned} Q^{red}(k_1) &= \frac{I(\alpha)}{\pi \sin \psi} Q^{omni} \left(\frac{k_1}{\sin \psi} \right) \\ &= \frac{I(\alpha) \sin^{\alpha-1} \psi}{\pi} Q^{omni}(k_1), \end{aligned} \quad (5.10)$$

where k_1 is equivalent to the radial component of \mathbf{k} , and $I(\alpha)$ is a pure number. In the first line, the argument of the omnidirectional spectrum, $k_1/\sin \psi$, may be interpreted as the component of \mathbf{k} lying in the plane of \mathbf{B}_0 and \mathbf{R} (see section C.2.2). Thus, the reduced spectra of 2D turbulence contain a *purely geometrical* factor, which depends on the local winding angle. In general, these geometrical correction factors alter not just the level, but also the radial profile of the raw spectral densities. However, they do not affect normalized quantities (*e.g.*, σ_c , r_A), since the ratio of two spectral densities is independent of such common factors. *Tu and Marsch* [1992, 1993] have also

³ See also the work of *Tu and Marsch* [1992, 1993] on “convective structures” and waves.

considered the influence of the angle between the sampling direction and \mathbf{B}_0 from their perspective, wherein the fluctuations are divided into Alfvén waves propagating along \mathbf{B}_0 , and “convected structures” in the planes perpendicular to \mathbf{B}_0 .

To facilitate interpretation of our subsequent results, we now compare the reduced (*i.e.*, observed) spectral amplitudes at some fixed inertial range k_1 , with the underlying or intrinsic omni-directional spectra at the corresponding wavenumber. First we treat the 2D case, for which equation (5.10) holds, and the corresponding wavenumber is $k_1/\sin\psi$. The left-hand panels of Figure 5.8 show the two spectral forms of P^\pm considered in this section, for the usual situation of “standard” boundary conditions, $R_0 = 10 R_{sun}$, and $V_{Ar0}/U = 1$. The curves shown are for the Kolmogorov case of $\alpha = \frac{5}{3}$, but because $I(\alpha)/\pi$ only varies between $\frac{1}{2}$ for $\alpha = 1$ and $\frac{1}{\pi}$ for $\alpha = 2$, the dependence of this factor on the spectral slope is relatively weak. However, this dependence does determine the amplitude at large distances, where $\sin\psi \approx 1$. Close to R_0 , $\sin\psi$ is small, so that, relative to the omni-directional spectra, the reduced spectral densities are greatly reduced in this region. In fact, the reduced spectral amplitudes are lower than the corresponding omni-directional ones at all distances, but, the difference between the two forms decreases as R increases. When comparing various model solutions to observational data, it will be important to keep points like this in mind.

The right-hand panels of Figure 5.8 show the radial evolution of the normalized forms of the cross helicity and energy difference, for the two cases $V_{Ar0}/U = 0$ and 1 (“standard” bc’s, $R_0 = 10 R_{sun}$). For 2D turbulence, the dependence of the normalized quantities on this parameter is evidently somewhat weaker than for the isotropic case, particularly away from R_0 . The reason is that, unlike M_{iso}^+ , M_{2D}^+ does not undergo a sign change as V_{Ar0}/U is increased, and thus no qualitative change in the nature of the de coefficients occurs (equation (4.38)). Note that beyond 0.5 AU almost all the small-scale energy is magnetic in character. The reason for this rapid evolution towards magnetic energy dominance is currently not well understood.

For non-“standard” boundary conditions on the fields, little difference is seen in the radial evolution of any of the spectral densities. For example, when $V_{Ar0} = U$, $P_0^- = 1$, $P_0^+ = 0.01$, and $F_0 = 0, 0.1$, or 0.2 , the normalized cross helicity and Alfvén ratio increase slightly as F_0 is varied from zero up to its maximum allowed value (0.2) for these conditions (*cf.* the discussion on page 105), indicating a minor weakening of “mixing.” Negative values of F_0 , on the other hand, cause a marginal increase in the strength of “mixing,” relative to the $F_0 = 0$ case. This is easily understood: the strength of the “mixing” effect, and in particular growth of P^+ , depends upon the size of F . At a given distance, the “mixing” term in the transport equation for P^+ is more

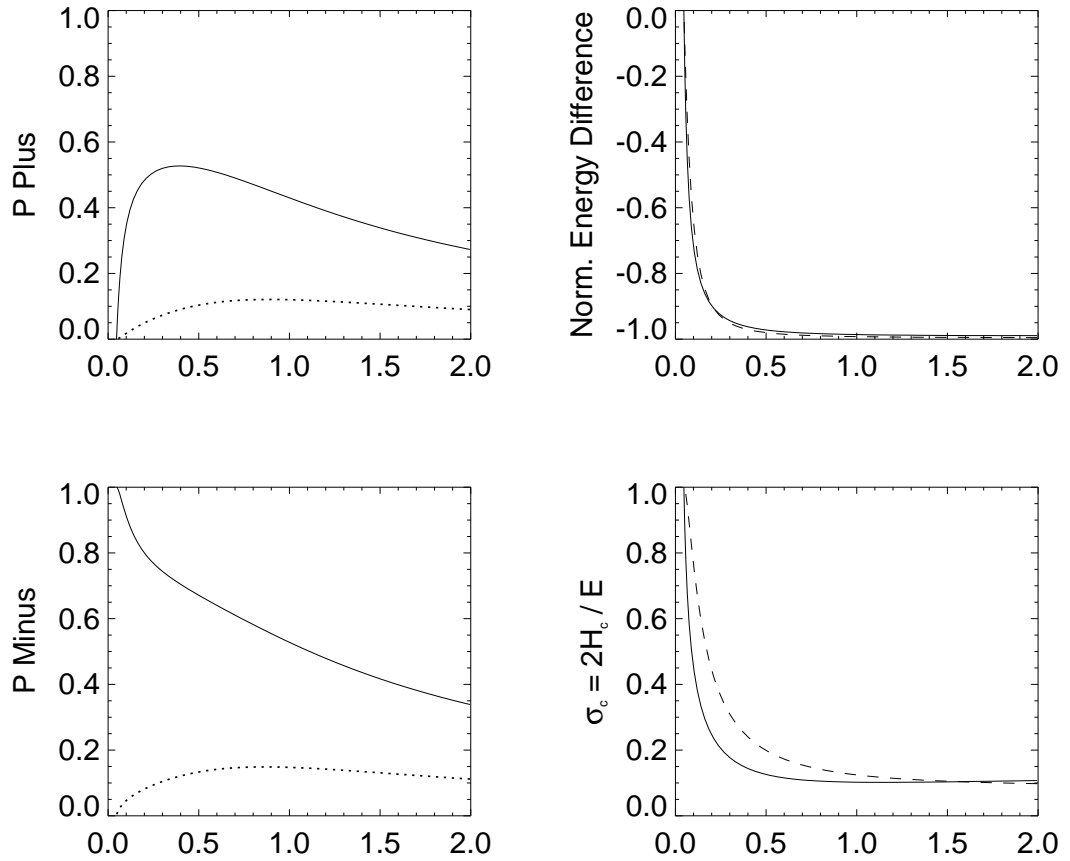


Figure 5.8: Radial evolution of various spectral densities for 2D turbulence (at an arbitrary inertial range wavenumber). All plots are for “standard” bc’s and $R_0 = 10 R_{sun}$. The left-hand panels show the omni-directional (solid curves) and reduced (dotted curves) spectra for the case $V_{Ar0} = U$. The right-hand panels display the normalized cross helicity and normalized energy difference for the two cases $V_{Ar0}/U = 0$ (dashed curves) and 1 (solid curves). As usual, the horizontal coordinate is heliocentric distance in AU.

effective for more negative values of F . Initially positive values of F cause a brief decay of P^+ , and delay the onset of its growth phase.

In summary, the solutions for two- and three-dimensional isotropic turbulence are quite similar in form, particularly beyond a few tenths of an AU. Furthermore, in both cases approximate saturation of the normalized quantities occurs, typically at a distance of about 1 AU. However, the “mixing” effect is substantially stronger for 2D turbulence.

5.2.4 Slab Fluctuations

Finally, we consider the slab geometry, for which $\mathbf{k} \parallel \mathbf{B}_0$ and the fluctuations are in the plane perpendicular to \mathbf{k} . Physically, this geometry is associated with Alfvén waves propagating along \mathbf{B}_0 . In contrast to the two previous geometries, J is no longer identically zero. This distinction between slab turbulence, and the 2D and isotropic forms will be taken up in the next subsection, where the approach to WKB is considered separately. As discussed in section 4.5, when $\mathbf{k} \cdot \mathbf{V}_A$ is non-zero, F and J exhibit tightly coupled oscillations, F about zero and J about a relatively small positive value which tends to zero as $R \rightarrow \infty$. As F is always small, “mixing” effects are effectively turned off, because at this order P^+ can grow only weakly if $F \approx 0$. As noted above, we therefore refer to the $\mathbf{k} \cdot \mathbf{V}_A$ factor as the “WKB enforcing” term.

Figure 5.9 shows an example for the case when $V_{Ar0}/U = 1$, $R_0 = 10 R_{sun}$, “standard” boundary conditions apply, and $k_1 = 50$ in code units (in physical units this corresponds to a wavenumber of approximately $7 \times 10^{-6} \text{ km}^{-1}$). The solutions are very close to the leading order WKB ones holding for the same boundary conditions; that is, at all distances $\sigma_c \approx 1$ and $r_A \approx 1$ ($\sigma_D = 0$). As R increases, the wavelength of the oscillations in F and J also increases because of the dependence of V_A on R .

The recovery of WKB-like solutions occurs for all values of $k_1 \gtrsim 5$ (code units⁴); this wavenumber corresponds to a physical wavelength $\sim \frac{1}{30}$ AU, which is about the same as the observed correlation length for the total energy at 1 AU. It follows that since solutions for scales much longer than those characteristic of inertial range fluctuations are WKB-like, the entire inertial range will also behave in this fashion. Clearly non-zero values of $\mathbf{k} \cdot \mathbf{V}_A$ strongly inhibit “mixing.” This dependence on $\mathbf{k} \cdot \mathbf{V}_A$ is essentially what was seen in *Heinemann and Olbert’s* [1980] investigation of the full wave equation (for toroidal geometry). For their simplified geometry, where *both* the large-scale flow and the large-scale magnetic field are radially directed, convergence of the (small amplitude) solutions to WKB was reported when k is not very small.

⁴ A unit wavenumber in code units has the physical value $2\pi/R_0$.

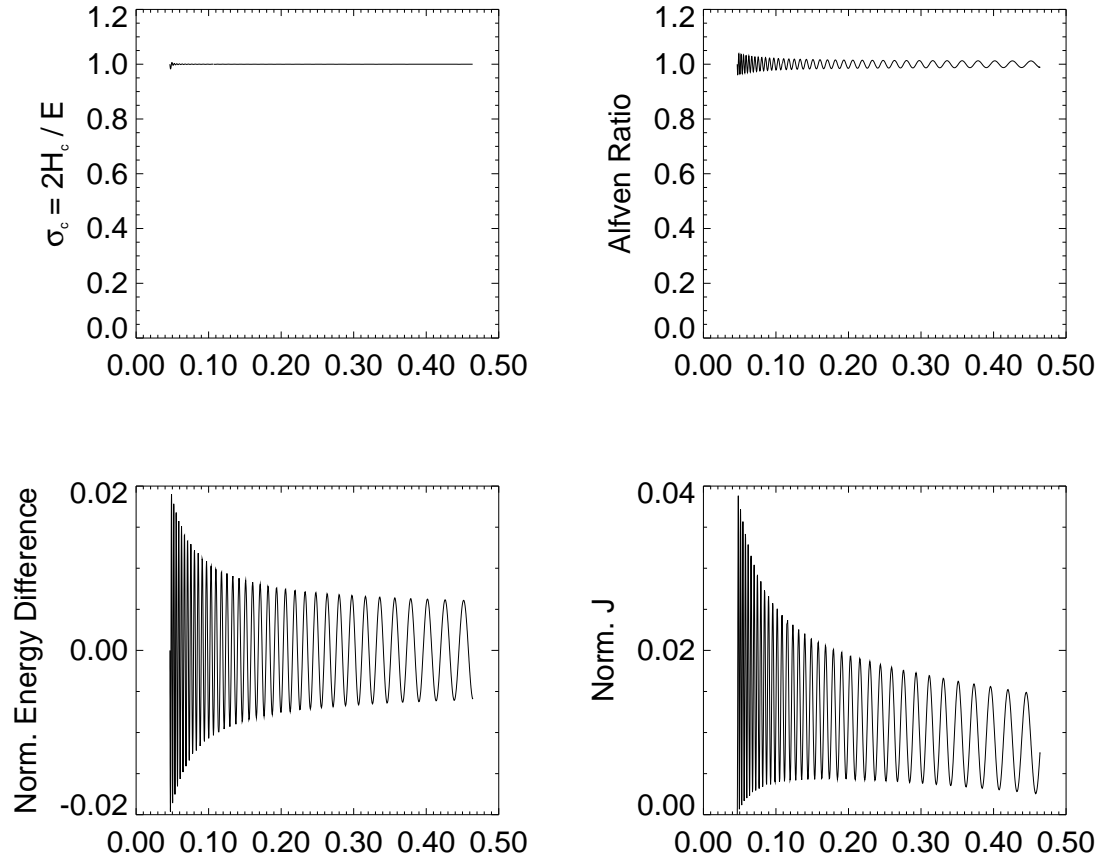


Figure 5.9: The radial evolution, or lack thereof, of various normalized quantities for slab fluctuations (spectral amplitudes at $k_1 = 50$). The solutions are for “standard” bc’s, $R_0 = 10 R_{sun}$, and $V_{Ar0} = U$. The lower plots should actually be plotted using vertical bounds of ± 1 , but such plots de-emphasize the oscillations. As usual, the horizontal coordinate is heliocentric distance in AU.

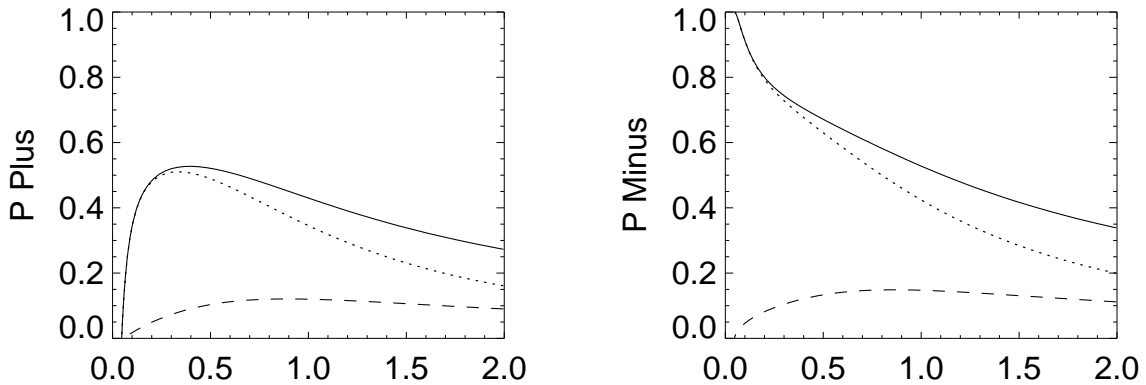


Figure 5.10: Comparison plots of the omni-directional and reduced spectral amplitudes for 2D and slab turbulence. All plots are for “standard” bc’s, $V_{Ar0} = U$, and $R_0 = 10 R_{sun}$. To avoid the oscillations seen in Figure 5.9, the slab curves are for $k_1 = 0$. Solid curves: omni-directional spectral amplitudes for both 2D and slab fluctuations; Dashed curves: reduced spectral amplitudes for 2D fluctuations; Dotted curves: reduced spectral amplitudes for slab fluctuations. The reduced curves are calculated for $\alpha = 5/3$. As usual, the horizontal coordinate is heliocentric distance in AU.

Solutions for the separate cases of $\mathbf{k} = 0$ and $\mathbf{V}_A = 0$, are highly reminiscent of the 2D solutions. When we recall that the two geometries have the same effective mixing operators (see section 4.4), this similarity is unsurprising; indeed the same analytic solution, showing strong “mixing,” holds for both types of fluctuations when $V_A = 0$ (Appendix D). If we compare instead the reduced spectral densities, the similarity vanishes, since for slab geometries the geometrical weighting factor is $1/\cos\psi$ (equation (C.27)), rather than the $1/\sin\psi$ appropriate for 2D turbulence. Figure 5.10 shows a comparison of the reduced spectral densities for 2D and slab fluctuations. The usual choice of parameters is in effect (“standard” bc’s, $V_{Ar0}/U = 1$, $R_0 = 10 R_{sun}$), and for the slab solutions $k_1 = 0$. While the omni-directional solutions are identical (solid curves), the reduced forms show substantial differences (broken curves). At smaller distances the reduced slab spectra differ little from their omni-directional forms, since $\cos\psi \approx 1$ in this region. As R increases, the geometrical factor leads to an increasing under-emphasis of the power in the slab fluctuations. The situation is more or less reversed for 2D fluctuations, since here the geometrical factor involves $\sin\psi$. As discussed in the previous section, normalized quantities are unaffected by reductions of this form.

The complementary character of the geometrical effects for 2D and slab reduced spectra can introduce an apparent radial evolution of the turbulence—independent of any turbulence dynamics.

To see this suppose that the interplanetary turbulence consists of two non-interacting components, namely 2D and slab fluctuations. Suppose also that for a given inertial range wavenumber, the omni-directional spectral amplitudes of the two components are equal, *i.e.*, $Q_{2D}^{omni}(k) = Q_{slab}^{omni}(k)$, at all distances. Then, assuming that the omni-directional spectra follow powerlaws ($k^{-\alpha}$), it follows that the ratio of the reduced spectral densities is given by

$$\frac{Q_{2D}^{red}(k_1)}{Q_{slab}^{red}(k_1)} = \frac{I(\alpha)}{\pi} \tan^{\alpha-1} \psi. \quad (5.11)$$

For $\alpha = 1$, which is often observed at distances less than 0.5 AU, this ratio is constant and less than unity at all distances, indicating that the 2D fluctuations are de-emphasized relative to the true power levels in the 2D and slab components. When $\alpha = \frac{5}{3}$, the ratio is unity at $\psi \simeq 80^\circ$; at this point a crossover occurs from over-emphasis of the slab component to over-emphasis of the 2D portion. Observationally $\psi \approx 45^\circ$ at 1 AU, so that under these conditions the crossover occurs well into the outer heliosphere. Assuming that the 2D component has triple the power of the slab portion moves the crossover into about 1 AU. In any case, even if the turbulence undergoes no dynamical evolution (between two points on the same radial), the reduced spectra of unnormalized quantities will still show radial evolution. This point has also been discussed by *Tu and Marsch* [1992, 1993]. Since for some time to come it is likely that only reduced spectra will be extractable from observational data, the problems associated with deconvolving geometrical and dynamical evolution effects will require further investigation. However, for analytic and numerical work on the linear equations, such problems do not arise since we always know what we started with.

5.2.5 Approach to WKB Solutions

The solutions presented in the previous subsections are in excellent agreement with the earlier discussion on the influence of the “mixing” terms (section 4.5). Specifically, “mixing” plays an increasingly important role as either \mathbf{V}_A/U or $\mathbf{k} \cdot \mathbf{V}_A$ approaches zero. Indeed, the impact of the “mixing” terms on the radial evolution of the physical quantities is crucially affected by the size of the “WKB enforcing” factor $\mathbf{k} \cdot \mathbf{V}_A$. As discussed above this factor is the coupling strength between the F and J fields. Since all the analytic solutions involve the restriction $V_{Ar0}/U = 0$, “mixing” is more or less maximal for these cases.

By way of summary we note that when $\mathbf{k} \cdot \mathbf{V}_A \approx 0$ (or $J = 0$) strong “mixing” occurs: the initial dominance of the “outward” modes causes growth of F , which in turn causes growth of the “inward” modes. Consequently, the normalized cross helicity, $\sigma_c = (P^- - P^+)/ (P^- + P^+)$ falls off significantly with increasing heliocentric distance. However, when F and J are strongly coupled, as is the case for slab fluctuations, the Alfvén waves impose near equipartition of kinetic

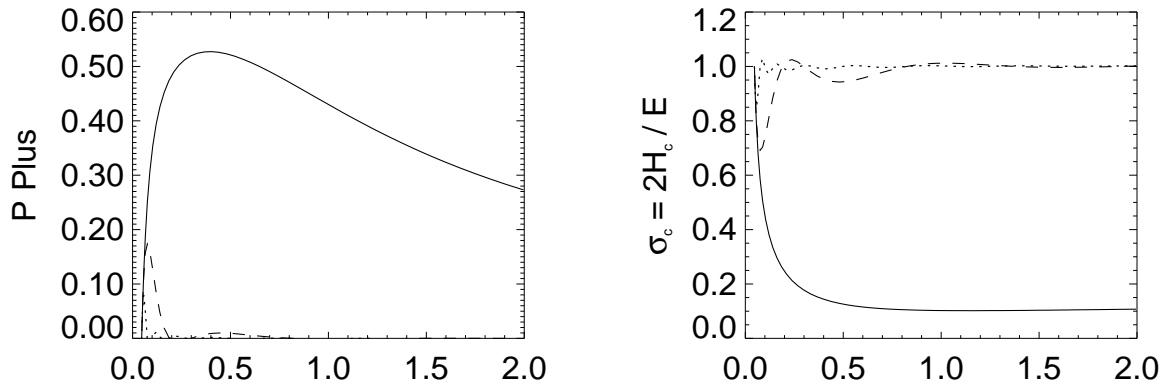


Figure 5.11: Plots showing the convergence of slab solutions towards WKB results as the wavenumber is increased (“standard” bc’s, $R_0 = 10 R_{sun}$, $V_{Ar0} = U$). Solid curves: $k = 0$; Dashed curves: $k = 2$; Dotted curves: $k = 5$. A unit wavenumber in code units is equivalent to $2\pi/R_0$ in physical units. This approach to WKB results has also been discussed by *Heinemann and Olbert* [1980] for linear toroidal waves. As usual, the horizontal coordinate is heliocentric distance in AU.

and magnetic energy, so that $F \approx 0$ and “mixing” is turned off. The energy in the “inward” fluctuations therefore remains a tiny fraction of that in the “outward” ones, leading to recovery of WKB-like solutions (Figure 5.11). See also *Heinemann and Olbert* [1980] for a discussion of related effects associated with toroidal waves.

The question arises as to the scale on which $\mathbf{k} \cdot \mathbf{V}_A$ is small. The natural terms to compare it to are the effective mixing operators. Denoting the angle between \mathbf{k} and \mathbf{V}_A by $\gamma(\mathbf{R})$, we construct the following ratio

$$\frac{\mathbf{k} \cdot \mathbf{V}_A}{M_{2D}^+} = \frac{2(V_{Ar0}/U)k \cos \gamma}{\cos^2 \psi + \frac{V_{Ar0}}{UR} (3 \cos^2 \psi - 2)}. \quad (5.12)$$

For $V_{Ar0}/U \leq 1$, the denominator is bounded above by 2, and decreases with increasing R ; we may therefore consider it to be at most an order unity quantity. For 2D fluctuations $\cos \gamma = 0$, so that the numerator is inherently zero and “mixing” is always strong. For slab fluctuations, however, $\cos \gamma = 1$, and the numerator increases without bound with k . If $V_{Ar0}/U \sim 1$, as is usually the case, the wavenumbers need only be $\gtrsim 10$ (in appropriate units), for WKB effects to nullify “mixing.” Such wavenumbers lie well below the inertial range, so that inertial range fluctuations are expected to be WKB in character when these conditions apply. The solutions presented in the previous sections provide numerical support for these arguments (see also Figure 5.11).

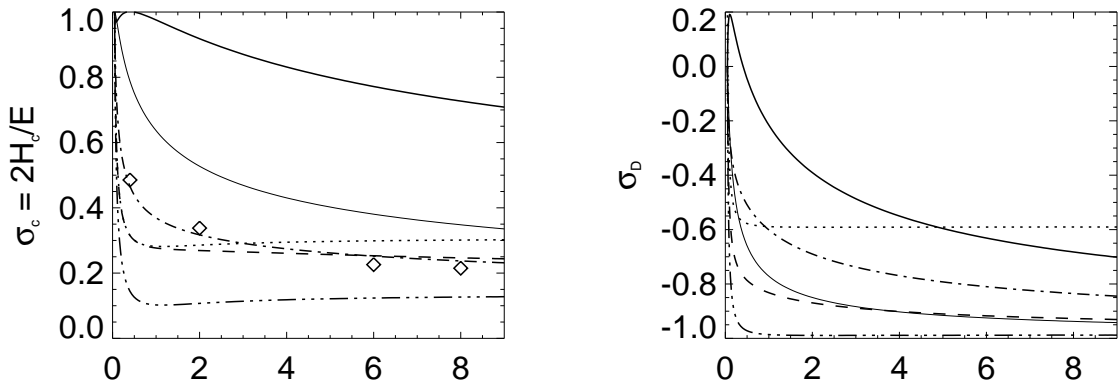


Figure 5.12: Plots of the numerical solutions to the linear transport equations for the normalized cross helicity and energy difference, with observational data points superimposed. The thick solid curves are for isotropic turbulence with $V_{Ar0}/U = 1$, and the dot-dot-dot-dash curves for 2D turbulence under the same conditions. The thin solid curve is the isotropic solution when $V_{Ar0}/U = 0$ (analytic). Dotted curves: 80% 2D, 20% slab; Dashed curves: 60% isotropic ($V_{Ar0}/U = 1$), 40% 2D; Dot-dash curves: 50% isotropic ($V_{Ar0}/U = 0$), 50% 2D. The diamonds denote observational data points obtained from three hour averages of Helios and Voyager data [Roberts *et al.*, 1987*a, b*]. All solutions are computed from the omni-directional spectra. The horizontal coordinate is heliocentric distance (AU).

5.2.6 Comparison with Observations

Figure 5.12 provides a summary of some of the linear solutions presented above. Curves for the normalized cross helicity and the normalized energy difference, in the case where the turbulence is isotropic or 2D, are shown, as are several linear combinations of these solutions (all at a fixed but arbitrary inertial range wavenumber). Because the slab solutions depend so weakly on k in the inertial range, it makes almost no difference which wavenumber is used here. Also shown are data points for σ_c derived from three hour averages of Helios and Voyager data [Roberts *et al.*, 1987*a, b*]. While data points for σ_D are not shown, observational analyses indicate that this quantity is approximately constant in the outer heliosphere, with a value of about -0.3 .

We note that, with the exception of the slab solutions, the curves for σ_c are in qualitative agreement with the observations, showing significant decay with heliocentric distance. The quantitative agreement is certainly not good enough to support claims of “mixing” providing the sole explanation for the observed decrease in σ_c ; nonetheless, it does suggest that “mixing” plays a role which (a) cannot be neglected, and (b) is capable of explaining some of the evolutionary trends.

Linear combinations of 2D and slab solutions have values of σ_D which are approximately

constant beyond 1 AU (*e.g.*, the 80-20 mix shown in Figure 5.12). Choosing a 30% 2D, 70% slab mix, would allow matching of the theory and observations for this quantity; however, σ_c for such a mixture is far too high to agree with observations. With a linear 2D-slab mixture, it is not possible to get good quantitative agreement between theory and observations for σ_c and σ_D simultaneously.

Recently, *Matthaeus et al.* [1990] constructed a two-dimensional correlation function of solar wind fluctuations using ISEE 3 data collected near 1 AU. As stated by the authors, the simplest way to interpret this correlation function is to “assume that the solar wind at 1 AU contains a population of Alfvénic [slablike] fluctuations, probably originating at the solar corona, along with a quasi-two-dimensional component that could be evidence of turbulent evolution between the sun and 1 AU.” The difficulties associated with obtaining enough suitable data meant that only a single such correlation function was calculated, so that without further examples, generalizations based on this “single event” must be handled with care. Nonetheless, an idealized model of the solar wind was postulated, viewing it as a fluid containing both slablike Alfvénic fluctuations *and* quasi-two-dimensional fluctuations. As (spectral) anisotropy seems to be a feature of turbulent evolution in the presence of a large-scale magnetic field [*e.g.*, *Shebalin et al.*, 1983]—meaning that the fluctuations evolve towards a quasi-2D state—*Matthaeus et al.* [1990] predicted that quasi-two-dimensionality would become more important in the outer heliosphere. Figure 5.12 shows that for (strong) 2D turbulence, σ_c and σ_D saturate at approximately constant values somewhere around a few AU. For ideal slab fluctuations, these normalized quantities are constant for all distances beyond R_0 , so that our numerical solutions support the prediction just referred to.

5.3 Modeling of the Non-linear Terms

5.3.1 Introduction

In order to proceed further with the inertial range model, we must incorporate appropriate approximations to the non-linear terms, which so far have been neglected. *Zhou and Matthaeus* [1990c] (hereafter ZM90c) have published appropriate forms for these terms, and here we concentrate on numerical implementations of such models. We will not delve deeply into the theory behind the modeling, since this is discussed in some detail in ZM90c. Portions of section 6.3, where modeling of the non-linear terms for the energy-containing eddies is considered, and Appendix A are also directly relevant to this section.

The strategy we adopt to arrive at models for the non-linear terms in weakly inhomogeneous transport theories requires some comment. We assume that the local non-linear processes are strong, acting rapidly enough to drive the local turbulence towards a state that can be described

by appeal to homogeneous turbulence mechanisms. This requires that the timescale characteristic of local non-linear couplings [Batchelor, 1970] is small compared to the time for changes of the large scale plasma parameters, induced by spatial transport. Typically the latter time scale may be estimated by $\tau_x = R/U$ where U is a speed characteristic of large scale spatial transport, possibly the solar wind speed, and R is the heliocentric coordinate, typifying gradients induced by inhomogeneities. The global non-linear time $\tau_{NL} = \lambda/\delta u$, where λ is a correlation scale and δu is an rms turbulent velocity field, is a standard estimate [Batchelor, 1970] of the time for establishing a universal turbulent state. Thus, for our strategy to be feasible, we require that $\tau_{NL} \ll \tau_x$, or that $\lambda \ll R$, since typically $U \gg \delta u$. We therefore arrive at the same condition for consistency of the transport model discussed during its derivation in Chapter 4; namely, that the scale of the turbulent structures be well-separated from the scale of the inhomogeneities. Consequently, reasoning based on homogeneous (and isotropic) turbulence will be invoked, and the large scale gradients that enter into the spatial transport terms of equations (5.1)–(5.3), for example, will not be involved in the models discussed below.

We turn now to the actual modeling. Suppose for the moment that we are only interested in incompressible hydrodynamic turbulence (*e.g.*, NS turbulence), with total energy per unit mass E and modal and omni-directional energy spectra $\hat{E}(k)$ and $E(k)$, respectively. While the non-linear terms are inherently non-local in wavenumber space—that is, modes with widely disparate wave-vectors are often strongly coupled—within the inertial range the net effect of all these couplings is spectral transfer of energy which is approximately *local* in k -space. This approximation is a key element of the well known Kolmogorov phenomenology [Kolmogorov, 1941; Batchelor, 1970], and amounts to the assertion that a continuous flux of energy density in three-dimensional wavenumber space exists [*e.g.*, Leith, 1967]. For isotropic turbulence this approximation may be written

$$\left(\frac{\partial E(k)}{\partial t}\right)_{NL} = -\frac{\partial f}{\partial k}, \quad (5.13)$$

where $f(k)$ is the flux through concentric spherical shells in k -space [ZM90c]. We consider two distinct but related models for $f(k)$.

5.3.2 Kolmogorov-style Approximations

The first model is based on a Kolmogorov-style treatment of the energy flux. One assumes that the turbulence is in a statistically steady state, so that f is independent of time. Moreover, in the inertial range, for which supply and dissipation contributions may also be neglected, the flux is also independent of the wave-vector k . Thus, if ϵ denotes the total rate of energy dissipation (equal to the rate of energy supply, on average), we have that $f \equiv \epsilon$ and $\partial f/\partial k = 0$. Kolmogorov

theory adopts the hypothesis that, with the above assumptions, the energy flux through a shell of radius k in the inertial range may depend only upon the energy in that shell, and upon the local wavenumber. Thus, using dimensional analysis one arrives at

$$f = \epsilon \sim E^{3/2}(k)k^{5/2}. \quad (5.14)$$

It follows immediately that,

$$E(k) = C_K \epsilon^{2/3} k^{-5/3}, \quad (5.15)$$

which is the famous *Kolmogorov* [1941] spectrum for fluid turbulence, involving the Kolmogorov constant C_K . Equation (5.14) may also be written as

$$\begin{aligned} \epsilon &= f \sim kE(k) \left[k^{3/2} E(k)^{1/2} \right] \\ &= \frac{u_k^2}{\tau_s}, \end{aligned} \quad (5.16)$$

where $u_k = \sqrt{kE(k)}$ is a speed characteristic of fluctuations with wavenumber k , and $\tau_s = [k^{3/2} E(k)^{1/2}]^{-1}$ is the appropriate spectral transfer time for inertial range energy in this Navier-Stokes case. For NS turbulence it is also true that $\tau_s = 1/(ku_k) = \tau_{NL}$, where τ_{NL} is the local non-linear (a.k.a. eddy turnover) time, associated with advection effects in the equation of motion. The form 5.16 is particularly useful, since it supports physically based generalizations to incompressible isotropic MHD turbulence. For MHD turbulence, timescales associated with Alfvén waves, $\tau_A = 1/kV_A$, must also be considered. All of the timescales mentioned to date are also connected with the *triple correlation* timescale, τ_3 , which is the effective time for relaxation of triads of correlated modes (*e.g.*, the “lifetime” of $\langle v_i(\mathbf{k})v_j(\mathbf{p})v_l(\mathbf{q}) \rangle$, see Appendix A). The following relations connecting the timescales are used [ZM90c]

$$\tau_s(k)\tau_3(k) \approx \tau_{NL}^2(k), \quad (5.17)$$

$$\frac{1}{\tau_3(k)} = \frac{1}{\tau_{NL}(k)} + \frac{1}{\tau_A(k)}, \quad (5.18)$$

the latter being the simplest relation amongst the three timescales also having the correct limiting forms when $V_A \rightarrow 0$ or $V_A \rightarrow \infty$ [Matthaeus and Zhou, 1989a; ZM90c].

Thus, in this simplest approximation to the phenomenology of energy spectral transfer, we infer models for the change of energy spectral density due to non-linear couplings, of the form,

$$\begin{aligned} \left(\frac{\partial E(k)}{\partial t} \right)_{NL} &= -\frac{\partial}{\partial k} \left(\frac{kE(k)}{\tau_s(k)} \right) \\ &= -\frac{\partial}{\partial k} \left(\frac{u_k^2}{\tau_s(k)} \right). \end{aligned} \quad (5.19)$$

This is the only functional form for the non-linear term that can be obtained within the context of the Kolmogorov-style dimensional analysis approach to evaluating f . It is noteworthy that the general form, for any model of the triple lifetime $\tau_3(k)$, takes on the intuitively appealing form written in the second line of (5.19), namely, the flux through a wavenumber shell is just the energy associated with the shell, divided by the associated spectral transfer time. The extension to MHD with uncorrelated velocity and magnetic fields (*i.e.*, zero cross helicity) is straightforward [*e.g.*, ZM90c], but we will not give the details here. However, the finite cross helicity case will be dealt with below, since it is of importance in the context of solar wind modeling.

5.3.3 Diffusion Approximations

Before discussing finite cross helicity effects, we introduce the second approach to modeling the k -space energy flux, where one adopts a *diffusion* approximation for the spectral transfer of energy [Leith, 1967; ZM90c]. With a diffusion coefficient D , the energy flux is then expressed as

$$f = -k^2 D \frac{\partial}{\partial k} \hat{E}(\mathbf{k}), \quad (5.20)$$

where $\hat{E}(\mathbf{k})$ is the modal spectrum.⁵ Dimensional analysis yields the following form for the diffusion coefficient

$$D = \gamma \tau_3(k) E(k) k^5, \quad (5.21)$$

where γ is a constant akin to the Kolmogorov constant, C_K . The diffusion approximation provides a simple model for the non-linear terms in a nonsteady spectral transport model of the kind considered throughout this thesis. In the diffusion approximation for isotropic turbulence the contribution of the non-linear terms becomes

$$\begin{aligned} \left(\frac{\partial E(k)}{\partial t} \right)_{NL} &= \frac{\partial}{\partial k} \left[k^2 D \frac{\partial \hat{E}(k)}{\partial k} \right] \\ &= \frac{\partial}{\partial k} \left[\frac{\gamma k^4}{4\pi \tau_s(k)} \frac{\partial}{\partial k} \left(\frac{E(k)}{k^2} \right) \right]. \end{aligned} \quad (5.22)$$

An appropriate choice of γ leads to recovery of the Kolmogorov law, complete with Kolmogorov constant, in the steady case. Again, in the absence of cross helicity, the extension to MHD is straightforward [*e.g.*, ZM90c].

Expanding the inner derivative of equation (5.22) reveals the relationship between the diffusion model and the simpler Kolmogorov-style form for the energy flux:

$$\frac{\gamma k^4}{4\pi \tau_s(k)} \frac{\partial}{\partial k} \left(\frac{E(k)}{k^2} \right) = \frac{\gamma}{4\pi} \left[\frac{k^2}{\tau_s(k)} \frac{\partial E(k)}{\partial k} - 2 \frac{kE(k)}{\tau_s(k)} \right] \quad (5.23)$$

⁵ Diffusion occurs at the modal level rather than for the entire shells that are associated with omni-directional spectra. Note however, that for isotropic turbulence $E(k) = 4\pi k^2 \hat{E}(\mathbf{k})$.

Thus, the diffusion approximation to the energy flux involves two additive pieces; one is identical in nature with the simpler Kolmogorov-style energy flux, while the other corresponds to “true” diffusion in wavenumber space with a k dependent diffusion coefficient (related to the spectral transfer time). In conditions of steady state, the net flux (*i.e.*, equation (5.23)) must be independent of k . Substituting the known powerlaw solution into the diffusion flux shows that each piece is separately proportional to the constant energy flux ϵ . Thus, the two terms do not balance each other in steady state.

5.3.4 Cross Helicity Effects

Up to this point we have assumed implicitly that turbulent energy transfer in MHD is governed locally in wavenumber, and solely by the energy spectral density (kinetic plus magnetic) itself. This simplifying assumption [Kraichnan, 1965] requires that kinetic and magnetic energy densities in inertial range wavenumbers be equal, and that the cross helicity spectral density be zero.⁶ In general, one expects that spectral transfer can be influenced by relaxation of various assumptions, including magnetic-kinetic energy equipartition or nonzero H_c , as well as by including effects such as inverse spectral transfer [*e.g.*, Frisch *et al.*, 1975]. Leaving aside the difficult problem of a general spectral transfer theory, we discuss here a simple way to include cross helicity in nonsteady spectral transfer models.

For discussion of MHD turbulence with cross helicity, we revert to using the Elsässer variables. In terms of these variables the incompressible MHD equations have the structure $\partial \mathbf{z}^\pm / \partial t \approx -\mathbf{z}^\mp \cdot \nabla \mathbf{z}^\pm$, where pressure and dissipation terms are neglected on the right-hand side. It is also convenient [*e.g.*, Grappin *et al.*, 1982, 1983] to introduce the wavenumber dependent characteristic z -field amplitudes z_k^+ and z_k^- that are related to their respective omni-directional spectra $P^\pm(k)$ by $z_k^\pm \equiv \sqrt{k P^\pm(k)}$. By inspection of the above Elsässer form of the MHD equations, and making use of the fact that non-linear convection-like effects are induced by the explicitly retained advection terms, one concludes that the non-linear times appropriate to this case are $\tau_{NL}^\pm = 1/k z_k^\mp$ [Dobrowolny *et al.*, 1980b]. These are analogs of the eddy turnover time τ_{NL} . By direct application of the ideas introduced earlier (see also Matthaeus and Zhou [1989a]), the timescales for decay of the triple correlations that give rise to spectral transfer of $P^\pm(k)$ can be approximated by

$$(\tau_3^\pm)^{-1} = \tau_A^{-1} + (\tau_{NL}^\pm)^{-1}. \quad (5.24)$$

⁶ Recall that the cross helicity is $H_c \equiv \langle \mathbf{v} \cdot \mathbf{b} \rangle / 2 = \int dk H_c(k)$, defining the omni-directional cross helicity spectrum as $H_c(k)$ [*e.g.*, Frisch *et al.*, 1975; Matthaeus and Goldstein, 1982a].

In addition, the z field amplitudes, their respective characteristic spectral transfer times τ_s^\pm , and ϵ^\pm should be related by the expression $\epsilon^\pm \equiv (z_k^\pm)^2/\tau_s^\pm$. This requires a relationship between the spectral transfer times and the non-linear and Alfvén times, according to equation (5.17), of the form

$$\tau_s^\pm = (\tau_{NL}^\pm)^2 \left(\frac{1}{\tau_A} + \frac{1}{\tau_{NL}^\pm} \right). \quad (5.25)$$

Using the above non-linear times, we find explicit forms for the spectral transfer rates of the Elsasser fields,

$$\epsilon^\pm \equiv \frac{(z_k^\pm)^2}{\tau_s^\pm} = \frac{k^3 P^+(k) P^-(k)}{V_A + \sqrt{k P^\mp(k)}}. \quad (5.26)$$

These forms for the spectral transfer rates reduce to the forms discussed by *Grappin et al.* [1982, 1983] when $\tau_A \ll \tau_{NL}^\pm$. However, in contrast to previously discussed theory [*Grappin et al.*, 1983; *Dobrowolny et al.*, 1980b; *Pouquet et al.*, 1986], the present treatment does not imply equal fluxes of “energy” in the two z -fields. In principle, equation (5.24) gives two equations that can be used to find steady state spectral laws for isotropic turbulence with cross helicity. We will not pursue this further here, since the procedure requires additional assumptions [*e.g.*, *Grappin et al.*, 1983] that go beyond our present scope.

These ideas concerning steady spectral transfer with non-zero cross helicity can also be included in further extensions to the nonsteady diffusion and Kolmogorov-style models discussed above. In terms of the energy spectra of the “ \pm ” fields, the contributions of the non-linear terms according to the dimensional analysis method would become

$$\begin{aligned} \left(\frac{\partial P^\pm(k)}{\partial t} \right)_{NL} &= -\frac{\partial}{\partial k} \left[\frac{(z_k^\pm)^2}{\tau_s^\pm(k)} \right] \\ &= -\frac{\partial}{\partial k} \left[\frac{k P^\pm(k)}{\tau_s^\pm(k)} \right]. \end{aligned} \quad (5.27)$$

In similar fashion the diffusion model can be extended by writing

$$\left(\frac{\partial P^\pm(k)}{\partial t} \right)_{NL} = \frac{\partial}{\partial k} \left[\frac{\gamma^\pm k^4}{4\pi \tau_s^\pm(k)} \frac{\partial}{\partial k} \left(\frac{P^\pm(k)}{k^2} \right) \right]. \quad (5.28)$$

Here, the “ \pm ”-energy flux through a wavenumber space sphere of radius k is approximated as $f^\pm = -k^2 D^\pm \partial \hat{P}^\pm(\mathbf{k})/\partial k$, where the omni-directional and modal spectra are related, as usual, by $P^\pm(\mathbf{k}) = 4\pi k^2 \hat{P}^\pm(\mathbf{k})$, and the diffusion coefficients associated with the “ \pm ” fields are identified as $D^\pm \equiv \gamma^\pm k^2/4\pi \tau_s^\pm(k)$, where $\tau_s^\pm(k)$ is given by equations (5.24) and (5.25). The quantities γ^\pm are order-unity constants, but may not be equal for the “ \pm ” fields, however in our work we shall take

them to be so. Specifically we choose them to have the value $\frac{12\pi}{11}$, so that the steady solutions in the case where $P^+ = P^-$, $V_A = 0$, and $\epsilon^+ = \epsilon^-$, have the Kolmogorov form $\epsilon^{2/3}k^{-5/3}$; *i.e.*, we set $C_K = 1$.

5.3.5 Energy Difference

Non-linear terms for this quantity are less well understood than those associated with the energy-like quantities discussed in preceding subsections. Apart from the fact that homogeneous turbulence theory has not yet addressed these quantities in detail, we are also lacking well developed guidelines concerning the structure or evolution of these spectra from either simulations or observational analysis. Because the energy difference is not a conserved quantity, one cannot model its k -space non-linear terms using simple conserved flux forms of the type used with the “energies.”

There is some current understanding of the basic physics involved in the behavior of difference between the kinetic and magnetic energies, even though it is not a globally conserved quantity. Nonzero $F(k)$ indicates lack of kinetic-magnetic energy equipartition in a wavenumber band, which is frequently observed in the solar wind [Matthaeus and Goldstein, 1982a; Roberts *et al.*, 1987a, b]. There are at least several physical effects that might be responsible for producing non-equipartition, including small scale magnetic reconnection effects [Matthaeus and Lamkin, 1986] and certain couplings to large scale inhomogeneities [Zhou and Matthaeus, 1990a]. Nevertheless, it is widely thought that there are strong tendencies in MHD to restore equipartition, in an order-one sense, according to a line of reasoning that is usually referred to as the “Alfvén effect” [Kraichnan, 1965; Kraichnan and Nagarajan, 1967; Fyfe *et al.*, 1977]. Recent three-dimensional MHD simulations [Stribling and Matthaeus, 1991] have also shown this to be the usual state of affairs, particularly prior to the onset of longer term selective decay effects.

To accomplish near-equipartition, it is necessary to allow for the possibility that, within a wavenumber shell, magnetic and kinetic energy can be converted into one another. This is manifestly the case for Alfvénic type couplings to the larger scale magnetic structures, which are often invoked as the simplest explanation for the Alfvén effect [Fyfe *et al.*, 1977]. Consequently, it is clearly inappropriate to model the non-linear term associated with $F(k)$ according to the method developed for conserved quantities such as the energy.

Lacking a more rigorous treatment, we make the following simple suggestion concerning the behavior of the energy difference spectrum. We expect that there are two tendencies; the first is associated with processes making $F(k)$ relax towards zero at some rate which we call τ_F . In

choosing a form for this timescale, we assume that the processes involved are mainly to do with Alfvén wave effects, neglecting for the present the suggestion of *Zhou and Matthaeus [1990c]*, that the kinetic energy may also play a role in determining this timescale. We do suggest, however, that, along with large-scale magnetic energy, the local small-scale magnetic energy, $kb^2(k)$, also contributes to this relaxation, and we obtain

$$\frac{1}{\tau_F(k)} = k\sqrt{V_A^2 + \frac{k}{4}(P^+ + P^- - F)}. \quad (5.29)$$

The second tendency we include attempts to drive F towards a negative value, in accord with solar wind observations [*Matthaeus and Goldstein, 1982a; Roberts et al., 1987a, b*] and closures and simulations [*Pouquet et al., 1976; Mangeney et al., 1991*]. We assume that this driving depends only on the kinetic energy of the system. The gist of the argument is that since the induction equation is linear in \mathbf{b} , such driving—which stems from spectral transfer of the energy, and is thus a non-linear process—should only depend on v^2 . See however the arguments of *Grappin et al. [1982, 1983]* and *Mangeney et al. [1991]*. A more detailed discussion, in the context of the non-linear terms associated with the energy-containing eddies, is also given on page 143. Thus, we write,

$$\left(\frac{\partial F(k)}{\partial t}\right)_{NL} = -\frac{F}{\tau_F} - \frac{v^2}{\tau_s^{tot}}, \quad (5.30)$$

where all quantities on the right are functions of the wavenumber k , and τ_s^{tot} is the spectral transfer time for the total energy, defined by

$$\frac{P^+}{\tau_s^+} + \frac{P^-}{\tau_s^-} = \frac{P^+ + P^-}{\tau_s^{tot}}. \quad (5.31)$$

Finally, we note that when the turbulence is isotropic in two-dimensions rather than three, V_A^2 should not contribute to any of the triple correlation times, spectral transfer times or to τ_F , since in this case the fluctuations do not feel the field—provided they remain in the planes perpendicular to it. Indeed, even for isotropic turbulence arguments can be made for only a fraction of V_A^2 contributing to these timescales. The reasons for this are discussed at the end of section 6.3.2. Modeling of the other non-linear terms appearing in the full transport model will not be considered in this document.

5.3.6 Numerics

Numerically, the models discussed above for the energy-like non-linear terms have been implemented using finite difference methods. Both the simpler Kolmogorov-style flux and the

diffusive flux have been numerically investigated, and in this section we report on numerical details and results. For those who wish to avoid reading this section, however, we summarize the results by noting that problems associated with the Kolmogorov-style models led to the use of the diffusion forms in production runs.

As noted in section 5.2.1, we use a non-uniform grid spacing for the wavenumbers; specifically, equal spacing of their logarithms is adopted. This allows several decades of wavenumbers to be covered with a relative lack of computational expense. Testing was performed with up to 80 wavenumbers per decade, but adequate resolution and accuracy was obtained with just 20 per decade. The wavenumbers will be denoted by k_1, k_2, \dots, k_M , and the spacings between them by Δk_i . Values used for M ranged from 60 to 200. Typically, in code units, $k_1 = 30$, because this value corresponds to a wavelength of approximately $\frac{1}{100}$ AU, which is a value relevant to the start of the inertial range in the solar wind. The two major production runs discussed in the next chapter used 60 wavenumbers, with 20 per decade and $k_1 = 30$.

To assist with testing, the code was run with the (linear) spatial transport terms switched off. Furthermore, any particular subset of the non-linear terms could be activated, supporting independent checking of the various pieces of the full model. Two cases in particular are of interest:

- (1) F decay switched off, so that the steady state forms for the “energies” may be confirmed. In this case the value of $F(k)$ is immaterial since the spectral transfer times τ_s^\pm are independent of it. There are several subcases of physical importance to consider: (a) $P^+ = P^-$, and (b) $P^+ \ll P^-$. For each subcase V_A may be zero or non-zero.
- (2) F decay switched on, but P^\pm non-linearities inactive. Analytic solutions for the steady state may then be compared with the numerical solutions.

We now discuss each case in turn.

The non-linear terms for P^\pm require imposition of a boundary condition at the low k end of the inertial range. This amounts to specifying the flux flowing into the inertial range. Operationally, $\partial f/\partial k$ at this point is calculated using formulae like

$$\left. \frac{\partial f^\pm}{\partial k} \right|_{k_1} = \frac{f^\pm(k_2) - \epsilon^\pm}{\Delta k_2}. \quad (5.32)$$

The interior derivatives are calculated using centered differences, and the derivative at the last k point is evaluated using a three point backward difference [*e.g.*, Fletcher, 1991]. As discussed above, the steady-state solutions are powerlaws, and the codes should achieve these forms in about one characteristic time.

Consider first the Kolmogorov-style modeling.⁷ We wish to solve equation (5.27). Euler integration is unconditionally unstable for hyperbolic problems of this form, so that we instead use either the Lax method or the quasi-second order (QSO) method [*e.g.*, Potter, 1973], both of which are stable for small enough timesteps (\sim CFL condition). The first test cases involved setting $V_A = 0$, $P^+ = P^-$ at $t = 0$, and choosing various constant values for ϵ^\pm . The initial spectra were chosen to be powerlaws ranging between k^{-1} and k^{-2} . The influence of the spectral amplitudes of the powerlaws was also investigated.

The Lax method [*e.g.*, Potter, 1973] introduces numerical diffusion with a viscosity proportional to $(\Delta k)^2/\Delta t$. Therefore, for a given Δk , reducing Δt increases the numerical diffusion; small enough values of Δt eventually lead to steady numerical solutions which are not powerlaws at all wavenumbers. The net result is that for a given set of Δk 's, there is only a narrow window of Δt 's which yield both stable and accurate solutions. Since this window will not necessarily be compatible with the stability requirements of the linear spatial transport, the Lax method might be unusable in this connection.

The QSO method does not suffer from this deficiency, but the timestepping requirements are somewhat more severe. For either method, provided the initial spectra were lower than the steady-state forms (*i.e.*, $\epsilon^{2/3}k^{-5/3}$), acceptable solutions could be obtained. However, initial spectra with amplitudes greater than the steady-state values caused numerical difficulties. We suspect the problems stem from the size and sign of the derivative at k_1 (*e.g.*, a boundary layer effect). For realistic application to the solar wind, the models must behave acceptably with such initial conditions, and we therefore abandoned this approach and turned to the diffusion models.

For the diffusion approximation, the equations to solve,

$$\left(\frac{\partial P^\pm(k)}{\partial t}\right)_{NL} = \frac{\partial}{\partial k} \left[\frac{\gamma^\pm k^4}{4\pi\tau_s^\pm(k)} \frac{\partial}{\partial k} \left(\frac{P^\pm(k)}{k^2} \right) \right]. \quad (5.33)$$

are parabolic, so that straightforward Euler or Adams-Bashforth time integration is conditionally stable. However, the stability requirements for our problems are rather severe (see below). When $P^+ = P^-$ initially and $V_A = 0$ (the Kolmogorov limit), solutions in excellent agreement with the steady-state forms are obtained, whether the initial spectrum amplitude is higher or lower than the steady-state value (Figure 5.13).

Since, in the solar wind, $P^+(k)$ is often one or even two orders of magnitude smaller than $P^-(k)$, testing of the models for such disparate spectral levels is important. In such cases, the non-linear terms are weak and spectral transfer is rather slow (the non-linear terms in the equations of

⁷ At this point we are assuming that F decay has been deactivated.

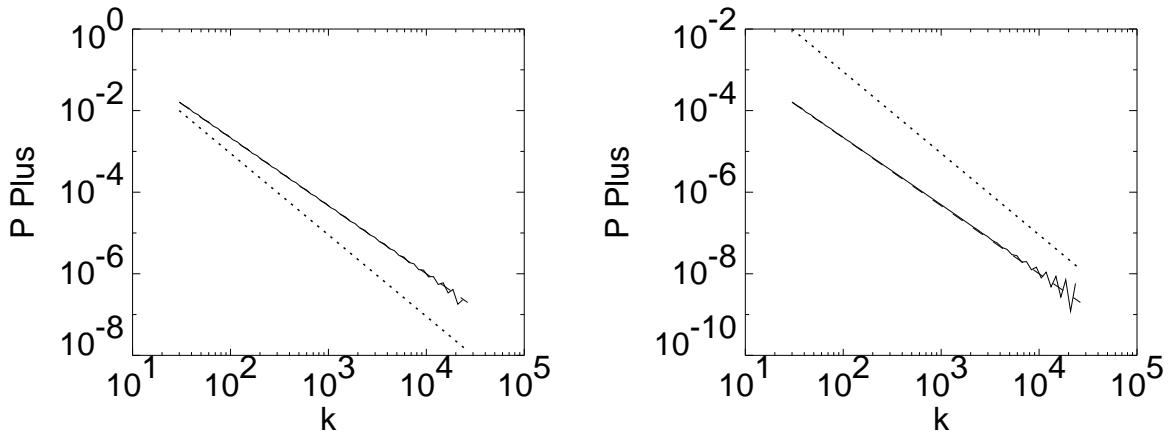


Figure 5.13: Numerical solutions for the spectrum of P^+ obtained using the diffusion model. There is no large-scale magnetic field imposed and $P^+ = P^-$. The initial conditions are shown as dotted lines, and the solutions after one characteristic time by the solid curves. The dashed lines, just visible underneath the solid curves, are the correct steady solutions ($\epsilon^{2/3}k^{-5/3}$). In the left-hand figure $\epsilon^\pm = 10$, and $\Delta t = 2.5 \times 10^{-6}$, while on the right $\epsilon^\pm = 0.01$, and $\Delta t = 2 \times 10^{-5}$. There are twenty wavenumbers per decade and $k_1 = 30$.

motion almost balance each other). The dashed curves in Figure 5.14 show numerical solutions for the case $P^+ = 0.01P^-$ at $t = 0$, $\epsilon^+ = 10^{-4}$, $\epsilon^- = 10^{-2}$, $V_A = 0$, and initial spectra proportional to k^{-2} . Clearly undesirable behavior is occurring at higher wavenumbers; in fact this behavior is associated with the other steady solutions to equations (5.33). Suppose $P^+ \propto k^2$, then $\partial P^+ / \partial t = 0$ because $\partial(P^+/k^2)/\partial k = 0$. If P^- is not proportional to k^2 , then its compatible steady-state solution is $\propto k^{-3.5}$. While it is not overly clear in Figure 5.14, in other test cases the high k powerlaws agree rather well with the analytic “second-solutions.”

The question is how can we avoid such solutions? A boundary condition will not do the trick since its influence does not extend far enough inside the computational domain. In particular when the energy flux is weak because of cross helicity effects, the high k flux condition is not strong enough to avoid the unwanted solution. To circumvent this problem we modify the wavenumber transport by including a (physically motivated) viscosity and resistivity. Specifically, we include in the equations additive terms of the form

$$\nu = \bar{\nu} \left(\frac{k}{k_1} \right)^2, \quad (5.34)$$

where $\bar{\nu}$ is a (small) number determining the location of the dissipation range. The value of k for which $\nu = 1$ defines the dissipation wavenumber, k_d . The solid curves in Figure 5.14 show numerical solutions for the same situation as in the dashed ones, except that $\bar{\nu} = 10^{-4}$ instead of

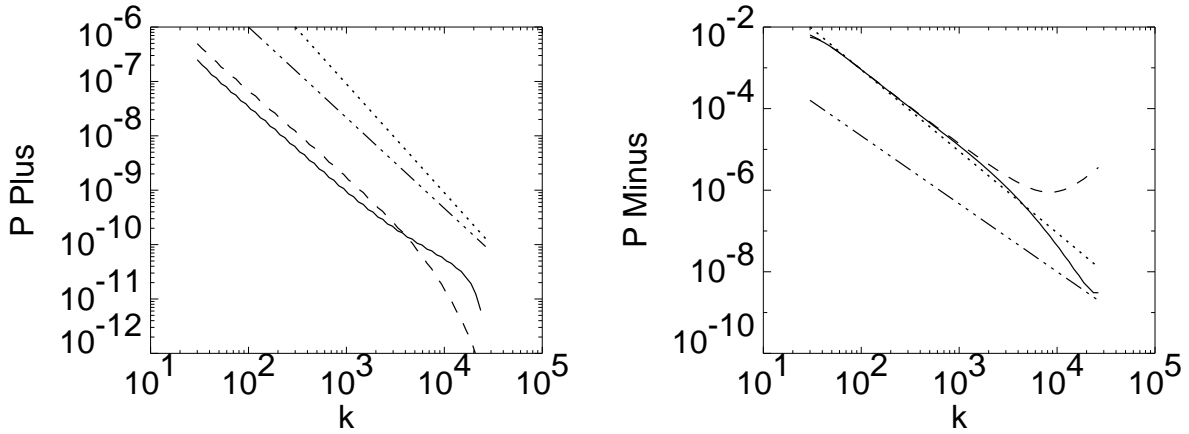


Figure 5.14: Numerical solutions for the spectra of P^\pm obtained using the diffusion model with and without viscosity. The plots shown are for $P^+ = 0.01P^-$ at $t = 0$, and $V_A = 0$. The initial conditions are shown as dotted lines, and the dash-dot-dot-dot lines are $k^{-5/3}$ curves provided for comparison. The other curves are solutions after one characteristic time. Dashed lines: no viscosity; Solid lines: $\bar{\nu} = 10^{-4}$. In both cases $\epsilon^+ = 10^{-4}$, $\epsilon^- = 10^{-2}$, and $\Delta t = 2.5 \times 10^{-6}$. Twenty wavenumbers per decade are used and $k_1 = 30$.

zero. Since $k_1 = 30$ for these runs, this corresponds to a dissipation wavenumber of $k_d = 3000$, which is substantially smaller than inferred values for the solar wind; nonetheless, approximately two decades of inertial range wavenumbers remain. Non-zero values of V_A do not introduce any further numerical difficulties of note.

The behavior of the non-linear terms for F must also be considered. As no k -space derivatives are involved in these terms, additional boundary conditions are not required. Furthermore, Euler time integration provides stable and accurate solutions for values of Δt compatible with the stability restrictions applying to other terms in the full model (its own stability restriction is a joke in this regard). For fixed and positive P^\pm , steady analytic solutions for F exist; comparing these solutions to the appropriate numerical ones indicates that four or five significant figures (single precision codes) are obtained when the Δt 's referred to above are used. The specific cases supporting steady analytic solutions are when either (a) $V_A = 0$, or (b) V_A is non-zero, but the “ b^2 ” term in τ_F is zero (see equation 5.29).

This completes our discussion on the modeling and testing of the non-linear inertial range terms. In order to use these approximations in a full inertial range model, we require values for the Elsässer energy fluxes (ϵ^\pm) at each point in space. Obtaining these fluxes entails development of an energy-containing range transport and turbulence model for the solar wind, and this is the

subject of the next chapter. Consequently our presentation of numerical results for an “active” inertial range is deferred until section 6.5.

Chapter 6

TRANSPORT OF ENERGY-CONTAINING FLUCTUATIONS

I think the danger is not so much in asking the “why,”
as in believing you have come up with the only answer.

— Margaret Weiss and Tracy Hickman: *Dragon Wing*

6.1 Introduction

In the previous chapter we discussed the evolution of inertial range fluctuations in the solar wind. By analogy with results from hydrodynamic turbulence, one expects the evolution in the inertial range to be governed by the dynamics of fluctuations with somewhat larger scales—a class of turbulent structures known as energy-containing eddies in classical turbulence theory. To develop a quantitative understanding of the turbulence as a whole, including the rate at which energy is supplied to the inertial range and the turbulent heating rate, one needs at least an approximate theory for the evolution of the energy-containing turbulent structures in the solar wind. In this chapter, we first develop such a model, and then present some initial solutions for it.

6.1.1 Historical Background

The relative concentration of turbulent energy at scales larger than the powerlaw inertial range is of great importance in classical hydrodynamic turbulence theory. The transfer or *cascade* of energy to smaller scales is accomplished by the interactions of eddies at each scale with all other eddies. In the inertial range, the nature of the couplings is thought to be self-similar and is readily treated by a theory that invokes statistical equilibrium for turbulence in a steady state [Kolmogorov, 1941; Batchelor, 1970]. The energy-containing structures in decaying turbulence, however, are never in a steady state; nevertheless, they are responsible for supplying the energy that drives inertial range transfer towards ever smaller scales. The inertial range couplings mediate this spectral transfer but do not control it. Eventually, the inertial range gives way to the dissipation range, and turbulent energy is lost to heating. Thus, it is clear that the energy-containing eddies determine the structure of the inertial range and the rate of turbulent heating. In hydrodynamic turbulence theory [Batchelor, 1970], it is recognized that the energy-containing structures require

a separate dynamical theory, generally known as quasi-equilibrium theory to distinguish it from the conditions of the steady inertial range. Note that this description applies to homogeneous Navier-Stokes turbulence and that the analogous situation for the MHD energy-containing range in the solar wind may involve important differences.

The need to develop a magnetohydrodynamic theory of the energy-containing range appears to have received relatively less attention in the space physics community than has consideration of properties of the inertial range. The reasons for this seem clear enough: observations, such as those in the solar wind, have afforded ample opportunity to study the inertial range of MHD turbulence in great detail. Moreover, the approximation of local homogeneity [*e.g.*, *Jokipii and Coleman*, 1968; *Matthaeus and Goldstein*, 1982*b*] works best at these relatively shorter scales. This provides the basis for comparison of observations with both analytical theories [*Dobrowolny et al.*, 1980*a, b*; *Grappin et al.*, 1982, 1983] and numerical simulations [*Matthaeus et al.*, 1983; *Pouquet et al.*, 1986, 1988; *Roberts et al.*, 1991, 1992] of homogeneous MHD turbulence. These studies have indicated that a reasonable understanding of local features of solar-wind MHD turbulence can be achieved by appealing to basic homogeneous turbulence theory.

In contrast, observational studies [*Bavassano et al.*, 1982*a, b*; *Bavassano and Bruno*, 1989; *Roberts et al.*, 1987*a, b*, 1990; *Bavassano and Smith*, 1986; *Grappin et al.*, 1990; *Tu et al.*, 1989*a, b*] have also demonstrated the need for a more sophisticated analytical framework in order to understand the radial evolution of solar wind turbulence on larger scales. Turbulent heating also seems to require a more extensive treatment [*e.g.*, *Barnes*, 1968, 1969; *Tu et al.*, 1989*c*; *Freeman*, 1988]; indeed, the original suggestion of *Coleman* [1968] clearly involved energy-containing structures and not solely inertial range fluctuations.

The most widely used basis for spatial transport of solar wind fluctuations has been WKB theory,¹ in which the fluctuations are treated as noninteracting waves that respond to long wavelength variations in the background plasma and magnetic-field parameters. *Tu et al.* [1984] recognized the possibility of incorporating *Coleman's* [1968] suggestion of turbulent heating into the WKB formalism and developed a fluctuation transport theory that enjoys some success in accounting for the radial evolution of the turbulent energy spectrum [*Tu et al.*, 1989*b*]. As discussed in Chapter 4, more complete theoretical formalisms involving various MHD spectra, *e.g.*, magnetic and kinetic energy and cross helicity, have been presented recently [*e.g.*, *Matthaeus et al.*, 1990*a*; *Marsch and Tu*, 1989, 1990*b*; *Tu and Marsch*, 1990*b*]. These theories have shown promise in explaining a number of features of observed inertial range spectra. In principle, the same basic

¹ See *Barnes* [1979] for a review, and the earlier chapters for further references.

spectral transport equations can also be used to describe the energy-containing fluctuations that govern the evolution of the turbulence as a whole, although they have not previously been used in this way as far as we are aware. An exception to this is the work of *Tu* [1987], which we believe is seriously flawed in its treatment of the energy-containing scales (see discussion below).

A more direct approach to the problem of transporting bulk turbulence has been employed by *Hollweg* [1986] and *Hollweg and Johnson* [1988] in the context of solar wind acceleration. Rather than consider the spectrally decomposed fluctuations, Hollweg suggests using a Kolmogorov-type heating rate as described by *Coleman* [1968], which contributes an additional term to the WKB equation for the transport of the mean-square fluctuating magnetic-field strength. This approach has the advantage of discarding unneeded inertial range spectral information and considerably simplifying the problem. However, by assuming the Alfvénic condition (pure cross helicity) associated with outward traveling waves, the theory of Hollweg and coworkers eliminates a number of potentially important MHD effects on turbulent evolution, spectral transfer, and heating due to turbulent decay. Although the Hollweg model is limited in the scope of physical effects included, and has been found to fall short of explaining solar wind observations [*e.g.*, *Isenberg*, 1990a], it includes the first proper treatment to our knowledge of quasi-equilibrium range Kolmogorov phenomenology in a quantitative solar wind model.

The purpose of this chapter is to develop a more complete phenomenological model for transport of energy and other rugged invariants such as cross helicity [*Frisch et al.*, 1975, *Kraichnan and Montgomery*, 1980; *Matthaeus and Goldstein*, 1982a] in the solar wind, and then present some initial solutions for the model. We do not base our approach on rigorous mathematical turbulence theory, but instead merge elements from two distinct types of approximate theories. First, we use a reduced version of the recently developed spectral transport formalism of *Zhou and Matthaeus* [1990a] to describe the spatial transport of the energy-containing eddies. As discussed in Chapter 4, this approach assumes a substantial separation between the turbulence length scales and the distance over which significant changes in the properties of the solar wind are experienced. Second, we develop a simple, phenomenological one-point closure for the development of local energy-containing MHD turbulence due to non-linear effects, including both free decay and the possibility of forcing terms that drive excitations at relevant scales. This second step amounts to an adaptation for MHD of the simplest Kolmogorov-Obukhoff-Batchelor theory for the decay of the energy-containing eddies in hydrodynamic turbulence, such as that produced by grid generation in wind tunnels. Note that for the present purposes, we entirely ignore the methods that have been proposed for modeling non-linear effects in the energy-conserving inertial range [*Tu et al.*,

1984; Tu, 1988; Zhou and Matthaeus, 1990b]. Those approaches are based on the equilibrium conditions of the inertial range and are inappropriate for the quasi-equilibrium conditions in the energy-containing range [Batchelor, 1970].

6.2 The Linear Transport Terms

Just as in the inertial range model, the fluctuations of interest (the energy-containing eddies), interact with a weakly inhomogeneous background solar wind plasma, as well as undergoing their own local dynamics. That is, scale separation is again used to obtain a simplified system of dynamical equations. In this section we construct the linear transport terms for these eddies.

For our phenomenological treatment of the energy-containing eddies, we do not require equations for the evolution of the full correlation functions; only bulk (spatial) quantities need be followed. For our purposes these quantities are the magnetic and kinetic energy densities, the cross helicity, and correlation scales for each quantity. This is equivalent to specifying the equations for the transport of the Elsässer “energies” of the fluctuations, their correlation scales, and the energy difference. In the most general case, the helicity of each field would also need to be followed, along with length scales for these quantities. However, we will assume non-helical turbulence.

The most direct way to obtain the required equations is to start with the evolution equations for the correlation tensors of the Elsässer variables, take their traces, and set the spatial separation variable equal to zero. The relevant equations are found in Zhou and Matthaeus [1990a] as equations (49) and (59), and in Chapter 4 as equations (4.11) and (4.18). Hereafter we will not reference equations in Zhou and Matthaeus, instead referring to the equivalent equations in Chapter 4.

We introduce the following notation,

$$\begin{aligned} Z_{\pm}^2 &= \langle |\mathbf{z}^{\pm}|^2 \rangle \\ &= H_{jj}(r=0), \end{aligned} \tag{6.1}$$

$$\begin{aligned} D &= \langle \mathbf{z}^+ \cdot \mathbf{z}^- \rangle \\ &= \Lambda_{jj}(r=0), \end{aligned} \tag{6.2}$$

which are respectively twice the Elsässer energies and the residual energy (energy difference) of these fluctuations. Particularly in association with the solar wind solutions, we will also use the more mnemonic symbols E^{\pm} in place of Z_{\pm}^2 . The correlation scales of Z_{\pm}^2 and D are denoted by λ_{\pm} and λ_D . For technical reasons (see Matthaeus *et al.* [1993a]), we will work with the energy weighted correlation lengths

$$L_{\pm} = Z_{\pm}^2 \lambda_{\pm}, \tag{6.3}$$

$$L_D = D\lambda_D, \quad (6.4)$$

rather than the more physical λ 's.

To close the set of equations for Z_{\pm}^2 , D , and λ_{\pm} describing the energy-containing MHD eddies, we assume that the helicities of the magnetic field and velocity field vanish, as does the induced MHD electric field. Furthermore, the turbulence is assumed to be isotropic, either in the usual 3D sense, or in the 2D sense defined in section 5.2.3. After some simple manipulations of the correlation function equations referred to above, we find

$$\frac{\partial Z_{\pm}^2}{\partial t} + (\mathbf{U} \mp \mathbf{V}_A) \cdot \nabla Z_{\pm}^2 + Z_{\pm}^2 \nabla \cdot \left(\frac{\mathbf{U}}{2} \pm \mathbf{V}_A \right) + M^{\pm} D = NL_E^{\pm}, \quad (6.5)$$

$$\frac{\partial D}{\partial t} + \mathbf{U} \cdot \nabla D + D \frac{\nabla \cdot \mathbf{U}}{2} + \frac{1}{2} [M^- Z_+^2 + M^+ Z_-^2] = NL_D. \quad (6.6)$$

For the energy-containing range, the effective mixing operators M^{\pm} are defined by

$$M_{iso}^{\pm} = \frac{1}{R} \left[\frac{U}{3} \mp V_{Ar} \right], \quad (6.7)$$

$$M_{2D}^{\pm} = \frac{1}{R} \left[U \cos^2 \psi \pm V_{Ar} (3 \cos^2 \psi - 2) \pm \frac{1}{2} V_{Ar0} \left(\frac{\Omega R_0}{U} \right) \left(2 - \frac{3R_0}{R} \right) \sin \theta \sin 2\psi \right], \quad (6.8)$$

and we have immediately specialized to the case where the large-scale fields are given by $\mathbf{U} = U\hat{\mathbf{R}}$, and $\mathbf{B}_0 = \mathbf{B}_{Parker}$ (see page 81). These mixing operators play the same role as the corresponding operators considered in the context of inertial range transport, being related to the strength of the coupling between the small-scale Elsässer fields. As in that case, they can be interpreted as representing the scattering of \mathbf{z}^{\pm} fluctuations off large-scale gradients and inhomogeneities in the slowly varying mean fields. Much of the information presented in section 4.4 and Appendix C is directly relevant to the energy-containing situation, and we will therefore not give the details regarding the particular forms for the M^{\pm} . As discussed in section 4.4, because the M^{\pm} operators are inversely proportional to R , their influence will be most important in the inner heliosphere (physically, the large-scale gradients of the mean fields are shallower in the outer heliosphere).

The terms on the right of equations (6.5)–(6.6) represent the non-linear interactions that are responsible for spectral transfer. In the energy containing range, these terms also cause the Elsässer energies to decay. Modeling of these terms will be discussed in a later section. Note that in deriving (6.6), a correlation tensor that depends upon the induced electric field has been neglected, since it vanishes when all spectral and correlation functions are isotropic. In a broader context, this term would have enforced oscillations in the dynamical behavior of D , with a frequency

proportional to V_A . This would drive D towards zero on average, and is in fact, the contribution of the uniform magnetic field to the Alfvén effect. This ingredient of the dynamics of D will be taken care of when the non-linear model for D is developed.

We define the Elsässer correlation lengths, in analogy with similar hydrodynamic quantities [*e.g.*, *Batchelor*, 1970], by

$$\begin{aligned}\lambda_{\pm} &= \frac{\int dr \langle \mathbf{z}^{\pm} \cdot \mathbf{z}^{\pm'} \rangle}{\langle |\mathbf{z}^{\pm}|^2 \rangle} \\ &= \frac{\int dr H_{jj}^{\pm}(r)}{H_{jj}^{\pm}(0)}.\end{aligned}\quad (6.9)$$

As in earlier Chapters, the primed and unprimed quantities are evaluated at spatial positions separated by distance r , the direction being immaterial for this definition of the correlation length when the turbulence is 3D isotropic. In the 2D case, r should be chosen to lie in the plane of the turbulence, but is otherwise unrestricted. Transport equations for the $L_{\pm} = Z_{\pm}^2 \lambda_{\pm}$ are obtained by integrating the contraction of equation (4.11) over the spatial separation variable r . The result is the pair of equations

$$\frac{\partial L_{\pm}}{\partial t} + (\mathbf{U} \mp \mathbf{V}_A) \cdot \nabla L_{\pm} + L_{\pm} \nabla \cdot \left(\frac{\mathbf{U}}{2} \pm \mathbf{V}_A \right) + \int \Pi_{ii}^{\pm}(\mathbf{r}) dr = NL_{\lambda}^{\pm}, \quad (6.10)$$

which contain the required dynamical information concerning the correlation scales λ_{\pm} . Here, from equations (4.12)–(4.13), and the definition $F_{ij}^s = 2R_{ij}^{Ds}$, introduced in Chapter 3, we have

$$\begin{aligned}\Pi_{ii}^{\pm}(r) &= -\nabla \cdot \left(\frac{\mathbf{U}}{2} \pm \mathbf{V}_A \right) R_{ii}^{Ds}(r) + 2R_{ij}^{Ds}(r) \left(\frac{\partial U_i}{\partial R_j} \pm \frac{1}{\sqrt{4\pi\rho}} \frac{\partial B_{0i}}{\partial R_j} \right) \\ &= 2R_{ij}^{Ds}(r) M_{ji}^{\pm}(\mathbf{R}),\end{aligned}\quad (6.11)$$

where R_{ij}^{Ds} is the index symmetric portion of the energy difference correlation tensor. The integration in (6.10) is over the local, small-scale separation variable r , so the large-scale variables and their derivatives are treated as constants. Because the small-scale turbulence is assumed to be incompressible and isotropic, there is a constraint between the diagonal and off-diagonal components of the symmetric part of the velocity correlation tensor R_{ij}^{vs} [*e.g.*, *Orszag*, 1977]. A similar statement is true for the magnetic fluctuation correlation tensor, leading to the expression:

$$\int_0^{\infty} R_{ij}^{Ds} dr = \frac{1}{4} D \lambda_D (\delta_{ij} + \hat{r}_i \hat{r}_j), \quad (6.12)$$

where $\hat{\mathbf{r}}$ is a unit vector in the direction over which the integration is carried out.² The correlation length scale for D , *i.e.*, λ_D , is defined by integrating $\langle \mathbf{z}^+ \cdot \mathbf{z}^{-'} \rangle$, in analogy with (6.9) for λ_{\pm} .

² The formula is still valid for 2D turbulence, provided $\hat{\mathbf{r}}$ lies in the plane of the turbulence.

Returning to (6.10), we may now show that

$$\int \Pi_{ii}^{\pm} dr = D\lambda_D \left[\mp \nabla \cdot \mathbf{V}_A + \frac{1}{2} \hat{\mathbf{r}} \hat{\mathbf{r}} : \left(\nabla \mathbf{U} \pm \frac{1}{\sqrt{4\pi\rho}} \nabla \mathbf{B}_0 \right) \right], \quad (6.13)$$

where the colon represents a double inner product. The presence of the $\hat{\mathbf{r}} \hat{\mathbf{r}}$ dyad in equation (6.13) reflects the formal inconsistency of treating the turbulence as locally isotropic when the large-scale flow is non-isotropic. Evidently, the coupling of the small-scale fields to the large-scale flow depends upon whether the fluctuations are along or normal to the mean flow. Since we are assuming small-scale isotropy, one option for simplifying equation (6.13) is to average $\hat{\mathbf{r}} \hat{\mathbf{r}}$ over the total solid angle, the result being $4/\pi$ times the identity tensor. Alternatively, one could choose $\hat{\mathbf{r}}$ to be in some particular direction and ignore the inconsistency. Choosing $\hat{\mathbf{r}}$ normal to the mean flow direction, for example, accentuates effects due to the expansion of solar wind, whereas $\hat{\mathbf{r}}$ parallel to the radial direction is consistent with the practicalities of spacecraft data acquisition. More specifically, the plasma and magnetic field data are collected as a time series at a (fat) point in space, while the mean flow hustles the turbulence by.

At this point we have five transport equations, one for each of the quantities Z_{\pm}^2 , D , and L_{\pm} . Even at the linear level, however, the model is not closed, since terms in λ_D (or equivalently L_D) appear in the equations for L_{\pm} (6.10). To avoid writing an equation for λ_D , we adopt the simple approximation³

$$\begin{aligned} \lambda_D &= \frac{Z_+^2 \lambda_+ + Z_-^2 \lambda_-}{Z_+^2 + Z_-^2} \\ &= \frac{L_+^2 + L_-^2}{Z_+^2 + Z_-^2}. \end{aligned} \quad (6.14)$$

This ‘‘center of mass’’ approximation constrains λ_D to be positive, whereas its definition imposes no such limitation. Indeed in the solar wind, D is usually negative [*e.g.*, *Roberts et al.*, 1987*a, b*], and using processed solar wind data listed in *Matthaeus and Goldstein* [1982*a*] it is straightforward to show that λ_D can be of either sign in the solar wind. As discussed below, we suspect that this approximation is connected with problems associated with numerical solutions of the five-equation model. However, for the moment we have a linear five-equation model.

³ As far as the linear terms are concerned, writing such an equation presents no problems: equation (4.18) need merely be integrated over r , in analogy with the derivation of equations for L_{\pm} . The non-linear terms for this quantity are more problematic however. See also the footnote on page 146.

6.3 Modeling of the Non-Linear Terms

6.3.1 Equilibrium and Quasi-equilibrium Kolmogorov Turbulence

The theory of turbulence due to Kolmogorov, Obukhoff, and others is well described in the classic text by *Batchelor* [1970]. Here we mention a few basic results to provide a background for the extension to MHD. We emphasize the distinction in the simplest theoretical picture between the treatments of inertial range fluctuations and that of energy-containing range fluctuations. This material is complementary in content to that of Appendix A.

The inertial range is most easily characterized by considering fluctuations at length scales that are well separated from both the energy-containing and the dissipation scales. In isotropic turbulence with a steady energy supply rate ϵ driven at wavenumbers much smaller than those in the inertial range, the flux of energy across any spherical shell of wavenumber radius k must equal ϵ . In the simplest form of Kolmogorov's spectral theory one uses dimensional analysis to deduce the relation of this constant ϵ to the wavenumber k and the omni-directional energy spectrum $E(k)$. This yields $E(k) \propto \epsilon^{2/3} k^{-5/3}$. Another approach is to consider the characteristic velocity and time scales for fluctuations near k . For the relevant kind of spectra, $u_k = \sqrt{kE(k)}$ is a typical velocity, while the characteristic time scale is $\tau_k = (ku_k)^{-1}$. From the Navier-Stokes equations, this is also estimated to be the characteristic time scale for non-linear interactions at k . Thus, one can conclude that $\epsilon = u_k^2/\tau_k$ is independent of k , a statement that is essentially equivalent to the Kolmogorov spectral law. The steady, driven inertial range is also sometimes called the equilibrium range of turbulence [*Batchelor*, 1970].

Chapter VII of *Batchelor* [1970] considers the dynamical decay of the energy-containing eddies (say, at scale l and with characteristic flow speed u), which cannot be treated in the manner described above for the inertial range. The key distinction is that these eddies govern the decay of the turbulence, but the timescale for their own decay is the same as that estimated for the non-linear processes affecting them. Consequently, strict equilibrium cannot be achieved. However, the basis of the quasi-equilibrium treatment applicable to this case, is the well known Kolmogorov estimate for the decay rate of the energy-containing eddies,

$$\frac{du^2}{dt} = -\epsilon = -\frac{u^3}{l}. \quad (6.15)$$

This equation forms the starting point for many phenomenological treatments of the decay of hydrodynamic turbulence. It has also been employed by *Coleman* [1968] and *Hollweg* [1986] as an estimate for the decay of solar wind fluctuations. As *Batchelor* [1970] points out, wind tunnel experiments involving grid generated (isotropic) turbulence indicate that the turbulent energy

behaves as $u^2 \propto (x - x_0)^{-1}$, where x is the distance downstream from the grid and x_0 is a constant. Using the *G. I. Taylor* [1938] frozen-in-flow principle, this corresponds to a solution to equation (6.15) of the form $u^2 \propto (t - t_0)^{-1}$, where t is the time and t_0 is a virtual origin in time. For consistency with (6.15), these observations require that $l \propto \sqrt{t - t_0}$, which has been corroborated by experimental evidence that $l \propto \sqrt{x - x_0}$ for distances downstream from the grid [*Batchelor*, 1970].

The behavior of $l(t)$ is crucial, but it is not determined solely by equation (6.15). One must either invoke additional observational information concerning $l(t)$, or make a simple assumption about its dynamics. One consistent possibility is that changes in l are solely due to the value of l and the eddy turnover time τ , the simplest expression of this form is

$$\frac{dl}{dt} = \frac{l}{\tau} = u. \quad (6.16)$$

This equation together with (6.15) forms a simple closed set that reproduces the basic wind tunnel phenomenology, up to order unity constants that could be inserted in either equation. However, to get the experimentally observed forms for $u^2(t)$ and $l(t)$, the ratio between these constants must take a specific value. In fact, inserting constants α and β on the right-hand sides of equations (6.15) and (6.16) respectively, we may obtain *exact* solutions. First rewrite (6.15) as $du/dt = -\alpha u^2/2l$, and divide it by (6.16) to give an equation for du/dl . This ode may be solved by separation of variables. Eventually one obtains

$$\begin{aligned} u &= u_0 [1 + A(t - t_0)]^{-\alpha/(\alpha+2\beta)}, \\ l &= l_0 [1 + A(t - t_0)]^{\frac{2\beta}{\alpha+2\beta}}, \end{aligned} \quad (6.17)$$

where $A = \frac{u_0}{l_0} \left(\frac{\alpha}{2} + \beta\right)$, and $u_0 = u(t_0)$, $l_0 = l(t_0)$ describe the initial data specified at a possibly virtual time t_0 . Clearly, these solutions only go over to the experimentally observed powerlaws if $\alpha = 2\beta$.

An important property of the quasi-equilibrium theory concerns the response of the inertial range eddies to the time dependent energy-containing eddies. In a suitably idealized case, the theory treats the inertial range as remaining in a state of approximate statistical equilibrium, but the energy transfer rate is now time-dependent, and is given by the rate of energy loss from the energy-containing eddies. Within the idealized inertial range of the wavenumber spectrum, one simply replaces the constant supply rate used in the equilibrium theory by $\epsilon(t) = u^3/l$. In this simplest form of the theory, the spectral amplitude in the inertial range is sensitive to the evolution of the energy-containing structures, but the spectral shape is not. This statement is expected to

be valid only in that part of the inertial range far removed from both dissipation wavenumbers and from the energy-containing structures where k is of the order of $1/l$. However, since in the initial application of this model to the solar wind we will only be concerned with steady cases, this issue will not be considered further.

The manner in which the decay of the energy determines the conversion of turbulent energy into heat at the dissipation scales is also clear in the quasi-equilibrium perspective. One can write a quite general equation for the evolution of the spectrum that includes, in principle, the energy-containing, inertial range, and dissipation range wavenumbers:

$$\frac{\partial E(k, t)}{\partial t} = T(k, t) + S(k, t) - \nu k^2 E(k, t), \quad (6.18)$$

[*Batchelor, 1970; Monin and Yaglom, 1971*]. In this equation, E is the wavenumber- and time-dependent omni-directional energy spectrum; T is the energy transfer function representing the changes in the spectrum due to the sum of all non-linear turbulent interactions; S represents the source terms; and the final term, involving the kinematic viscosity ν , is the rate of energy dissipation. The source and dissipation terms are negligible in the inertial range. Because non-linear interactions among eddies conserve total energy, it is always true that $\int dk T(k, t) = 0$. Integrating equation (6.18) over all wavenumbers shows that the heating rate is equal to the driving rate for equilibrium, driven turbulence. In contrast, for freely decaying turbulence, the time derivative of the total energy is balanced by the viscous heating rate. As discussed above, the quasi-equilibrium estimate for the decay rate of the energy-containing eddies is $\epsilon = u^3/l$, which is also the local energy flux function at all higher wavenumbers. Thus, the dissipation rate must be equal to u^3/l . Such an approximation ignores fluctuations in dissipation due to “intermittency” effects [*e.g., Monin and Yaglom, 1971*]

6.3.2 Homogeneous MHD Turbulence

A simple quasi-equilibrium model for the evolution of homogeneous MHD turbulence can be developed in analogy to the well-known hydrodynamic turbulence theory reviewed above. This type of model is usually known as a one-point closure, referring to the use of information (correlation functions) at one point in time and space. Although there has been some discussion in the literature of one-point closure arguments for the evolution of cross helicity [*e.g., Dobrowolny et al., 1980b*], most efforts in the development of MHD phenomenology have concentrated on more elaborate [*e.g., Orszag, 1970, 1977*] two-point closures [*Pouquet et al., 1976; Grappin et al., 1982, 1983*] that require solution of cumbersome spectral evolution equations. Simple one-point closure models may be less accurate than more involved theories, but the physics underlying the turbulence is modeled

in a transparent way, while affording a description that can be readily applied to systems such as the solar wind. To our knowledge, a complete one-point phenomenology of homogeneous MHD turbulence has not been put forth previously. However, most of the required ingredients, such as estimates of time scales for spectral transfer and evaluation of approximate spectral fluxes, have been described elsewhere [*Kraichnan*, 1965; *Pouquet et al.*, 1976; *Dobrowolny et al.*, 1980*b*; *Grappin et al.*, 1982, 1983]. Here, we develop a phenomenology based on many of these previous ideas to describe the decay of MHD turbulence due to direct spectral transfer of energy to ever higher wavenumbers.⁴ We wish to consider isotropic turbulence in both two and three dimensions. However, we will develop the model for 3D isotropic turbulence, deferring consideration of the two-dimensional version until the end of the subsection.

The results of this section are important both in their own right, and as a component of a full solar wind transport model. The former reason encourages us to make this section more or less self-contained, even though it will entail some repetition of earlier definitions.

Denoting by $\mathbf{v}_A = \mathbf{b}/\sqrt{4\pi\rho}$, the fluctuating magnetic field measured in Alfvén speed units, with an assumed constant density, the dissipationless dynamical equations for the fluctuations are then

$$\frac{\partial z^\pm}{\partial t} \mp \mathbf{V}_A \cdot \nabla z^\pm = -\frac{1}{\rho} \nabla P^{tot} - (\mathbf{z}^\mp \cdot \nabla \mathbf{z}^\pm). \quad (6.19)$$

Note that the mean velocity $\langle \mathbf{v} \rangle$ is assumed to be zero; this can always be accomplished for homogeneous conditions by a suitable Galilean transformation. Of particular relevance to the present discussion are estimates for the turbulent decay of the mean-square values of the Elsässer fields, $Z_+^2 \equiv \langle |\mathbf{z}^+|^2 \rangle$ and $Z_-^2 \equiv \langle |\mathbf{z}^-|^2 \rangle$, and of the mean value $D \equiv \langle \mathbf{z}^+ \cdot \mathbf{z}^- \rangle$, where as before $\langle \dots \rangle$ denotes a volume average over a representative parcel of homogeneous turbulence. For completeness, we note again that the kinetic and magnetic energies per unit mass are $E_v = \langle |\mathbf{v}|^2 \rangle / 2$ and $E_b = \langle |\mathbf{v}_A|^2 \rangle / 2$, respectively, and the total turbulent energy per unit mass is $E = E_v + E_b$. The cross helicity is defined as $H_c = \langle \mathbf{v} \cdot \mathbf{v}_A \rangle / 2$, and the difference between the kinetic and magnetic energies (a.k.a. the residual energy) is $E_D \equiv E_v - E_b = D/2$. Note that $Z_\pm^2 = 2(E \pm 2H_c)$. The quantities Z_\pm^2 and D form a convenient set of variables to describe the amplitudes of MHD turbulence, particularly when $\mathbf{V}_A \neq 0$. In addition, we will associate correlation lengths λ_+ and λ_- with the Z_+^2 and Z_-^2 fluctuations, respectively. These lengths reflect the typical size of eddies in the energy-containing range.

⁴ For the present, we ignore the important possibility that inverse spectral transfer to lower wavenumbers may occur in MHD when magnetic helicity is present [*Frisch et al.*, 1975].

As described by *Kraichnan* [1965], *Dobrowolny et al.* [1980b], and *Grappin et al.* [1982, 1983], the decay rates and spectral fluxes of Z_{\pm}^2 and D may be estimated by examining the structure of equation (6.19). To do so, it is necessary to consider several characteristic timescales associated with non-linear couplings among the turbulent MHD fields. First, the non-linear time scale τ_{nl}^{\pm} , analogous to the eddy-turnover time in hydrodynamics, can be estimated as $\tau_{nl}^{\pm} = \lambda_{\pm}/Z_{\mp}$ [*Dobrowolny et al.*, 1980b].

A second important MHD time scale is associated with propagation of Alfvén waves. Packets of \mathbf{z}^{\pm} tend to propagate in opposite directions relative to the local magnetic field direction, under the influence of the large scale magnetic field. This propagation enhances the decay of triple correlations associated with spectral transfer [*Kraichnan*, 1965]. The contribution to this decorrelation due to the uniform component of the magnetic field, for each of the Elsässer fields, depends upon the corresponding time scales $\tau_A^{\pm*} = \lambda_{\pm}/V_A$, where the uniform part of the Alfvén speed is denoted as V_A . However, *Kraichnan*’s original discussion, as well as arguments based upon an examination of closure equations [*Pouquet et al.*, 1976; *Grappin et al.*, 1982, 1983] suggest that the Alfvén wave decorrelation effect, which is highly nonlocal in wavenumber space, depends upon both the uniform component of the magnetic field and also upon the fluctuating magnetic field strength. Consequently, for purposes of estimating effects of wave propagation upon spectral transfer, we use an Alfvén time scale $\tau_A^{\pm} = \lambda_{\pm}/\sqrt{V_A^2 + \langle v_A^2 \rangle}$. This also allows us to incorporate the effect of a varying v_A/V_A , commonly referred to as “ $\delta B/B$ ” in much of the space physics literature.

A third essential timescale is the characteristic lifetime of the triple correlations, which reflects the decay of the energy-containing eddies via the mechanism of spectral transfer [*Kraichnan*, 1965]. In ordinary hydrodynamics, this timescale is the same as the non-linear timescale τ_{nl}^{\pm} , but for MHD the triple lifetime may be governed by effects that propagate at the Alfvén speed [*Kraichnan*, 1965]. It is reasonable to assume that the triple correlations decay at a rate that is the sum of contributions due to both convection and Alfvén wave propagation. Using this argument, one estimates triple correlation lifetimes τ_3^{\pm} for the energy-containing structures that satisfy $(\tau_3^{\pm})^{-1} = (\tau_{nl}^{\pm})^{-1} + (\tau_A^{\pm})^{-1}$ [*Kraichnan*, 1971; *Pouquet et al.*, 1976; *Matthaeus and Zhou*, 1989a]. This expression reduces either to the usual hydrodynamic estimate or to *Kraichnan*’s [1965] estimate in the appropriate limit of the Alfvén speed.

A final important time scale is that associated with spectral transfer and therefore, in the quasi-equilibrium picture, with the turbulent decay of each MHD turbulence variable. In particular, the turbulent decay rate of Z_{\pm}^2 will be of the form Z_{\pm}^2/τ_s^{\pm} , which defines the spectral transfer (or

turbulent decay) time τ_s^\pm for the two Elsässer fields. In theories of spectral dynamics in MHD, rules relating the triple-correlation lifetime, the non-linear time scale, and the spectral transfer rate have been proposed [*e.g.*, *Dobrowolny et al.*, 1980*b*]. We adopt a more general form here [*Matthaeus and Zhou*, 1989*a*; *Zhou and Matthaeus*, 1990*b*] that incorporates the composite triple correlation lifetime described above. Adapting this rule to the energy-containing scales, one finds that $\tau_s^\pm = (\tau_n^\pm)^2 / \tau_3^\pm$.

The one-point estimates for the decay rate of the Elsässer fields can now be easily assembled. The decay rates of Z_\pm^2 are defined by

$$\epsilon_\pm = \frac{Z_\pm^2}{\tau_s^\pm}. \quad (6.20)$$

For purely decaying turbulence, one can then explicitly write an expression for the decay of the Z_\pm^2 amplitudes as

$$\frac{dZ_\pm^2}{dt} = -\frac{Z_\pm^2 Z_\mp^2}{\lambda_\pm (V_A + Z_\mp)}. \quad (6.21)$$

Equations to describe the time evolution of the correlation lengths λ_\pm are also needed, and we can develop them in a manner analogous to the argument leading to (6.16). However, it would be inappropriate to simply write that $d\lambda_\pm/dt = Z_\pm$, since this would lead to correlation lengths that continue to evolve when either one of the Elsässer fields vanishes. As is well known, all turbulent spectral transfer is halted in that case, and the surviving fluctuations continue to propagate as finite-amplitude Alfvén waves [*e.g.*, *Cowling*, 1957]. To resolve this difficulty, one can reinterpret the argument leading to (6.16) in the following way. Let dl/dt depend on l and $\epsilon = u^3/l$, rather than on l and u . For freely decaying hydrodynamic turbulence, one arrives again at the result expressed in (6.16) that $dl/dt = (l\epsilon)^{1/3} = u$. In the same fashion, we can compute $d\lambda_\pm/dt = (\lambda_\pm \epsilon_\pm)^{1/3}$, arriving at

$$\frac{d\lambda_\pm}{dt} = \left(\frac{Z_\pm^2 \lambda_\pm}{\tau_s^\pm} \right)^{1/3}, \quad (6.22)$$

as an acceptable description that gives steady values for both of the correlation lengths when either of the Elsässer fields vanish.

Next, we consider the evolution of the energy difference as represented by the variable $D = 2(E_v - E_b)$. Estimating its turbulent decay rate is not as straightforward as for the Elsässer fields, mainly because it is not an invariant of ideal MHD and therefore is not conserved by non-linear interactions in either the energy-containing or the inertial range. However, on the basis of closure equations [*Pouquet et al.*, 1976] and other arguments [*Fyfe et al.*, 1977], one can argue

that D tends to relax towards zero. This conjectured tendency of MHD towards equipartition of energy between magnetic and kinetic disturbances is known as the ‘‘Alfvén effect’’ [Kraichnan, 1965; Pouquet *et al.*, 1976; Fyfe *et al.*, 1977]. However, this assumption of ‘‘equipartition’’ must be adopted with caution, since closures [Pouquet *et al.*, 1976, Grappin *et al.*, 1983], observations in the solar wind [Matthaeus and Goldstein, 1982a; Roberts *et al.*, 1987a, b], and direct simulations [Matthaeus and Lamkin, 1986; Biskamp and Welter, 1989] all suggest that the magnetic energy in the inertial range may be somewhat larger than the kinetic energy.⁵ In fact, within the inertial range, E_b is frequently on the order of $2E_v$, so including only fluctuations at the relevant scales, $E_D/E \approx -1/3$ [Zhou and Matthaeus, 1989b, 1990a]. The physics of this phenomenon is not yet completely clear. For example, Matthaeus and Lamkin [1986] associated departures of inertial range equipartition with structures appearing in zones of magnetic reconnection, but closures [*e.g.*, Grappin *et al.*, 1983] also show nonequipartition, although they presumably cannot include effects of these coherent structures. Anticipating that a better understanding of departures from the Alfvén effect may be available in the future, we follow the development described by Grappin *et al.* [1983] and Mangeney *et al.* [1991] for assembling a simple phenomenology for the behavior of the energy difference D .

First, the dynamical tendency for the energy difference to decay towards zero due to the Alfvén effect is estimated by a relaxation time $\tau_{AD} = \lambda_D / \sqrt{V_A^2 + v_A^2}$, where λ_D is the correlation scale of D , in accord with the suggestion of Pouquet *et al.* [1976]. Next, the net effect of local wavenumber couplings upon the value of D is estimated using a modification of the arguments of Grappin *et al.* [1983] for the inertial range. The essence of their reasoning was that D is driven at a rate equal to the net spectral transfer rate of the total energy, which from equation (6.20) above is given by $Z_+^2/\tau_s^+ + Z_-^2/\tau_s^-$. This amounts to asserting that as the fields \mathbf{z}^\pm are carried by spectral transfer to higher wavenumber, so is their correlation $D = \langle \mathbf{z}^+ \cdot \mathbf{z}^- \rangle$. The sign of this coupling to D , is that associated with negative values of D in the inertial range, in accord with simulations, closures, and observations [Pouquet *et al.*, 1976; Mangeney *et al.*, 1991]. We instead suppose that only the kinetic energy is involved in this spectral transfer, since the induction equation is linear in \mathbf{b} . The associated spectral transfer time should probably be that associated with the kinetic energy, but to avoid further complicating the model, we assume that this is equal to the spectral transfer time for the total energy, τ_s^{tot} , defined by

$$\frac{d}{dt}(Z_+^2 + Z_-^2) = -\frac{Z_+^2}{\tau_s^+} - \frac{Z_-^2}{\tau_s^-}$$

⁵ In addition, the very largest scale magnetic fluctuations may contain excess energy due to inverse cascade effects [Frisch *et al.*, 1975; Fyfe and Montgomery, 1976].

$$= -\frac{Z_+^2 + Z_-^2}{\tau_s^{tot}}. \quad (6.23)$$

Thus we arrive at a model equation for the time development of D due to homogeneous decay processes,

$$\frac{dD}{dt} = -\frac{D}{\tau_{AD}} - \frac{u^2}{\tau_s^{tot}}, \quad (6.24)$$

where $u^2 = (Z_+^2 + Z_-^2 + 2D)/4$, is twice the fluctuation kinetic energy.

Finally, to determine the relaxation time scale τ_{AD} , the evolution of λ_D is needed. In principle, λ_D requires an additional dynamical equation, however as discussed in section 6.2, to keep the model as simple as possible, we assume that λ_D is determined by the correlation scales λ_{\pm} , and keep dynamical equations for these two length scales only. Rather than simply averaging the independent lengths, we weight them by the amount of the associated energy, and close the model using

$$\begin{aligned} \lambda_D &= \frac{\lambda_+ Z_+^2 + \lambda_- Z_-^2}{Z_+^2 + Z_-^2} \\ &= \frac{L_+ + L_-}{Z_+^2 + Z_-^2}. \end{aligned} \quad (6.25)$$

The preceding arguments lead to a closed, one-point dynamical model for decaying quasi-equilibrium homogeneous MHD turbulence, including magnetic energy, kinetic energy, cross helicity, and two correlation lengths. Not all of the arguments, especially those dealing with the energy difference, are entirely satisfactory, and none of the development is rigorous. In addition, we have entirely neglected the role of the turbulent electric fields and the effect of helicities associated with the magnetic and velocity fields, as well as more exotic quantities such as the ‘‘helicity of the electric field’’ or the ‘‘helicity of the cross helicity,’’ all of which may in principle play a role in MHD turbulence (see *Zhou and Matthaeus [1990a]*, and Chapters 3 and 4). Nevertheless, we assemble the above developments to arrive at the following set of equations:

$$\frac{dZ_{\pm}^2}{dt} = -\frac{Z_{\pm}^2}{\tau_s^{\pm}}, \quad (6.26)$$

$$\frac{dD}{dt} = -\frac{D}{\tau_{AD}} - \frac{u^2}{\tau_s^{tot}}, \quad (6.27)$$

$$\frac{d\lambda_{\pm}}{dt} = (\lambda_{\pm} \epsilon_{\pm})^{1/3}. \quad (6.28)$$

However approximate this model may be, we propose this five-equation model as a phenomenological description of the decay of isotropic MHD energy-containing eddies as a close analogy to the classic, hydrodynamic turbulence models reviewed in section 6.3.1. The inclusion of driving

terms, in the form of energy sources, is relatively straightforward but is left to a future publication [Matthaeus *et al.*, 1993a].

Finally in this section we consider how the above arguments are modified if the turbulence is isotropic in two dimensions rather than three. The only modification we propose is to remove the influence of V_A from the spectral transfer times. Since the turbulence is confined to planes perpendicular to \mathbf{B}_0 , it cannot feel this field, and consequently the dynamics should be independent of \mathbf{B}_0 . The role of the large-scale field is to keep the turbulence two dimensional;⁶ however, implicit in our treatment of 2D turbulence is the assumption that it stays 2D, so that in some sense the role of the applied field has already been played. The net effect then, is that V_A is set to zero wherever it appears in τ_s^\pm , τ_{AD} , or τ_s^{tot} . In this connection we also reevaluate the appropriateness of this term for 3D isotropic turbulence. The term really enters in the form $\sqrt{(\mathbf{k} \cdot \mathbf{V}_A)^2}$, which is directly related to the timescale arising from Alfvén wave effects. It would therefore seem appropriate to average this rate over all directions of \mathbf{k} . For 2D turbulence we have $\mathbf{k} \cdot \mathbf{V}_A = 0$ even without averaging, so that the arguments of the previous paragraph are at least consistent with this conjecture. For 3D turbulence, we average $\cos^2 \theta$ over a wave period to obtain a factor of $\frac{1}{2}$, and we therefore replace V_A^2 in the various spectral transfer times with $V_A^2/2$.

6.4 Application to the Solar Wind

6.4.1 The Model

In equations (6.5), (6.6), and (6.10), the non-linear effects due to triple correlations among the fluctuating fields have been grouped symbolically into terms on the right sides of the equations, NL_E^\pm , NL_D and NL_λ^\pm . The models for homogeneous MHD turbulence given in section 6.3.2 provide simple approximations to these terms, permitting us to close the equations. In this way we arrive at a closed five-equation model for the evolution and transport of locally homogeneous and incompressible MHD turbulence, in externally specified, weakly inhomogeneous, compressible large-scale background fields. This model can now be fully assembled and summarized.

Before proceeding any further with this five-equation model, however, we note that some of its numerical solutions display unphysical behavior. For example, with non-zero large-scale Alfvén velocity, and the non-linear terms “switched on,” seemingly reasonable choices for code parameters produce solutions with significantly negative values of $L_- = Z_-^2 \lambda_-$, at some heliocentric distances. This despite the fact that

⁶ In the solar wind \mathbf{B}_0 also produces a geometrical turning effect, while in the photosphere it is associated with line tying.

- (a) solutions to the linear equations behave acceptably, and
- (b) the code accurately reproduces analytic solutions associated with
 - (i) the linear equations in the limit $\mathbf{V}_A = 0$, and
 - (ii) just the non-linear terms in the Kolmogorov limit where $Z_+^2 = Z_-^2$.

It is our belief that at least part of the problem is associated with the approximation we are using for L_D , namely

$$\begin{aligned}
 L_D &= D\lambda_D && \text{(by definition)} \\
 &\approx L_+ + L_- \\
 &\geq 0.
 \end{aligned} \tag{6.29}$$

However, since neither D nor λ_D are positive definite quantities, L_D should not be constrained in this way. It seems the approximation is missing some important physics. Since we are primarily interested in transport of the various “energies,” as distinct from the correlation lengths, we now simplify the model still further to a four equation version.⁷ Further work related to the five and six equation models is in progress (see also *Matthaeus et al.* [1993a]), but the results here will deal solely with the four equation version of the model.

Defining the single correlation length, λ , by $L = L_+ + L_- = (Z_+^2 + Z_-^2)\lambda$, and adding equations (6.10) we obtain

$$\frac{\partial L}{\partial t} + \mathbf{U} \cdot \nabla L + L\nabla \cdot \frac{\mathbf{U}}{2} + (\hat{\mathbf{r}}\hat{\mathbf{r}} : \nabla\mathbf{U})D\lambda_D = NL_L, \tag{6.30}$$

where we have dropped terms involving $L_+ - L_-$. This may be motivated on several grounds. First, it is equivalent to insisting that this quantity evolves independently in WKB-like fashion ($\sim 1/R$), with no non-linear terms. Second, solar wind observations near 0.3 AU [*Tu et al.*, 1989a] may be used to obtain estimates for λ_{\pm} and L_{\pm} . The values obtained suggest that the L_{\pm} are approximately equal (to within a factor of 2 or so), in both high and slow speed streams. On the other hand for the plasma samples shown in their paper, λ_+ is some 6 or 7 times bigger than λ_- , again more or less independent of the mean flow speed.

The non-linear terms for L are modeled as

$$NL_L = -\lambda \left(\frac{Z_+^2}{\tau_s^+} + \frac{Z_-^2}{\tau_s^+} \right) + (Z_+^2 + Z_-^2)\sqrt{Z_+Z_-}, \tag{6.31}$$

⁷ A six equation model involving a separate equation for the transport of L_D is another possibility. Integration of equation (4.18) with respect to the small-scale separation parameter \mathbf{r} , yields the linear terms, and appropriate non-linear terms may be devised. Unfortunately, numerical solutions to this set of equations display inconsistencies similar to those of the five-equation model.

i.e., $d\lambda/dt = \sqrt{Z_+ Z_-}$. In accordance with the discussion of section 6.3.2 and theory, the right-hand side of this last equation vanishes when either Elsässer variable vanishes, while retaining the character of being a characteristic velocity (\sim a length over a time).

Using equations (6.26)–(6.28) in (6.5)–(6.6), and substituting the large-scale fields defined on page 81, we arrive at the complete model for the non-linear evolution of MHD energy-containing eddies in the solar wind:

$$\frac{\partial Z_{\pm}^2}{\partial t} + (U \mp V_{AR}) \frac{\partial Z_{\pm}^2}{\partial R} + \frac{(U \pm V_{AR})}{R} Z_{\pm}^2 + M^{\pm} D = -\frac{Z_{\pm}^2}{\tau_s^{\pm}}, \quad (6.32)$$

$$\frac{\partial D}{\partial t} + U \frac{\partial D}{\partial R} + \frac{U}{R} D + \frac{1}{2} [Z_+^2 M^- + Z_-^2 M^+] = -\frac{D}{\tau_{AD}} - \frac{u^2}{\tau_s^{tot}}, \quad (6.33)$$

$$\frac{\partial L}{\partial t} + U \frac{\partial L}{\partial R} + \frac{U}{R} L = -\lambda \left(\frac{Z_+^2}{\tau_s^+} + \frac{Z_-^2}{\tau_s^-} \right) + (Z_+^2 + Z_-^2) \sqrt{Z_+ Z_-}. \quad (6.34)$$

For isotropic turbulence we choose $\hat{\mathbf{r}}$ parallel to the mean flow, so that the dyadic term involving it in equation (6.30) is zero. For the 2D case, we take $\hat{\mathbf{r}}$ perpendicular to both \mathbf{R} and \mathbf{B}_0 , so that again the term involving the dyadic vanishes.

For completeness, recall that the spectral transfer times can be written, according to the approximations leading to (6.20) and (6.21), as

$$\tau_s^{\pm} = \lambda \frac{V_A + Z_{\mp}}{Z_{\mp}^2}, \quad (6.35)$$

where we have replaced the λ_{\pm} in equation (6.20) by the single correlation scale remaining in the model, λ . One should note that analytical estimates of τ_s^{\pm} might also be obtained from more elaborate theoretical treatments than the one described above. For example, an MHD eddy-viscosity theory could be developed along the lines of the Heisenberg theory, or by using renormalization group methods [Zhou *et al.*, 1988, 1989; Zhou and Vahala, 1990] or MHD Direct Interaction approximations [*e.g.*, Yoshizawa, 1988, 1990]. It would then be straightforward to use such results by substituting the appropriate expressions into (6.32)–(6.34) rather than using (6.35). We also recall that, with the approximations cited in Section 6.3.2, the Alfvénic relaxation time τ_{AD} of the energy difference is

$$\begin{aligned} \tau_{AD} &= \frac{\lambda}{\sqrt{V_A^2 + v_A^2}} \\ &= \frac{\lambda}{\sqrt{V_A^2 + (Z_+^2 + Z_-^2 - 2D)/4}}. \end{aligned} \quad (6.36)$$

The λ which appears in this equation should really be a λ_D , however this quantity is not available in the four equation model. In its place, we insert the single correlation scale being used to characterize

the turbulence. Likewise, if an improved treatment of the decay of the energy difference becomes available, a more precise relaxation time could be used in place of (6.36) in solving (6.33).

6.4.2 Numerics

The general numerical method used to solve the transport equations has been discussed in section 5.2.1, in this brief section we will touch on a few specific points related to the energy-containing model. To begin with, since the modeled non-linear terms are all algebraic, *i.e.*, they do not involve derivatives, no special techniques need be adopted to handle them: Direct construction of the terms occurs in “real” space.

Numerous tests of the code were performed. As for the inertial range codes, known analytic solutions for the cases where $V_A = 0$, and the non-linear terms are “off,” are recovered with high accuracy. This provided useful testing of the linear terms for the 2D and isotropic models. The code may also be run with just the non-linear terms active. For the case of no energy decay, steady analytic solutions for D (in terms of E^\pm) exist when $V_A = 0$. Furthermore, if we set the v_A^2 term in τ_{AD} to zero while keeping V_A finite, another analytic solution obtains. In both cases, comparison of numerical and analytic solutions showed at least four significant figures of accuracy.

Another test involved running the codes with $E^+ = E^-$ (no cross helicity), no linear terms, and $V_A = 0$. This Kolmogorov limit of the modeled non-linear terms should correspond to the pure decay problem associated with equations (6.15)–(6.16). Indeed, the exact solutions (6.17) should be recovered. Various choices of initial data (u_0, l_0) and the constants α and β , all produced numerical solutions in excellent agreement with the analytic ones, at all times investigated. In particular, the non-powerlaw behavior of early times, and the powerlaws applicable for late times were both recovered.

As well as allowing run-time specification of the timestep, type of turbulence (2D or isotropic), boundary conditions, values for U, V_{Ar0} , and R_0 , the codes also contained input switches acting as constants multiplying each non-linear term. This simplified testing of the code, as well as supporting physically motivated adjustments to the strength of the non-linear terms, since they are only determined to within order unity constants. However, as discussed in section 6.3.1, in the Kolmogorov limit, the ratio of the multiplicative constants attached to the energy and correlation length terms must take the value $\frac{1}{2}$ in order to recover the experimentally observed solutions. In all the production runs discussed below this was the case, specifically the constants associated with the energy terms (*e.g.*, α_\pm) were set equal to unity, and those attached to the λ (or λ_\pm) terms set equal to 0.5. Unless otherwise noted, the other constants are also unity.

Finally, for each run out to 2 AU discussed below, 65 Chebyshev modes were retained and Δt was $\approx 5 \times 10^{-4}$. Time integration was carried out for twenty characteristic times, these being defined as $T_0 = R_0/U_0$ or ≈ 20 hours in physical units ($U_0 = 100$ km/sec, $R_0 = 10 R_{sun}$).

6.4.3 Solutions

Several numerical solutions will now be presented for the four equation version of the energy-containing model. For each set of initial and boundary conditions, the codes have been run in two states: (a) non-linear terms off, (b) non-linear terms on. Any differences in the results will be clearly attributable to the modeled non-linear terms. Two values of U , the constant solar wind speed, will be considered. In dimensionless code units these are 4 and 7, corresponding to 400 and 700 km/sec respectively. This allowed investigation of the evolution which may occur within high and low speed streams. Recall that typically $U \approx 400$ km/sec in the solar wind. Additionally, for each value of U we will consider two values of V_{Ar0} , namely 0 and 4. As discussed in the preceding chapters, the $V_{Ar0} = 0$ case may be interpreted as corresponding to current sheet type conditions, while $V_{Ar0} = U$ defines an Alfvénic critical point.

Observational values for the fields and correlation lengths at $10 R_{sun}$ are difficult to obtain, so that instead we attempt to choose values for E_0^- and L_0 leading to at least rough agreement with observations at 1 AU. However, such a strategy conflicts with another aim of the investigation, which is to see how the evolution varies when the boundary conditions are fixed, but (i) the type of turbulence changes, and (ii) the non-linear terms are switched on or off. These “all other things being equal” runs provide a clear indication of the effect of the varied parameter(s). It turns out that the values at 1 AU span quite a wide range when such runs are performed, so that it has not been possible to simultaneously hold the boundary conditions fixed and get matching at 1 AU.

Because of the non-linearities involved, significantly different solutions may occur when the boundary conditions are changed. For this reason, and also for those mentioned in the preceding paragraph, we present solutions for only a few sets of boundary conditions. In particular, we will use the “standard” Alfvénic bc’s for the fields, discussed in Chapter 5 (*i.e.*, at R_0 only E^- is non-zero). For the solutions discussed below it is usually the case that $E_0^- = 2$ and $L_0 = 0.4$ in code units. In real units these become $E_0^- = 2 \times 10^4$ km²/sec³ and $\lambda_0 = 2 R_{sun} \approx \frac{1}{100}$ AU. For the $U = 4$ case, these boundary conditions correspond to a $\delta E/U = 1/8$, where δE is the total energy in the fluctuations (recall that $E^+ + E^-$ is four times the physical energy). Note that when $V_{Ar0} \neq U$, R_0 is not the Alfvénic critical point, and consequently the energy in the “inward” modes need not be zero. However, for the reasons discussed above, we use the same bc’s for all values of

U and V_{Ar0} .

We are now ready to present solutions for the two types of energy-containing fluctuations considered. Since definitions of isotropic turbulence and two-dimensional turbulence have been given previously we will not repeat them here (see Chapter 5).

6.4.3.1 Isotropic Turbulence

Figure 6.1 shows the radial evolution for various quantities when the small-scale turbulence is isotropic, the bc's discussed above are imposed, and the solar wind speed is 400 km/sec. Consider first the solid curves, for which $V_A = 0$. The thin lines are the steady solutions to the *linear* equations, which also have an analytic form,⁸ whereas the thick lines denote solutions to the full model including the non-linear effects. While striking quantitative differences in the evolution of E^\pm , σ_c , and σ_D occur, the curves are all qualitatively the same; the linear case showing substantially stronger “mixing.” The two sets of curves indicate that, at least as modeled, the non-linear terms have an important and non-negligible impact on the evolution of the turbulence, with the general effect being to reduce “mixing” and drive the solutions somewhat closer to the WKB forms. Note, however, that they are still far from being WKB in character. As was the case for the inertial range model, the general tendencies for σ_c and σ_D are similar to those observed. For the full model, σ_D saturates at ≈ -0.45 , which is somewhat more negative than the observed value (≈ -0.3), while the normalized cross helicity is approximately flat at a value substantially in excess of the average observed profile.

The broken curves depict the same scenario, except that now $V_{Ar0} = 4 (= U)$; dashed curves are the linear solutions, dotted the full solutions. Again, while the non-linear terms do not change the qualitative behavior of the evolution (except for λ , see below), they do strongly curb “mixing” effects. Indeed, with the non-linear terms on, the $U = V_{Ar0} = 4$ case is essentially WKB-like, with almost unit values of σ_c and r_A prevailing. The growth-decay-growth of E^+ in the near critical point region occurs for the same reasons as in the inertial range case (*i.e.*, M^+ changes sign, see section 5.2.2). Note that the non-linear terms have only a weak effect on E^- (and thus E^{tot}) for this case.

So far we have not mentioned the correlation length λ , which does show a qualitative difference in its radial evolution when the non-linear terms are switched on. When the non-linear terms are off, λ appears to be tending to a constant value. If we were following a length scale for each energy, as in the five-equation model, both lengths would, in fact, be rigorously constant at all

⁸ For these conditions, formal equivalence of the energy-containing and inertial range transport equations occurs, so that they have identical analytic solutions!

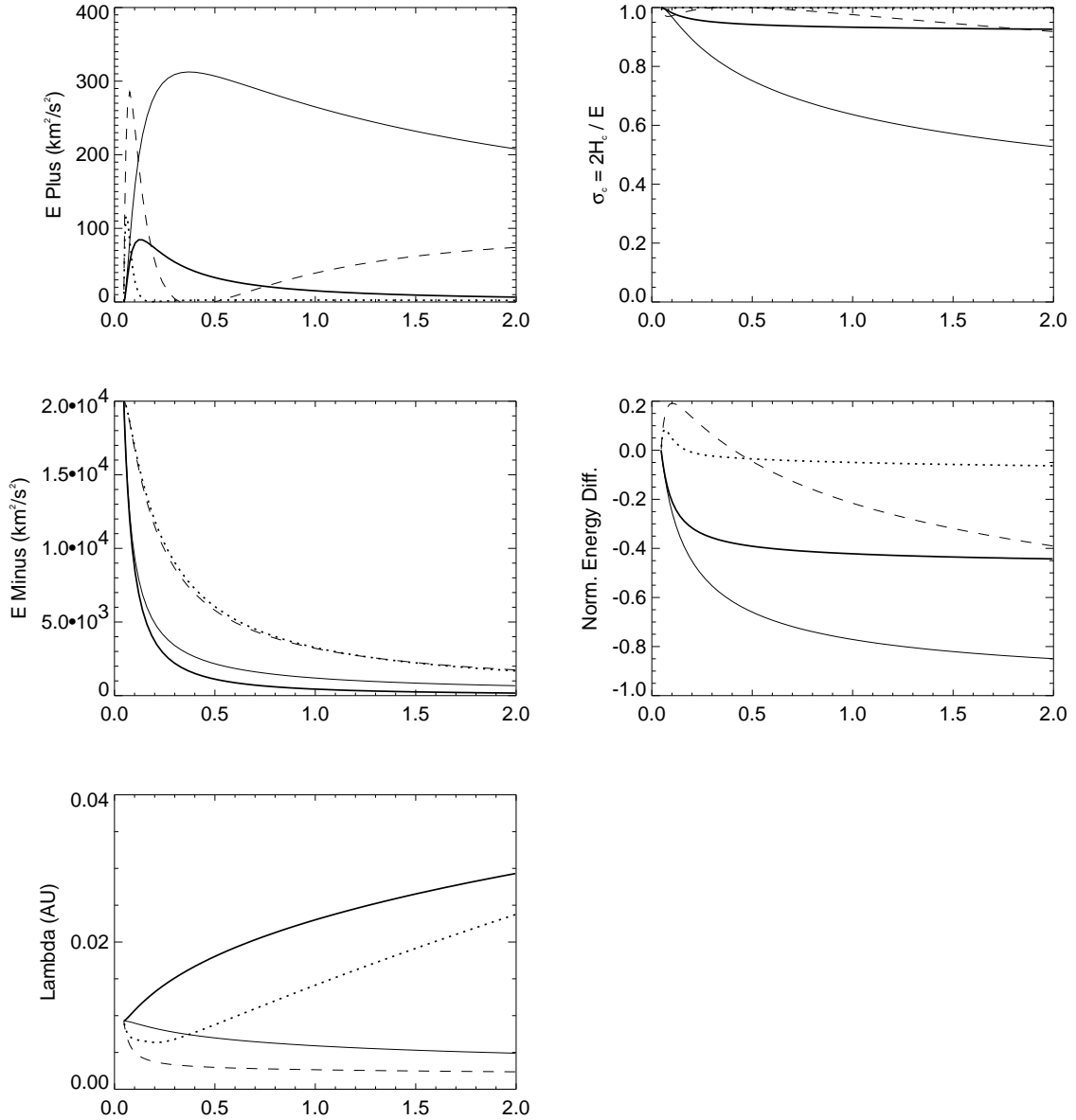


Figure 6.1: Radial evolution of various bulk quantities for isotropic turbulence when $U = 4$ (*i.e.*, solar wind speed of 400 km/sec). Thin solid curves: $V_{Ar0} = 0$, linear terms only; Thick solid curves: $V_{Ar0} = 0$, all terms; Dashed curve: $V_{Ar0} = 4$, linear terms only; Dotted curve: $V_{Ar0} = 4$, all terms. The horizontal coordinate is heliocentric distance (AU).

R . This behavior occurs because the spherical shells characterizing the essentially one-dimensional model have constant thickness, and thus when no non-linearities are involved the scale of the turbulence does not change. In the four equation model there is only a single characteristic length scale, and since it is an average of two distinct and differently evolving length scales, λ only exhibits a tendency towards constancy. Note that in both cases the growth is slower than linear.

Figure 6.2 is identical in kind with Figure 6.1, the difference being that the solar wind speed is now 700 km/sec, which is characteristic of high speed streams. Overall, the behavior shown here is essentially the same as in the corresponding $U = 4$ cases: the non-linear terms reduce “mixing” and generally cause somewhat faster radial decay of E^+ and E^- . While again the non-linear terms have little impact on the evolution of the “outward” energy, for $V_{Ar0} = 4$ the overall level is significantly lower than in the $U = 4$ case: stronger conversion of “outward” energy into “inward” energy has occurred, *i.e.*, stronger “mixing.” As they should be, the linear $U = 7$, $V_A = 0$ solutions are identical to the $U = 4$, $V_A = 0$ ones, the linear equations depending only of the ratio V_{Ar0}/U .

Cross comparisons of the two figures in this subsection show that the $U = 7$ cases mix slightly more than their $U = 4$ counterparts, both in an absolute sense (*e.g.*, the level of E^+) and in the normalized sense (*e.g.*, σ_c). The reasons for this are twofold: (1) the magnitude of the mixing operators increases as U increases (there is more energy available in the large-scale flow), and (2) the distance where M^+ changes sign has decreased because V_{Ar0}/U is no longer unity, *i.e.*, R_0 is not the Alfvénic critical point (see also sections 4.4 and 5.2.2). Qualitatively, however, no differences in the solutions exist.

To summarize, these results suggest that for isotropic turbulence with these boundary conditions

- (1) “Mixing” is relatively unimportant when V_{Ar0}/U is of order unity (or bigger) *and* the non-linear terms are switched on.
- (2) The non-linear terms reduce “mixing” effects, but in general do not remove them.
- (3) Approximate saturation of the normalized quantities occurs within about 1 AU.

As mentioned above, a more extensive investigation of the parameter space will be required in order to verify that these features apply in a wider context.

6.4.3.2 Two-Dimensional Turbulence

Figures 6.3 and 6.4 show the same situations discussed in the previous section for two-dimensional turbulence. We will not discuss these plots in as much detail, since the results are

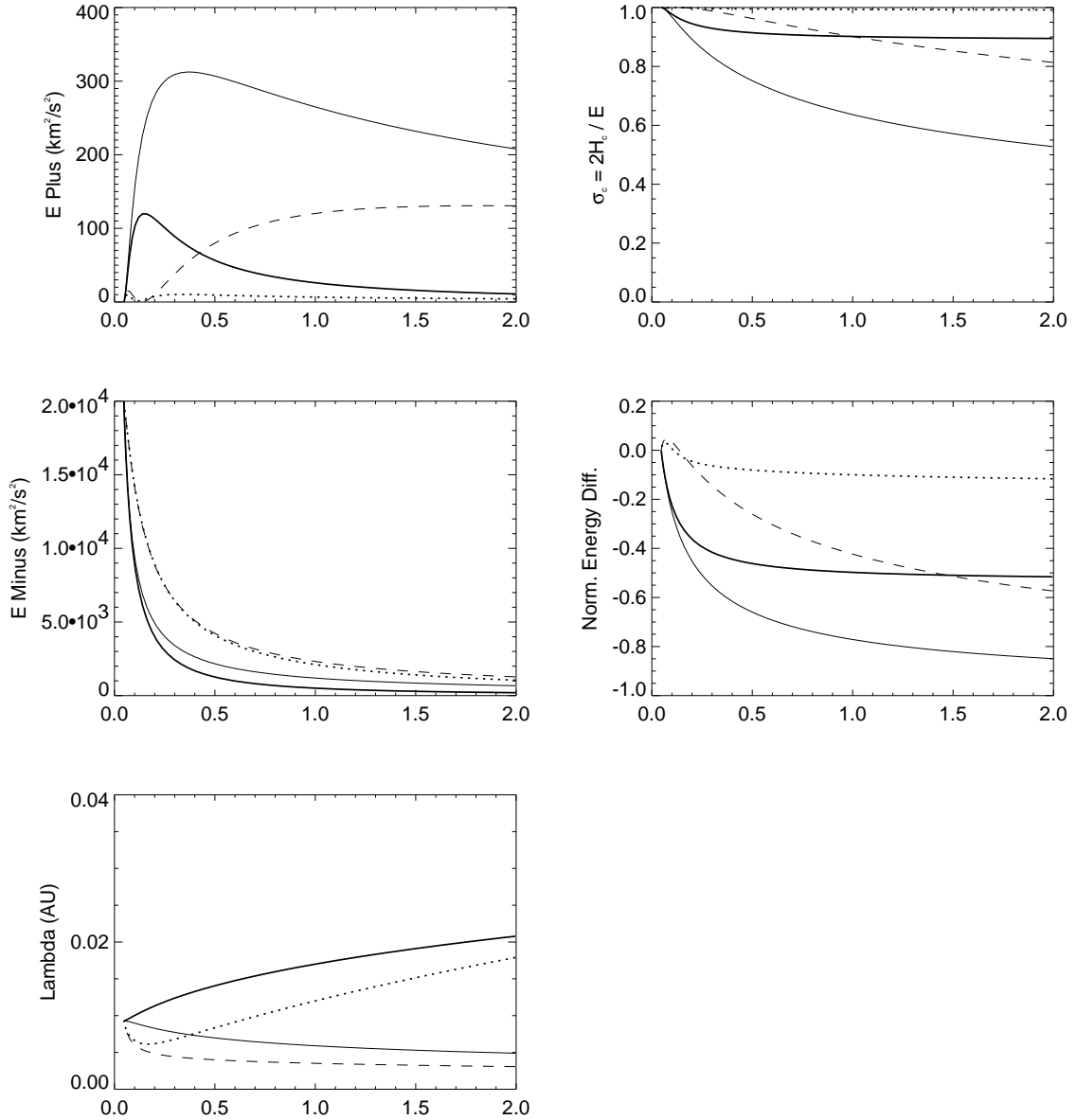


Figure 6.2: Radial evolution of various bulk quantities for isotropic turbulence when $U = 7$ (*i.e.*, solar wind speed of 700 km/sec). Thin solid curves: $V_{Ar0} = 0$, linear terms only; Thick solid curves: $V_{Ar0} = 0$, all terms; Dashed curves: $V_{Ar0} = 4$, linear terms only; Dotted curves: $V_{Ar0} = 4$, all terms. The horizontal coordinate is heliocentric distance (AU).

largely similar to the $V_A = 0$ isotropic cases. However, there are a few points that merit mention.

First, “mixing” is much stronger for 2D turbulence. The mixing operator M^+ is always positive, so that the “inward” energy does not suffer the decay phase occurring in isotropic turbulence. The mixing operators are also bigger in magnitude for the 2D case. As before, the non-linear terms cause a net reduction in “mixing.”

Second, it appears that when the non-linear terms are switched on, after an initially strong “mixing” phase, *dynamic alignment* [Dobrowolny *et al.*, 1980a, b] becomes the predominant evolutionary process. This is a turbulent relaxation process wherein the majority Elsässer species becomes more and more dominant. As this evolution proceeds the non-linear terms get progressively weaker, since they are strongest for approximate equipartition of Elsässer energies, and zero when either field vanishes. A diagnostic for the process is a steady increase in σ_c with time (or heliocentric distance in the supersonic solar wind). The plots shown display such an increase beyond about half an AU, for both the $V_{Ar0} = 0$ and 4 cases. In the high speed solar wind, the process is somewhat slower but still present. We believe that the physics of the situation is as follows. Initially, mixing dominates, producing a substantial component of “inward” modes. When the fraction of the “inward” modes becomes sufficiently large (*i.e.*, σ_c gets sufficiently small) and the mixing operators sufficiently small, a threshold is crossed, elevating the importance of the non-linear terms and allowing dynamic alignment to control the subsequent turbulent evolution. Such evolution is not seen in the solar wind; however, it is possible that it is there and merely masked by other effects.

6.4.4 Heating of the Solar Wind

Figure 6.5 shows the total steady-state heating rate and fractional heating rate for some of the cases considered in the two previous subsections. We define the heating rate by

$$\begin{aligned} \epsilon &= -\frac{dE}{dt} \\ &= -\frac{d}{dt}(E^+ + E^-) \\ &= \frac{E^+}{\tau_s^+} + \frac{E^-}{\tau_S^-}, \end{aligned} \tag{6.37}$$

and the fractional heating rate as $1/E$ times this, or $-d(\log E)/dt$. Since the heating question is sensitive to the actual amount of energy present in the fluctuations, and the simulation values are not the correct ones, these plots do not necessarily describe the correct heating profile for the solar wind, even assuming that the model is correct. However they do serve as indications of the type of heating resulting from such models. The upper panels show the situation for isotropic turbulence

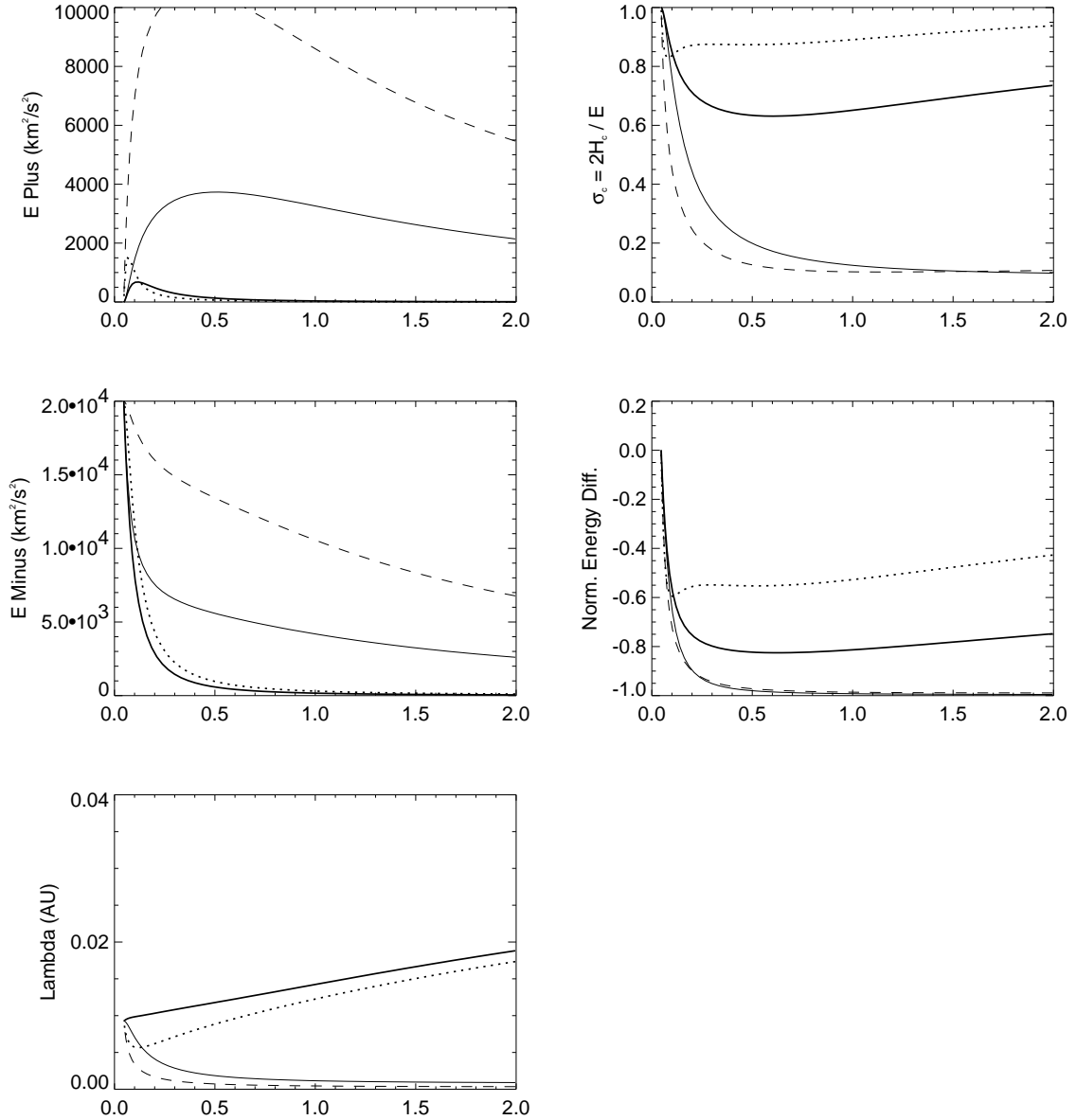


Figure 6.3: Radial evolution of various bulk quantities for 2D turbulence when $U = 4$ (*i.e.*, solar wind speed of 400 km/sec). Thin solid curves: $V_{Ar0} = 0$, linear terms only; Thick solid curves: $V_{Ar0} = 0$, all terms; Dashed curves: $V_{Ar0} = 4$, linear terms only; Dotted curves: $V_{Ar0} = 4$, all terms. Yet again the horizontal coordinate is heliocentric distance (AU).

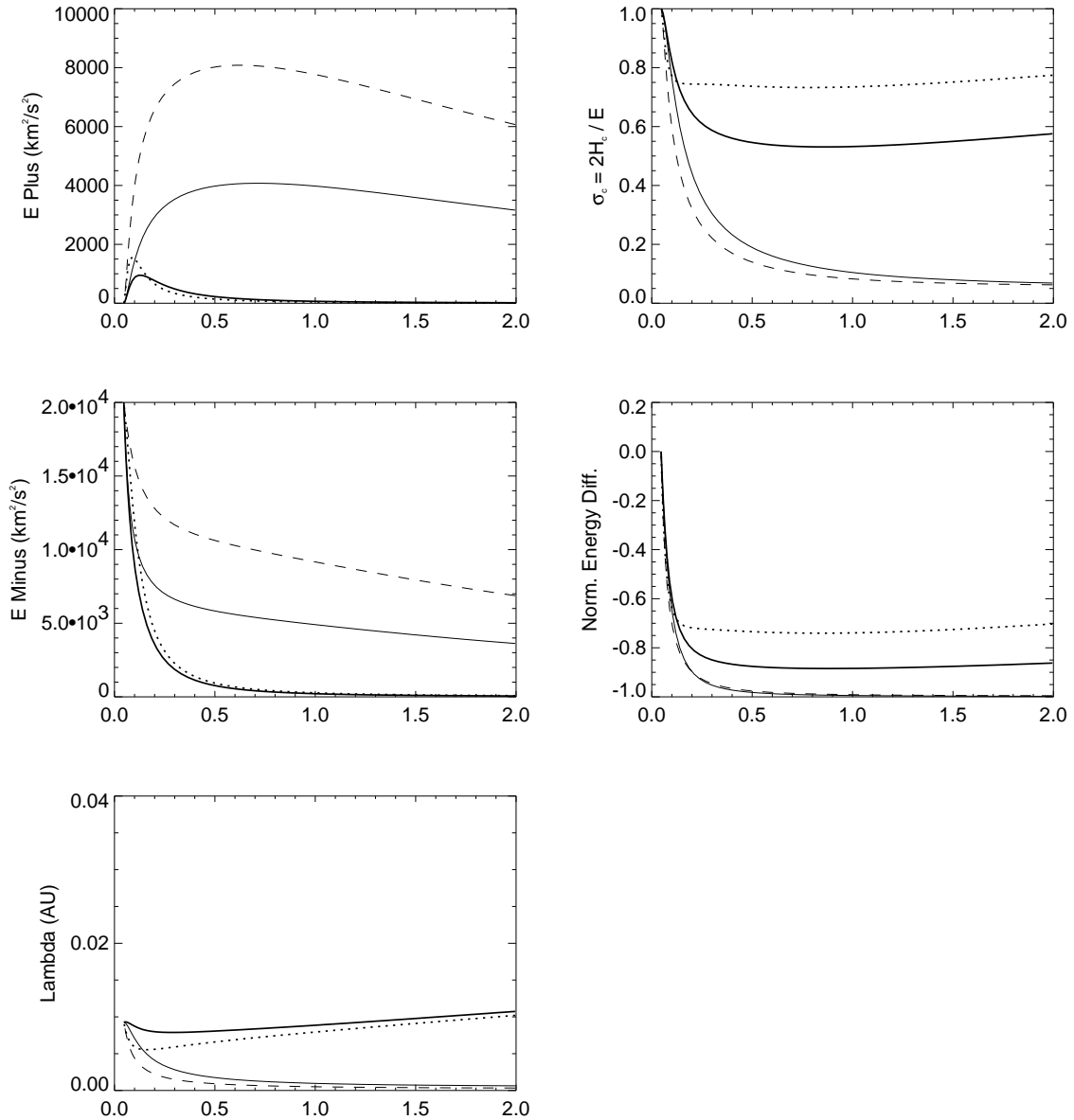


Figure 6.4: Radial evolution of various bulk quantities for 2D turbulence when $U = 7$ (i.e., solar wind speed of 700 km/sec). Thin solid curves: $V_{Ar0} = 0$, linear terms only; Thick solid curves: $V_{Ar0} = 0$, all terms; Dashed curves: $V_{Ar0} = 4$, linear terms only; Dotted curves: $V_{Ar0} = 4$, all terms. The horizontal coordinate is still heliocentric distance in AU.

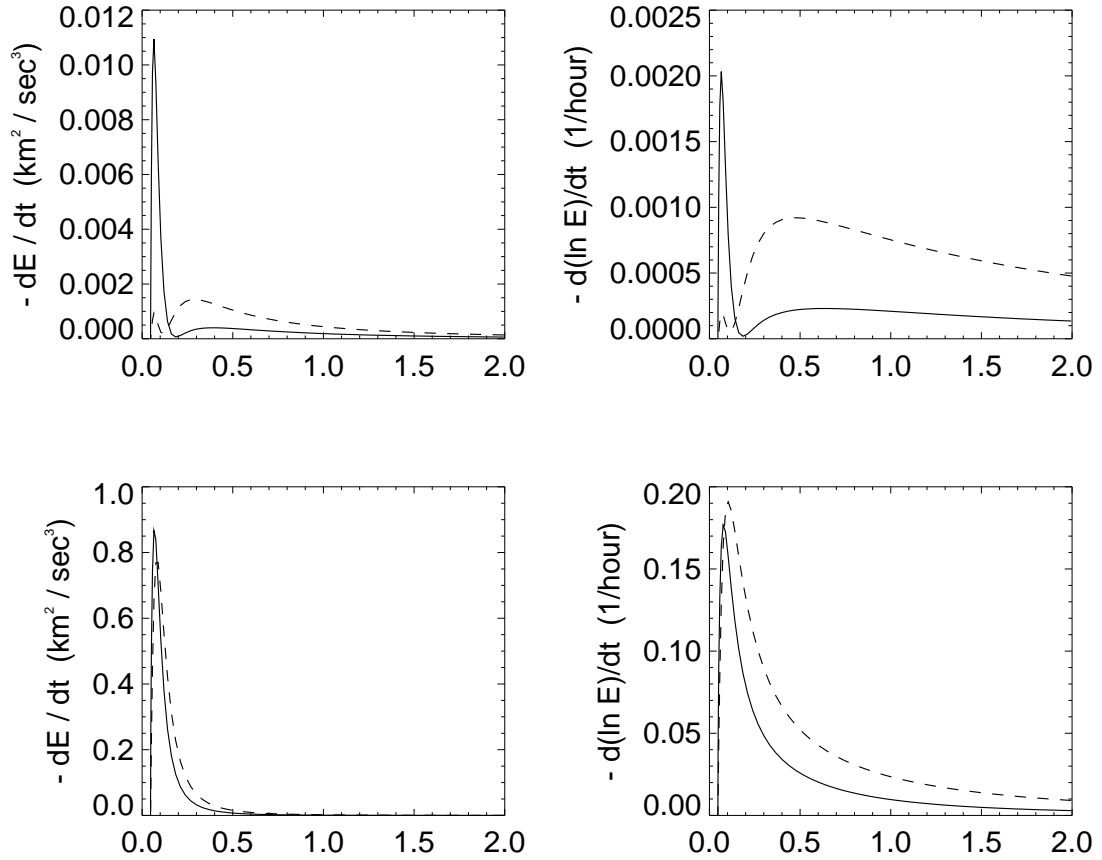


Figure 6.5: Radial profiles of the energy decay rate and fractional energy decay rate, for some of the solutions discussed in section 6.4.3. The “energy” $E = E^+ + E^- = 4(E^v + E^b)$. Upper panels: isotropic turbulence; Lower panels: 2D turbulence. Solid curves: $U = 4$, $V_{Ar0} = 4$; Dashed curves: $U = 7$, $V_{Ar0} = 4$. In each case the boundary conditions were $E_0^+ = D_0 = 0$, $E_0^- = 2$, $L_0 = 0.4$, and $R_0 = 10 R_{sun}$. Once again the horizontal coordinate is heliocentric distance (AU).

and the lower ones for 2D turbulence; solid curves are the $U = 4 = V_{Ar0}$ case, while broken curves are for $U = 7$, $V_{Ar0} = 4$. Some general features are evident.

There is a fairly sharp pulse of heating around 0.1 AU, or about $2 R_0 = 20 R_{sun}$. The pulse height is at least an order of magnitude bigger than the “background” heating associated with other distances. For the high speed wind the pulse is somewhat broader, consistent with the heating occurring over a wider area because the turbulence is being carried along faster. In any case, essentially all of the turbulent energy contributing to the heating of the solar wind is deposited in this region. When the boundary corresponds to an Alfvénic critical point and the turbulence is isotropic, the growth-decay-growth of E^+ serves to localize the pulse more sharply than in the 2D case.

Such a pulse is apparently what is qualitatively required to explain the observed heating profile in the solar wind [*e.g.*, *Isenberg, 1990a*]. Recent work [*Hollweg, 1986; Hollweg and Johnson, 1988; Isenberg, 1990a*] has suggested that solar wind heating occurs beyond the sonic critical point and that localized heating due to turbulence is a viable candidate for such heating. Additionally, it is known that the solar wind properties at 1 AU depend strongly on the spatial heating profile [*Holzer, 1977; Leer and Holzer, 1980*]. However, since we have not included a heat transport equation in the model we will defer further comments along these lines to a later time.

Clearly, all other things being equal, 2D turbulence is a more effective heating agent than isotropic turbulence, the difference being two orders of magnitude for both the absolute and fractional rates. The stronger generation of “inward” modes, coupled with the shorter spectral timescales, are factors responsible for this relative increase; stronger “mixing” giving stronger heating.

6.5 Results from the Full Inertial Range Model

We are finally in a position to produce solutions for the full inertial range transport model. The Elsässer energy fluxes at each point in space, ϵ^\pm , are available from the energy-containing runs, and, as discussed in section 5.3.6, these are used as low k inputs for the spectra in the inertial range model. Computing limitations restricted the number of production runs performed to just two, one isotropic and one 2D. The values of Δt required for stability in these runs were about 2×10^{-6} , and since (for $U = 4$) at least 11 characteristic times must pass for steady-state to be achieved throughout the domain, these runs took a substantial number of Cray hours to complete. Furthermore, while we would have liked to investigate spectra at the boundary with a k^{-1} dependence, runs of this form require still smaller timesteps and have not been achieved to

date. Instead we impose k^{-2} spectra at R_0 , and allow the turbulence to evolve under the influence of the linear transport terms and the modeled non-linear terms. The other run parameters are given in section 5.3.6.

The isotropic run was performed with $U = 4$, and $V_A = 0$. In code units the boundary conditions were $P_0^+ = 10^{-4}$, $P_0^- = 10^{-2}$, and $F = 0$. These values do not lead to spectral amplitudes (as a function of R) that are overly representative of the solar wind, but as noted, we have not yet achieved runs which are. Sample spectra at several heliocentric distances are shown in the top panels of Figure 6.6. As detailed in the figure caption, laboratory units are used in the plots. On the left the radial evolution of $P^\pm(k)$ can be seen. As the inertial range turbulence moves outwards, it decreases in amplitude and evolves towards an approximate Kolmogorov powerlaw. The evolution away from the initial k^{-2} spectrum is rather rapid, for the “inward” fluctuations the spectral slope is approximately $-\frac{5}{3}$ by 0.3 AU. In general, the powerlaws for the “inward” modes are sharper than those for the “outward” fluctuations, an observation that also holds for the 2D run. Between 0.3 AU and 1 AU almost no spectral evolution is seen for the “inward” modes (apart from the overall amplitude decrease), they are in a “steady” state. For the “outward” fluctuations however, spectral evolution is still occurring over this distance. Indeed, there is a slight upward bow to the P^- spectrum at 1 AU. *Roberts et al.* [1991] have recently noted that the lower amplitude of the “inward” fluctuations supports faster evolution toward the inertial range powerlaws, and this run is consistent with their argument.

While not shown, the normalized cross helicity spectrum is almost flat at about 0.95, and shows little radial evolution. For these energy-containing inputs, the non-linear terms have sharply curtailed “mixing” effects. The normalized energy difference is also rather flat, particularly at intermediate wavenumbers. After an initial burst of radial evolution little further change is seen in the spectra: σ_D is saturating at $\approx -1/10$. Recall that the Alfvén effect is associated with greater equipartition of kinetic and magnetic energy at higher and higher wavenumbers.

We may also look at the information in another way. The lower panels in Figure 6.6 depict the radial evolution of the same quantities for a “low,” an “intermediate,” and a “high” wavenumber. In the lower left-hand plot, the thick curves are for P^- , the thin for P^+ . Evidently, at low k there is too much energy in the “outward” modes relative to the supplied fluxes from the energy containing range. However, at higher wavenumbers this situation reverses, in accord with the imposed k^{-2} boundary spectra, which are steeper than the steady spectra. The radial evolution of σ_D for the same three wavenumbers is shown at the bottom right of the figure. As was evident from the spectral plots, after an initial decrease, σ_D saturates at a somewhat k dependent

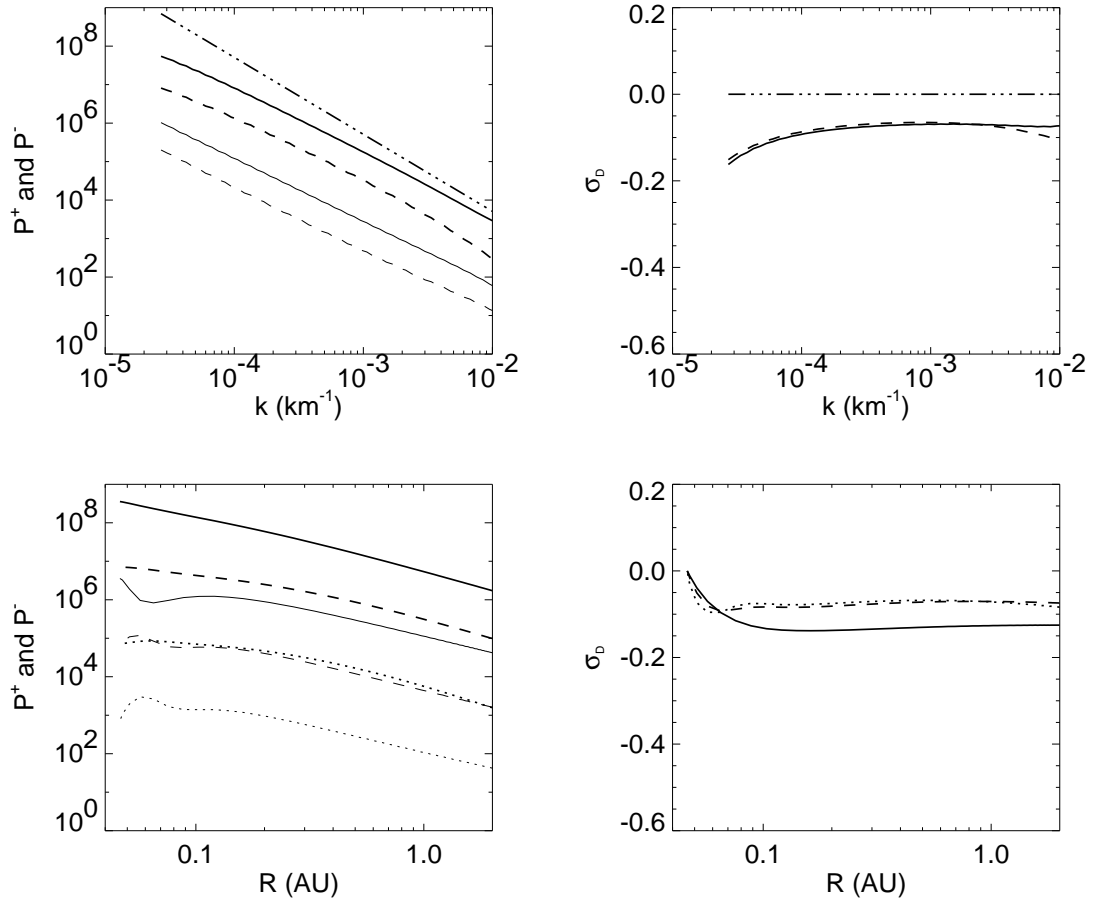


Figure 6.6: Omni-directional spectra at several heliocentric distances, and radial evolution plots for several wavenumbers for the isotropic full inertial range model. In the left-hand panels $P^+(R, k)$ is represented with thin curves, and P^- with thick ones. The power is measured in units of $(\text{km}/\text{sec})^2/\text{km}^{-1}$. Upper panels: Spectra, horizontal coordinate is wavenumber in km^{-1} . Dash-dot-dot-dot: Spectrum of P^- (left) and σ_D (right) at R_0 . Solid curves: $R = 0.3$ AU; Dashed curves: $R = 1$ AU. Lower panels: Radial evolution as a function of heliocentric distance (AU). Solid curves: $k = 3.8 \times 10^{-5} \text{ km}^{-1}$; Dashed curves: $k = 2.7 \times 10^{-4} \text{ km}^{-1}$; Dotted curves: $k = 2.7 \times 10^{-3} \text{ km}^{-1}$.

value, in about a tenth of an AU. The flatness of its spectrum away from the low k end is also evident in this plot.

We turn now to the 2D turbulence run that has been performed. This was a $U = V_{Ar0} = 4$ run, so that R_0 represents the Alfvénic critical point. Despite this, the boundary conditions are the same as those for the isotropic run just discussed, *i.e.*, $P_0^+ = 10^{-4}$, $P_0^- = 10^{-2}$, and $F = 0$ (code units). The same set of wavenumbers spanning three decades was also used. Figure 6.7 is in the same format as Figure 6.6 for the isotropic run. The upper plots are qualitatively similar to the isotropic case, as is to be expected since the non-linear terms are of the same form, and the mixing operators have the same structure for these two cases. This would not be true for an isotropic run with $V_A \neq 0$, as then the M^+ operator changes sign and the Alfvén speed enters into the spectral timescales. The “inward” spectra again quickly evolve to a Kolmogorov powerlaw, which then merely decreases in amplitude as R increases. The “outward” spectra are still evolving at 1 AU, the “upward bow” again being in evidence. The decrease in spectral amplitude with increasing heliocentric distance is comparable for the two runs.

The spectra of the normalized energy difference display a stronger k dependence than those in the isotropic run. Furthermore the actual level is significantly more negative at low wavenumbers. In contrast to the isotropic run, $\sigma_D(k)$ is still evolving between 0.3 AU and 1 AU, in general moving towards zero, and developing a flatter spectrum. Plots for the normalized cross helicity are shown in Figure 6.8. Its spectrum is rather flat but does show radial evolution. We believe this to be a consequence of dynamic alignment, and this will be discussed further below.

Turning now to the radial evolution at a given wavenumber, we see that there is far too little energy in the “inward” fluctuations at the boundary, when compared to the levels associated with the supplied fluxes from the energy-containing range. This deficit of “inward” energy is associated with the strong “mixing” occurring in this region. The rapid growth in the “inward” energies at all wavenumbers leads to a sharp decrease in σ_c close to R_0 (Figures 6.7 and 6.8). However, it appears that this decrease then triggers dynamic alignment, the normalized cross helicity increasing steadily thereafter. The approach towards equipartition of kinetic and magnetic energy ($\sigma_D \rightarrow 0$) is consistent with this conjecture, the final state associated with dynamic alignment being one of the Alfvénic ones (*i.e.*, $v^2 = b^2$).

6.6 Discussion and Closing Remarks

A major aim of the thesis was to elucidate the importance and relevance of “mixing” effects in the solar wind, expanding on the initial work of *Zhou and Matthaeus [1990a, b, c]*. These

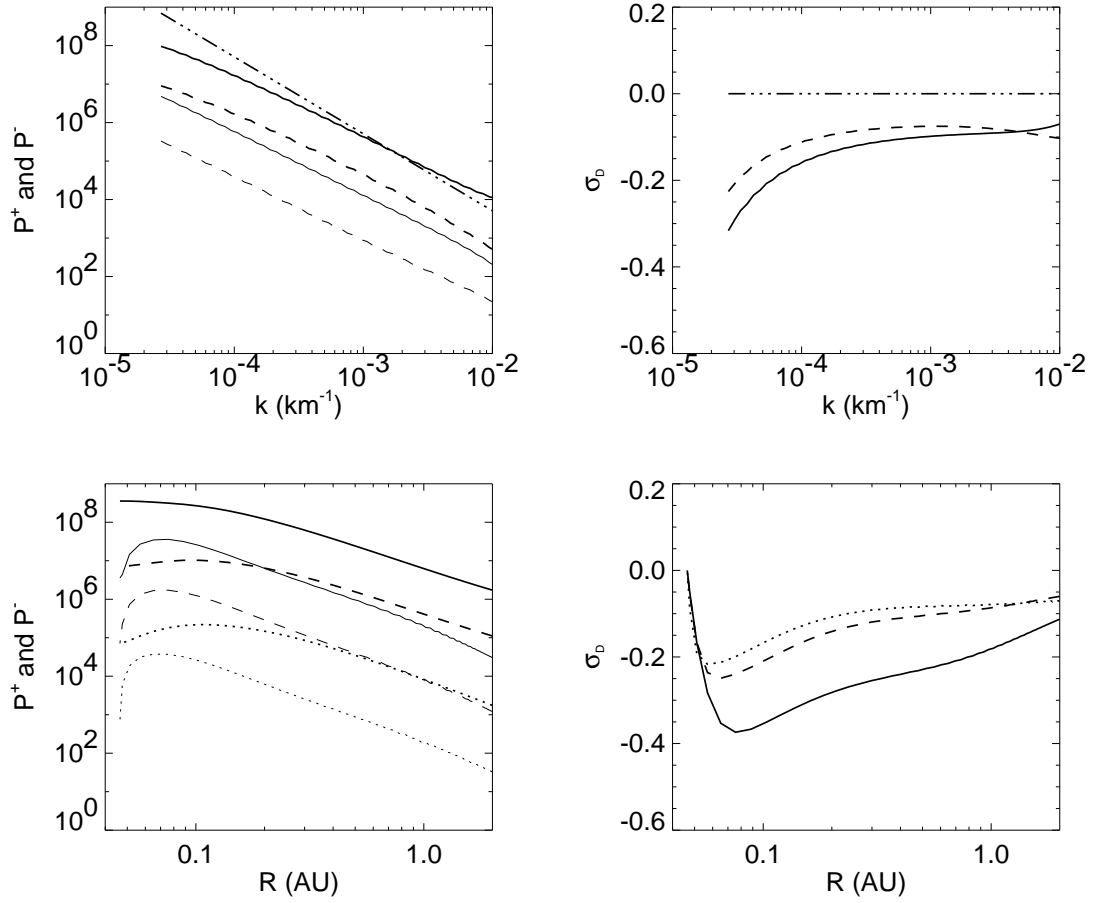


Figure 6.7: Omni-directional spectra at several heliocentric distances, and radial evolution plots for several wavenumbers for the 2D full inertial range model. In the left-hand panels $P^+(R, k)$ is represented with thin curves, and P^- with thick ones. The power is measured in units of $(\text{km}/\text{sec})^2/\text{km}^{-1}$. Upper panels: Spectra, horizontal coordinate is wavenumber in km^{-1} . Dash-dot-dot-dot: Spectrum of P^- (left) and σ_D (right) at R_0 . Solid curves: $R = 0.3$ AU; Dashed curves: $R = 1$ AU. Lower panels: Radial evolution as a function of heliocentric distance (AU). Solid curves: $k = 3.8 \times 10^{-5}$ km^{-1} ; Dashed curves: $k = 2.7 \times 10^{-4}$ km^{-1} ; Dotted curves: $k = 2.7 \times 10^{-3}$ km^{-1} .

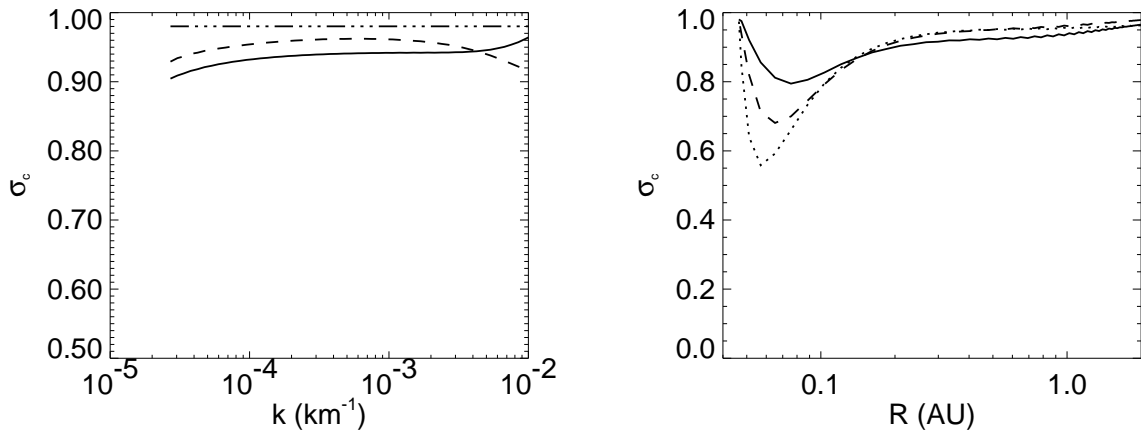


Figure 6.8: Spectra and radial evolution plots for the normalized cross helicity in the full 2D inertial range model run. See Figure 6.7 for details regarding the legend and units.

linear terms can exert leading order influences on the evolution of energy-containing and inertial range fluctuations in the interplanetary medium. In Chapter 5, on the linear evolution of inertial range fluctuations, it was found that small-scale turbulence that is either two-dimensional (with respect to the large-scale magnetic field) or isotropic, is strongly influenced by “mixing” effects in the inner heliosphere, the effect being strongest for 2D turbulence. In this chapter, similar results were achieved when just the linear terms in the energy-containing range model were active. By contrast, inertial range slab fluctuations have been shown to effectively turn off “mixing,” by enforcing equipartition of kinetic and magnetic energy. In general, then, we may say that the more transverse the fluctuations are (relative to \mathbf{B}_0), the more important “mixing” is. These numerical results are in complete agreement with the theoretical analysis presented by *Zhou and Matthaeus* [1990b], and summarized in section 4.5. In this connection, however, we draw attention to the slightly increased “mixing” seen in 2D turbulence as V_{Ar0}/U is increased. This might be thought to be at odds with the tendency identified by *Zhou and Matthaeus* [1990c], which indicates that “mixing” should decrease for such a case. However, fluctuations in the 2D geometry obey $\mathbf{k} \cdot \mathbf{V}_A \equiv 0$, and are therefore already in the resonant “mixing” state; consequently the “inward” and “outward” mode frequencies (ω^\pm , see section 4.5) are equal—*independent* of the value of V_{Ar0}/U . Thus, in this geometry, the speed ratio assists in determining the strength of “mixing” in a way unrelated to arguments concerning whether or not “mixing” is an order one effect.

In section 4.4 it was shown that because in the outer heliosphere the magnitude of the mixing operators is substantially smaller than the other coefficients in the linear equations, “mixing” is unlikely to be an important *direct* effect beyond 1 AU. However, the fluctuations in this region

will still be subject to the indirect influence of “mixing,” in the sense that the properties of the fluid arriving in this region have been determined (in part) by the evolution undergone in the inner heliosphere, where “mixing” is significant for non-slablike fluctuations.

A qualifying statement regarding the weakness of “mixing” in the outer heliosphere should be made at this point. This weakness is in part a consequence of our assumed forms for the large-scale fields. If in place of a constant speed wind, we use one with a more realistic structure, including for example high and low speed streams, their interaction regions, forward and reverse shocks, *etc.*, then “mixing” effects in the outer heliosphere will presumably increase in strength. In fact, we have defined “mixing” rather loosely in this thesis. The general form of the “mixing” tensors (Chapter 4) shows that *any* large-scale gradients in the background fields can couple the small-scale fields together. In this sense, stream interactions and interplanetary shocks, which are dynamical features of the large-scale structure of the solar wind, can also be considered to contribute to “mixing” (see below). The large-scale fields we have used for simplicity provide a lower bound on the *background* influence of “mixing” effects. We should keep in mind that it is really only appropriate to compare the numerical results obtained here with observations from plasma samples that have avoided contact with stream interaction regions, *etc.*, since such contact will lead to locally enhanced “mixing” (in the general sense) which has not been included in the current numerical models.

For isotropic and 2D turbulence, the radial profiles resulting from solutions of the linear transport equations are qualitatively evocative of observational results. This similarity holds for both inertial range and energy-containing range fluctuations. The evolution of the normalized quantities σ_c and σ_D , is particularly pleasing in this regard, since all the solutions tend to have decreasing normalized cross helicity and a saturating normalized energy difference. While this is suggestive of the relevance of “mixing” in the solar wind, inclusion of the non-linear terms indicates that it may be much less relevant than had been postulated [Zhou and Matthaeus, 1990a].

The summary just given has really only considered the *linear* terms in the transport equations. The situations for which this approximation is valid warrant some comment. There are at least two ways in which the full inertial range transport equations can reduce to the linear approximation. First, the non-linear terms can simply be weak and of higher order because the non-linear processes are themselves weak. In this case it is probably, strictly speaking, incorrect to describe the fluctuations as turbulence. Second, the turbulence may be strong enough to keep the inertial range fluctuations close to a statistically steady state, in which case the non-linear terms appear to vanish, at least for conserved quantities like $P^\pm(R, k)$. Despite the common absence of

non-linear terms at order one, the two cases are physically quite distinct. In the former case the non-linearities are weak and largely ineffectual (*i.e.*, higher order), whereas in strong turbulence the non-linear terms act so fast that local equilibrium is always the order of the day (*i.e.*, lower order).

Assuming that the interplanetary turbulence is strong, the results of Chapter 5 suggest several possibilities regarding the evolution of solar wind fluctuations. For example, an approximate idea of the situation prevailing if the turbulence consists of two components, namely a slablike piece with a k^{-1} spectrum [*e.g.*, *Matthaeus and Goldstein*, 1986; *Bieber et al.*, 1993a] and a 2D component with a $k^{-5/3}$ spectrum, may be obtained if we neglect interactions between the components. Even when the turbulence is strong, so that the 2D non-linear terms are effectively zero,⁹ non-linear couplings between the components will still exist in general, and will need to be considered in a complete treatment of the problem.

However, neglecting these effects, the geometrical biasing of the reduced spectra relative to the omni-directional ones (*e.g.*, section 5.2.4) in such a 2D-slab composite, could explain at least part of the observed radial evolution in spectral shapes [*e.g.*, *Tu et al.*, 1989a; *Grappin et al.*, 1990]. Moving radially outwards, the observable reduced spectra would pickup an increasing fraction of the 2D turbulence and a decreasing fraction of the slab fluctuations. This affords another explanation for the “knee” or breakpoint region seen in the spectra, where regions of distinct spectral slopes merge. For such a situation the position of the knee (in k -space) could show radial evolution compatible with the observational results.

While this possibility requires that a substantial fraction of the turbulence is two-dimensional, it is not out of the question that this is the case. Indeed, a correlation function constructed from ISEE 3 data collected at 1 AU admits the interpretation that solar wind fluctuations have both slablike and two-dimensional components [*Matthaeus et al.*, 1991]. We note in passing, that arguments recently presented [*Bieber and Matthaeus*, 1992; *Bieber et al.*, 1993b, c] in the context of cosmic ray scattering and modulation, are consistent with a substantial fraction of the interplanetary turbulence being 2D fluctuations.

What of the cases when the local non-linear terms are of the same order as the linear transport terms? What then is the role of “mixing”? What about the relative strengths of the linear and non-linear terms? The one-point closures used to model the non-linear terms permit these questions to be answered, at least to the extent that such models capture the relevant physics of the processes; we now summarize some of the results obtained with this modeling.

⁹ Recall that for perfect Alfvén waves the non-linear terms exactly cancel.

The relationship of the MHD turbulence models developed for the evolution of the energy-containing eddies and the evolution of the inertial range spectrum [Zhou and Matthaeus, 1989, 1990b; Marsch and Tu, 1990b; Tu and Marsch, 1990b] has been discussed at several points in the thesis, but it is crucial enough to require further amplification. The general picture we envision is largely consistent with the theory of homogeneous hydrodynamic turbulence in the quasi-equilibrium range. Accordingly, most of the turbulent energy resides in the largest of the turbulent eddies, and these energy-containing structures may also be supplied by driving terms acting at their characteristic length scales. Non-linear interactions of the turbulent energy-containing structures subsequently transfer excitations to smaller scales. Much of the dynamical behavior of the smaller scale turbulence is in or near a steady state, and can be viewed as an inertial range where the equilibrium assumptions apply. Ultimately, excitations are transferred to the dissipation range, where MHD flow and magnetic-field energy are converted to heat. The present perspective is that the *rate* at which this spectral transfer occurs is ultimately controlled by the energy-containing eddies. We suggest that the dynamics of the energy-containing structures develop according to the transport theory developed here, in which the wavelengths near the energy-containing scales are treated collectively, and disregard all spectral information pertaining to turbulence at longer wavelengths.

With regard to the turbulent eddies in the inertial range, the important output of the present model is the set of decay rates ϵ^\pm and ϵ_D , which provide boundary data at the low k end of the inertial range of wavenumber space. We have not assumed that the non-linear interactions influencing the energy-containing structures are local in wavenumber [*e.g.*, Rose and Sulem, 1978; Zhou and Matthaeus, 1990b]; however, the dynamics of the inertial range have been treated in this way, as is common in hydrodynamic theory. Consequently, the energy fluxes at the low k end of the inertial range determine the entire structure of the equilibrium near-powerlaw inertial range fluctuations. In our spectral transport model for the evolution of solar wind MHD turbulence in the inertial range, we have included the effects of the evolution of energy-containing structures by using the (steady-state) Elsässer energy fluxes (ϵ^\pm) computed in this range, as boundary conditions for the energy fluxes in the inertial range model. It should also be noted that although the heating rate is associated with the transfer of energy out of the inertial range into the dissipation range, the perspective just outlined views the heating rate as actually being determined by decay rates that are established by the evolution of the energy containing turbulent eddies.

The numerical solutions presented in this chapter included the effects of the modeled nonlinearities, in both the energy-containing and inertial ranges. We draw several conclusions regarding the non-linear terms in the parameter regimes investigated to date. First, the non-linear terms should not be neglected in either the inertial range or the energy-containing range, their influence is significant and in some cases substantial. Second, when both “mixing” and non-linear terms are involved, the net result is generally a reduced, but not removed, “mixing” effect. Third, for 2D turbulence inclusion of the non-linear terms resulted in the activation of the non-linear relaxation process known as dynamic alignment [Dobrowolny *et al.*, 1980*a*, *b*]. In the solutions presented in this chapter, this process took charge of the local dynamics at relatively small heliocentric distances, and subsequently steered the turbulence towards a highly Alfvénic state ($\sigma_c \rightarrow 1$). Unfortunately this behavior is counter to that observed in the solar wind [*e.g.*, Roberts *et al.*, 1987*a*, *b*]. It had been thought that the resolution of this mystery might be “mixing.” However, with the inclusion of the non-linear terms in the solar wind models discussed in this thesis, it appears that this is no longer a viable possibility¹⁰—unless the *effective* impact of the non-linear terms can be reduced. Investigations along these lines are in progress.

For example, it may be that we have over-estimated the strength of the non-linear terms. Perhaps the appearance of dynamic alignment in the numerical solutions for two-dimensional turbulence is a consequence of such an over-estimation. Another possibility is that we have made the decay time for the energy difference too small, thus driving it towards zero so quickly that “mixing” is turned off almost as soon as it starts. As the modeling of the turbulence can be fine-tuned by introducing order unity constants in several of our estimates of the non-linear terms, generally speaking, it may be necessary to optimize these parameters to obtain the best possible agreement of this kind of model with data from observations or numerical simulations. For simplicity, we have largely ignored these constants in this work—the single exception being the relationship between constants associated with the non-linear terms for the energies and correlation length(s) in the energy-containing model, which was chosen to afford agreement with experimental results from hydrodynamics in appropriate limits [*e.g.*, Batchelor, 1970]. We are currently investigating physically motivated adjustments to these order unity constants. Such adjustments may also be justifiable on the basis of the multiple scales analysis used to derive the transport equation hierarchy [Matthaeus *et al.*, 1993*b*], indeed, their origin may be such that adjustments of their strength relative to the linear terms is mandated. One point closure theory has little to say regarding the

¹⁰ We are again speaking of the “background” “mixing” arising from the simple, essentially structureless form of the large-scale solar wind used throughout the document, rather than the more localized “mixing” resulting from stream interactions for example.

values of these constants, and indeed, in engineering treatments of inhomogeneous hydrodynamic turbulence, for example K - ϵ models [Jones and Launder, 1972; Bradshaw *et al.*, 1981], these constants are obtained by fits to experimental data. These fits may be useful as guidelines in attempts to optimize the behavior of the MHD model.

A key approximation in the current development has been that the large-scale density, velocity field, and magnetic field have been treated as *a priori* specified functions of space and time. All of the solutions presented in this work, have been based on the simplest picture of the large scale structure of the solar wind; namely, that it can be represented by constant speed radial flow, a Parker spiral magnetic field, and a density field proportional to $1/R^2$. In view of the energetic dominance of the nearly radial solar wind flow, this approximation is generally regarded as reasonable for many applications.

Without abandoning this approach, we may take into account the important possibility that the turbulence is driven by shear stream instabilities [Roberts *et al.*, 1992]. Simplistically, these instabilities inject energy into the turbulence but not cross helicity, so that their presence at multiple distances can lead to a decrease of σ_c with distance. Such effects could be included in the present model, in an approximate way, by including driving terms in the energy-containing model [Matthaeus *et al.*, 1993a]. Presumably these terms could be approximated by consideration of MHD Kelvin-Helmholtz growth rates, and estimation of stream shear strength and associated length scales. For example, in the five-equation model for homogeneous MHD turbulence (section 6.3.2), the equations for the evolution of the length scales (6.28) may be simply adapted to include driving effects [Matthaeus *et al.*, 1993a]. However, to investigate transient phenomena, the effects of stream structure, *etc.*, one would need to allow the large-scale fields to have both time dependence and more complicated space dependencies. In principle, the present models for computing the approximate evolution of the turbulence are general enough to be adapted for such extended treatments, provided that the local rotational symmetry properties of the turbulence (*e.g.*, isotropic, 2D) remain an acceptable approximation. Moreover, it is feasible to utilize the local turbulence models described above while also allowing the large-scale fields to change according to a set of coupled dynamical equations, such that the influence of the turbulence on the large-scale dynamics might be incorporated.

While we have obtained some important insights and results from this work, much remains to be done. The MHD turbulence models developed above for inertial range and energy-containing range wavenumbers, are far from being an exact treatment of inhomogeneous turbulence in the solar wind. However, a number of important physical effects are incorporated here that have

been neglected in previous treatments of the problem. Local turbulence is treated by one-point closures, including direct energy transfer for each of the \mathbf{z}^{\pm} Elsässer fields, so that the influence of cross helicity is maintained at some reasonable level. The influence of a possible imbalance in the kinetic and magnetic energy densities is also included, albeit incompletely since we have only a crude estimate of the decay rate of the energy difference and the effect of the energy difference on the cascade of the Elsässer fields has not been included. On the linear side, transport equations for both “inward” and “outward” fluctuations are included, along with those for other quantities pertaining to the small-scale turbulence. Large-scale inhomogeneous effects treated in the models include advection, Alfvén wave propagation, expansion, large-scale density gradients, and “mixing” effects that couple the “ \pm ” fields. Absent are the effects of induced electric fields and of magnetic and kinetic helicities; investigation of their role in solar wind transport theory must await the development of more complete models.

In closing we note that many questions regarding the solar wind have yet to be answered, either at all or with sufficient clarity and understanding. For example, observations have been largely confined to the near ecliptic regions of the heliosphere. The continuing journeys of the Pioneer and Voyager interplanetary spacecraft will rectify this deficiency somewhat, as will data received from the recently launched Ulysses probe as it wends its way over the sun’s polar regions. Such data will no doubt prove invaluable in correcting and refining current models and theories of the solar wind, and perhaps also in the seeding of entirely new thinking regarding the physics of the medium. We anticipate that refinements to models such as those presented here may be useful in examining and understanding the dynamical behavior uncovered by these experimental explorations.

Consummatum est.

Appendix A

MHD TURBULENCE

A.1 Introduction

This appendix is intended to provide a brief overview of some salient features pertaining to MHD turbulence, and, to a lesser extent, Navier-Stokes (NS) turbulence. It is by no means either comprehensive or detailed. As yet, there are few non-journal references available on MHD turbulence. The lecture notes on the topic by *Montgomery* [1989] are a good introduction. *Krause and Rädler's* [1980] book contains much information in the context of mean-field MHD and dynamo theory, and *Stanišić's* [1988] graduate level text has a major section on MHD turbulence. For incompressible Navier-Stokes turbulence the classic reference is *Batchelor* [1970]; other useful works include *Orszag* [1977], *Tennekes and Lumley* [1972], and *Lesieur* [1990].

Historically the investigation of fully developed turbulence has centered on two distinct cases: (a) turbulent flow states which are driven or (statistically) steady, and (b) the free decay of initially turbulent flows. Not surprisingly there are many important differences between these cases. The solar wind is driven from relatively low in the solar atmosphere, and then undergoes more or less free decay above the critical points. Furthermore, is also statistically steady to varying degrees.

What is the origin of MHD turbulence? To paraphrase Montgomery the answer is the same as for the Navier-Stokes case, namely gradients—gradients in density, pressure, velocity (shear flow), vorticity, temperature, magnetic fields, current density, *etc.* Laminar states will only support shallow gradients and if particular thresholds are exceeded “*violent motions arise to smooth gradients out. When boundary conditions obstruct such smoothing, steady-state turbulence results; all steady-state turbulence is driven through boundary conditions*” [Montgomery, 1989]. Note that by definition a boundary implies the presence of a gradient in some quantity.

The solar wind has an abundance of gradients. For example, gradients occur at interfaces between high and low speed flows; density, pressure, velocity and magnetic field gradients are intrinsic to shocks; and the observed variation in the density and magnetic field over large distances requires a gradient in each of these quantities.

There are however significant differences between Navier-Stokes and MHD turbulence. The presence of anisotropic and/or inhomogeneous magnetic fields, for example, tends to give the turbulence an anisotropic or inhomogeneous cast. *Shebalin et al.* [1983] performed a series of periodic two-dimensional (2D) turbulent MHD simulations for an incompressible dissipative fluid in the presence of a strong d.c. magnetic field (\mathbf{B}_0) perpendicular to the x - y plane. They found that an initially isotropic energy spectrum evolved into an anisotropic one. Energy transfer to the Fourier modes perpendicular to \mathbf{B}_0 was observed to proceed far more rapidly than transfer to the parallel modes. The simulations suggested that the degree of anisotropy increased with increasing mechanical and magnetic Reynolds numbers, and was greater at higher wavenumbers. Their explanation for this effect is based on a perturbative, Elsässer variable treatment of the appropriate MHD equations, and the interaction of triads of \mathbf{k} -modes. The resonant interaction mechanism is the most efficient way to achieve fast energy transfer between modes, since the individual frequencies are then all in phase. For such triads they showed that it is “impossible” for any $|k_z|_{max}$ to increase. However no such constraint exists for $|k_\perp|_{max}$, and thus we have a possible explanation for the preferential transfer to perpendicular modes. Higher order terms do allow the energy to be transferred in the k_z direction, but dissipation acts to suppress such transfer. Dissipation is thus essential for the *continuation* of the perpendicular transfer process, despite the fact that the explanation just given assumed that the fluid was ideal. The conjecture is that in driven MHD turbulence with a strong mean magnetic field, the energy spectrum will be Kolmogorov in nature for k_\perp and display exponential falloff in k_\parallel [*e.g.*, *Montgomery*, 1989]. This situation may be relevant to the solar wind, given the presence of a Parker spiral magnetic field, however it has not been observed.

The spectral transfer of energy is another aspect which can behave differently in the two cases. Specifically, for driven 2D Navier-Stokes turbulence, energy *inverse* cascades to longer wavenumbers (bigger structures), while in the corresponding MHD situation there is a *direct* cascade of energy (down) towards the dissipation end of the spectrum [*e.g.*, *Fyfe and Montgomery*, 1976; *Fyfe et al.*, 1977b; *Frisch and Sulem*, 1984; *Herring and McWilliams*, 1985].

When considering spectral dynamics, it is often convenient to work in Fourier (\mathbf{k}) space. The Fourier transformed incompressible Navier-Stokes equation may be written [*e.g.*, *Orszag*, 1977; *Lesieur*, 1990]

$$\left(\frac{\partial}{\partial t} + k^2\right) v_\alpha(\mathbf{k}, t) = -i k_\alpha p(\mathbf{k}, t) - i \int q_\beta v_\beta(\mathbf{k} - \mathbf{q}, t) v_\alpha(\mathbf{q}, t) d\mathbf{q} \quad (\text{A.1})$$

$$= -\frac{i}{2} P_{\alpha\beta\gamma}(\mathbf{k}) \int v_\beta(\mathbf{q}, t) v_\gamma(\mathbf{k} - \mathbf{q}, t) d\mathbf{q}, \quad (\text{A.2})$$

where

$$P_{\alpha\beta\gamma}(\mathbf{k}) = k_\beta \left(\delta_{\alpha\gamma} - \frac{k_\alpha k_\gamma}{k^2} \right) + k_\gamma \left(\delta_{\alpha\beta} - \frac{k_\alpha k_\beta}{k^2} \right). \quad (\text{A.3})$$

The “ k^2 ” term on the left of (A.1) represents dissipation (∇^2 in configuration (x) space), and thus it is clear that dissipation acts most strongly at the smallest length-scales. In fact, for sufficiently high Reynolds numbers, there will exist a range of dynamically important length-scales which are simultaneously much smaller than the stirring length of the turbulence (*e.g.*, the box size, L), and also much larger than scales where dissipation is important ($k \gtrsim k_d$): $1/L \ll k \ll k_d$. Since for such wave-vectors, the dominant term in the equation of motion is the inertial one, this range is known as the *inertial subrange*, first predicted by *Kolmogorov* [1941*a*]. Consideration of the MHD equations in k -space, leads to equations and results similar to those holding for NS turbulence.

For large enough Reynolds numbers, there are theoretical, numerical, and in some cases experimental grounds, for believing that energy spectra exhibit powerlaw behavior in the inertial range [*e.g.*, *Kolmogorov*, 1941; *Batchelor*, 1970; *Kraichnan*; 1967*b*; *Pouquet et al.*, 1976; *Grant et al.*, 1962]. Since the bulk of the energy is concentrated in “structures” with length scales near the stirring length, L , this set of scales is referred to as the *energy-containing range* [*e.g.*, *Batchelor*, 1970]. The dynamics occurring in this range have important differences from those associated with the inertial range. In particular, for strongly turbulent fluids, the inertial range is assumed to be in a state of statistical equilibrium, whereas the energy-containing range will only be in a quasi-equilibrium state [*e.g.*, *Batchelor*, 1970; *Matthaeus et al.*, 1993*a*].

The non-linear nature of the pressure in an incompressible fluid can be seen by taking the divergence of the NS equation. In x -space, this leads to a Poisson equation for the pressure:

$$\nabla^2 p = -\nabla \cdot [(\mathbf{v} \cdot \nabla)\mathbf{v}], \quad (\text{A.4})$$

so that once \mathbf{v} is known p is determined. In fact, in incompressible fluid dynamics the pressure acts only to enforce the incompressibility. This is easier to see in k -space, where $\nabla \cdot \mathbf{v} = 0$ becomes $\mathbf{k} \cdot \mathbf{v} = 0$. The pressure, $p(\mathbf{k})$, is equivalent to a projection operator acting on $\mathbf{v}(\mathbf{k})$ in such a way as to enforce the constraint of incompressibility for all \mathbf{k} (see equation (A.2)).

A similar Fourier analysis of the equation for the evolution of the energy ($\sim v^2$) suggests that the non-linear terms tend to act in particular ways [*Batchelor*, 1970]. If \mathbf{k} and \mathbf{k}' are two wave-vectors in a Cartesian coordinate system with axes x, y, z , then the pressure, $p(\mathbf{k})$, appears to act so as to redistribute the energy in this \mathbf{k} mode equally among its three Cartesian components—it is an “isotropizing agent.” The inertial terms move energy between different wave-vectors, but for

the same directional component, from k_x to k'_x for example. These tendencies are true in a global (integrated over all \mathbf{k}) sense, and seem to also apply for individual wave-vectors, at least in the inertial range.

Turbulence requires that a non-linear dynamical process be associated with the flow field. To see this recall that turbulence is characterized by the presence of a wide range of dynamical time and length scales. If the flow initially contains only a few such scales, the transition to a turbulent state can occur only if it is possible to generate the other scales from those already present. If we consider the spatial structure of the flow in terms of a weighted sum of plane waves, *i.e.*, an expansion in Fourier modes, it is clear that without the existence of non-linear terms there can be no coupling together of the modes (scales) to generate new/other modes. Spectral transfer of physical quantities cannot occur unless a non-linear interaction mechanism is present. Note that in incompressible Navier-Stokes turbulence, the two non-linear terms ($\mathbf{v} \cdot \nabla \mathbf{v}$ and ∇p) conserve the appropriate rugged invariants (*e.g.*, energy. See below.), while moving them around both spectrally and spatially. An analogous situation pertains to the incompressible MHD case under the duress of suitable boundary conditions [*e.g.*, *Matthaeus and Goldstein, 1982a*].

Magnetofluid turbulence may be partitioned into three more or less distinct regimes based on the relative quantities of turbulent kinetic and magnetic energy present in the flow. We assume that any mean velocity has been “subtracted out” by, for example, a Galilean transformation. A mean magnetic field cannot be so removed. The partitioning is given by

(a) kinetic regime

Here the turbulent kinetic energy greatly exceeds the magnetic energy. The magnetic field has little effect on the dynamics and is easily pushed about by the velocity field. The field is a sort of “passive vector.”

(b) magnetic regime

A strong mean or large-scale magnetic field is present such that the energy associated with it is much greater than that in either of the fluctuating fields. In either case, the magnetic field exerts substantial influence on the dynamics of the velocity field.

(c) equipartition regime

Here the fluctuating kinetic and magnetic energies are of the same order, and there is no dominating mean \mathbf{B} field. Hence, neither field may be neglected relative to its effects on the other. This situation applies to the solar wind in its (local) rest frame.

Note that turbulence initially in the equipartition regime can build up an “excess” of magnetic energy at the large-scales through dynamo action or inverse cascade, thus boosting itself into the magnetic regime. The distinction between these two cases can therefore be somewhat blurry, so that the categorization scheme should be considered as a guideline rather than as a definitive breakdown.

A.2 Rugged Invariants

In attempting to understand, explain, and characterize turbulent flows, it has proved advantageous to utilize a description involving the so-called “*rugged invariants*” [Frisch *et al.*, 1975; Kraichnan and Montgomery, 1980]. These are the globally conserved, quadratic quantities of ideal non-dissipative incompressible MHD. There are three known rugged invariants in 3D MHD: the *total energy* per unit mass E , equal to the sum of the kinetic (E_v) and magnetic (E_b) energy components; the *cross helicity*, $H_c = \frac{1}{2} \int \mathbf{v} \cdot \mathbf{b} dV$ a measure of the degree of alignment between the velocity and magnetic fields; and the *magnetic helicity*, $H_m = \frac{1}{2} \int \mathbf{A} \cdot \mathbf{B} dV$, where \mathbf{A} is the vector potential of $\mathbf{B} = \nabla \times \mathbf{A}$ [Moffatt, 1978]. The spectral forms of these quantities have also proved useful [*e.g.*, Zhou and Matthaeus, 1990a] and will be denoted by, for example, $H_c(\mathbf{k})$. Note that the cross-helicity and total energy are defined in terms of a magnetic field measured in Alfvén speed units, while the magnetic helicity definition uses standard (*e.g.*, cgs) units. While not necessary, this dichotomy is convenient in practice.

The magnetic helicity measures the level of magnetic flux linkage present in the field. Two simply linked tubes have a magnetic helicity proportional to the product of the magnetic flux in each tube, whereas unlinked tubes have identically zero magnetic helicity. Thus magnetic helicity is a topological property of the magnetic field. When the magnetic helicity is “large,” \mathbf{A} and \mathbf{B} are strongly aligned, and thus so are \mathbf{j} and \mathbf{B} . Hence the Lorentz $\mathbf{j} \times \mathbf{B}$ force is small, and the flow is not strongly forced by magnetic effects; magnetic helicity tends to quieten the flow.

The quantities are invariant because they are (ideally) conserved, and rugged since this is true even if the equations of motion are truncated at an arbitrary spatial scale; their conservation does *not* require the existence of infinitesimally small spatial scales. Since in any real system the continuum approximation always breaks down below some “small” scale (*e.g.*, intermolecular spacing, ion gyroradius, *etc.*), the rugged invariants are of considerable physical importance. All physical systems support some level of dissipation, and no matter how weak this dissipation is, it will enforce a lower bound on the minimum spatial scales of dynamical importance. Thus, in comparison to ideal invariants which do require arbitrarily small scales, it seems reasonable to

ascribe elevated significance to those invariants which are rugged in nature.

Statistical mechanical theories of turbulence also make use of the rugged invariants [*e.g.*, Kraichnan, 1967b; Frisch *et al.*, 1975; Kraichnan and Montgomery, 1980; Ting *et al.*, 1986; Stribling and Matthaeus, 1990, 1991]. In this case, each rugged invariant has an inverse “temperature” associated with it, and for ideal non-dissipative systems it is possible to apply Gibbsian (canonical) ensemble theory to the turbulence. The application of various limits and variational principles leads to some important results which may also be of relevance to dissipative systems. For example, spectral transfer directions appear to remain the same when small levels of dissipation are incorporated into the ideal systems. As noted by Kraichnan [1973] the absolute equilibrium results are expected to have relevance to dissipative fluids, in the sense that the directions of spectral transfer for the rugged invariants will still be valid. Briefly, the reasoning associated with this argument is as follows: within each k -band the eddy turnover time and the time to relax to absolute equilibrium are of the same order; hence, the fluid will tend to be in approximate absolute equilibrium.

Building on the foundations laid by Frisch *et al.* [1975], Stribling and Matthaeus [1990, 1991] have examined the absolute equilibrium (non-dissipative) statistical mechanics of 3D ideal incompressible MHD. They find several inequalities which must be obeyed. First, the magnetic energy must be at least as large as the kinetic energy, a feature which is compatible with spectral back-transfer of magnetic energy (*i.e.*, energy flow towards larger length-scales). Second, they find that $\langle H_c(k) \rangle / \langle E_b(k) \rangle$ is a constant, where the angle brackets indicate ensemble averaging. This suggests that if magnetic helicity is back-transferred, then the concomitant increase in large-scale magnetic energy associated with this inverse cascade will also lead to back-transfer of cross helicity. Indeed, Stribling and Matthaeus [1990] present evidence and arguments in support of this picture of back-transfer of both magnetic and cross helicity, the later occurring with relatively less strength. In contrast, the energy shows a preference for uniform spectral density, although a non-zero fraction of the energy must remain in the shortest wavelengths in order to satisfy several kinematic constraints. They also suggest that in the dissipative case whenever H_m is back-transferred, it is likely that H_c will be transported towards longer wavelengths as well, but in a weaker way.

Besides their theoretical importance, the rugged invariants also have relevance to computational work. Any numerical simulation contains a finite minimum scale, which is equivalent to a truncation of the equations of motion at this scale. Hence, for a well constructed non-dissipative code, the rugged invariants will be conserved to the accuracy of the numerical algorithm, while other ideal invariants may not.

Conservation laws impose constraints on the dynamics of the system. The degree to which these constraints, or perhaps related ones, are relevant to non-ideal dissipative systems is theoretically unclear. For systems with both large mechanical and large magnetic Reynolds numbers, the dissipation timescales are correspondingly long, and in this sense the systems are almost ideal. Thus we might suppose that a useful description of turbulence featuring the rugged invariants exists. Mathematically, however, the zero dissipation limits are highly singular, casting a shadow on the validity of this supposition.

The nature of this singularity may be seen in the following way. Consider for simplicity the NS equation

$$\nu \nabla^2 \mathbf{v} - \frac{\partial \mathbf{v}}{\partial t} - \mathbf{v} \cdot \nabla \mathbf{v} + \nabla p = 0. \quad (\text{A.5})$$

This is a second order partial differential equation for \mathbf{v} . However, if $\nu = 0$, it reduces to a first order pde. Thus, the nature of the equation of motion changes profoundly when ν vanishes, which makes the limit $\nu \rightarrow 0$ (*i.e.*, Reynolds number approaching infinity) problematic. Physically, for small but finite values of the viscosity, there will always exist (narrow) regions of flow near the system boundaries (“boundary layers”), where the gradients in \mathbf{v} are large enough to make $\nu \nabla^2 \mathbf{v}$ an important term in the equation of motion. This issue is related to the topic of singular perturbation problems, but we will say no more about it. Despite these problems, we will now discuss some spectral aspects of MHD turbulence in terms of the rugged invariants.

A.3 Spectral Transfer

In driven turbulence we expect to see an energy spectrum containing one or more inertial subranges of the Kolmogorov type, *i.e.*, powerlaw in wavenumber, provided of course that the Reynolds numbers are sufficiently large. These spectral subranges are associated with the cascading, direct and/or inverse, of the rugged invariants. Simulations of forced incompressible 3D MHD show a direct cascade of energy and an inverse cascade of magnetic helicity, which leads to a dominance of magnetic energy over kinetic [Pouquet and Patterson, 1978; Meneguzzi *et al.*, 1981]. As noted by Pouquet and Patterson [1978], cross helicity tends to reduce the strength of the non-linear terms and thus weaken spectral transfer and slow the dynamics of the turbulence. They also observe that accompanying the transfer of magnetic energy and magnetic helicity to large scales, is a transport of cross helicity in the same direction. This indicates that the back-transfer of magnetic helicity (and the magnetic energy it carries) is paralleled by an increase in the correlations between the long wavelength components of the velocity and magnetic fields. As noted

above, more recent work [*Stribling and Matthaeus*, 1990, 1991] also indicates that cross helicity tends to be back-transferred, although not as strongly as magnetic helicity.

Under the assumptions of isotropy¹ dimensional analysis yields values for the spectral slopes of the inertial subranges [*e.g.*, *Kolmogorov*, 1941; *Batchelor*, 1970; *Kraichnan*, 1965, 1967*b*; *Montgomery*, 1989]. In general, simulation results are not inconsistent with these values despite the computing limitations which currently hinder resolution of inertial subranges.

In k -space, a rugged invariant, E say, can always be written as the sum of quadratic terms in the fields, for example,

$$E = \sum_{\mathbf{k}} |\mathbf{v}(\mathbf{k})|^2. \quad (\text{A.6})$$

It turns out that the rugged invariants are rugged because they involve sums over interacting triads of wave-vectors whose vector sum is zero.² While the wave-vectors of any three Fourier modes contributing to the dynamics are locked into this vector triangle, the *phases* of the same modes are not locked at all. In fact, in the inertial range the non-linear terms cause the velocity triple correlations, *e.g.*, $\langle u_i(\mathbf{k})u_j(\mathbf{p})u_l(\mathbf{q}) \rangle$, where $\mathbf{k} + \mathbf{p} + \mathbf{q} = 0$, to relax towards a quasi-equilibrium state [*Orszag and Kruskal*, 1968; *Orszag*, 1977]. This relaxation occurs in a time $\sim \tau_3(\mathbf{k}, \mathbf{p}, \mathbf{q})$, known as both the *triple relaxation time* and the *triple correlation time*; it is the time for which the phase relations between the three modes are maintained, and is of prime importance in determining spectral slopes. Roughly speaking, τ_3 will be about the time for the phase of a single mode to change appreciably. Note that while the non-linear terms are non-local in k -space, their *net* effect in the inertial subrange is equivalent to an approximately local interaction. Thus, we will approximate $\tau_3(\mathbf{k}, \mathbf{p}, \mathbf{q})$ by $\tau_3(\mathbf{k})$.

The classical Kolmogorov $k^{-5/3}$ spectrum is obtained when $\tau_3(\mathbf{k})$ is taken as the non-linear eddy turnover time (*i.e.*, convection decorrelates the phases of the triples), and is considered appropriate for hydrodynamics. *Kraichnan* [1965] showed that for the situation where magnetic energy dominates in the energy-containing range, a more appropriate choice for $\tau_3(\mathbf{k})$ is the Alfvén timescale, leading to a $k^{-3/2}$ dependence in the inertial subrange (*i.e.*, Alfvén waves are responsible for the phase decorrelation). *Matthaeus and Zhou* [1989*a*] have recently shown that these results can be interpreted as complementary limits of a more general case, allowing continuous variation of the powerlaw index between $-\frac{3}{2}$ and $-\frac{5}{3}$. The result rests on the identification of the dependence of

¹ Note that the *Shebalin et al.* [1983] results referred to earlier make the isotropy of MHD turbulence debatable if a mean magnetic field is present.

² Geometrically $\mathbf{k} + \mathbf{p} + \mathbf{q} = 0$ is a triangle with legs given by k, p, q .

the triple correlation timescale on both the Alfvén and the non-linear timescales (more specifically it depends on *all* the appropriate timescales present in the turbulence).

A.4 The Alfvén Effect

If the small-scale fluctuations are considered as perturbations to the energy containing scales, and the separation between these scale ranges is large enough, then the Alfvén effect is predicted to occur: namely, that for the small-scales, the energy per unit wavenumber will be approximately equipartitioned between the turbulent kinetic and turbulent magnetic components [Kraichnan, 1965]. Physically this may be justified by visualizing a purely kinetic small-scale fluctuation $\delta\mathbf{v}$ as a superposition of two oppositely propagating Alfvénic wave-packets, $\delta\mathbf{v} \pm \delta\mathbf{B}/\sqrt{4\pi\rho_0}$, where we assume a locally constant density ρ_0 . If these wave-packets propagate away at the large-scale Alfvén speed $B_0/\sqrt{4\pi\rho_0}$, an approximate equipartition of the fluctuating kinetic and magnetic energies will result [Matthaeus and Goldstein, 1982a].

Also, the small-scales are always in the presence of some large-scale magnetic field, even if a d.c. field is absent. This follows because there is substantially more energy in the lower k modes than the higher ones. Thus, the energy-containing magnetic fluctuations essentially appear as a large-scale field to the inertial range fluctuations, assuming that the Reynolds numbers are sufficiently large to establish such distinct scale ranges. In the presence of a large-scale field, leading order perturbations in a magnetofluid are linear Alfvén waves. Such waves have equal amounts of kinetic and magnetic energy, leading to the Alfvén effect at these scales [*e.g.*, Fyfe and Montgomery, 1976; Pouquet and Patterson, 1978].

A.5 Relaxation Processes

Finally in this section, we mention some aspects of decaying MHD turbulence. At least two dynamical processes appear to operate in such a way that the fluid can relax into stable, long-lived states. The associated timescales are simultaneously much less than the viscous decay time and much greater than the turbulent decay time. Both mechanisms seek to make various ratios of the rugged invariants extremal. Physically the processes occur because of differences in the fractional and absolute decay rates of the rugged invariants [Matthaeus and Montgomery, 1980, 1984; Ting *et al.*, 1986].

Selective decay results when one rugged invariant decays on a timescale much faster than that of another. Thus, for each “small” time interval, the first invariant decays as if the second is approximately constant. This results in either an effective or an actual back-transfer of the less rapidly decayed ideal invariant, and a forward transfer of the more rapidly decayed one. The

best known example is the selective decay of enstrophy relative to energy in 2D Navier-Stokes turbulence. In incompressible 2D and 3D MHD selective decay operates to reduce the kinetic energy relative to the magnetic energy, although the ratio which is striving to achieve its minimum is the *total* energy over the magnetic invariant (H_m in 3D, mean square vector potential in 2D) [Matthaeus and Montgomery, 1980].

A recently completed 2D NS simulation indicates that a type of *minimum dissipation-maximum entropy* process may also act over these intermediate timescales [Matthaeus et al., 1991a, b; Montgomery et al., 1992]. Details are available in the original papers and in Daniel Martínez’s Ph.D. thesis [Martínez’s, 1993].

Dynamic alignment is associated with attempts by the system to make the velocity and magnetic fields equal in absolute magnitude, thus making the turbulence more Alfvénic in nature. The mechanism may be explained using an Elsässer variable description [Matthaeus and Montgomery, 1984]. The equations of motion are such that if one Elsässer species is assumed to contain the majority of the energy, then this majority species will dispense with the minority one by transferring it towards higher wavenumbers and the associated preferential dissipation, thus enhancing the dominance of the majority species.

Note that since the tendencies are for selective decay to reduce $|\mathbf{v}^2|$ relative to $|\mathbf{b}^2|$, and for dynamic alignment to equalize $|\mathbf{v}|$ and $|\mathbf{b}|$, these two processes have “final” states which are mutually exclusive and thus they compete against each other. A numerical study of 2D incompressible MHD by Ting et al. [1986] yielded a rough parameterization of the “final” state of the turbulence in terms of the initial values of kinetic and magnetic energy and cross helicity. In region I, characterized by initially small H_c and $E_v \lesssim E_b$, the final state tends to be one given by the selective decay of E relative to H_m , with the kinetic energy becoming less and less important relative to the magnetic. For $E_v \gg E_b$ initially, the fluid exhibits Navier-Stokes type behavior and this defines region II. Region III is associated with large initial H_c and $E_v \sim E_b$, and here dynamic alignment tends to prevail. The remaining areas of parameter space (small H_c , large E_v and E_b) display characteristic long-time behavior whose outcome is unclear.

A strong tendency to relax into states dominated by the $k_{min}^2 = 1$ contributions was also seen by Ting et al., almost independent of the initial states. Such states are *not* always ones of minimum energy. Of course this relaxation occurs even in the absence of non-linear modal transfer since smaller scales are more strongly dissipated, but such a mechanism significantly decreases the time taken to achieve domination by the large-scale components.

Another feature common to the vast majority of the runs was the near perfect *geometrical*

alignment of the velocity and magnetic fields. By this it is meant that the cosine of the angle between the fields approached unity in magnitude, indicating that the fields tend to become either parallel or anti-parallel. Hence, if the vector fields do not increase in magnitude, it is necessary for the strength of the Lorentz force to decrease, and clearly for perfect alignment the magnetic force acting on the fluid is identically zero; \mathbf{b} is then a “force free” field. Geometrical alignment appears to occur independently of dynamic alignment.

Relaxation processes in 3D MHD turbulence have recently been investigated by *Stribling and Matthaeus* [1991]. We refer the reader to this paper and the references in it for more information on the subject.

A.6 Compressional Turbulence

As a consequence of its inherently greater difficulty, the theory of compressible MHD turbulence is still an immature field. Its importance with regard to astrophysical situations is substantial, since magnetic fields are, at least galactically, pervasive and most astrophysical plasmas are compressible. Fortunately simulations are helping to develop its standing. A recent paper by *Ghosh and Matthaeus* [1990] reported on a simulation study of compressible 2D MHD at low to moderate Mach number. They observe that in low Mach number situations the results are essentially the same as for the incompressible case, namely the *Ting et al.* phase space parameterization still holds, although the boundaries of the regions shift somewhat. As the Mach number is increased, however, the turbulent fluid tends to increasingly favor the selective decay process over dynamic alignment. Consistent with the compressible nature of the fluid, acoustic fluctuations are also evident in the simulations.

Finally, recent analytic and numerical work on *nearly incompressible* hydro and magnetohydrodynamics has clarified the relationship of incompressible flows, both turbulent and otherwise, to low Mach number fluids [*Montgomery et al.*, 1987; *Matthaeus and Brown*, 1988; *Zank et al.*, 1990; *Zank and Matthaeus*, 1990*a*, 1991, 1992*a, b*, 1993; *Matthaeus et al.*, 1991]. Brief discussions of the applicability of this approach in the solar wind are given in Chapters 2 and 4.

Appendix B

SCALAR POTENTIALS FOR SOLENOIDAL VECTOR FIELDS

Consider the solenoidal field \mathbf{b} with vector potential \mathbf{A}

$$\mathbf{b}(\mathbf{x}) = \nabla \times \mathbf{A}(\mathbf{x}), \quad (\text{B.1})$$

so that in k -space

$$\mathbf{b}(\mathbf{k}) = i \mathbf{k} \times \mathbf{A}(\mathbf{k}). \quad (\text{B.2})$$

In general we expect three independent components for $\mathbf{A}(\mathbf{k})$. Call these $\psi_1(\mathbf{k})$, $\psi_2(\mathbf{k})$, and $\psi_3(\mathbf{k})$, and work in a k dependent coordinate system with an arbitrary uniform vector \mathbf{e} , so that

$$\mathbf{A}(\mathbf{k}) = \psi_1 \mathbf{e} + \frac{\psi_2}{k} \mathbf{k} \times \mathbf{e} + \frac{\psi_3}{k^2} \mathbf{k} \times (\mathbf{k} \times \mathbf{e}). \quad (\text{B.3})$$

In this form the ψ 's all have the same dimensions. Substituting into (B.2) we obtain

$$\begin{aligned} \mathbf{b}(\mathbf{k}) &= i \mathbf{k} \times \mathbf{e} \psi_1 + i \mathbf{k} \times (\mathbf{k} \times \mathbf{e}) \frac{\psi_2}{k} + i \mathbf{k} \times \left[\frac{\mathbf{k}(\mathbf{k} \cdot \mathbf{e})}{k^2} - \mathbf{e} \right] \psi_3 \\ &= i \mathbf{k} \times \mathbf{e} [\psi_1 - \psi_3] + i \mathbf{k} \times (\mathbf{k} \times \mathbf{e}) \frac{\psi_2}{k}. \end{aligned} \quad (\text{B.4})$$

Thus, there are really only two independent scalar potentials defining a solenoidal field, and we may as well absorb ψ_3 into ψ_1 . These are the poloidal and toroidal components. In fact it is convenient to associate an “ i ” with each \mathbf{k} , so that with a few minor redefinitions

$$\mathbf{b}(\mathbf{k}) = i \mathbf{k} \times \mathbf{e} \psi_1 - \mathbf{k} \times (\mathbf{k} \times \mathbf{e}) \frac{\psi_2}{k}, \quad (\text{B.5})$$

or, back in x -space,

$$\begin{aligned} \mathbf{b}(\mathbf{x}) &= \nabla \times (\mathbf{e} \psi_1) + \nabla \times (\nabla \times \mathbf{e} \phi) \\ &= -\mathbf{e} \times \nabla \psi_1 - \nabla \times (\mathbf{e} \times \nabla \phi), \end{aligned} \quad (\text{B.6})$$

where we work with ϕ despite its lack of dimensional matching with ψ_1 .

A customary mnemonic notation in x -space is

$$\mathbf{b}(\mathbf{x}) = -\nabla \times (\mathbf{e} \times \nabla P) - \mathbf{e} \times \nabla T \quad (\text{B.7})$$

where P is the *poloidal* component of the field, and T the *toroidal* [e.g., Krause and Rädler, 1980].

This implies the k -space form

$$\mathbf{b}(\mathbf{k}) = [k^2 \mathbf{e} - \mathbf{k}(\mathbf{e} \cdot \mathbf{k})] P(\mathbf{k}) - i \mathbf{e} \times \mathbf{k} T(\mathbf{k}), \quad (\text{B.8})$$

or, for dimensionally equivalent k -space potentials

$$\mathbf{b}(\mathbf{k}) = [k^2 \mathbf{e} - \mathbf{k}(\mathbf{e} \cdot \mathbf{k})] \frac{P(\mathbf{k})}{k} - i \mathbf{e} \times \mathbf{k} T(\mathbf{k}). \quad (\text{B.9})$$

Appendix C

SPECTRAL FORMS AND EVALUATION OF THE MIXING TENSORS

C.1 Matrix Forms for M_{ki}^\pm

Substitution of the standard large-scale fields used in Chapter 4, that is equations (4.25)–(4.29), into the general form of the mixing tensors

$$M_{ki}^\pm(\mathbf{R}) = \frac{\partial \mathbf{U}_i}{\partial \mathbf{R}_k} \pm \frac{1}{\sqrt{4\pi\rho}} \frac{\partial \mathbf{B}_{0i}}{\partial \mathbf{R}_k} - \frac{1}{2} \delta_{ik} \nabla \cdot \left(\frac{\mathbf{U}}{2} \pm \mathbf{V}_A \right), \quad (\text{C.1})$$

permits an explicit matrix form to be written for the tensors, which does not involve any derivatives. For generality, in this appendix we redefine the constant B_{0r}^0 of equation (4.27) to be $B_{0r}^0 f(\theta)$. Taking $f(\theta) = \cos \theta$, for example, produces the same θ dependence as that of the radial component of a dipole magnetic field. However, our specified form for \mathbf{B}_0 is *not* dipolar: $B_\theta = 0$, and $B_r \propto 1/R^2$ not $1/R^3$. Also, while $B_\phi = 0$ for $R \lesssim R_0$, this is not true above R_0 . Between the photosphere and R_0 the mean magnetic field is supposed to be purely radial (= monopole when $f(\theta) = 1$), in accord with the assumption that it rotates rigidly with the sun out to R_0 . Since we will not investigate the properties of the solutions below R_0 , this region can subsequently be ignored. Choosing $f(\theta) = \cos \theta$ also introduces a planar current sheet at the equator ($\theta = \pi/2$).

The details of the substitution are now given. The components of the large-scale fields are expressed in heliocentric spherical polar coordinates (R, θ, ϕ) , where R is the radial distance from the center of the sun, θ the co-latitude with respect to the solar rotation axis, and ϕ the azimuthal angle. The “1” coordinate corresponds to R , *etc.*, so that, for example, the “1-3” component of the matrix form for $\nabla \mathbf{B}_0$ is given by evaluation of $\hat{\mathbf{R}} \cdot \frac{\partial}{\partial R} (\hat{\phi} B_{0\phi})$.

Consider first the divergence terms in M_{ki}^\pm . It is straightforward to show that

$$\begin{aligned} \nabla \cdot \frac{\mathbf{U}}{2} &= \frac{1}{2R^2} \frac{\partial}{\partial R} (R^2 U) \\ &= \frac{U}{R}, \\ \nabla \cdot \mathbf{V}_A &= \frac{\mathbf{B}_0}{\sqrt{4\pi}} \cdot \nabla \frac{1}{\sqrt{\rho(R)}} \end{aligned} \quad (\text{C.2})$$

$$\begin{aligned}
&= \frac{B_{0r}}{\sqrt{4\pi\rho}} \frac{1}{R} \\
&= \frac{V_{Ar}}{R},
\end{aligned} \tag{C.3}$$

since $\nabla \cdot \mathbf{B}_0 = 0$. Thus,

$$\delta_{ik} \nabla \cdot \left(\frac{\mathbf{U}}{2} \pm \mathbf{V}_A \right) = \begin{pmatrix} 1 & 0 & 0 \\ 0 & 1 & 0 \\ 0 & 0 & 1 \end{pmatrix} \frac{U \pm V_{Ar}}{R}, \tag{C.4}$$

Similarly

$$\begin{aligned}
\nabla \mathbf{U} &= \frac{\partial \mathbf{U}}{\partial \mathbf{R}} = \left[\hat{\mathbf{R}} \frac{\partial}{\partial R} + \frac{\hat{\boldsymbol{\theta}}}{R} \frac{\partial}{\partial \theta} + \frac{\hat{\boldsymbol{\phi}}}{R \sin \theta} \frac{\partial}{\partial \phi} \right] (U \hat{\mathbf{R}}) \\
&= \begin{pmatrix} 0 & 0 & 0 \\ 0 & 1 & 0 \\ 0 & 0 & 1 \end{pmatrix} \frac{U}{R},
\end{aligned} \tag{C.5}$$

and

$$\nabla \mathbf{B}_0 = \begin{pmatrix} -2 & 0 & 0 \\ f'/f & 1 & 0 \\ 0 & 0 & 1 \end{pmatrix} \frac{B_{0r}}{R} + \begin{pmatrix} 0 & 0 & -\frac{R-2R_0}{R-R_0} \\ 0 & 0 & \cot \theta + f'/f \\ -1 & -\cot \theta & 0 \end{pmatrix} \frac{B_{0\phi}}{R}, \tag{C.6}$$

where $f' = df/d\theta$, and care must be taken with the unit vectors, since they also exhibit coordinate dependence [*e.g.*, *Book*, 1986]. Combining these pieces appropriately, we obtain the final forms

$$M_{ki}^{\pm} = \begin{pmatrix} -1 & 0 & 0 \\ 0 & 1 & 0 \\ 0 & 0 & 1 \end{pmatrix} \frac{U}{2R} \pm \begin{pmatrix} -5 & 0 & 0 \\ 2f'/f & 1 & 0 \\ 0 & 0 & 1 \end{pmatrix} \frac{V_{Ar}}{2R} \pm \begin{pmatrix} 0 & 0 & -\frac{R-2R_0}{R-R_0} \\ 0 & 0 & \cot \theta + f'/f \\ -1 & -\cot \theta & 0 \end{pmatrix} \frac{V_{A\phi}}{R}. \tag{C.7}$$

Zhou and Matthaeus [1990*a*] performed this calculation for the $\mathbf{B}_0 = 0$ case, which is relevant when $V_A/U \ll 1$, in the outer heliosphere for example.

C.2 Contraction with the small-scale tensors

The mixing tensors never appear in isolation, but only contracted, on either one or both indices, with a small-scale tensor field. Denoting such a small-scale field by Q_{jk} , the most general form of the contraction which we need to consider is $Q_{jk} M_{ki}^{\pm}$, the full contraction obviously being obtained by setting $i = j$. In order to calculate these contractions we need to know something

of the form of Q_{jk} . Imposing particular symmetry properties on the turbulence provides this information, at least in the three cases we consider here: turbulence which is isotropic, 2D, or slab. We now consider such contractions for inertial range fluctuations.

Since the small-scale coordinates (\mathbf{x} and \mathbf{r}) are considered to be independent of the large-scale coordinate (\mathbf{R}), we are in principle free to choose any coordinate system we wish, to describe the small-scale fluctuations. A sensible choice, and the one we adopt in this thesis, is to work in a Cartesian system which is *locally* aligned with the large-scale coordinate system discussed in the previous section. Denoting the unit vectors of this system by \mathbf{e}_1 , \mathbf{e}_2 , and \mathbf{e}_3 , we are therefore insisting on the following relationships:

$$\begin{aligned}\mathbf{e}_1 &\parallel \hat{\mathbf{R}}, \\ \mathbf{e}_2 &\parallel \hat{\theta}, \\ \mathbf{e}_3 &\parallel \hat{\phi}.\end{aligned}$$

It will sometimes also be convenient to work with a small-scale coordinate system which has the “1” direction aligned with the local value of \mathbf{B}_0 . We denote quantities associated with this coordinate system by primes ($'$), with unit vectors \mathbf{e}'_1 , \mathbf{e}'_2 , and \mathbf{e}'_3 . In order to make transforming between the radially (unprimed) and field (primed) aligned systems as simple as possible, we choose $\mathbf{e}'_2 = \mathbf{e}_2$, so that \mathbf{B}_0 lies in the \mathbf{e}_1 - \mathbf{e}_3 plane. The transformation is then simply a rotation about $\mathbf{e}_2 = \hat{\theta}$ by $-\psi$. It follows that to transform a second rank tensor in the field aligned system, say \mathbf{T}' , to one in the radially aligned system, say \mathbf{T} , we need only apply the following rule:

$$\mathbf{T} = \mathbf{O}\mathbf{T}'\mathbf{O}^T, \quad (\text{C.8})$$

where superscript T indicates the transpose operation, and

$$\mathbf{O} = \begin{pmatrix} \cos \psi & 0 & \sin \psi \\ 0 & 1 & 0 \\ -\sin \psi & 0 & \cos \psi \end{pmatrix} \quad (\text{C.9})$$

is the appropriate rotation matrix.

C.2.1 Isotropic Turbulence

When the small-scale turbulence is isotropic, with no helicity, both theory and experiment suggest that the modal spectrum of inertial range fluctuations exhibits a powerlaw dependence

on the wavenumber \mathbf{k} [e.g., *Kolmogorov*, 1941a; *Kraichnan*, 1965; *Grant et al.*, 1962]. Denote the appropriate modal spectrum by

$$\Sigma_{jk}(\mathbf{k}) = \frac{Q^{omni}(k)}{8\pi k^2} \left(\delta_{jk} - \frac{k_i k_j}{k^2} \right), \quad (\text{C.10})$$

where

$$Q^{omni}(k) = \int \Sigma_{\beta\beta}(\mathbf{k}) d\mathbf{A}(\mathbf{k}), \quad (\text{C.11})$$

is the average of $\Sigma_{\beta\beta}(\mathbf{k})$ over all wave-vectors \mathbf{k} of the same magnitude k . It can also be shown that the full omni-directional spectrum takes the form

$$\begin{aligned} Q_{jk}^{omni}(k) &= \int \Sigma_{jk}(\mathbf{k}) d\mathbf{A}(\mathbf{k}) \\ &= \frac{1}{3} \delta_{jk} Q^{omni}(k). \end{aligned} \quad (\text{C.12})$$

Defining the reduced spectrum along the radial direction by

$$Q_{jk}^{red}(k_1) = \int dk_2 dk_3 \Sigma_{jk}(\mathbf{k}), \quad (\text{C.13})$$

and assuming that $Q_{11}^{red}(k_1) \propto k_1^{-\alpha}$, it can be shown that

$$Q_{jk}^{red}(k_1) = \frac{1}{2+\alpha} \begin{pmatrix} 1 & 0 & 0 \\ 0 & (1+\alpha)/2 & 0 \\ 0 & 0 & (1+\alpha)/2 \end{pmatrix} Q^{red}, \quad (\text{C.14})$$

where

$$\begin{aligned} Q^{red}(k_1) &= Q_{\beta\beta}^{red}(k_1) \\ &\equiv \frac{1}{2} \int_{k_1}^{\infty} dk \frac{Q^{omni}(k)}{k}, \end{aligned} \quad (\text{C.15})$$

is the trace of the reduced spectral matrix [e.g., *Batchelor*, 1970; *Zhou and Matthaeus*, 1990a]. Important values of α include those associated with the theories of Kolmogorov ($\alpha = 5/3$) and Kraichnan ($\alpha = 3/2$). The factor $1/(2+\alpha)$ is purely for normalization purposes.

Note that if $Q^{omni}(k) \propto k^{-\alpha}$, then $Q^{red}(k_1)$ exhibits the same powerlaw dependence. In fact, for such a situation the two forms are related by

$$Q^{red}(k_1) = \frac{1}{2\alpha} Q^{omni}(k_1), \quad (\text{C.16})$$

a relation we will have occasion to use when comparing our results with observational data.

We are now ready to evaluate the contractions of the small-scale tensors with the mixing ones. Using the omni-directional spectral tensor we obtain

$$\begin{aligned} Q_{ik}^{omni} M_{ki}^{\pm} &= \frac{1}{2R} \left[\frac{U}{3} \mp V_{Ar} \right] Q^{omni}(k) \\ &= M_{iso}^{\pm} Q^{omni}(k), \end{aligned} \quad (\text{C.17})$$

where we refer to M_{iso}^{\pm} as the *effective mixing operators* for the omni-directional spectra of (non-helical) isotropic turbulence. The subscript “iso” will often be dropped, since the type of turbulence being considered is usually clear from the context. Note the sign change in M^+ at $R = 3R_0$ ($V_{Ar} \propto R_0/R$).

Using equations (C.7) and (C.14) we may also evaluate the mixing contraction using the reduced spectral tensor:

$$\begin{aligned} Q_{ik}^{red} M_{ki}^{\pm} &= \frac{\alpha}{\alpha + 2} \frac{1}{2R} \left[U \mp \left(\frac{4}{\alpha} - 1 \right) V_{Ar} \right] Q^{red}(k_1) \\ &= M_{iso}^{\pm} Q^{red}(k_1), \end{aligned} \quad (\text{C.18})$$

where now M_{iso}^{\pm} are the effective mixing operators for the reduced spectra of isotropic turbulence. Note the dependence on the spectral slope α , and that for large enough V_{Ar0}/U , M^+ undergoes a sign change. The case $\alpha = 1$ displays formal equivalence to the omni-directional contraction.

The diagonal forms of Q_{jk}^{red} and Q_{jk}^{omni} have precluded the picking up of any of the matrix terms in M_{ki}^{\pm} which involve θ . As it turns out, this is also true for 2D and slab turbulence (apart from the θ dependence of $V_{A\phi}$). Thus, any θ dependence of B_{0r} , *i.e.*, $f(\theta) \neq const$, contributes to the mixing operators only through its inclusion in V_{Ar} and/or $V_{A\phi}$; terms in f' certainly appear in M_{ki}^{\pm} , but they are “missed” when the full contraction with Q_{jk}^{red} or Q_{jk}^{omni} is calculated. It is also evident that the M_{iso}^{\pm} operators do not depend on $V_{A\phi}$, and, in fact, such dependence will be lacking for all Q_{jk} which are diagonal in the radially aligned coordinate system.

One might have expected that, since the turbulence is isotropic, the mixing operators appropriate for use with reduced spectra would be obtainable via the correct integration of equation (C.17) for the omni-directional contractions (*cf.* equation (C.15)). This is not so. Further discussion of this apparent paradox is to be found in section 5.2.2; here we note only that the non-isotropic nature of the mixing tensors is responsible for the “discrepancy.”

C.2.2 Two-Dimensional Turbulence

This is defined in section 5.2.3. For the moment let us work in the field aligned coordinate system introduced above. Then it can be shown that Q_{jk}^{omni} takes the form

$$Q_{jk}^{omni}(k_{\perp}) = \frac{1}{2} \begin{pmatrix} 0 & 0 & 0 \\ 0 & 1 & 0 \\ 0 & 0 & 1 \end{pmatrix} Q^{omni}(k_{\perp}) \delta(k_{\parallel}), \quad (\text{C.19})$$

where k_{\perp} is the magnitude of the projection of the wave-vector into the 2D plane perpendicular to \mathbf{B}_0 , and k_{\parallel} is the component along \mathbf{B}_0 . Making use of equation (C.8) to transform to the radially aligned system we obtain

$$Q_{jk}^{omni}(k) = \frac{1}{2} \begin{pmatrix} \sin^2 \psi & 0 & \sin \psi \cos \psi \\ 0 & 1 & 0 \\ \sin \psi \cos \psi & 0 & \cos^2 \psi \end{pmatrix} Q^{omni}(k_{\perp}) \delta(k_{\parallel}), \quad (\text{C.20})$$

and so

$$\begin{aligned} Q_{ik}^{omni} M_{ki}^{\pm} &= \frac{1}{2R} [U \cos^2 \psi \pm V_{Ar} (3 \cos^2 \psi - 2) \\ &\quad \pm \frac{1}{2} V_{Ar0} \left(\frac{\Omega R_0}{U} \right) \left(2 - \frac{3R_0}{R} \right) \sin \theta \sin 2\psi] Q^{omni}(k_{\perp}) \\ &= M_{2D}^{\pm} Q^{omni}(k_{\perp}). \end{aligned} \quad (\text{C.21})$$

For 2D turbulence we will also compare our solutions with spacecraft data, so that the relationship between $Q_{\beta\beta}^{omni}$ and $Q_{\beta\beta}^{red}$ is again required:

$$\begin{aligned} Q^{red}(k_1) &= \int_{-\infty}^{\infty} dk_2 \frac{Q^{omni}(k_{\perp})}{2\pi k_{\perp}} \\ &= \frac{1}{\pi \sin \psi} \int_{\frac{k_1}{\sin \psi}}^{\infty} dx \frac{Q^{omni}(x)}{\sqrt{x^2 - k_1^2 / \sin^2 \psi}}, \end{aligned} \quad (\text{C.22})$$

where the change of variables $x^2 = k_2^2 + k_1^2 / \sin^2 \psi = k_{\perp}^2$ has been used. When $\psi = 0$ a slightly different form (not shown) holds. The quantity $\frac{k_1}{\sin \psi}$ may be interpreted as the magnitude of the projection of \mathbf{k}_{\perp} onto the \mathbf{e}'_1 - \mathbf{e}'_3 plane, or more specifically onto the \mathbf{e}'_3 axis, since \mathbf{k}_{\perp} lies in the \mathbf{e}_2 - \mathbf{e}'_3 plane. A related perspective is that it corresponds the component of \mathbf{k}_{\perp} in the plane of \mathbf{B}_0 .

If we now assume $Q^{omni}(x) \propto x^{-\alpha}$, then the variable substitution $\sqrt{t} = \frac{k_1}{x \sin \psi}$, leads to

$$Q^{red}(k_1) = \frac{I(\alpha)}{\pi \sin \psi} Q^{omni} \left(\frac{k_1}{\sin \psi} \right), \quad (\text{C.23})$$

where

$$\begin{aligned}
I(\alpha) &= \frac{1}{2} \int_0^1 t^{\frac{1}{2}-1} (t-1)^{\frac{\alpha}{2}-1} dt \\
&= \frac{1}{2} B\left(\frac{1}{2}, \frac{\alpha}{2}\right) \\
&= \frac{1}{2} \frac{\Gamma\left(\frac{1}{2}\right) \Gamma\left(\frac{\alpha}{2}\right)}{\Gamma\left(\frac{\alpha+1}{2}\right)} \tag{C.24}
\end{aligned}$$

and Γ and B denote the well known gamma (factorial) and beta functions. The following values of $I(\alpha)$ are of particular interest

$$\begin{aligned}
I(1) &= \frac{1}{2} \frac{\Gamma\left(\frac{1}{2}\right) \Gamma\left(\frac{1}{2}\right)}{\Gamma(1)} \\
&= \frac{\pi}{2}, \\
I\left(\frac{3}{2}\right) &= 2\sqrt{\pi} \frac{\Gamma\left(\frac{3}{4}\right)}{\Gamma\left(\frac{1}{4}\right)} \\
&\simeq 1.1982 \\
I\left(\frac{5}{3}\right) &= \frac{3\sqrt{\pi}}{2} \frac{\Gamma\left(\frac{5}{6}\right)}{\Gamma\left(\frac{1}{3}\right)} \\
&\simeq 1.1203 \\
I(2) &= 1.
\end{aligned}$$

C.2.3 Slab Turbulence

As discussed in section 5.2.4, for slab turbulence the wave-vectors (magnitude k_{\parallel}) are parallel to the mean magnetic field \mathbf{B}_0 , with all the power being in directions perpendicular to \mathbf{B}_0 . If we further assume that the power is distributed isotropically over these directions, then the omnidirectional spectra are of the form

$$Q_{jk}^{omni}(k_{\parallel}) = \frac{1}{2} \begin{pmatrix} 0 & 0 & 0 \\ 0 & 1 & 0 \\ 0 & 0 & 1 \end{pmatrix} Q^{omni}(k_{\parallel}) \delta(k_{\perp}), \tag{C.25}$$

in the field aligned coordinate system. The formal similarity to the 2D case is evident. Hence we may immediately write down the effective mixing operators for slab turbulence in the radially aligned coordinate system:

$$M_{slab}^{\pm} = \frac{1}{2R} [U \cos^2 \psi \pm V_{Ar} (3 \cos^2 \psi - 2)]$$

$$\pm \frac{1}{2} V_{Ar0} \left(\frac{\Omega R_0}{U} \right) \left(2 - \frac{3R_0}{R} \right) \sin \theta \sin 2\psi \Big] \quad (\text{C.26})$$

In the limit that $\psi \rightarrow 0$, these operators become those applicable for slab waves which propagate parallel to the radial direction.

For slab turbulence, the relation between the (traced) omni-directional spectra and the reduced spectra is

$$Q^{red}(k_1) = \frac{1}{\cos \psi} Q^{omni} \left(\frac{k_1}{\cos \psi} \right). \quad (\text{C.27})$$

The quantity $\frac{k_1}{\cos \psi} = |\mathbf{k}| = k_{\parallel}$ is clearly the magnitude of the full wave-vector.

Appendix D

ANALYTIC SOLUTIONS FOR THE INERTIAL RANGE EQUATIONS

When the non-linear terms may be neglected and $V_{Ar0}/U \rightarrow 0$, it is possible to find analytic solutions for the inertial range transport equations. In this Appendix we show how to construct these solutions for the three types of turbulence considered in Chapter 5. Note, that we need only consider three-equation models since when $V_{Ar0}/U = 0$, F and J are uncoupled.

Reference to equations (4.40)–(4.39) and Appendix C, shows that in the limit $V_{Ar0}/U \rightarrow 0$, the effective mixing operators may all be written in the following form

$$\begin{aligned} M^\pm &= \frac{U}{2R} [\gamma + \mu \cos^2 \psi] \\ &= UM^0, \end{aligned} \tag{D.1}$$

where R is again measured in units of R_0 , and γ and μ are constants depending on the nature of the small-scale turbulence and the type of spectra used (*e.g.*, omni-directional, reduced). Table D.1 lists the values of γ and μ appropriate for isotropic, 2D, and slab turbulence. The functional form of $\cos^2 \psi$ is given by

$$\cos^2 \psi = \frac{B_{0\phi}^2}{B_{0r}^2 + B_{0\phi}^2}$$

Table D.1: Coefficients in the general form of the mixing operators when $V_{Ar0}/U = 0$. See equation (D.1). Unless otherwise noted, these coefficients apply to the mixing operators appropriate for omni-directional spectra. See section 4.4 and Appendix C for further details regarding the mixing operators.

Type of Turbulence	γ	μ
Isotropic (Reduced)	$\frac{\alpha}{\alpha+2}$	0
Isotropic	$\frac{1}{3}$	0
2D and Slab	0	1

$$\begin{aligned}
&= \frac{1}{1 + (B_{0\phi}/B_{0r})^2} \\
&= \frac{1}{1 + A^2(R-1)^2}, \tag{D.2}
\end{aligned}$$

where $A = (\Omega R_0/U) \sin \theta$. Note that the value is mathematically well defined in the limit $B_{0r}^0 \rightarrow 0$, even though the field itself vanishes. See equation (4.32). Taking the limits noted above and assuming time-steady solutions, the transport equations (5.1) and (5.2) become

$$U \frac{dP^\pm}{dR} + U \frac{P^\pm}{R} + UM^0 F = 0, \tag{D.3}$$

$$U \frac{dF}{dR} + U \frac{F}{R} + 2UM^0[P^+ + P^-] = 0. \tag{D.4}$$

Defining $P = P^+ + P^-$, leads immediately to

$$\frac{dP}{dR} + \frac{P}{R} + 2M^0 F = 0, \tag{D.5}$$

$$\frac{dF}{dR} + \frac{F}{R} + 2M^0 P = 0. \tag{D.6}$$

Note that the solar wind velocity U has scaled out of the equations. Now letting $f^\pm = P \pm F$, and adding and subtracting (D.6) to/from (D.5) we obtain

$$\frac{df^\pm}{dR} + \frac{f^\pm}{R} \pm 2M^0 f^\pm = 0, \tag{D.7}$$

$$\Rightarrow \frac{df^\pm}{dR} + \frac{1 \pm \gamma}{R} f^\pm + \frac{\mu}{1 + A^2(R-1)^2} \frac{f^\pm}{R} = 0, \tag{D.8}$$

a differential equation which may be solved via separation of variables. Recalling that we are working in units where $R_0 = 1$, the result is

$$\begin{aligned}
\log \frac{f^\pm}{f_0^\pm} &= \log \left(\frac{1}{R} \right)^{1 \pm \gamma} \pm \mu \left[\frac{1}{2(1 + A^2)} \log \left\{ A^2 - \frac{2A^2}{R} + \frac{1 + A^2}{R^2} \right\} \right. \\
&\quad \left. - \frac{A}{1 + A^2} \tan^{-1}[A(R-1)] \right] \\
\Rightarrow \frac{f^\pm}{f_0^\pm} &= \frac{1}{R^{1 \pm \gamma}} \left[A^2 - \frac{2A^2}{R} + \frac{1 + A^2}{R^2} \right]^{\pm \mu/2(1+A^2)} \exp \left\{ \mp \frac{\mu A}{1 + A^2} \tan^{-1}[A(R-1)] \right\}, \tag{D.9}
\end{aligned}$$

where a zero subscript denotes evaluation of the dependent variable at $R = R_0$. Physically f^\pm are proportional to the kinetic and magnetic energies of the fluctuations. In this connection *Tu and Marsch* [1993] have noted that when $\mathbf{V}_A = 0$ and the non-linear terms are neglected, the coupling between the Elsässer variables is somewhat misleading, since the equations of motion for \mathbf{v} and \mathbf{b} are actually decoupled (see equations (4.5)–(4.6) and the discussion in section 4.4).

Subtraction of equations (D.3) from each other leads immediately to solutions for the cross helicity:

$$P^- - P^+ = \frac{P_0^- - P_0^+}{R}, \quad (\text{D.10})$$

or, in more customary notation, $H_c = H_{c0}/R$. The approach to zero as R tends to infinity is evident. Note that P^- is associated with “outward” fluctuations, so that an excess of “outward” fluctuations over “inward” ones, leads to positive cross helicity.

Various combinations of (D.9) and (D.10) may now be assembled to yield solutions for the quantities of primary interest:

$$P^\pm = \frac{f^+ + f^-}{4} \mp \frac{P_0^- - P_0^+}{2R}, \quad (\text{D.11})$$

$$F = \frac{f^+ - f^-}{2}, \quad (\text{D.12})$$

$$\begin{aligned} \sigma_c &= \frac{P^- - P^+}{P^- + P^+} \\ &= \frac{2}{R} \frac{P_0^- - P_0^+}{f^+ + f^-}, \end{aligned} \quad (\text{D.13})$$

$$\begin{aligned} \sigma_D &= \frac{F}{P^+ + P^-} \\ &= \frac{f^+ - f^-}{f^+ + f^-}, \end{aligned} \quad (\text{D.14})$$

$$\begin{aligned} r_A &= \frac{1 - \sigma_D}{1 + \sigma_D} \\ &= \frac{f^+}{f^-}. \end{aligned} \quad (\text{D.15})$$

Observe that setting $\gamma = \mu = 0$, we recover the leading order WKB solutions [*e.g.*, *Hollweg*, 1973, 1974], with $P^\pm \propto 1/R$. Further properties of these solutions for each type of turbulence are discussed in section 5.2.

Appendix E

PHYSICAL SCALES IN THE SOLAR WIND

Table E.1: Characteristic Properties of the Solar Wind at 1 AU.

Ion number density	$\sim 8 \text{ cm}^{-3}$
Magnetic field magnitude	$\sim 5 \text{ nT}$
Magnetic Field Direction	$\approx 45^\circ$ to radial
Electron Temperature	$\sim (0.4 - 1) \times 10^5 \text{ K}$
Proton Temperature	$\sim (1 - 2) \times 10^5 \text{ K}$

Table E.2: Characteristic Lengths associated with the Solar Wind.

Astronomical Unit (1 AU)	$1.5 \times 10^{13} \text{ cm}$
Radius of sun	$7 \times 10^{10} \text{ cm}$ ($\frac{1}{215}$ AU)
Radius of heliosphere (estimate)	$\sim 100 \text{ AU}$
Distance over which large-scale features vary	$\sim 1 \text{ AU}$
Energy Correlation Length, λ_c (1 AU)	$\sim 5 \times 10^{11} \text{ cm}$ ($\approx \frac{1}{30}$ AU)
Proton Gyroradius (1 AU) ~ Smallest “fluid” length scale ~ dissipation scale	$\sim 100 \text{ km}$
Electron Gyroradius (1 AU)	$\sim 1 \text{ km}$
Debye Length (1 AU)	$\approx 6 \text{ m}$

Table E.3: Characteristic Speeds associated with the Solar Wind.

Flow speed range	$\approx 250 - 1000$ km/sec
Typical flow speed	≈ 400 km/sec
Alfvén speed (1 AU)	≈ 35 km/sec
Ion sound speed (1 AU)	≈ 50 km/sec

Table E.4: Characteristic Times associated with the Solar Wind.

Solar magnetic cycle period	$\simeq 22$ years
Solar rotation period	$\simeq 27$ days
Typical transit time of a solar wind parcel from sun to earth	≈ 4 days
Alfvén transit time = λ_c/V_A (1 AU)	~ 40 hours
Proton gyrofrequency (1 AU)	≈ 0.08 Hz

Table E.5: Approximate Limits of the Inertial Range of Solar Wind Power Spectra at 1 AU. The frequencies and periods are those in the spacecraft frame, while the wavenumbers are calculated using the “frozen-in” flux approximation [*e.g.*, *Matthaeus and Goldstein, 1982a, b*].

	Frequencies (Hz)	Periods	Wavenumbers (km^{-1})
Low End	$\sim 10^{-4}$	~ 3 hours	$\sim 10^{-6}$
High End	$\sim 10^{-1}$	~ 10 sec	$\sim 10^{-3}$

REFERENCES

- A. Barnes. Collisionless heating of the solar-wind plasma, 1. theory of the heating of collisionless plasma by hydromagnetic waves. *Astrophys. J.*, **154**:751, 1968.
- A. Barnes. Collisionless heating of solar wind plasma, 2, application of the theory of plasma heating by hydromagnetic waves. *Astrophys. J.*, **155**:311, 1969.
- A. Barnes. Hydromagnetic waves and turbulence in the solar wind. In E. N. Parker, C. F. Kennel, and L. J. Lanzerotti, editors, *Solar System Plasma Physics, vol. I*, page 251, Amsterdam, 1979. North-Holland.
- A. Barnes and J. V. Hollweg. Large amplitude hydromagnetic waves. *J. Geophys. Res.*, **79**:2302, 1974.
- G. K. Batchelor. *The Theory of Homogeneous Turbulence*. Cambridge University Press, 1970.
- B. Bavassano and R. Bruno. Evidence of local generation of Alfvénic turbulence in the solar wind. *J. Geophys. Res.*, **94**:11 977, 1989.
- B. Bavassano, M. Dobrowolny, F. Mariani, and N. F. Ness. Radial evolution of power spectra of interplanetary Alfvénic turbulence. *J. Geophys. Res.*, **87**:3617, 1982a.
- B. Bavassano, M. Dobrowolny, G. Fanfoni, F. Mariani, and N. F. Ness. Statistical properties of mhd fluctuations associated with high-speed streams from Helios-2 observations. *Solar Phys.*, **78**:373, 1982b.
- B. Bavassano and E. Smith. Radial variation of interplanetary Alfvénic fluctuations: Pioneer 10 and 11 observations between 1 and 5 au. *J. Geophys. Res.*, **91**:1706, 1986.
- J. W. Belcher and L. Davis. Large-amplitude Alfvén waves in the interplanetary medium, 2. *J. Geophys. Res.*, **76**:3534, 1971.
- J. W. Bieber and W. H. Matthaeus. Particle transport from a turbulence perspective. In G. P. Zank and G. T. K., editors, *Particle Acceleration in Cosmic Plasmas*, page 86, New York, 1992. AIP. AIP Conference Proceedings 264.
- J. W. Bieber, J. Chen, W. H. Matthaeus, C. W. Smith, and M. A. Pomerantz. Long-term variations of interplanetary magnetic field spectra with implications for cosmic ray modulation. *J. Geophys. Res.*, **98**:3585, 1993a.

- J. W. Bieber, W. H. Matthaeus, and C. W. Smith. A turbulence theory solution of the quasilinear theory puzzle. In *Proceedings of the 23rd International Cosmic Ray Conference*. to be published, 1993b.
- J. W. Bieber, W. H. Matthaeus, C. W. Smith, W. Wanner, M. Kallenrode, and G. Wibberenz. Proton and electron mean free paths: the Palmer consensus revisited. *Astrophys. J.*, :submitted, 1993c.
- D. Biskamp and H. Welter. Dynamics of decaying two-dimensional magnetohydrodynamics turbulence. *Phys. Fluids B*, **1**:1964, 1989.
- D. L. Book. *NRL Plasma Formulary*. NRL Publication 0084-4040, Washington, DC, 1987.
- P. Bradshaw, T. Cebeci, and J. Whitelaw. *Engineering Calculation Methods for Turbulent Flow*. Academic Press, London, U.K., 1981.
- J. C. Brandt. *Introduction to the Solar Wind*. W. H. Freeman and Company, San Francisco, 1970.
- C. Canuto, M. Y. Hussaini, A. Quarteroni, and T. A. Zang. *Spectral Methods in Fluid Mechanics*. Springer Series in Computational Physics. Springer-Verlag, New York, 1988.
- S. Chandrasekhar. The theory of axisymmetric turbulence. *Phil. Trans. R. Soc. London Ser. A*, **242**:557, 1950.
- S. Chandrasekhar. The invariant theory of isotropic turbulence in magneto-hydrodynamics. *Proc. Roy. Soc. London Ser. A*, **204**:435, 1951a.
- S. Chandrasekhar. The invariant theory of isotropic turbulence in magneto-hydrodynamics. II. *Proc. Roy. Soc. London Ser. A*, **207**:301, 1951b.
- S. Chapman. Notes on the solar corona and the terrestrial ionosphere. *Smithsonian Contrib. Astrophys.*, **2**:1, 1957.
- H. Chen and D. Montgomery. Turbulent MHD transport coefficients: An attempt at self consistency. *Plasma Phys. Controlled Fusion*, **29**:205, 1987.
- P. J. Coleman. Hydromagnetic waves in the interplanetary plasma. *Phys. Rev. Lett.*, **17**:207, 1966.
- P. J. Coleman. Wave-like phenomena in the interplanetary plasma: Mariner 2. *Planet. Space Sci.*, **15**:953, 1967.
- P. J. Coleman. Turbulence, viscosity, and dissipation in the solar wind plasma. *Astrophys. J.*, **153**:371, 1968.
- T. G. Cowling. *Magnetohydrodynamics*. Interscience, New York, 1957.
- M. Dobrowolny, A. Mangeney, and P. Veltri. Properties of magnetohydrodynamic turbulence in the solar wind. *Astron. and Astrophys.*, **83**:26, 1980a.

- M. Dobrowolny, A. Mangeney, and P. Veltri. Fully developed anisotropic hydromagnetic turbulence in interplanetary space. *Phys. Rev. Lett.*, **45**:144, 1980b.
- W. M. Elsässer. The hydromagnetic equations. *Phys. Rev.*, **79**:183, 1950.
- C. A. J. Fletcher. *Computational Techniques for Fluid Dynamics, vol I*. Springer-Verlag, Berlin, 1991.
- J. Freeman. Estimates of solar wind heating inside 0.3 au. *Geophys. Res. Lett.*, **15**:88, 1988.
- U. Frisch, A. Pouquet, J. Léorat, and A. Mazure. Possibility of an inverse cascade of magnetic helicity in magnetohydrodynamic turbulence. *J. Fluid Mech.*, **68**:769, 1975.
- U. Frisch and P. L. Sulem. Numerical simulation of the inverse cascade in two-dimensional turbulence. *Phys. Fluids*, **27**:1921, 1984.
- D. Fyfe and D. Montgomery. High beta turbulence in two-dimensional magnetohydrodynamics. *J. Plasma Phys.*, **16**:181, 1976.
- D. Fyfe, D. Montgomery, and G. Joyce. Dissipative, forced turbulence in two-dimensional magnetohydrodynamics. *J. Plasma Phys.*, **17**:369, 1977.
- S. Ghosh and W. H. Matthaeus. Relaxation processes in a turbulent compressible magnetofluid. *Phys. Fluids B*, **2**:1520, 1990.
- M. L. Goldstein, D. A. Roberts, and W. H. Matthaeus. Numerical simulation of interplanetary and magnetospheric phenomena: The Kelvin-Helmholtz instability. In J. H. Waite, J. L. Burch, and R. L. Moore, editors, *Solar System Plasma Physics, Geophys. Monogr. Ser. Bolkesjø, Norway*, volume 54, page 113, Washington, D.C., 1989. AGU.
- D. Gottlieb and S. A. Orszag. *Numerical Analysis of Spectral Methods: Theory and Applications*. SIAM, 1977.
- H. L. Grant, R. W. Stewart, and A. Moilliet. Turbulence spectra from a tidal channel. *J. Fluid Mech.*, **12**:241, 1962.
- R. Grappin, U. Frisch, J. Léorat, and A. Pouquet. Alfvénic fluctuations as asymptotic states of MHD turbulence. *Astron. and Astrophys.*, **105**:6, 1982.
- R. Grappin, A. Pouquet, and J. Léorat. Dependence of MHD turbulence spectra on the velocity field-magnetic field correlation. *Astron. and Astrophys.*, **126**:51, 1983.
- R. Grappin, A. Mangeney, and E. Marsch. On the origin of solar wind mhd turbulence: Helios data revisited. *J. Geophys. Res.*, **95**:8197, 1990.
- R. Grappin, M. Velli, and A. Mangeney. “Alfvénic” versus “standard” turbulence in the solar wind. *Ann. Geophys.*, **9**:416, 1991.

- R. Grappin, M. Velli, and A. Mangeney. Nonlinear wave evolution in the expanding solar wind. *Phys. Rev. Lett.*, submitted, 1992.
- A. Hasegawa and T. Sato. *Space Plasma Physics 1. Stationary Processes*. Springer-Verlag, New York, 1989.
- M. Heinemann and S. Olbert. Non-WKB Alfvén waves in the solar wind. *J. Geophys. Res.*, **85**:1311, 1980.
- J. R. Herring and J. C. McWilliams. Comparison of direct numerical simulation of two-dimensional turbulence with two-point closure: the effects of intermittency. *J. Fluid Mech.*, **153**:229, 1985.
- J. V. Hollweg. Alfvén waves in a two-fluid model of the solar wind. *Astrophys. J.*, **181**:547, 1973a.
- J. V. Hollweg. Alfvén waves in the solar wind: Wave pressure, Poynting flux, and angular momentum. *J. Geophys. Res.*, **78**:3643, 1973b.
- J. V. Hollweg. Transverse Alfvén waves in the solar wind: Arbitrary \mathbf{k} , \mathbf{v}_0 , \mathbf{B}_0 and $\delta\mathbf{b}$. *J. Geophys. Res.*, **79**:1539, 1974.
- J. V. Hollweg. Transition region, corona, and solar wind in coronal holes. *J. Geophys. Res.*, **91**:4111, 1986.
- J. V. Hollweg. On WKB expansions for Alfvén waves in the solar wind. *J. Geophys. Res.*, **95**:14,873, 1990.
- J. V. Hollweg and W. Johnson. Transition region, corona, and solar wind in coronal holes: Some two fluid models. *J. Geophys. Res.*, **93**:9547, 1988.
- T. Holzer. Effects of rapidly diverging flow, heat addition, and momentum addition in the solar wind and stellar winds. *J. Geophys. Res.*, **82**:23, 1977.
- A. J. Hundhausen. *Coronal Expansion and the Solar Wind*. Springer-Verlag, New York, 1972.
- P. A. Isenberg. A turbulence-driven solar wind model. *J. Geophys. Res.*, **95**:6437, 1990a.
- P. A. Isenberg. The solar wind. In J. A. Jacobs, editor, *Geomagnetism, Vol. IV*, page 1, San Diego, Calif., 1990b. Academic Press.
- J. D. Jackson. *Classical Electrodynamics*. Wiley, New York, 2nd edition, 1975.
- S. A. Jacques. Momentum and energy transport by waves in the solar atmosphere and solar wind. *Astrophys. J.*, **215**:942, 1977.
- J. Jokipii and P. Coleman. Cosmic-ray diffusion tensor and its variation observed with Mariner 4. *J. Geophys. Res.*, **73**:5495, 1968.

- W. P. Jones and B. Launder. Calculation of low-Reynolds-number phenomena with a 2-equation model of turbulence. *Int. J. Heat Mass Transf.*, **15**:301, 1972.
- T. von Kármán and L. Howarth. On the statistical theory of isotropic turbulence. *Proc. Roy. Soc. London Ser. A*, **164**:192, 1938.
- L. W. Klein, D. A. Roberts, and M. L. Goldstein. Anisotropy and minimum variance directions of solar wind fluctuations in the outer heliosphere. *J. Geophys. Res.*, **96**:3779, 1991.
- A. N. Kolmogorov. Local structure of turbulence in an incompressible viscous fluid at very high Reynolds numbers. *C.R. Acad. Sci. U.R.S.S.*, **30**:301, 1941.
- R. H. Kraichnan. Inertial-range spectrum of hydromagnetic turbulence. *Phys. Fluids*, **8**:1385, 1965.
- R. H. Kraichnan. Inertial ranges in two-dimensional turbulence. *Phys. Fluids*, **10**:1417, 1967.
- R. H. Kraichnan. Inertial-range transfer in two- and three-dimensional turbulence. *J. Fluid Mech.*, **47**:525, 1971.
- R. H. Kraichnan. Helical turbulence and absolute equilibrium. *J. Fluid Mech.*, **59**:745, 1973.
- R. H. Kraichnan and D. C. Montgomery. Two-dimensional turbulence. *Reports on the Progress of Physics*, **43**:547, 1980.
- R. H. Kraichnan and S. Nagarajan. Growth of turbulent magnetic field. *Phys. Fluids*, **10**:859, 1967.
- F. Krause and K.-H. Rädler. *Mean-Field Magnetohydrodynamics and Dynamo Theory*. Akademie-Verlag, Berlin, 1980.
- E. Leer and T. Holzer. Energy addition in the solar wind. *J. Geophys. Res.*, **85**:4681, 1980.
- C. E. Leith. Diffusion approximation to inertial energy transfer in isotropic turbulence. *Phys. Fluids*, **10**:1409, 1967.
- M. Lesieur. *Turbulence in Fluids*. Nijhoff, Dordrecht, The Netherlands, 1990.
- N. A. Lotova. The solar wind transsonic region. *Solar Phys.*, **117**:399, 1988.
- N. A. Lotova, D. F. Blums, and K. V. Vladimirkii. Interplanetary scintillation and the structure of the solar wind transonic region. *Astron. Astrophys.*, **150**:266, 1985.
- A. Mangeney, R. Grappin, and M. Velli. MHD turbulence in the solar wind. In E. R. Priest and A. W. Hood, editors, *Advances in Solar System Magnetohydrodynamics*, page 327. Cambridge University Press, 1991.
- E. Marsch. MHD turbulence in the solar wind. In R. Schwenn and E. Marsch, editors, *Physics of the Inner Heliosphere*, Vol. 2, page 159, New York, 1991. Springer-Verlag.

- E. Marsch and A. Mangeney. Ideal mhd equations in terms of compressive Elsässer variables. *J. Geophys. Res.*, **92**:7363, 1987.
- E. Marsch and C.-Y. Tu. Dynamics of correlation functions with Elsässer variables for inhomogeneous mhd turbulence. *J. Plasma Phys.*, **41**:479, 1989.
- E. Marsch and C.-Y. Tu. On the radial evolution of mhd turbulence in the inner heliosphere. *J. Geophys. Res.*, **95**:8211, 1990a.
- E. Marsch and C.-Y. Tu. Spectral and spatial evolution of compressible turbulence in the inner solar wind. *J. Geophys. Res.*, **95**:11 945, 1990b.
- E. Marsch and C. Y. Tu. Electric field fluctuations and possible dynamo effects in the solar wind. In E. Marsch and R. Schwenn, editors, *Proceedings of Solar Wind 7, COSPAR Colloq. Ser.*, volume 3, page 505, Oxford, UK, 1992. Pergamon.
- D. Martínez. *Topics in Lattice Gas Methods, Lattice Boltzmann Methods, and Turbulence*. Ph.D. thesis, University of Delaware, Newark, Delaware, 19716, 1993.
- W. H. Matthaeus and D. Montgomery. Selective decay hypothesis at high mechanical and magnetic Reynolds numbers. *Annals of the New York Academy of Sciences*, **357**:203, 1980.
- W. H. Matthaeus and C. Smith. Structure of correlation tensors in homogeneous anisotropic turbulence. *Phys. Rev. A*, **24**:2135, 1981.
- W. H. Matthaeus and M. L. Goldstein. Measurement of the rugged invariants of magnetohydrodynamic turbulence in the solar wind. *J. Geophys. Res.*, **87**:6011, 1982a.
- W. H. Matthaeus and M. L. Goldstein. Stationarity of magnetohydrodynamic fluctuations in the solar wind. *J. Geophys. Res.*, **87**:10 347, 1982b.
- W. H. Matthaeus, M. L. Goldstein, and C. W. Smith. Evaluation of magnetic helicity in homogeneous turbulence. *Phys. Rev. Lett.*, **48**:1256, 1982.
- W. H. Matthaeus and M. L. Goldstein. Magnetohydrodynamic turbulence in the solar wind. In *Proceedings of Solar Wind 5*, page 73. NASA Conference Publication 2280, 1983.
- W. H. Matthaeus, M. L. Goldstein, and D. C. Montgomery. Turbulent generation of outward-traveling interplanetary Alfvénic fluctuations. *Phys. Rev. Lett.*, **51**:1484, 1983.
- W. H. Matthaeus, J. J. Ambrosiano, and M. L. Goldstein. Particle acceleration by turbulent magnetohydrodynamic reconnection. *Phys. Rev. Lett.*, **53**:1449, 1984.
- W. H. Matthaeus and D. Montgomery. Dynamic alignment and selective decay in mhd. In C. W. J. Horton and L. E. Reichl, editors, *Statistical Physics and Chaos in Fusion Plasmas*, page 285, New York, 1984. Wiley.
- W. H. Matthaeus and M. L. Goldstein. Low-frequency 1/f noise in the interplanetary magnetic field. *Phys. Rev. Lett.*, **57**:495, 1986.

- W. H. Matthaeus and S. L. Lamkin. Turbulent magnetic reconnection. *Phys. Fluids*, **29**:2513, 1986.
- W. H. Matthaeus and M. R. Brown. Nearly incompressible magnetohydrodynamics at low Mach number. *Phys. Fluids*, **31**:3634, 1988.
- W. H. Matthaeus and Y. Zhou. Extended inertial range phenomenology of magnetohydrodynamic turbulence. *Phys. Fluids B*, **1**:1929, 1989a.
- W. H. Matthaeus and Y. Zhou. Nearly incompressible mhd turbulence in the solar wind. In A. Pouquet, M. Meneguzzi, and P. L. Sulem, editors, *Nonlinear Phenomena in MHD Turbulence*, page 93, Amsterdam, The Netherlands, 1989. Elsevier Science Publishers B.V. (North Holland).
- W. H. Matthaeus, M. L. Goldstein, and D. A. Roberts. Evidence for the presence of quasi-two-dimensional nearly incompressible fluctuations in the solar wind. *J. Geophys. Res.*, **95**:20 673, 1990.
- W. H. Matthaeus, L. W. Klein, S. Ghosh, and M. R. Brown. Nearly incompressible magnetohydrodynamics, pseudosound, and solar wind fluctuations. *J. Geophys. Res.*, **96**:5421, 1991.
- W. H. Matthaeus, W. T. Stribling, D. Martínez, S. Oughton, and D. Montgomery. Decaying, two-dimensional, Navier-Stokes turbulence at very long times. *Physica D*, **51**:531, 1991.
- W. H. Matthaeus, W. T. Stribling, D. Martínez, S. Oughton, and D. Montgomery. Selective decay and coherent vortices in two-dimensional incompressible turbulence. *Phys. Rev. Lett.*, **66**:2731, 1991.
- W. H. Matthaeus, Y. Zhou, S. Oughton, and G. P. Zank. Weakly inhomogeneous mhd turbulence and transport of solar wind fluctuations. In E. Marsch and R. Schwenn, editors, *Proceedings of Solar Wind 7, COSPAR Colloq. Ser.*, volume 3, page 511, Oxford, UK, 1992. Pergamon.
- W. H. Matthaeus, S. Oughton, D. Pontius, and Y. Zhou. Evolution of energy containing eddies. *J. Geophys. Res.*, submitted, 1993a.
- W. H. Matthaeus, G. P. Zank, S. Oughton, and Y. Zhou. *J. Geophys. Res.*, in preparation, 1993b.
- M. Meneguzzi, U. Frisch, and A. Pouquet. Helical and nonhelical turbulent dynamos. *Phys. Rev. Lett.*, **47**:1060, 1981.
- H. K. Moffatt. The degree of knottedness of tangled vortex lines. *J. Fluid Mech.*, **35**:117, 1969.
- H. K. Moffatt. *Magnetic Field generation in Electrically Conducting Fluids*. Cambridge University Press, New York, 1978.
- A. Monin and A. Yaglom. *Statistical Fluid Mechanics, vols 1 and 2*. MIT Press, Cambridge, Mass., 1971 and 1975.

- D. Montgomery. Theory of hydromagnetic turbulence. In *Proceedings of Solar Wind 5*, page 107. NASA Conference Publication 2280, 1983.
- D. Montgomery and H. Chen. Turbulent amplification of large-scale magnetic fields. *Plasma Phys. Controlled Fusion*, **26**:1199, 1984.
- D. Montgomery, M. R. Brown, and W. H. Matthaeus. Density fluctuation spectra in mhd turbulence. *J. Geophys. Res.*, **92**:282, 1987.
- D. Montgomery. *Lecture Notes on Turbulence*, page 75. World Scientific, 1989. Lecture Notes from the NCAR-GTP Summer School, June 1987.
- D. Montgomery, W. H. Matthaeus, W. T. Stribling, D. Martínez, and S. Oughton. Relaxation in two dimensions and the “sinh-Poisson” equation. *Phys. Fluids A*, **4**:3, 1992.
- N. F. Ness, C. S. Scarce, and J. B. Seek. Initial results of the IMP 1 magnetic field experiment. *J. Geophys. Res.*, **69**:3531, 1964.
- M. Neugebauer. The quasi-stationary and transient states of the solar wind. *Science*, **252**:404, 1991.
- M. Neugebauer and C. W. Snyder. Mariner 2 observations of the solar wind, 1, Average properties. *J. Geophys. Res.*, **71**:4469, 1966.
- M. Neugebauer and C. W. Snyder. Mariner 2 observations of the solar wind, 2, Relation of plasma properties to the magnetic field. *J. Geophys. Res.*, **72**:1823, 1967.
- D. R. Nicholson. *Introduction to Plasma Theory*. Krieger, 1983.
- S. Orszag. Analytical theories of turbulence. *J. Fluid Mech.*, **41**:363, 1970.
- S. A. Orszag. Lectures on the statistical theory of turbulence. In R. Balian and J.-L. Peube, editors, *Fluid Dynamics*, page 235, New York, 1977. Gordon and Breach. Les Houches Summer School, 1973.
- S. A. Orszag and M. D. Kruskal. Formulation of the theory of turbulence. *Phys. Fluids*, **11**:43, 1968.
- E. N. Parker. Dynamics of the interplanetary gas and magnetic fields. *Astrophys. J.*, **123**:644, 1958.
- E. N. Parker. Dynamical theory of the solar wind. *Space Science Reviews*, **4**:666, 1965.
- E. N. Parker. *Cosmical Magnetic Fields: Their Origin and Activity*. Oxford University Press, Oxford, England, 1979.
- G. K. Parks. *Physics of Space Plasmas: An Introduction*. Addison-Wesley, 1991.
- D. Potter. *Computational Physics*. Wiley, 1973.

- A. Pouquet, U. Frisch, and J. Léorat. Strong mhd helical turbulence and the nonlinear dynamo effect. *J. Fluid Mech.*, **77**:321, 1976.
- A. Pouquet, M. Meneguzzi, and U. Frisch. Growth of correlations in magnetohydrodynamic turbulence. *Phys. Rev. A*, **33**:4266, 1986.
- A. Pouquet, M. Meneguzzi, and P. Sulem. Influence of velocity-magnetic field correlations of decaying magnetohydrodynamic turbulence with neutral X points. *Phys. Fluids*, **31**:2635, 1988.
- A. Pouquet and G. S. Patterson. Numerical simulation of helical magnetohydrodynamic turbulence. *J. Fluid Mech.*, **85**:305, 1978.
- E. R. Priest. *Solar Magnetohydrodynamics*. Reidel, 1982.
- K.-H. Rädler, W. H. Matthaeus, and S. Oughton. In preparation, 1993.
- D. A. Roberts. Heliocentric distance and temporal dependence of the interplanetary density-magnetic field magnitude correlation. *J. Geophys. Res.*, **95**:1087, 1990a.
- D. A. Roberts, L. W. Klein, M. L. Goldstein, and W. H. Matthaeus. The nature and evolution of magnetohydrodynamic fluctuations in the solar wind: Voyager observations. *J. Geophys. Res.*, **92**:11 021, 1987a.
- D. A. Roberts, M. L. Goldstein, L. W. Klein, and W. H. Matthaeus. Origin and evolution of fluctuations in the solar wind: Helios observations and Helios-Voyager comparisons. *J. Geophys. Res.*, **92**:12 023, 1987b.
- D. A. Roberts, M. L. Goldstein, and L. W. Klein. The amplitudes of interplanetary fluctuations: Stream structure, heliocentric distance, and frequency dependence. *J. Geophys. Res.*, **95**:4203, 1990.
- D. A. Roberts, S. Ghosh, M. L. Goldstein, and W. H. Matthaeus. Magnetohydrodynamic simulation of the radial evolution and stream structure of solar-wind turbulence. *Phys. Rev. Lett.*, **67**:3741, 1991.
- D. A. Roberts and M. L. Goldstein. Turbulence and waves in the solar wind. *Reviews of Geophysics, Supplement*, page 932, 1991.
- D. A. Roberts, M. L. Goldstein, and S. Matthaeus, William H. Ghosh. Velocity shear generation of solar-wind turbulence. *J. Geophys. Res.*, **97**:17 115, 1992.
- H. P. Robertson. The invariant theory of isotropic turbulence. *Proc. Camb. Phil. Soc.*, **36**:209, 1940.
- H. A. Rose and P. L. Sulem. Fully developed turbulence and statistical mechanics. *Journal de Physique*, **39**:43, 1978.

- J. W. Sari and G. C. Valley. Interplanetary magnetic field power spectra: Mean field radial or perpendicular to radial. *J. Geophys. Res.*, **81**:5489, 1976.
- J. V. Shebalin, W. H. Matthaeus, and D. Montgomery. Anisotropy in mhd turbulence due to a mean magnetic field. *J. Plasma Phys.*, **29**:525, 1983.
- J. A. Shercliff. *A Textbook of Magnetohydrodynamics*. Pergamon Press, Oxford, 1965.
- C. W. Snyder and M. Neugebauer. Interplanetary solar wind measurements by Mariner 2. *Space Res.*, **4**:89, 1964.
- C. V. Solodyna and J. W. Belcher. On the minimum variance direction of magnetic field fluctuations in the azimuthal velocity structure of the solar wind. *Geophys. Rev. Lett.*, **3**:565, 1976.
- M. M. Stanišić. *The Mathematical Theory of Turbulence*. Springer-Verlag, New York, 1988.
- T. Stribling and W. H. Matthaeus. Statistical properties of ideal three-dimensional magnetohydrodynamics. *Phys. Fluids B*, **2**:1979, 1990.
- T. Stribling and W. H. Matthaeus. Relaxation processes in a low order three-dimensional magnetohydrodynamics model. *Phys. Fluids B*, **3**:1848, 1991.
- G. I. Taylor. Statistical theory of turbulence. Parts 1-4. *Proc. R. Soc. London Ser. A*, **151**:421, 1935.
- G. I. Taylor. The spectrum of turbulence. *Proc. R. Soc. London Ser. A*, **164**:476, 1938.
- H. Tennekes and J. L. Lumley. *A First Course in Turbulence*. MIT Press, Cambridge, MA, 1972.
- A. C. Ting, W. H. Matthaeus, and D. Montgomery. Turbulent relaxation processes in magnetohydrodynamics. *Phys. Fluids*, **29**:3261, 1986.
- C. Tu. A solar wind model with the power spectrum of Alfvénic fluctuations. *Solar Phys.*, **109**:149, 1987.
- C.-Y. Tu. The damping of interplanetary Alfvénic fluctuations and the heating of the solar wind. *J. Geophys. Res.*, **93**:7, 1988.
- C.-Y. Tu, Z.-Y. Pu, and F.-S. Wei. The power spectrum of interplanetary Alfvénic fluctuations: Derivation of the governing equation and its solution. *J. Geophys. Res.*, **89**:9695, 1984.
- C.-Y. Tu, E. Marsch, and K. M. Thieme. Basic properties of solar wind mhd turbulence near 0.3 au analyzed by means of Elsässer variables. *J. Geophys. Res.*, **94**:11 739, 1989a.
- C.-Y. Tu, D. A. Roberts, and M. L. Goldstein. Spectral evolution and cascade of solar wind Alfvénic turbulence. *J. Geophys. Res.*, **94**:13 575, 1989b.

- C. Tu, J. Freeman, and R. Lopez. The proton temperature and the total hourly variance of the magnetic field components in different solar wind speed regions. *Solar Phys.*, **119**:197, 1989c.
- C.-Y. Tu and E. Marsch. Evidence for a “background” spectrum of solar wind turbulence in the inner heliosphere. *J. Geophys. Res.*, **95**:4337, 1990a.
- C.-Y. Tu and E. Marsch. Transfer equations for spectral densities of inhomogeneous mhd turbulence. *J. Plasma Phys.*, **44**:103, 1990b.
- C.-Y. Tu and E. Marsch. The evolution of mhd turbulence in the solar wind. In E. Marsch and R. Schwenn, editors, *Proceedings of Solar Wind 7, COSPAR Colloq. Ser.*, volume 3, page 549, Oxford, UK, 1992. Pergamon.
- C.-Y. Tu and E. Marsch. A model of solar wind fluctuations with two components: Alfvén waves and convective structures. *J. Geophys. Res.*, **98**:1257, 1993.
- G. C. Valley. Propagation of hydromagnetic waves in a stochastic magnetic field. *Astrophys. J.*, **168**:251, 1971.
- G. C. Valley. Scattering of Alfvén waves by random density fluctuations. *Astrophys. J.*, **188**:181, 1974.
- M. Velli, R. Grappin, and M. André. The effect of large scale gradients on the evolution of Alfvénic turbulence in the solar wind. In M. A. Dubois, F. Bely-Dubau, and D. Gresillon, editors, *Plasma Phenomena in the Solar Atmosphere*, page 115, France, 1989. Les Editions de Physique.
- M. Velli, R. Grappin, and M. André. Turbulent cascade of incompressible unidirectional Alfvén waves in the interplanetary medium. *Phys. Rev. Lett.*, **63**:1807, 1989.
- M. Velli, R. Grappin, and M. André. Solar wind expansion effects on the evolution of hydro-magnetic turbulence in the interplanetary medium. *Computer Physics Communications*, **59**:153, 1990a.
- M. Velli, R. Grappin, and M. André. Physical consistency in modeling interplanetary magnetohydrodynamic fluctuations. *Phys. Rev. Lett.*, **64**:2592, 1990b.
- M. Velli, R. Grappin, and M. André. Alfvén wave propagation in the solar atmosphere and models of mhd turbulence in the solar wind. In E. Marsch and R. Schwenn, editors, *Proceedings of Solar Wind 7, COSPAR Colloq. Ser.*, volume 3, Oxford, UK, 1992. Pergamon.
- H. J. Völk and W. Alpers. The propagation of Alfvén waves in the azimuthally-dependent interplanetary medium. *Astrophys. Space Sci.*, **36**:383, 1975.
- E. J. Weber and L. Davis. The angular momentum of the solar wind. *Astrophys. J.*, **148**:217, 1967.
- S. Weinberg. Eikonal method in magnetohydrodynamics. *Phys. Rev.*, **126**:1899, 1962.

- Y. C. Whang. Alfvén waves in spiral interplanetary field. *J. Geophys. Res.*, **78**:7221, 1973.
- Y. C. Whang. A magnetohydrodynamic model for corotating interplanetary structures. *J. Geophys. Res.*, **85**:2285, 1980.
- A. Yoshizawa. Ensemble-mean modeling of two-equation type in magnetohydrodynamic turbulent shear flows. *Phys. Fluid*, **31**:311, 1988.
- A. Yoshizawa. Self-consistent turbulent dynamo modeling of reversed field pinches and planetary magnetic fields. *Phys. Fluids*, **B2**:1589, 1990.
- G. P. Zank and W. H. Matthaeus. Nearly incompressible hydrodynamics and heat conduction. *Phys. Rev. Lett.*, **64**:1243, 1990.
- G. P. Zank, W. H. Matthaeus, and L. W. Klein. Temperature and density anti-correlations in the solar wind. *Geophys. Res. Lett.*, **17**:1239, 1990.
- G. P. Zank and W. H. Matthaeus. The equations of nearly incompressible fluids. I. Hydrodynamics, turbulence, and waves. *Phys. Fluids A*, **3**:69, 1991.
- G. P. Zank and W. H. Matthaeus. The equations of reduced magnetohydrodynamics. *J. Plasma Phys.*, **48**:85, 1992a.
- G. P. Zank and W. H. Matthaeus. Waves and turbulence in the solar wind. *J. Geophys. Res.*, **97**:17189, 1992b.
- G. P. Zank and W. H. Matthaeus. Nearly incompressible fluids II: Magnetohydrodynamics, turbulence, and waves. *Phys. Fluids A*, **5**:257, 1993.
- Y. Zhou and W. H. Matthaeus. Non-WKB evolution of solar wind fluctuations: A turbulence modeling approach. *Geophys. Res. Lett.*, **16**:755, 1989.
- Y. Zhou and W. H. Matthaeus. Transport and turbulence modeling of solar wind fluctuations. *J. Geophys. Res.*, **95**:10291, 1990a.
- Y. Zhou and W. H. Matthaeus. Remarks on transport theories of interplanetary fluctuations. *J. Geophys. Res.*, **95**:14863, 1990b.
- Y. Zhou and W. H. Matthaeus. Models of inertial range spectra of interplanetary magnetohydrodynamic turbulence. *J. Geophys. Res.*, **95**:14881, 1990c.
- Y. Zhou, G. Vahala, and M. Hossain. Renormalization-group theory for the eddy viscosity in subgrid modeling. *Phys. Rev. A*, **37**:2590, 1988.
- Y. Zhou, G. Vahala, and M. Hossain. Renormalized eddy viscosity and Kolmogorov's constant in forced Navier-Stokes turbulence. *Phys. Rev. A*, **40**:5865, 1989.
- Y. Zhou and G. Vahala. Hydrodynamic turbulence and subgrid scale closure. *Phys. Lett. A*, **147**:43, 1990.